České vysoké učení technické v Praze, Fakulta strojní, Czech Republic

Von Karman Institute for Fluid Dynamics, Sint-Genesius-Rode, Belgium

Université Libre de Bruxelles, Bruxelles, Belgium

**Disertační práce**
v oboru matematické a fyzikální inženýrství

**Thesis**
in order to obtain the degree of Docteur en Sciences Appliquées

# Numerical Algorithms for the Computation of Steady and Unsteady Compressible Flow over Moving Geometries – Application to Fluid-Structure Interaction

Školitel/supervisor: Prof. Jaroslav Fořt
Prof. Herman Deconinck

2007

Ing. Jiří Dobeš

České vysoké učení technické v Praze, Fakulta strojní, Czech Republic

Von Karman Institute for Fluid Dynamics, Sint-Genesius-Rode, Belgium

Université Libre de Bruxelles, Bruxelles, Belgium

**Disertační práce**
v oboru matematické a fyzikální inženýrství

**Thesis**
in order to obtain the degree of Docteur en Sciences Appliquées

# Numerical Algorithms for the Computation of Steady and Unsteady Compressible Flow over Moving Geometries – Application to Fluid-Structure Interaction

Školitel/supervisor: Prof. Jaroslav Fořt
Prof. Herman Deconinck

2007

Ing. Jiří Dobeš

***Consultation*** ***AUTORISEE***

***(biffez la mention inutile)***

***INTERDITE***

Signature :

Název práce: **Numerické metody pro výpočet stacionárního a nestacionárního stlačitelného proudění s uvažováním pohyblivých geometrií – s aplikací na interakce tekutiny s tělesy**

Autor: Ing. Jiří Dobeš

## Anotace

Tato práce se zabývá vývojem numerických metod pro výpočty stlačitelného proudění s aplikací na interakci tekutiny a elastického tělesa.

Nejprve se zabýváme vývojem numerických metod založených na schématech využívajících distribuci residua (RD). Je presentován rozbor teoretických výsledků pro stabilitu a řád aproximace RD schémat. Reziduální schémata formulovaná pro řešení nestacionárních problémů jsou dále rozšířena pro případ výpočtů na časově proměnných sítích. Dále je pro řešení proudění vyvinuta metoda konečných objemů v cell centered i vertex centered formulaci. RD metoda je srovnána s metodou konečných objemů jednak teoreticky pomocí modifikované rovnice v jednorozměrném případě, tak i porovnáním numerických výsledků řešení skalární rovnice a systému Eulerových rovnic. Je presentováno množství dvou a trojrozměrných stacionárních i nestacionárních případů, dokládajících vlastnosti vyvinutých numerických metod. Výsledky jsou porovnány s teoretickým řešením a experimenty.

Ve druhé části disertační práce je vyvinuta numerická metoda pro řešení problémů interakce proudící tekutiny s tělesy. Problém je rozdělen na tři jednodušší problémy: problém dynamiky tekutin na pohyblivé výpočetní síti, problém pohybu tělesa a problém pohybu výpočetní sítě. Pohyb tělesa je popsán soustavou parciálních diferenciálních rovnic druhého řádu pro elastické anizotropní kontinuum a řešen metodou konečných prvků. Metoda je rozšířena pro výpočet vlastních kmitů tělesa. Pohyb sítě je formulován jako pohyb pseudo-elastického kontinua a opět řešen metodou konečných prvků. Uvedené tři problémy jsou spolu svázány iterační metodou. Vlastnosti metody jsou demonstrovány na případě 2D supersonického třepotání panelu (panel flutter) a 3D transsonického třepotání AGARD křídla. V prvním případě jsou výsledky srovnány s teoretickým řešením a výpočty publikovanými v literatuře, ve druhém případě s experimentem.

Title: **Numerical Algorithms for the Computation of Steady and Unsteady Compressible Flow over Moving Geometries – Application to Fluid-Structure Interaction**

Author: Jiří Dobeš

## Abstract

This work deals with the development of numerical methods for compressible flow simulation with application to the interaction of fluid flows and structural bodies.

First, we develop numerical methods based on multidimensional upwind residual distribution (RD) schemes. Theoretical results for the stability and accuracy of the methods are given. Then, the RD schemes for unsteady problems are extended for computations on moving meshes. As a second approach, cell centered and vertex centered finite volume (FV) schemes are considered. The RD schemes are compared to FV schemes by means of the 1D modified equation and by the comparison of the numerical results for scalar problems and system of Euler equations. We present a number of two and three dimensional steady and unsteady test cases, illustrating properties of the numerical methods. The results are compared with the theoretical solution and experimental data.

In the second part, a numerical method for fluid-structure interaction problems is developed. The problem is divided into three distinct sub-problems: Computational Fluid Dynamics, Computational Solid Mechanics and the problem of fluid mesh movement. The problem of Computational Solid Mechanics is formulated as a system of partial differential equations for an anisotropic elastic continuum and solved by the finite element method. The mesh movement is determined using the pseudo-elastic continuum approach and solved again by the finite element method. The coupling of the problems is achieved by a simple sub-iterative approach. Capabilities of the methods are demonstrated on computations of 2D supersonic panel flutter and 3D transonic flutter of the AGARD 445.6 wing. In the first case, the results are compared with the theoretical solution and the numerical computations given in the references. In the second case the comparison with experimental data is presented.

**Key words:** Residual distribution scheme, Finite volume method, ALE method, Unsteady method, Implicit method, Parallel method, Unsteady flows, Aeroelasticity, Three field formulation, Finite element method, CFD, AGARD 445.6 wing, Panel flutter.

# Contents

# List of Symbols

$\mathcal{A}_t$ – ALE mapping
$CFL$ – Courant–Friderichs–Lewy number [CFL28, CFL67]
$E$ [J·kg$^{-1}$] – specific total energy
$E$ – element
$E$ [Pa] – Young's modulus
$E_i$ – element with index $i$
$G$ [Pa] – shear modulus
$H$ [J·kg$^{-1}$] – specific total enthalpy
$\mathbf{I}$ – indentity matrix
$J_{\mathcal{A}_t}$ – determinant of the Jacobian of the ALE mapping
$Ma$ [1] – Mach number
$N \equiv (\sum_{i \in E} k_i^+)^{-1}$ – see eq. (3.36)
$\mathbf{N} \equiv (\sum_{i \in E} \mathbf{k}_i^+)^{-1}$ – see eq. (3.39)
$\mathbb{R}$ – set of real numbers
$S_i$ – median dual cell around node $i$
$U$ – algebraic vector of all degrees of freedom in the domain
$\vec{Y}$ [m] – Cartesian system of coordinates in reference configuration

$c_p$ [1] – pressure coefficient
$d$ – number of spatial dimensions
$\vec{\mathbf{f}}$ – vector of flux functions, $\vec{\mathbf{f}}(\mathbf{u}) : \mathbb{R}^q \rightarrow \mathbb{R}^{q \times d}$
$\vec{f}$ [N] – force vector
$h$ – reference mesh spacing
$h^{\text{ball}}$ – equivalent mesh spacing
$k_j$ – upwind parameter for node $j$
$\mathbf{k}_j$ – upwind matrix of size $q \times q$ for node $j$
$m$ – pseudo (or dual) time–step level
$m_{ij}^E$ – element contribution to the mass matrix
$n$ – time–step level
$\vec{n}_i^E$ – normal to the face opposite of node $i$ scaled by its surface, pointing inwards with respect to elemet $E$
$q$ – number of conserved variables
$p$ [Pa] – static pressure

$t$ [s] – time
$u$ – conserved variable, $u(\vec{x}, t) : \mathbb{R}^{d+1} \rightarrow \mathbb{R}$
$u^0$ – initial conditions; $u(\vec{x}, 0) = u^0(\vec{x})$
$\mathbf{u}$ – conserved set of variables, $\mathbf{u}(\vec{x}, t) : \mathbb{R}^{d+1} \rightarrow \mathbb{R}^q$
$\vec{u}$ [m] – displacement vector
$V$ [m·s$^{-1}$] – magnitude of fluid velocity
$\mathbf{v}$ – primary variable
$\vec{v}$ [m·s$^{-1}$] – gas velocity
$\vec{w}$ [m·s$^{-1}$] – domain velocity
$\vec{x} \equiv (x, y, z)$ [m] – Cartesian system of coordinates (in current configuration)
$\mathbf{z}$ – Roe's parameter vector

$\beta_i$ – distribution coefficient
$\beta_i$ – distribution matrix of size $q \times q$
$\gamma$ – ratio of specific heats; $\gamma = 1.4$ if not specified otherwise
$\delta_{ij}$ – Kronecker delta symbol ($\delta_{ij} = 1$ if $i = j$, else $\delta_{ij} = 0$)
$\varepsilon$ [1] – strain tensor
$\rho$ [kg·m$^{-3}$] – density
$\phi^E$, $\phi$ – element residual
$\phi_i^E$, $\phi_i$ – portion of the residual $\phi^E$ of element $E$ distributed to node $i$
$\psi_i$ – trial function; unit at node $i$, zero for all the other nodes
$\mu$ [Pa] – Lamé parameter
$\nu$ [1] – Poisson ratio
$\vec{\lambda}(\vec{x}, t) \equiv \partial \vec{\mathbf{f}} / \partial \mathbf{u}$ – vector of Jacobian matrices (or advection vector for scalar advection equation)
$\lambda$ [Pa] – Lamé parameter
$\sigma$ [Pa] – stress tensor
$\varphi_i$ – test function
$\tau$ – pseudo-time (or dual time)
$\mathcal{T}^h$ – computational mesh
$\partial \cdot$ – boundary of $\cdot$
$\mu(\cdot)$ – measure of $\cdot$ (volume or surface)
$\Pi^E(x)$ – is characteristic function of the element, unit inside element $E$, zero elsewhere
$\Gamma$ – set of states

$\nabla \equiv (\partial/\partial x, \partial/\partial y, \dots)$ – Hamilton's nabla operator
$[\cdot, \cdot]$ – closed interval
$]\cdot, \cdot[$ – open interval
$\cdot$ – dot product

## Subscripts and superscripts

| | |
|---|---|
| $\mathbf{1}$ | – unit vector |
| $h$ | – numerical approximation |
| $+$ | – non-negative number, $(\cdot)^+ \equiv \max(\cdot, 0)$ |
| $+$ | – positive part of matrix, $(\cdot)^+ \equiv \mathbf{R}\mathbf{\Lambda}^+\mathbf{L}$, $\mathbf{\Lambda}^+ = \mathrm{diag}(\lambda_i^+)$ |
| $-$ | – non-positive number, $(\cdot)^- \equiv \min(\cdot, 0)$ |
| $-$ | – negative part of matrix, $(\cdot)^- \equiv \mathbf{R}\mathbf{\Lambda}^-\mathbf{L}$, $\mathbf{\Lambda}^- = \mathrm{diag}(\lambda_i^-)$ |
| overbar $(\bar{\cdot})$ | – variable from Roe-Struijs-Deconinck linearization [DRS93], see section 3.1. |

## Typographical convention

| | |
|---|---|
| **boldface** | – vector of size $q$, typically unknowns or fluxes |
| **boldface** | – matrix |
| arrow $\vec{\cdot}$ | – spatial vector (which transforms as it is defined in the tensor theory) |

## Loop notation

| | |
|---|---|
| $E \in \mathcal{D}_i$ | – all elements $E$ sharing node $i$. |
| $i \in E$ | – all nodes $i$ in element $E$. |
| $j \in \mathcal{D}_i$ | – all nodes $j$ belonging to elements $E \in \mathcal{D}_i$ |
| $i \in \mathcal{T}^h$ | – all the nodes in the computational domain |
| $E \in \mathcal{T}^h$ | – all the elements in the computational domain |

## Abbreviations

| | |
|---|---|
| 3BDF | – three points backward differentiation formula, see eq. (3.79) |
| ALE | – arbitrary Lagrangian–Eulerian |
| B | – blended scheme [CDP01] |
| Bx | – blended scheme [DD05a] |
| CC | – cell centered finite volume scheme |
| CFD | – computational fluid dynamics |
| CSM | – computational structural mechanics |
| CV | – vertex centered finite volume scheme |
| DOF | – degree of freedom |
| FE | – finite element |
| FEM | – finite element method |
| FSI | – flud–structure interaction |
| FV | – finite volume (method in a sense of [Krö97]) |

| | |
|---|---|
| FV1 | – finite volume method with constant reconstruction |
| FV2 | – finite volume method with linear reconstruction |
| FVM | – finite volume method |
| GCL | – geometrical conservation law |
| LDA | – low diffusion A scheme |
| N | – narrow scheme |
| PG | – Petrov-Galerkin |
| RD | – residual distribution |
| RDS | – residual distribution scheme (method in a sense of [Krö97]) |
| ST | – space–time |
| VC | – vertex centered finite volume scheme |

# Chapter 1.

# Introduction

## 1.1. Motivation and global objectives of the thesis

A large number of methods is available for the solution of compressible flows today. They operate on structured or unstructured meshes. Since structured mesh generation is one of the biggest bottlenecks for industrial type simulations, see e.g. [Ath05], we will focus on methods working on unstructured meshes. One of the most commonly used methods for industrial type compressible flow simulations on unstructured meshes is the finite volume method in cell centered or vertex centered settings, see e.g. [Krö97, BO04]. Despite its large popularity, there are still some problems unresolved, namely accuracy for the flow features not aligned with the mesh, and dependence of the scheme on 1D physics introduced by the numerical flux.

As a cure to the above-mentioned problems, the residual distribution (RD) schemes were suggested in [Roe82]. Since then, a successful development was sought. Nowadays, RD schemes can be used to solve complex problems such as 3D inviscid flows around a full aircraft or 3D turbulent flow past a wing. A first objective of the thesis is to select several residual distribution schemes and to investigate their properties for well defined test cases. Then the schemes should be applied to technically important problems and problems of mathematical physics.

The fluid–structure interaction problems ultimately call for highly accurate methods. Since RD schemes are expected to be more accurate than traditional finite volume schemes, the use of RD methods for fluid–structure interaction problems is appealing. Until recently, only first order RD schemes for moving grids computations were available, see [MSD03]. Hence, a second objective of the thesis is to explore possible extension of higher order accurate RD schemes for computations on moving meshes with application to aeroelastic simulations.

## 1.2. Survey of state-of-the-art technique in the field

### 1.2.1. Numerical methods for fluid dynamics

Current state-of-the-art CFD methods can be characterized by their nature as methods working on structured meshes and methods working on unstructured meshes. The structured mesh generation procedure for industrial type of computations is difficult and it is one of the biggest bottlenecks [Ath05] for numerical simulations. For this reason, we focus exclusively on the computational methods utilizing unstructured meshes.

From modern numerical methods for compressible flows *working on unstructured meshes* one can select several important groups:

- Finite element methods with continuous solution approximation, see e.g. [TS06, Tez04].

  The streamline upwind Petrov-Galerkin method for compressible flow simulations was pioneered by [TH82]. The finite element test functions are modified by inclusion of extra term, such that the stabilization of the method is achieved. The scheme was supplemented by a shock capturing term in [HFM87]. An overview of the development can be found in [Tez04]. This scheme in space-time setting was successfully used for large scale computations, e.g. flow past full helicopter or large eddy simulation of turbulent flows.

- Finite volume methods, see e.g. [Bar94, BO04, LeV02, Krö97, Jam04].

  Finite volume schemes on unstructured meshes were pioneered by [JBW86], [MJ87]. They used a central scheme with artificial dissipation of scalar type. The method is formally second order accurate on smooth flows and satisfies the discrete maximum principle for scalar problems. This was one of the first methods capable to solve the system of Euler equations for full aircraft configuration on unstructured meshes.

  The vertex centered upwind finite volume method was among others developed by [BJ89]. The integral form of the conservation form was expressed on each control volume. In this case, the control volume was constructed using the dual mesh to the computational grid. Higher order of accuracy was achieved by the linear reconstruction. Non-oscillatory properties of the scheme are guaranteed with help of limiters. This method has proven to be very successful, it was later extended to many variants. The numerical flux on the boundary of the finite volume is approximated by solving a Riemann problem or other types of flux splitting, e.g. Roe's Riemann solver [Roe81] or AUSM scheme [LCJS93]. The higher order spatial accuracy can be achieved with the aid of linear, quadratic [BF90, Bar93], or even higher order [Shu03] reconstruction. The time derivative can be discretized with explicit Euler or Runge-Kutta

methods [GS98, GST01], implicit backward differentiation formula or implicit Runge-Kutta methods [JMC03]. The important references for the extension of the method to moving mesh computations include [KF99, Far04]. Similar method exist in the cell centered settings.

- Discontinuous Galerkin methods, see e.g. [Coc04, Coc99].

  The method is based on a finite element discretization, however jumps in the solution on each face of an element are allowed. Similar to the above described finite volume method, a numerical flux has to be approximated on the element edges. Limiters [Coc04] or artificial viscosity [KvdVvdV06] are used for stabilization in case of shocks. The solution is advanced by Runge-Kutta scheme, or alternatively the discontinuous Galerkin method is re-casted in a space-time formulation and a steady problem in space-time is solved [KvdVvdV06]. Currently, the method in its second order space-time version is used e.g. for 3D aeroelastic simulation of aircraft wings.

- Residual distribution methods, see e.g. [DSA00, AM04, Dec03, DRS03, AM03a].

  The scheme can be seen either as a finite volume method, where the residual is computed over a finite element and subsequently distributed, or as a finite element method with explicitly given test function. Second order accurate non-oscillatory schemes are available for technical computations of inviscid [GW01] and turbulent flows [SD03]. Extension to higher order of accuracy is subject of current research [RVAD05, RVAD07, HL05, CF05, Hub06, TA06]. Most of the available theory on the RD schemes is included in von Karman lecture series [Dec03] and [DR05], journal papers [Abg01, AM04, AM03a] and PhD thesis [Ric05]. As the other sources we can cite [SR95, HR00, AR03, NR04], [AB02] and [CPNP96, PPRN05]. The development of the RD schemes can be tracked by a number of PhD thesis [Pai95, Iss97, vdW98, Car00, Csí02, Mez02, Ric05] and von Karman Lecture series 1991–01, 1993–04, 1994–05, 1995–02, 1997–02, 1998–03, 2003–05, 2006–01.

- There exist a number of methods under development, which do not naturally belong to any of the mentioned groups. We mention the residual based compact schemes of [CBK06], which are the extension of the work of [LC01] to unstructured meshes. The performance of the method was demonstrated on 2D inviscid transonic airfoil simulation [CBK06]. An other approach is the spectral volume method, see e.g. [SWL06] and references therein, allowing to construct schemes of arbitrary high order of accuracy with non-oscillatory properties. The performance of this method was demonstrated on several well known test cases and low speed 3D flow around a rotating propeller.

In this thesis we focus on the finite volume (FV) methods and on residual distribution (RD) methods. For the first part of the thesis the most important references are

[Bar94, Roe81, Dec03, AM04, AM03a, Far04] and [Ric05]. An excellent (but rather expensive) reference for the modern methods in computational fluid dynamics is [SdBH04].

### 1.2.2. Fluid-structure interaction problems

Methods for the computation of fluid-structure interaction problems have emerged aside of the development of accurate methods for computational fluid dynamics. These include fluid-structure interaction between bodies with two degrees of freedom [AJ94], or later bodies modeled by the finite element method [ZT00a, DT85]. For a survey of the high-speed-flow computational aeroelasticity, see [Far04], which is also the most important reference for the second part of the thesis.

## 1.3. Specific objectives of the thesis

The goals of the presented work are:

1. To develop a numerical method based on selected schemes of residual distribution type and to analyse some of their properties. Eventually find possible improvements for particular flow problems. Develop an extension for problems involving a time dependent domain of solution.

2. To develop a numerical method based on a finite volume method in cell centered or vertex centered formulation. Include the possibility of handling a time dependent domain of solution.

3. To test selected numerical methods on problems of scalar conservation law and system of Euler equations, with particular attention to the accuracy of the schemes and monotone capturing of complex solution features.

4. To develop a finite element method for the problem of elasticity, where the material is modeled as an elastic continuum allowing large displacements and taking into account possible anisotropic material properties.

5. To develop and validate the numerical method for fluid structure interaction problems, where the flow is modeled as a inviscid perfect gas and the body either as a elastic continuum or by a system of two ordinary differential equations.

# Part I.

# Numerical methods for fluid dynamics

# Chapter 2.

# Mathematical formulation of the problem

The basic formulation of problems governed by conservation laws is described in many mathematical books, see, e.g. [GR96, LeV99, LeV02, Fei93, FFS03]. The formulation on moving domains using the Arbitrary Lagrangian-Eulerian (ALE) method can be found in [FN04, FN99, FGG01, HS02, Fei93, GR96] and many articles in leading scientific journals, e.g. in *Journal of Computational Physics* and *Computer Methods in Applied Mechanics and Engineering.*

## 2.1. The system of conservation laws in a fixed reference frame

In this section, we shall introduce a general formulation of a system of conservation laws in $d$ spatial dimensions with classical and weak solutions of the problem. The problems of finite domain and boundary conditions are not discussed. The discussion of the appropriate boundary conditions is postponed to the sections related to the concrete physical system of conservation laws.

### 2.1.1. System of conservation laws

Let $\Gamma$ be an open subset of $\mathbb{R}^q$, and let $\mathbf{f}_j$, $1 \leq j \leq d$, be $d$ smooth functions from $\Gamma$ into $\mathbb{R}^q$; the general form of a system of conservation laws in $d$ space variables is

$$\frac{\partial \mathbf{u}}{\partial t} + \sum_{j=1}^{d} \frac{\partial}{\partial x_j} \mathbf{f}_j(\mathbf{u}) = \mathbf{0}, \qquad \vec{x} = (x_1, \ldots, x_d) \in \mathbb{R}^d, \quad t > 0, \tag{2.1}$$

where

$$\mathbf{u} = (u_1, \ldots, u_q) \tag{2.2}$$

is a vector-valued function from $\mathbb{R}^d \times [0, +\infty[$ into $\Gamma$. The set $\Gamma$ is called the set of states and the functions

$$\mathbf{f}_j = (f_{j_1}, \ldots, f_{j_q}) \tag{2.3}$$

are called flux functions. One says that the system (2.1) is written in *conservative form*.

### 2.1.2. Initial value problem

The system of conservation laws has to be equipped with initial and boundary conditions. Since the formulation involving boundary condition is still an open problem [Fei93], we shall introduce only the initial value problem, and the boundary conditions are discussed separately within the context of the concrete physical systems in section 2.3. The boundary conditions and initial-boundary value problem are discussed in, e.g., [Fei93] and [GR96].

Let us define the *Cauchy problem*, or *initial value problem (IVP)*: Find a function $\mathbf{u} : (\vec{x}, t) \in \mathbb{R}^d \times [0, +\infty[ \rightarrow \mathbf{u}(\vec{x}, t) \in \Gamma$ such that (2.1) holds and the initial condition

$$\mathbf{u}(\vec{x}, 0) = \mathbf{u}^0(\vec{x}), \qquad \vec{x} \in \mathbb{R}^d, \tag{2.4}$$

is satisfied. The function $\mathbf{u}^0 : \mathbb{R}^d \rightarrow \Gamma$ is the initial comdition.

**Definition 1 (Classical solution).** We shall say that a function $\mathbf{u} : \mathbb{R}^d \times [0, +\infty[ \rightarrow \Gamma$ is the *classical solution* of (2.1), (2.4) if the function $\mathbf{u} \in C^1(\mathbb{R}^d)$ and satisfies the equations (2.1), (2.4) pointwise.

The essential feature of the problem (2.1), (2.4) is that there do not exist in general classical solutions of (2.1), (2.4) beyond some finite time interval, even when the initial condition $\mathbf{u}^0$ is a very smooth function, see, e.g., [GR96, LeV99, LeV02, Maj84].

**Definition 2 (Weak solution).** Assume that the function $\mathbf{u}^0 \in L^\infty_{\mathrm{loc}}(\mathbb{R}^d)^q$. A function $\mathbf{u} \in L^\infty_{\mathrm{loc}}(\mathbb{R}^d \times [0, +\infty[)^q$ is called a *weak solution* of the Cauchy problem (2.1), (2.4) if $\mathbf{u}(\vec{x}, t) \in \Gamma$ almost everywhere and satisfies

$$\int_0^\infty \int_{\mathbb{R}^d} \left( \mathbf{u} \frac{\partial \varphi}{\partial t} + \sum_{j=1}^{d} \mathbf{f}_j(\mathbf{u}) \frac{\partial \varphi}{\partial x_j} \right) \mathrm{d}\vec{x}\, \mathrm{d}t + \int_{\mathbb{R}^d} \mathbf{u}^0(\vec{x})\, \varphi(\vec{x}, 0)\, \mathrm{d}\vec{x} = \mathbf{0} \tag{2.5}$$

for any function $\varphi \in C_0^1(\mathbb{R}^d \times [0, +\infty[)^q$.

Additional information about classical and weak solutions can be found in references [GR96, LeV99, LeV02, RR92, Fei93].

## 2.2. System of conservation laws in the moving reference frame

In this section the system of conservation laws in the moving reference frame is derived with the aid of the Arbitrary Lagrangian-Eulerian (ALE) formulation.

### 2.2.1. ALE mapping

First, the family of homeomorphic mappings $\mathcal{A}_t$ is defined. The mapping $\mathcal{A}_t$ is called the ALE mapping [FN04], which for each $t \in [0, +\infty[$ associates a point $\vec{Y}$ of reference configuration $\Omega_0$ to a point $\vec{x}$ on the current domain configuration $\Omega_t$:

$$\mathcal{A}_t : \Omega_0 \subset \mathbb{R}^d \to \Omega_t \subset \mathbb{R}^d, \qquad \vec{x}(\vec{Y}, t) = \mathcal{A}_t(\vec{Y}). \tag{2.6}$$

Let $f : \Omega_t \times [0, +\infty[ \to \mathbb{R}$. We will denote by $\hat{f} := f \circ \mathcal{A}_t$ the corresponding function on the ALE reference frame, i.e.

$$\hat{f} : \Omega_0 \times [0, +\infty[ \to \mathbb{R}, \qquad \hat{f}(\vec{Y}, t) = f(\mathcal{A}_t(\vec{Y}), t). \tag{2.7}$$

For later use, the mapping has to satisfy the assumptions of Theorem 3. Note, that the mapping is rather arbitrary except for the fact that $\mathcal{A}_t(\partial\Omega_0) = \partial\Omega_t$ for all $t \in [0, +\infty[$.

The Jacobian of the ALE mapping exists and its determinant is defined as

$$\mathbf{J}_{\mathcal{A}_t} = \frac{\partial \vec{x}}{\partial \vec{Y}}, \qquad J_{\mathcal{A}_t} = \det(\mathbf{J}_{\mathcal{A}_t}). \tag{2.8}$$

We define the domain velocity $\hat{\vec{w}}$ as

$$\hat{\vec{w}}(\vec{Y}, t) = \frac{\partial \vec{x}(\vec{Y}, t)}{\partial t}. \tag{2.9}$$

It can be expressed in terms of current domain coordinates, where

$$\vec{w}(\vec{x}, t) = \left.\frac{\partial \vec{x}}{\partial t}\right|_{\vec{Y}} (\vec{Y}(\vec{x}, t), t) \tag{2.10}$$

is the corresponding function in $\Omega_t \times [0, +\infty[$.

The relation between the time derivative of the Jacobian $J_{\mathcal{A}_t}$ and the divergence of the domain velocity $\vec{w}$ is given by the following theorem. For the reference, see, e.g. [Fei93] and [GR96].

**Theorem 3.** *Let $t \in [0, +\infty[$, $\vec{Y} \in \Omega_0$ and the following conditions be satisfied*

1. *Mapping $\mathcal{A}_t$ (see (2.6)) has continuous first order partial derivatives with respect to the variables $t$, $Y_i, \ldots, Y_d$ and continuous second order derivatives $\partial^2 x_i / \partial t \, \partial Y_j$, $i, j = 1, \ldots, d$.*

2. *Mapping (2.6) is a continously differentiable one-to-one mapping of $\Omega_0$ onto $\Omega_t$ with the Jacobian $J_{\mathcal{A}_t}$ (defined by (2.8)), which is continuous and bounded and satisfies the condition*

$$J_{\mathcal{A}_t}(\vec{Y}, t) > 0 \qquad \forall \vec{Y} \in \Omega_0, \quad \forall t \in [0, +\infty[. \tag{2.11}$$

3. *The domain velocity* $\vec{w}(\vec{x},t)$ *(defined by* (2.10)*) has continuous bounded first order derivatives on the set* $\{(\vec{x},t); t \in [0,+\infty[, \vec{x} \in \Omega_t\}$.

*Then the function* $J_{\mathcal{A}_t} = J_{\mathcal{A}_t}(\vec{Y},t)$ *has a continuous and bounded partial derivative* $\partial J_{\mathcal{A}_t}/\partial t$ *for* $\vec{Y} \in \Omega_0$, $t \in [0,+\infty[$ *and*

$$\frac{1}{J_{\mathcal{A}_t}(\vec{Y},t)} \frac{\partial J_{\mathcal{A}_t}}{\partial t}(\vec{Y},t) = \nabla_x \cdot \vec{w}(\vec{x},t). \tag{2.12}$$

*Proof.* See [Fei93, GR96]. Jacobian determinant $J_{\mathcal{A}_t}(\vec{Y},t)$ can be expanded by its $i$-th row:

$$J_{\mathcal{A}_t}(\vec{Y},t) = \sum_{\alpha=1}^{d} \frac{\partial x_i}{\partial Y_\alpha}(\vec{Y},t) D_{i,\alpha}(\vec{Y},t), \tag{2.13}$$

where $D_{i,\alpha}$ denotes the cofactor of element $\partial x_i/\partial Y_\alpha$. For $\alpha, \beta = 1, \ldots, d$, the cofactors $D_{i,\beta}$ are independent of $\partial x_i/\partial Y_\alpha$. Hence,

$$\frac{\partial J_{\mathcal{A}_t}}{\partial \left(\frac{\partial x_i}{\partial Y_\alpha}\right)} = D_{i,\alpha}. \tag{2.14}$$

In order to calculate the derivative $\partial J_{\mathcal{A}_t}/\partial t$ we consider the determinant $J_{\mathcal{A}_t}(\vec{Y},t)$ as a function dependent on elements $\partial x_i/\partial Y_\alpha$ which depend on $t$:

$$\frac{\partial J_{\mathcal{A}_t}}{\partial t} = \sum_{\alpha=1}^{d} \frac{\partial J_{\mathcal{A}_t}}{\partial \left(\frac{\partial x_i}{\partial Y_\alpha}\right)} \frac{\partial}{\partial t}\left(\frac{\partial x_i}{\partial Y_\alpha}\right) = \sum_{\alpha=1}^{d} D_{i,\alpha} \frac{\partial^2 x_i}{\partial Y_\alpha \partial t}. \tag{2.15}$$

Now let us deal with derivative $(\partial^2 x_i/\partial Y_\alpha \partial t)(\vec{Y},t)$. Under the assumptions of the Theorem 3 we get

$$\frac{\partial^2 x_i}{\partial Y_\alpha \partial t}(\vec{Y},t) = \frac{\partial^2 x_i}{\partial t \partial Y_\alpha}(\vec{Y},t) = \frac{\partial}{\partial Y_\alpha} w_i(\vec{x}(\vec{Y},t),t)) = \sum_{j=1}^{d} \frac{\partial w_i}{\partial x_j}(\vec{x},t) \frac{\partial x_j}{\partial Y_\alpha}(\vec{Y},t). \tag{2.16}$$

Substituting into the equation (2.15), we have

$$\frac{\partial J_{\mathcal{A}_t}}{\partial t} = \sum_{i,\alpha=1}^{d} D_{i,\alpha} \sum_{j=1}^{d} \frac{\partial x_j}{\partial Y_\alpha} \frac{\partial w_i}{\partial x_j} = \sum_{i,j=1}^{d} \left( \sum_{\alpha=1}^{d} \frac{\partial x_j}{\partial Y_\alpha} D_{i,\alpha} \right) \frac{\partial w_i}{\partial x_j}. \tag{2.17}$$

For determinants following holds

$$\sum_{\alpha=1}^{d} \frac{\partial x_j}{\partial Y_\alpha} D_{i,\alpha} = J_{\mathcal{A}_t} \delta_{ij} \tag{2.18}$$

and thus

$$\frac{\partial J_{\mathcal{A}_t}}{\partial t} = J_{\mathcal{A}_t} \sum_{i,j=1}^{d} \delta_{ij} \frac{\partial w_i}{\partial x_j} = J_{\mathcal{A}_t} \sum_{i=1}^{d} \frac{\partial w_i}{\partial x_i} = J_{\mathcal{A}_t} \nabla_x \cdot \vec{w}. \tag{2.19}$$

□

### 2.2.2. System of conservation laws

The total amount of the conserved quantity $\mathbf{u}$ in the time dependent control volume $\Omega_t$ can be computed as

$$\int_{\Omega_t} \mathbf{u} \, \mathrm{d}\vec{x}. \tag{2.20}$$

The flux bringing the quantity inside the control volume is given by the physical flux $\vec{\mathbf{f}}(\mathbf{u})$ minus the flux induced by the movement of the boundary of the control volume

$$\vec{\mathbf{f}}^{\mathrm{ALE}}(\mathbf{u}) = \vec{\mathbf{f}}(\mathbf{u}) - \mathbf{u}\vec{w}. \tag{2.21}$$

The system of conservation laws can be written in the integral form as

$$\left.\frac{\partial}{\partial t}\right|_{\vec{Y}} \left( \int_{\Omega_t} \mathbf{u} \, \mathrm{d}\vec{x} \right) + \oint_{\partial\Omega_t} [\vec{\mathbf{f}}(\mathbf{u}) - \mathbf{u}\vec{w}] \cdot \mathrm{d}\vec{n} = \mathbf{0}, \tag{2.22}$$

where $\vec{n}$ is the outer normal to the surface $\partial\Omega_t$. The second integral is recast from the contour integral to the volume integral using the Gauss-Ostrogradski theorem

$$\left.\frac{\partial}{\partial t}\right|_{\vec{Y}} \left( \int_{\Omega_t} \mathbf{u} \, \mathrm{d}\vec{x} \right) + \int_{\Omega_t} \vec{\nabla}_x \cdot [\vec{\mathbf{f}}(\mathbf{u}) - \mathbf{u}\vec{w}] \, \mathrm{d}\vec{x} = \mathbf{0}. \tag{2.23}$$

The ALE mapping is a homeomorphism with the continuous partial derivatives and $J_{\mathcal{A}_t} \neq 0$, hence we can use the substitution theorem in the first integral, see, e.g. [Rek95],

$$\left.\frac{\partial}{\partial t}\right|_{\vec{Y}} \left( \int_{\Omega_0} \mathbf{u} J_{\mathcal{A}_t} \, \mathrm{d}\vec{Y} \right) + \int_{\Omega_0} \vec{\nabla}_x \cdot [\vec{\mathbf{f}}(\mathbf{u}) - \mathbf{u}\vec{w}] J_{\mathcal{A}_t} \, \mathrm{d}\vec{Y} = \mathbf{0}. \tag{2.24}$$

The reference domain $\Omega_0$ and the coordinates $\vec{Y}$ do not depend on time $t$, the integrand is integrable, hence

$$\int_{\Omega_0} \left( \left.\frac{\partial J_{\mathcal{A}_t}\mathbf{u}}{\partial t}\right|_{\vec{Y}} + \vec{\nabla}_x \cdot [\vec{\mathbf{f}}(\mathbf{u}) - \mathbf{u}\vec{w}] J_{\mathcal{A}_t} \right) \mathrm{d}\vec{Y} = \mathbf{0}. \tag{2.25}$$

The equation has to be valid independently of the control volume $\Omega_0$, i.e. the integrand has to be zero almost everywhere. Jacobian $J_{\mathcal{A}_t}$ being nonzero, the equation can be rewritten as

$$\left.\frac{1}{J_{\mathcal{A}_t}} \frac{\partial J_{\mathcal{A}_t}\mathbf{u}}{\partial t}\right|_{\vec{Y}} + \vec{\nabla}_x \cdot [\vec{\mathbf{f}}(\mathbf{u}) - \mathbf{u}\vec{w}] = \mathbf{0}. \tag{2.26}$$

This is the *conservative Arbitrary Lagrangian-Eulerian form of the system of conservation laws*. If the solution is sufficiently smooth, it is equal to

$$\left.\frac{1}{J_{\mathcal{A}_t}} \frac{\partial J_{\mathcal{A}_t}\mathbf{u}}{\partial t}\right|_{\vec{Y}} + \vec{\nabla}_x \cdot \vec{\mathbf{f}}(\mathbf{u}) - \vec{w} \cdot \vec{\nabla}_x \mathbf{u} - \mathbf{u}\vec{\nabla}_x \cdot \vec{w} = \mathbf{0}. \tag{2.27}$$

The last term, $\mathbf{u}\vec{\nabla}_x \cdot \vec{w}$, is the *geometrical source term* and it is equal to zero for non-deforming meshes. Another way to obtain this equation is via the Reynolds transport theorem, see e.g. [Mar99].

Similarly as in Definition 2, we can define the weak solution of the equation (2.26):

**Definition 4 (Weak solution of the ALE problem).** Assume that $\mathbf{u}^0 \in L^\infty_{\mathrm{loc}}(\mathbb{R}^d)^q$. A function $\mathbf{u} \in L^\infty_{\mathrm{loc}}(\mathbb{R}^d \times [0, +\infty[)^q$ is called the *weak solution* of the Cauchy problem (2.26), (2.4), if the function $\mathbf{u}(\vec{x}, t) \in \Gamma$ almost everywhere and

$$\int_{\mathbb{R}^+}\int_{\mathbb{R}^d}\left(\mathbf{u}\left.\frac{\partial J_{\mathcal{A}_t}\varphi}{\partial t}\right|_{\vec{Y}} + \sum_{j=1}^{d}[\mathbf{f}_j(\mathbf{u}) - w_j\mathbf{u}]\frac{\partial J_{\mathcal{A}_t}\varphi}{\partial x_j}\right)\mathrm{d}\vec{x}\,\mathrm{d}t + \int_{\mathbb{R}^d}\mathbf{u}^0(\vec{x})\,\varphi(\vec{x},0)\,\mathrm{d}\vec{x} = \mathbf{0} \quad (2.28)$$

holds for any function $\varphi \in C^1_0(\mathbb{R}^d \times [0, +\infty[)^q$.

The system of conservation laws admits an arbitrary nonzero constant function $\mathbf{u}^c \in \Gamma \subset \mathbb{R}^q$ as exact solution. Then $\vec{\nabla}_x \cdot \vec{\mathbf{f}}(\mathbf{u}^c)$ is identically zero and the conserved variable $\mathbf{u}^c$ can be taken out of the differential operators, which leads to the important equivalence

$$\frac{1}{J_{\mathcal{A}_t}}\left.\frac{\partial J_{\mathcal{A}_t}}{\partial t}\right|_{\vec{Y}} = \nabla_x \cdot \vec{w}. \quad (2.29)$$

This is the (continuous) *Geometric Conservation Law*. It is the same relation as (2.12).

## 2.3. Examples of physical systems written as conservation laws

In this section we shall introduce concrete physical models for the conservation laws discussed in this thesis.

### 2.3.1. Scalar conservation laws

We consider scalar conservation laws, i.e. the number of conserved variables is $q = 1$.

#### 2.3.1.1. Constant advection equation

The vector of flux functions is defined as $\vec{f}(u) = \vec{\lambda}u$, where $\vec{\lambda} \in \mathbb{R}^d$ is an arbitrary constant nonzero vector.

#### 2.3.1.2. 2D and 3D circular advection equation

The flux vector is defined as

$$\vec{f}(u; x, y) = (-yu, xu) \tag{2.30}$$

for the 2D case, and $\vec{f}(u; x, y, z) = (-yu, xu, 0)$ for the 3D case.

#### 2.3.1.3. 1D Burgers equation and 2D variant

The flux vector is defined as $\vec{f}(u) = (u^2/2)$. This case can be extended to two dimensions (see, e.g. [Pai95, Bar94]): the flux vector is defined as $\vec{f}(u) = (u^2/2, u)$.

### 2.3.2. System of Euler equations

The Euler equations in $d$ spatial dimensions is the system of $q = d + 2$ conservation laws (2.1) given by conserved variables

$$\mathbf{u} = (\rho, \rho\vec{v}, E), \tag{2.31}$$

where $\rho$ is the density, $\vec{v} = (v_1, \ldots, v_d)$ are the components of the velocity vector and $E$ is the total energy. The flux is

$$\mathbf{f}_i = (\rho v_i, \rho v_i v_j + \delta_{ij} p, [E + p] v_i), \qquad 1 \leq j \leq d, \tag{2.32}$$

where $p$ is the static pressure and $\delta_{ij}$ is Kronecker delta symbol. The system is closed by a thermodynamic equation for the pressure $p = f(\mathbf{u})$. We will only consider a perfect gas, then the equation is given by

$$p = (\gamma - 1)\left(E - \frac{1}{2}\rho \sum_{i=1}^{d} v_i^2\right). \tag{2.33}$$

The ratio of the specific heat for a diatomic gas is used, i.e. $\gamma = 1.4$ (if not specified otherwise). The system is equipped with an entropy inequality, see, e.g. [GR96, LeV99, LeV02, Fei93, FFS03, Mar99, Krö97].

# Chapter 3.

# Residual distribution scheme

Several methods based on the distribution of the residual have been developed in the past, see e.g. [Ni81, Roe82], for a survey see e.g. [Pai95]. This part of the work deals with residual distribution schemes as defined in [Krö97], i.e. schemes, which are usually written as in section 3.2 and 3.3. Such schemes will be referred as *residual distribution schemes.*

The class of residual distribution (RD) schemes (or fluctuation splitting schemes) was introduced by P. L. Roe in [Roe82]. Since then the schemes were developed for many situations. Most recent closely related works are the Ph.D. theses [Pai95, vdW98, Csí02, Ric05], the journal papers [DRS93, Abg01, AM03a, AM04] and the conference proceedings [DSA00]. The important developments until 2003 are summarized in VKI Lecture Series *33rd Computational Fluid dynamics Course, Von Karman Institute for Fluid Dynamics* [Dec03], the developments until 2005 in [DR05]. An extensive overview on RDS is presented in [DSA00]. The state-of-the-art RDS development is included in the PhD thesis of Mario Ricchiuto [Ric05].

After short statement of the notation, the guidelines for the design of the RD schemes are mentioned. Then, the RD schemes for steady problems are introduced. Finally, we introduce the RD schemes for unsteady problems with novel extension for computations on moving meshes.

## 3.1. On mesh and notation

The polygonal domain $\Omega$ is triangulated by a mesh denoted by $\mathcal{T}^h$, i.e. $\bar{\Omega} = \bigcup_{E \in \mathcal{T}^h} E$. The nodes (vertices) of the mesh are denoted by indices $i$, $j$. All the vertices in the mesh will be denoted by $i \in \mathcal{T}^h$. The mesh elements are denoted by $E$. All the elements in the mesh will be denoted similarly by $E \in \mathcal{T}^h$. All nodes of the element $E$ are denoted by $i \in E$.

For the RD schemes only simplex elements will be considered. The simplex element in one dimension is a line segment, a triangle in two dimensions and a tetrahedron in three spatial dimensions. Note that each simplex in $d$ spatial dimensions has $d+1$ vertices.

The finite element type trial function is denoted by $\psi$. The $\psi_i$ vary linearly over each element and takes unit value at node $i$, zero for all the other nodes. The trial function can be expressed within the element $E$ sharing node $i$

$$\psi_i^E(\vec{x}) = 1 - \frac{\vec{n}_i \cdot (\vec{x}_i - \vec{x})}{d\,\mu(E)}, \tag{3.1}$$

where $\vec{n}_i$ is the normal perpendicular to the face opposite to the node $i$ scaled by its measure, $\vec{x}_i$ is the coordinate of node $i$, $d$ is the number of spatial coordinates and $\mu(E)$ is the measure of the element $E$. The gradient of the trial function is constant over the element $E$, i.e.

$$\nabla\psi_i^E(\vec{x}) = \frac{\vec{n}_i}{d\,\mu(E)}. \tag{3.2}$$

The following part of this section is devoted to the conservative evaluation of the residual

$$\phi^E \approx \int_E \nabla \cdot \vec{\mathbf{f}}\,\mathrm{d}\vec{x}. \tag{3.3}$$

As was noted by P. Roe, see [Roe81], it can be advantageous to describe the spatial distribution of the solution $\mathbf{u}(\vec{x})$ and the fluxes $\vec{\mathbf{f}}(\vec{x})$ using the *parameter vector*, denoted by $\mathbf{v}(\vec{x})$, here called the *primary variable*, instead of the spatial distribution of the conserved variable $\mathbf{u}(\vec{x})$ itself. The primary variable is chosen such that both solution $\mathbf{u}$ and flux $\vec{\mathbf{f}}$ are at most quadratic functions of $\mathbf{v}$, raising the possibility to evaluate exactly (given the piecewise linear distribution of the primary variable $\mathbf{v}$) the integral (3.3).

We introduce the *primary variable* $\mathbf{v}$ with regular one-to-one mapping to the conserved variable $\mathbf{u} \mapsto \mathbf{v}(\mathbf{u})$ with Jacobian

$$\frac{\partial \mathbf{u}}{\partial \mathbf{v}}. \tag{3.4}$$

The primary variable is suitable chosen, i.e. for the set of Euler equations the primary variable is Roe's parameter vector

$$\mathbf{v} = (\sqrt{\rho}, \sqrt{\rho}\vec{v}, \sqrt{\rho}H) \qquad \text{(usually denoted } \mathbf{z}\text{)} \tag{3.5}$$

and for scalar equations considered in this thesis the primary variable is the conserved variable $\mathbf{u} \equiv \mathbf{v}$.

The primary variable is approximated by the trial functions over the element as

$$\mathbf{v}^h(\vec{x})\Big|_E = \sum_{j \in E} \mathbf{v}_j \psi_j(\vec{x}), \tag{3.6}$$

where $\mathbf{v}_j$ is the nodal value, and over the whole computational domain

$$\mathbf{v}^h(\vec{x}) = \sum_{j \in \mathcal{T}^h} \mathbf{v}_j \psi_j(\vec{x}). \tag{3.7}$$

The solution $\mathbf{u}$ is approximated by $\mathbf{u}^h$, i.e.

$$\mathbf{u}^h(\vec{x}) \equiv \mathbf{u}(\mathbf{v}^h(\vec{x})). \tag{3.8}$$

The gradient of the approximation of the primary variable reads

$$\nabla \mathbf{v}^h(\vec{x}) = \sum_{j \in E} \mathbf{v}_j \nabla \psi_j(\vec{x}) = \sum_{j \in E} \mathbf{v}_j \frac{\vec{n}_j}{d\,\mu(E)}. \tag{3.9}$$

The flux approximation is denoted by $\vec{\mathbf{f}}^h$.

The element residual is defined as

$$\phi^E = \int_E \nabla \cdot \vec{\mathbf{f}}^h \,\mathrm{d}\vec{x} = \int_E \frac{\partial \vec{\mathbf{f}}^h}{\partial \mathbf{v}^h} \cdot \nabla \mathbf{v}^h \,\mathrm{d}\vec{x}. \tag{3.10}$$

Now, with the use of the piecewise linearity of the approximation $\mathbf{v}^h$, we have

$$\phi^E = \nabla \mathbf{v}^h \cdot \int_E \frac{\partial \vec{\mathbf{f}}^h}{\partial \mathbf{v}^h} \,\mathrm{d}\vec{x}. \tag{3.11}$$

For a certain class of the problems, the primary variable $\mathbf{v}$ can be chosen such that the flux $\vec{\mathbf{f}}$ is at most a quadratic function of the primary variable $\mathbf{v}$. Most notably this holds for the system of Euler equations[1]. Then the Jacobian $\partial \vec{\mathbf{f}}^h / \partial \mathbf{v}^h$ is at most a linear function of the variable $\mathbf{v}^h$. The last integral can be exactly computed using the arithmetic average of the nodal values $\mathbf{v}_i$, i.e.

$$\int_E \frac{\partial \vec{\mathbf{f}}^h}{\partial \mathbf{v}^h} \,\mathrm{d}\vec{x} = \mu(E) \frac{\partial \vec{\mathbf{f}}^h}{\partial \mathbf{v}^h}(\bar{\mathbf{v}}), \qquad \bar{\mathbf{v}} = \frac{\sum_{i \in E} \mathbf{v}_i}{d+1}. \tag{3.12}$$

The residual can be expressed with aid of (3.9) as

$$\begin{aligned}
\phi^E = \mu(E) \frac{\partial \vec{\mathbf{f}}^h}{\partial \mathbf{v}^h}(\bar{\mathbf{v}}) \cdot \nabla \mathbf{v}^h &= \mu(E) \frac{\partial \vec{\mathbf{f}}^h}{\partial \mathbf{u}^h}(\bar{\mathbf{v}}) \frac{\partial \mathbf{u}^h}{\partial \mathbf{v}^h}(\bar{\mathbf{v}}) \cdot \nabla \mathbf{v}^h \\
&= \mu(E) \frac{\partial \vec{\mathbf{f}}^h}{\partial \mathbf{u}^h}(\bar{\mathbf{v}}) \frac{\partial \mathbf{u}^h}{\partial \mathbf{v}^h}(\bar{\mathbf{v}}) \cdot \sum_{j \in E} \frac{\mathbf{v}_j \vec{n}_j}{d\,\mu(E)} \\
&= \sum_{j \in E} \left( \frac{\partial \vec{\mathbf{f}}^h}{\partial \mathbf{u}^h}(\bar{\mathbf{v}}) \cdot \frac{\vec{n}_j}{d} \right) \left( \frac{\partial \mathbf{u}^h}{\partial \mathbf{v}^h}(\bar{\mathbf{v}})\, \mathbf{v}_j \right) = \sum_{j \in E} \bar{\mathbf{k}}_j \bar{\mathbf{u}}_j,
\end{aligned} \tag{3.13}$$

with

$$\bar{\mathbf{k}}_j = \frac{\partial \vec{\mathbf{f}}^h}{\partial \mathbf{u}^h}(\bar{\mathbf{v}}) \cdot \frac{\vec{n}_j}{d} \tag{3.14}$$

$$\bar{\mathbf{u}}_j = \frac{\partial \mathbf{u}^h}{\partial \mathbf{v}^h}(\bar{\mathbf{v}})\, \mathbf{v}_j, \tag{3.15}$$

[1] and all the systems of conservation laws considered in this work

where we have introduced the *upwind parameter* $\bar{\mathbf{k}}_j$. In the scalar case the Jacobian corresponds to the advection vector

$$\vec{\lambda} = \frac{\partial \vec{\mathbf{f}}^h}{\partial \mathbf{u}^h}(\bar{\mathbf{v}}). \tag{3.16}$$

In the subsequent chapters, when no confusion can be made, the over-bars $\bar{\mathbf{k}}_j$, $\bar{\mathbf{u}}_j$ are dropped to simplify the notation. The advantage of this approach is that the residual is evaluated using a continuous approximation of the flux the $\vec{\mathbf{f}}^h$ in the domain, which is needed for the conservativity of the scheme. It was introduced in [DRS93] (Deconinck-Roe-Struijs linearization), following [Roe81]. If the flux $\vec{\mathbf{f}}$ and the conserved variable $\mathbf{u}$ cannot be expressed as second order polynomials of the primary variable $\mathbf{v}$, we refer to the work of [CRD02, RCD05, Csí02, Ric05] or [AB02].

## 3.2. Introduction and general framework

The residual distribution schemes for steady problems generally involve the following steps:

1. Compute the *residual* as the integral of the convective terms of the equation (2.1) over element $E$ with aid of (3.13)

$$\phi^E = \int_E \nabla \cdot \vec{\mathbf{f}}^h \, \mathrm{d}\vec{x} = -\int_E \frac{\partial \mathbf{u}^h}{\partial t} \, \mathrm{d}\vec{x} = \sum_{i \in E} \bar{\mathbf{k}}_i \bar{\mathbf{u}}_i. \tag{3.17}$$

2. *Distribute* the residual $\phi^E$ to the nodes of element $E$ via distribution matrix $\beta_i$

$$\phi_i^E = \beta_i^E \phi^E, \quad \text{such that} \sum_{i \in E} \phi_i^E = \phi^E. \tag{3.18}$$

3. Update the solution in all the nodes of the computational domain

$$\mathbf{u}_i^{h,n+1} = \mathbf{u}_i^{h,n} - \alpha_i \sum_{E \in i} \phi_i^E, \tag{3.19}$$

where $n$ is the index of the time level and $\alpha_i > 0$ is a relaxation parameter, to be specified later.

Certain class of the schemes define directly the residual contribution $\phi_i^E$ to the node $i$. The distribution coefficient is then defined implicitly from eq. (3.18). The

relaxation parameter $\alpha_i$ is proportional to the value of the time step. Then, the scheme can be written as

$$\frac{\mathbf{u}_i^{n+1} - \mathbf{u}_i^n}{\Delta t} = -\frac{1}{\mu(S_i)} \sum_{E \in \mathcal{D}_i} \phi_i^E = -\frac{1}{\mu(S_i)} \sum_{E \in \mathcal{D}_i} \beta_i^E \phi^E, \tag{3.20}$$

where $\mu(S_i)$ is the volume of the median dual cell around the node $i$ and $E \in \mathcal{D}_i$ denotes all elements sharing node $i$. The RD scheme will be recast in the following abstract form, see, e.g. [Ric05]

$$\mathbf{u}_i^{n+1} = \mathbf{u}_i^n - \frac{\Delta t}{\mu(S_i)} \sum_{E \in \mathcal{D}_i} \underbrace{\sum_{j \in E} \mathbf{c}_{ij}^E (\mathbf{u}_i^n - \mathbf{u}_j^n)}_{\phi_i^E} = \sum_{j \in D_i} \tilde{\mathbf{c}}_{ij} \mathbf{u}_j^n. \tag{3.21}$$

## 3.3. RD schemes for unsteady problems

The above-stated RD scheme is first order accurate at most for unsteady problems even if a high order time discretization scheme is used, see, e.g. [FD97, Mae96, Ric01, DSA00]. The reason is that, there exists a coupling between spatial and temporal discretization through a finite element type mass matrix. The accuracy problem was treated by two distinct approaches: schemes formulated using a mass matrix, see, e.g. [FD97, Mae96, RD99, DD05a, DDF05a, PPRN05, Ric05, DD06d] and space-time schemes, see, e.g. [CRDP01, CD01, CD02, CRD03, Ric01, RAD03, Csí02, RCD05, RCD04, AM01, MA02, AM03a, MRAD03, Dob02, DRD03b, DRD03a, DRD03c, DRD05, DD05b, CCF01, CF05]. Although the schemes were derived using different frameworks, they can be reduced to a common base. Namely, we can formulate the unsteady problem (2.1) using the pseudo time stepping (or dual time), i.e.

$$\frac{\partial \mathbf{u}}{\partial \tau} + \frac{\partial \mathbf{u}}{\partial t} + \sum_{j=1}^{d} \frac{\partial}{\partial x_j} \mathbf{f}_j(\mathbf{u}) = \mathbf{0}, \tag{3.22}$$

and we seek for an unsteady solution of (2.1) as a steady solution of (3.22)

$$\lim_{\tau \to \infty} \frac{\partial \mathbf{u}}{\partial \tau} = \mathbf{0}. \tag{3.23}$$

Hence we can proceed with a similar solution method as in section 3.2:

1. Compute the approximation of the *unsteady residual* as the integral of the equation (2.1) over the space-time element $E^{\mathrm{ST}}$ between time levels $n$ and $n+1$

$$\phi^{E^{\mathrm{ST}}} = \int_{E^{\mathrm{ST}}} \left( \frac{\partial \mathbf{u}^h}{\partial t} + \nabla \cdot \vec{\mathbf{f}}^h \right) \mathrm{d}\vec{x}\,\mathrm{d}t = \int_{[t^n, t^{n+1}]} \int_E \left( \frac{\partial \mathbf{u}^h}{\partial t} + \nabla \cdot \vec{\mathbf{f}}^h \right) \mathrm{d}\vec{x}\,\mathrm{d}t. \tag{3.24}$$

2. *Distribute* residual $\phi^{E^{\mathrm{ST}}}$ to the nodes of the element $E^{\mathrm{ST}}$ located on the time level $n+1$ via the distribution parameter (matrix) $\beta_i$

$$\phi_i^{E^{\mathrm{ST}}} = \beta_i^{E^{\mathrm{ST}}} \phi^{E^{\mathrm{ST}}} \quad \text{with} \quad \sum_{i \in E} \phi_i^{E^{\mathrm{ST}}} = \phi^{E^{\mathrm{ST}}}. \tag{3.25}$$

   Because we have an initial value problem with data at $n$, the distribution is constrained to nodes at $n+1$.

3. Update the solution in all the nodes of the computational domain at the time level $n+1$

$$\mathbf{u}_i^{h,n+1,m+1} = \mathbf{u}_i^{h,n+1,m} - \alpha_i \sum_{E \in i} \phi_i^{E^{\mathrm{ST}}}, \tag{3.26}$$

   where $m$ is the index of the pseudo-time step and $\alpha_i$ is the relaxation coefficient. The value of the coefficient $\alpha_i$ is given by relation (3.73).

4. The steps 1. to 3. are repeated until a steady solution in pseudo-time is found. Then, the next layer of the space-time elements is considered $[t^n, t^{n+1}] \rightarrow [t^{n+1}, t^{n+2}]$.

The problem to find a stationary point of equation (3.26)

$$\mathbf{u}_i^{h,n+1,m+1} = \mathbf{u}_i^{h,n+1,m} \quad \text{i.e.} \quad \sum_{E \in i} \phi_i^{E^{\mathrm{ST}}} = 0 \tag{3.27}$$

is explained in more details in section 3.8.

## 3.4. Design principles

### 3.4.1. Upwinding

From the theory of characteristics it is known in which directions the quantities are propagated. The *multidimensional upwind* schemes update nodes only in the relevant directions.

**Definition 5 (Multidimensional Upwind scheme [DSBR93]).** If all the eigenvalues of $\mathbf{k}_i$ are negative, then $\phi_i = 0$.

### 3.4.2. Linearity preservation

The key concept to show the second order accuracy of the scheme is the *linearity preservation* property, see, e.g. [Abg01, Ric05].

**Definition 6.** The scheme is *linearity preserving*, if it is able to reproduce exactly every solution $\mathbf{u}$, for which the primary variable $\mathbf{v} = \mathbf{v}(\mathbf{u})$ is a linear function.

The linearity preserving scheme is second order accurate at steady state. The proof was first published in [AM01] for the system of Euler equations and later extended for the RD schemes of arbitrary order of accuracy [AR03]. A slightly different form of the proof is used in [Abg05] and [RVAD05]. The additional information for the original proof as well as the extension for the case with presence of source terms can be found in [Ric05] and [RAD06].

**Theorem 7.** *The scheme evaluating element residual $\phi^E$ using (3.13) and distributing the residual with uniformly bounded distribution coefficients (matrices) $\beta_i$ is linearity preserving.*

*Proof.* Consider a steady state solution of (2.1), for which the primary variable is a linear function $\mathbf{v}(\vec{x})$. Since $\mathbf{u} = \mathbf{u}(\mathbf{v})$ is the solution of (2.1), the element residual (3.17) is $\phi^E = 0$ for each element $E$ and it is evaluated by scheme (3.13) exactly due to the linearity of $\mathbf{v}$. The distribution coefficients $\beta_i$ are bounded, hence all the nodal contributions $\phi_i$ are zero. Hence, this solution is a steady state solution of (3.19) and it is is exactly reproduced (preserved). □

A similar statement holds for the schemes for the unsteady problems in pseudo-time stepping formulation. The uniformly bounded distribution coefficients are the key issue for the construction of the so called N-modified scheme, see section 3.5.4, page 39, and section 3.6.4, page 52.

### 3.4.3. Positivity for scalar problems

**Definition 8 (Positivity of the scalar RD scheme).** The fully discrete scheme (3.21) for the scalar equation is *positive*, if all the coefficients $\tilde{c}_{ij}$ are non-negative with

$$\sum_{j \in \mathcal{D}_i} \tilde{c}_{ij} = 1. \tag{3.28}$$

For the construction of the N-modified scheme, see section 3.5.4, page 39, and section 3.6.4, page 52, a stricter condition is needed.

**Definition 9 (Sub-element positivity of the scalar RD scheme).** The fully discrete scheme (3.21) for scalar equation is sub-element positive, if all coefficients $c_{ij}^E$ are non-negative and the time step $\Delta t$ satisfies

$$\Delta t \leq \min_{i \in T^h} \sum_{E \in \mathcal{D}_i} \sum_{j \in E} \frac{\mu(E)}{(d+1)\, c_{ij}^E}. \tag{3.29}$$

The sub-element positivity of the scheme is a sufficient condition for positivity. Positivity of an implicit space-time scheme can be defined using the matrix analysis, see, e.g. [RCD05, AM04], or using the space-time formulation. The time can be treated as an additional spatial direction and the positivity can be defined in the space-time domain.

**Theorem 10.** *Positivity of the scheme* (3.21) *implies the discrete maximum principle, i.e.*

$$\min_{i \in \mathcal{T}^h} u_i^{0,h} \leq u^{h,n} \leq \max_{i \in \mathcal{T}^h} u_i^{0,h} \qquad \forall n \in [0, 1, 2, \ldots, N], \tag{3.30}$$

*where* $u^{h,n}$ *is the approximation of the solution in the n-th time layer. Moreover, the scheme* (3.21) *is stable in* $L_\infty$ *norm, i.e.*

$$\|u^h(x,t)\|_{L_\infty} \leq \|u^{0,h}(x)\|_{L_\infty}, \qquad t \in [0,T], \tag{3.31}$$

*where* $u^{0,h}$ *is the approximation of the initial condition.*

As the solution at each node at time level $n = 1$ lies within the convex hull of the nodal values at time level $n = 0$, hence the discrete maximum principle is satisfied. The mathematical induction is used for the case $n > 1$. If the local maximal values of the solution do not increase and the local minimal values do not decrease, the scheme is said to be *local extremum diminishing (LED)*. The concept of positivity and LED property is discussed for RD schemes in [Pai95, AM04, vdW98, Ric05], for the FV methods in [Bar94, Jam]. The positivity of the scheme is closely related to the TVD property, see [Har83]. In 1D the TVD property and the LED property are equivalent, see [Tad88].

### 3.4.4. Linearity

The scheme for the scalar linear equation is said to be linear, if the distribution coefficients $\beta_i$ do not depend on the solution.

From the Godunov theorem for RD schemes [DSBR93] it is known, that a linear scheme cannot be both second order accurate and positive. Since both properties are important, we will focus on the nonlinear schemes.

### 3.4.5. Geometric conservation law

The scheme obeys the geometric conservation law (GCL) if any constant solution is exactly preserved on a deforming mesh. An overview of the current status of the geometrical conservation law is given in [MY06, Far04] or [Lep04].

Let us mention several results concerning the geometrical conservation law (GCL):

- GCL is a sufficient condition for the scheme to achieve first order temporal accuracy, see [GF00].
- GCL is not a necessary condition for achieving design accuracy of the underlying time integration scheme, see [GGF03].
- GCL is a necessary and sufficient condition for respecting nonlinear stability of the underlying time integration scheme, see [FGG01].

- GCL is a sufficient condition for the Euler backward time integration to be unconditionally stable, see [FN99].
- GCL is not a necessary condition for the convergence of the numerical method to the weak solution of the conservation law (2.28), see [DFD07b, DFD07a].
- If GCL is not respected, an incorrect flutter boundary can be predicted, see [Far04].

These results encourage to use schemes respecting the GCL. All the schemes (RD and FV) considered in this thesis satisfy the GCL.

### 3.4.6. Extension for a hyperbolic system of equations

The work was pioneered by E. van der Weide in his PhD thesis [vdW98] by introducing so called *matrix schemes*. The later important development include [Abg01, AM04, AM03a, Mez02, Csí02, Ric05] with excellent summary in [Ric05]. Generally, the RD schemes for scalar problems extend to systems of equations, where upwind and distribution coefficients are replaced by matrixes of size $q \times q$, with addition and multiplication operators replaced by their matrix counterparts.

The matrix $\mathbf{k}_i$ is the Jacobian matrix in the direction of the normal $\vec{n}_i$, see eq. (3.14). The notation $\mathbf{k}_i^+$ and $\mathbf{k}_i^-$ means positive and negative part of the matrix in the sense of eigen-decomposition

$$\mathbf{k}_i^{\pm} = \mathbf{r}_i \, \Lambda_i^{\pm} \, \mathbf{l}_i, \tag{3.32}$$

where matrices $\mathbf{r}_i$ and $\mathbf{l}_i$ contain right and left eigenvectors of matrix $\mathbf{k}_i$ and the matrix $\Lambda_i^{\pm}$ contains positive or negative eigenvalues of the matrix. In the following text, we drop the subscript $i$ for simplification. For the computations on moving meshes, the upwind matrix has to reflect the mesh velocity, also for the scalar case (3.104). In this case, the matrix $\Lambda$ in equation (3.32) contains eigenvalues of the matrix $\mathbf{k}_i$ minus the averaged mesh velocity on the element in the direction of the normal $\vec{n}_i$

$$\Lambda = \underset{m \in [1,2,\ldots,q]}{\operatorname{diag}} (\lambda_m - \bar{\vec{w}} \cdot \vec{n}_i). \tag{3.33}$$

The element residual can be expressed in particularly simple form

$$\phi^E = \sum_{j \in E} \bar{\mathbf{k}}_j \bar{\mathbf{u}}_j, \qquad \bar{\mathbf{k}}_j = \left( \frac{\partial \vec{\mathbf{f}}}{\partial \mathbf{u}} - \bar{\vec{w}} \right) \cdot \vec{n}_j, \tag{3.34}$$

where $\bar{\vec{w}}$ is the approximation of the mesh velocity in the element. The precise state for the linearization on moving meshes is given in section 3.7.8.

| Scheme | Linear | Positive | Linearity preserving | Formal order of accuracy |
|---|---|---|---|---|
| N | ✓ | ✓ | | 1 |
| LDA | ✓ | | ✓ | 2 |
| N-modified | | ✓ | ✓ | 2 |
| B | | | ✓ | 2 |
| Bx | | | | 2 |

Table 3.1.: Properties of the RD schemes

## 3.5. RD schemes for steady problems

The properties of the RD schemes are listed in Table 3.1.

In the following sections, we will introduce schemes used in the course of this work. We start with first order N scheme.

### 3.5.1. N scheme

The N scheme is given by the nodal contribution from element $E$

$$\phi_i = k_i^+(u_i - u_{\text{in}}), \qquad u_{\text{in}} = -N\sum_{j\in E} k_j^- u_j, \tag{3.35}$$

where

$$N \equiv (\sum_{i\in E} k_i^+)^{-1} \tag{3.36}$$

and $k^\pm = \pm\max(0, \pm k)$. If the Euler explicit time-stepping procedure is used, the scheme is sub-element positive under time-step restriction (3.29).

*Proof.* It is easy to verify that the scheme can be written as (3.21), where

$$c_{ij}^E = -k_i^+ \left(\sum_{j\in E} k_j^+\right)^{-1} k_j^-. \tag{3.37}$$

Because $k^+$ is positive or zero and $k^-$ is negative or zero, the coefficients $c_{ij}^E$ are always non-negative. □

The scheme for the system of equations is given by

$$\phi_i = \bar{\mathbf{k}}_i^+(\bar{\mathbf{u}}_i - \mathbf{u}_{\text{in}}), \qquad \mathbf{u}_{\text{in}} = -\mathbf{N}\sum_{j\in E} \bar{\mathbf{k}}_j^- \bar{\mathbf{u}}_j, \tag{3.38}$$

with

$$\mathbf{N} = \left( \sum_{j \in E} \bar{\mathbf{k}}_j^+ \right)^{-1}. \tag{3.39}$$

The N scheme is very robust, however it is only first order accurate. The following scheme is second order accurate.

### 3.5.2. LDA scheme

The LDA scheme is defined by the distribution coefficient

$$\beta_i = k_i^+ N, \tag{3.40}$$

and by the distribution matrix in the system case

$$\beta_i = \bar{\mathbf{k}}_i^+ \mathbf{N}. \tag{3.41}$$

The LDA scheme is linear and second order accurate. One can compute even some transonic flows with discontinuities, see e.g. Fig. 3.1. The discontinuities are not captured in a monotone manner, the scheme is not positive. As is known from the Godunov theorem, a second order positive scheme has to be non-linear. Precisely for this reason a number of non-linear schemes were developed in the past. Now, we will focus on them.

### 3.5.3. B scheme

Part of this section was published in [DDF07].

The B scheme was introduced by van der Weide (unpublished 1997) and it is described in e.g. [CDP01]. The scheme combines the first order N scheme and the second order LDA scheme

$$\phi_i^{\mathrm{B}} = (1 - \theta)\phi_i^{\mathrm{LDA}} + \theta \phi_i^{\mathrm{N}} \tag{3.42}$$

using the blending coefficient

$$\theta = \frac{|\phi^E|}{\sum_{j \in E} |\phi_j^{\mathrm{N}}|}. \tag{3.43}$$

For the system of equations, the N scheme and the LDA are blended by components, where for each component of the vector the blending coefficient is computed using equation (3.43).

The B scheme is linearity preserving at convergence limit, as is was proven in [AM01].

**Theorem 11.** *Schemes in the form* (3.42), *with* $\theta \in [0,1]$, *i.e. convex element-wise combinations of the N scheme and the LDA scheme, cannot be locally positive in two spatial dimensions, whatever choice of* $\theta \in [0,1]$ *except the case* $\theta = 1$, *i.e. N scheme.*

*Proof.* Consider a triangle $E$ with vertices numbered 1, 2, 3. Without loss of generality, we will consider the case of $k_1 > 0$, $k_2 > 0$ (giving $k_3 < 0$), i.e. two target triangle, and focus on node 1. The B scheme can be written as

$$\phi_1^{\mathrm{B}} = k_1(u_1 - u_3) + \underbrace{\left[-(1-\theta)\frac{k_1 k_2}{k_1 + k_2}\right]}_{c_{12}^E}(u_1 - u_2). \tag{3.44}$$

Coefficient $c_{12}^E$ is negative for any $0 \leq \theta < 1$. By Definition 9, see page 33, scheme is not locally positive. □

This finding is in a contradiction with the wide-spread belief in the positivity of the blended scheme. To support our theoretical result, an oscillatory behavior of the B scheme is briefly mentioned in [AM03b]. Although the B scheme is not (locally) positive, it performs in a *very similar* manner as the positive N-modified scheme, see section 3.5.4, pg. 39.

Example of the construction of a positive scheme using the blending with $\theta \in \mathbb{R}$ is given in [Abg01]. Let us state one more theoretical result concerning the construction of the nonlinear schemes.

**Theorem 12.** *Any scalar multidimensional upwind scheme (denoted by Scheme 3) in two spatial dimensions can be constructed by the blending of two distinct arbitrary multidimensional upwind schemes (denoted by Scheme 1 and 2) in the form*

$$\phi_i^{\mathrm{Scheme3}} = (1-\theta)\phi_i^{\mathrm{Scheme1}} + \theta\phi_i^{\mathrm{Scheme2}}, \tag{3.45}$$

*with* $\theta \in \mathbb{R}$.

This means, that *any* scheme can be constructed using *any* pair of other multidimensional upwind schemes, as far as $\phi_i^{\mathrm{Scheme1}} \neq \phi_i^{\mathrm{Scheme2}}$. On the contrary, there does not exist any multidimensional upwind scheme, which cannot by expressed as a blend of two distinct schemes, e.g. N scheme and LDA scheme.

*Proof.* For one target case (i.e. $k_1 > 0$, $k_2 < 0$, $k_3 < 0$) the situation is easy: all the multidimensional upwind schemes distribute the element residual $\phi^E$ to the downwind node $\phi_1 = \phi^E$ and equation (3.45) is identically satisfied. For the two target case we will denote the downwind nodes by numbers 1 and 2. The nodal contribution for the Scheme 3 can be constructed from the Scheme 1 and Scheme 2 only by the choice of the blending parameter $\theta \in \mathbb{R}$: all the schemes distribute the same element residual $\phi^E$, i.e.

$$\phi_1^{\mathrm{Scheme1}} + \phi_2^{\mathrm{Scheme1}} = \phi_1^{\mathrm{Scheme2}} + \phi_2^{\mathrm{Scheme2}} = \phi_1^{\mathrm{Scheme3}} + \phi_2^{\mathrm{Scheme3}} = \phi^E. \tag{3.46}$$

Therefore it is sufficient to know one nodal contribution $\phi_1$, the other is uniquely given by the relation

$$\phi_2 = \phi^E - \phi_1. \tag{3.47}$$

The schemes are distinct, if the nodal residuals are different, i.e.

$$\phi_1^{\text{Scheme1}} \neq \phi_1^{\text{Scheme2}}. \tag{3.48}$$

The nodal contribution of is given by

$$\phi_1^{\text{Scheme3}} = (1-\theta)\phi_1^{\text{Scheme1}} + \theta\phi_1^{\text{Scheme2}}. \tag{3.49}$$

from which one can easily compute the desired value of the blending parameter

$$\theta = \frac{\phi_1^{\text{Scheme3}} - \phi_1^{\text{Scheme1}}}{\phi_1^{\text{Scheme2}} - \phi_1^{\text{Scheme1}}}. \tag{3.50}$$

□

### 3.5.4. N-modified scheme

The N scheme is defined by nodal contributions (3.35) and it can be understood as a scheme distributing residual (3.17), (3.18) with implicitly defined distribution coefficients

$$\beta_i = \frac{\phi_i}{\phi^E}. \tag{3.51}$$

Clearly, the distribution coefficients of the N scheme are not uniformly bounded. We would like to construct linearity preserving scheme (with uniformly bounded distribution coefficients) for its second order accuracy. The task is to find a continuous nonlinear mapping, see [Ric05, RCD05]

$$\mathbb{R}^{d+2} \to \mathbb{R}^{d+1} : \Phi(\phi^E, \beta_1, \beta_2, \ldots, \beta_{d+1}) \mapsto (\beta_1^{\text{modif}}, \beta_2^{\text{modif}}, \ldots, \beta_{d+1}^{\text{modif}}), \tag{3.52}$$

in 2D it is $\mathbb{R}^4 \to \mathbb{R}^3 : \Phi(\phi^E, \beta_1, \beta_2, \beta_3) \mapsto (\beta_1^{\text{modif}}, \beta_2^{\text{modif}}, \beta_3^{\text{modif}})$, such that

$$\phi^E = 0 \implies \beta_i^{\text{modif}} = 0 \qquad \forall i = [1, 2, \ldots, d+1] \tag{3.53}$$

$$\beta_i\, \beta_i^{\text{modif}} \geq 0 \qquad \forall i = [1, 2, \ldots, d+1] \tag{3.54}$$

$$\beta_i^{\text{modif}} < \infty \qquad \forall i = [1, 2, \ldots, d+1] \tag{3.55}$$

$$\sum_{i \in E} \beta_i^{\text{modif}} = 1 \tag{3.56}$$

Then, the modified scheme has uniformly bounded distribution coefficients and the scheme remains positive.

The uniform boundedness of the distribution coefficients comes from eq. (3.55). The sub-element positivity of the modified scheme can be understand from eq. (3.21)

$$\beta_i = \frac{\phi_i}{\phi^E} = \sum_{j \in E} \frac{c_{ij}^E}{\phi^E}(u_i^n - u_j^n). \tag{3.57}$$

The modified scheme has distribution coefficients

$$c_{ij}^{E,\text{modif}} = \frac{\beta_i^{\text{modif}} c_{ij}^E}{\beta_i}, \tag{3.58}$$

which are positive due to (3.54). The existence and well posedness of the mapping is proven in [Ric05].

One possible mapping is the following:

$$\beta_i^{\text{modif}} = \frac{\beta_i^+}{\sum_{j \in E} \beta_j^+}. \tag{3.59}$$

This construction is well known for a long time, see, e.g. [Pai95, AM03b]. New theoretical results concerning this mapping were published in [RCD04, RCD05, Ric05].

For the system of equations, the limiting procedure (3.52) is performed on *simple waves*. Given a system of hyperbolic conservation laws in quasilinear form

$$\frac{\partial \mathbf{u}}{\partial t} + \sum_{j=1}^{d} \mathbf{A}_j \frac{\partial \mathbf{u}}{\partial x_j} = \mathbf{0}, \tag{3.60}$$

and spatial vector $\vec{\xi} = (\xi_1, \xi_2, \ldots, \xi_d)$, the matrix

$$\mathbf{A} = \sum_{j=1}^{d} \mathbf{A}_j \xi_j \tag{3.61}$$

is diagonizable with matrix of left and right eigenvectors $\mathbf{l}$ and $\mathbf{r}$. The element residual and the nodal contributions are projected on the eigenvectors

$$\tilde{\phi}^E = \mathbf{l}\phi^E, \qquad \tilde{\phi}_i = \mathbf{l}\phi_i \tag{3.62}$$

and the modification procedure is applied on the components of the projected residuals with mapping

$$\mathbb{R}^{d+2} \to \mathbb{R}^{d+1} : \Phi(\tilde{\phi}^E, \tilde{\beta}_1, \tilde{\beta}_2, \ldots, \tilde{\beta}_{d+1}) \mapsto (\tilde{\beta}_1^{\text{modif}}, \tilde{\beta}_2^{\text{modif}}, \ldots, \tilde{\beta}_{d+1}^{\text{modif}}). \tag{3.63}$$

As the direction $\xi$ we chose vector $(1,0)$ or $(1,0,0)$ and the Jacobian is evaluated in the state of the arithmetic average $\bar{\mathbf{v}}$ of the solution in the element. The modified nodal contributions are projected back with $\phi_i^{\text{modif}} = \mathbf{r}\,\tilde{\phi}_i^{\text{modif}}$.

Both B and N-modified schemes are second order accurate, however they suffer of poor iterative convergence and they lack accuracy in smooth parts of the flow. This served as a momentum to develop another non-linear scheme as part of this thesis, named Bx scheme [DD06d, DD05a]. The following scheme is not positive (and it cannot be, as it was proven in Theorem 11), but it is surprisingly robust and accurate.

### 3.5.5. Bx scheme for the Euler equations

The Bx scheme has the general form (3.42). To define the blending parameter $\theta$, we first construct an element-wise shock capturing sensor

$$sc = \left( \frac{\vec{\nabla} p \cdot \vec{v}}{\delta_{pv}} \right)^{+} \approx \left( \frac{\int_T \vec{\nabla} p \, \mathrm{d}x}{\delta_{pv} \mu(E)} \cdot \vec{v} \right)^{+}, \tag{3.64}$$

where $\vec{v}$ is the approximation of the velocity vector in the element, $p$ is the static pressure and $\mu(E)$ is the area of the element. The $\delta_{pv} \approx (p_{\max} - p_{\min})\,\bar{v}$ is a global pressure variation scale multiplied by the magnitude of the mean velocity in the domain. The sensor $sc$ is positive in a shock and compression, zero in expansion, and of order $sc = \mathcal{O}(1)$ in smooth regions. One of the important properties of the scheme is its second order of accuracy. For 2D, in equation (3.42) the left hand side has to give $\mathcal{O}(h^3)$ [Ric05], where $h$ is a diameter of a circle with the same area as the element (or sphere in 3D). The contribution from the N scheme gives $\mathcal{O}(h^2)$ and from the LDA scheme $\mathcal{O}(h^3)$ in 2D. Hence, the blending factor $\theta$ has to be of order $\mathcal{O}(h)$. Multiplication of the shock sensor $sc$ by $h$ does not lead to sufficient damping in the shock regions. If multiplied by $\sqrt{h}$, then the amount of the numerical viscosity is correct, but the scheme is only $\mathcal{O}(h^{1.5})$ accurate. The solution is to take a blending factor as

$$\theta = \min\left(1, \left(sc\sqrt{h}\right)^2\right) = \min\left(1, sc^2\, h\right), \tag{3.65}$$

which gives the right amount of artificial viscosity together with second order of accuracy in smooth regions. The nodal contribution of the Bx scheme is then given by (3.66) with the blending coefficient given by (3.64) and (3.65)

$$\phi_i^{\mathrm{Bx}} = (1-\theta)\phi_i^{\mathrm{LDA}} + \theta\phi_i^{\mathrm{N}}. \tag{3.66}$$

The blending coefficient is smooth and allows to use the complete 2nd order Jacobian for the implicit calculations (even though we use its numerical approximation), which noticeably speeds up the convergence rate. For all the other nonlinear schemes in this thesis a first order approximation of the Jacobian had to be taken (from the N scheme).

Since this is a novel scheme, we present immediately some numerical results showing the performance of the scheme. More results are included later in chapter 5.

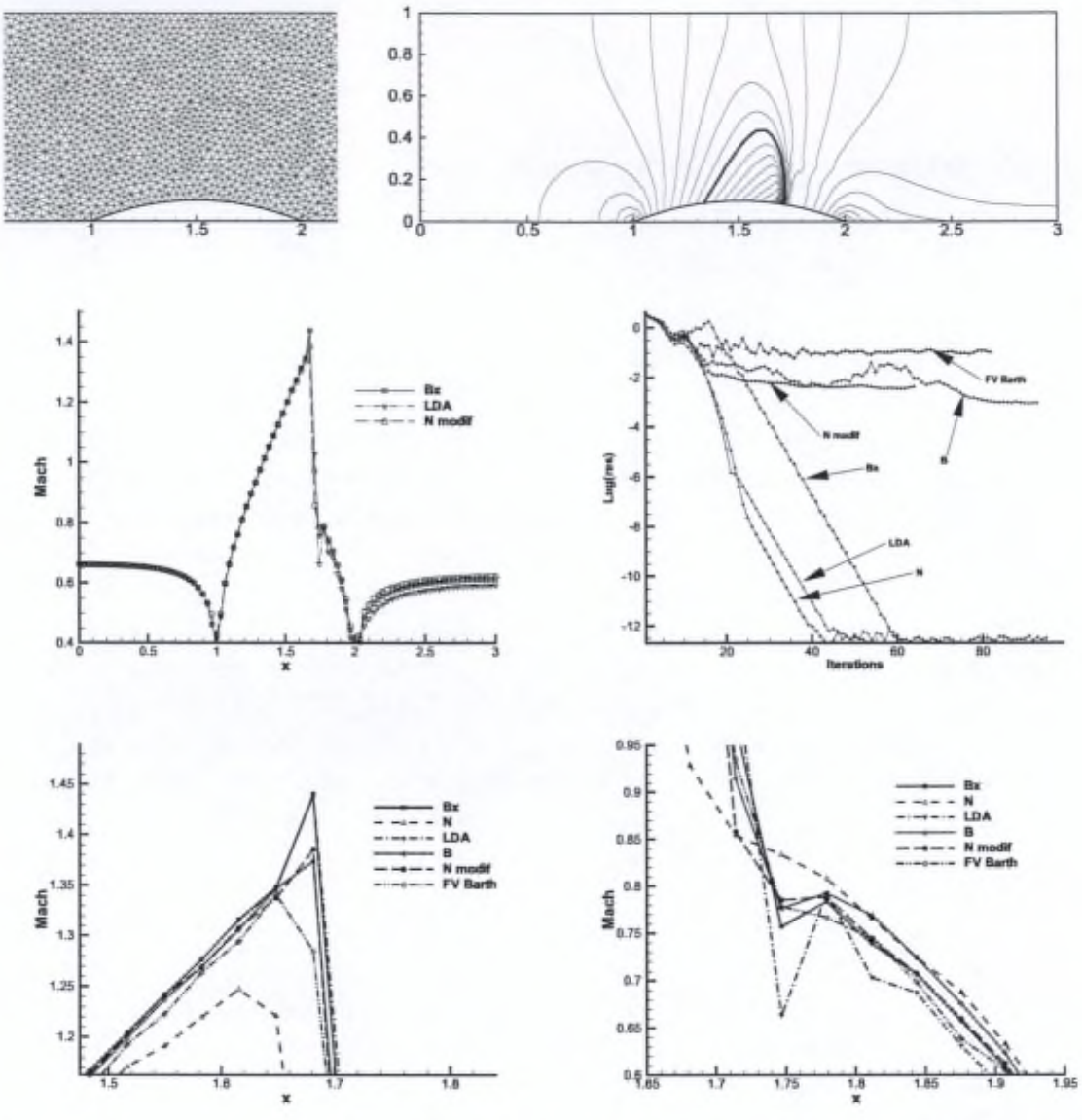


Figure 3.1.: Ni channel. Top: Part of the Weatherill mesh and the Mach number isolines for the Bx scheme, $\Delta M = 0.05$, the bold line is $M = 1$. Middle: the distribution of the Mach number along the bottom wall and the convergence histories for different schemes. Bottom: distribution of the Mach number along the wall, zoom before and after the shock.

First, we present numerical results for transonic flow in the so-called Ni channel [Ni81]. The flow is defined by the ratio of the outlet static pressure to the isentropic total pressure $p_2/p_{0is}$ corresponding to $M_{2is} = 0.675$. The length of the channel is 3 with unit width and 10 % circular bump. We use an unstructured grid consisting of 2762 nodes and 5281 elements, with 31 nodes along the bump, utilizing Weatherill type triangulation [Ath05]. This mesh gives a better idea of the behavior of the scheme in the case of changing connectivity, as is usual in 3D, avoids false cancellation of the error and does not prefer any direction. The Euler backward scheme is used for the time integration with numerical approximation of the Jacobian. For the N-modified and the B scheme we had to use the Jacobian of the N scheme. We start with the CFL number of 100 and every iteration we multiply it by the factor 1.2 until it reaches $10^6$.

In Fig. 3.1 isolines of the Mach number for the present Bx scheme are shown. One can observe a supersonic pocket on the bump. The isolines do not exhibit wiggles and they run straight into the shock, which corresponds to a not very dissipative scheme. The comparison of the Mach number distribution along the bottom wall is shown on the next figure together with a zoom to the beginning and the end of the shock. Before the shock, the Bx scheme follows the LDA scheme an creates a small overshoot on the Mach number distribution. After the shock the Bx scheme behaves very similar as both the N-limited and the B schemes in terms of capturing after-shock singularity. For comparison, the solution for the vertex centered finite volume method with Barth limiter and Roe's Riemann solver, from section 4.2 is shown. The FV scheme is clearly more dissipative than all the nonlinear RD schemes, as can be observed on the last point before the shock and mainly in the more diffusive capture of the after-shock singularity. Convergence of the norm of the residual is also presented. The new formulation gives a convergence rate very similar to the linear schemes, while all the other nonlinear schemes stall after a few orders of magnitude.

The next test examines robustness of the new scheme on a Mach 20 bow shock in front of the cylinder. The solution was computed using the Bx, N and N-modified scheme on mesh consisting of 10531 nodes and 20632 elements. The B scheme always gives negative pressure in the shock, even if started from a converged solution with extremely small CFL number. In Fig. 3.2 the isolines of Mach number are shown, the left part of the figure is the N-modified scheme, while the right one presents the Bx scheme. One can notice that the Bx scheme better captures irregularities of the solution, resulting from the interaction of the shock wave with the Weatherill type of mesh. The next part of the figure shows a cut along the streamline to the stagnation point. Points correspond to the intersection of the cut line with the edges of the triangles. As we can expect from the design of the scheme, there are no oscillations in the vicinity of the shock, nor anywhere else in the computational domain. The solution obtained by all the schemes gives practically the same result. Convergence properties of the schemes are considerably worse than for the transonic flows, as is known also from other methods. On the other hand, one can employ a

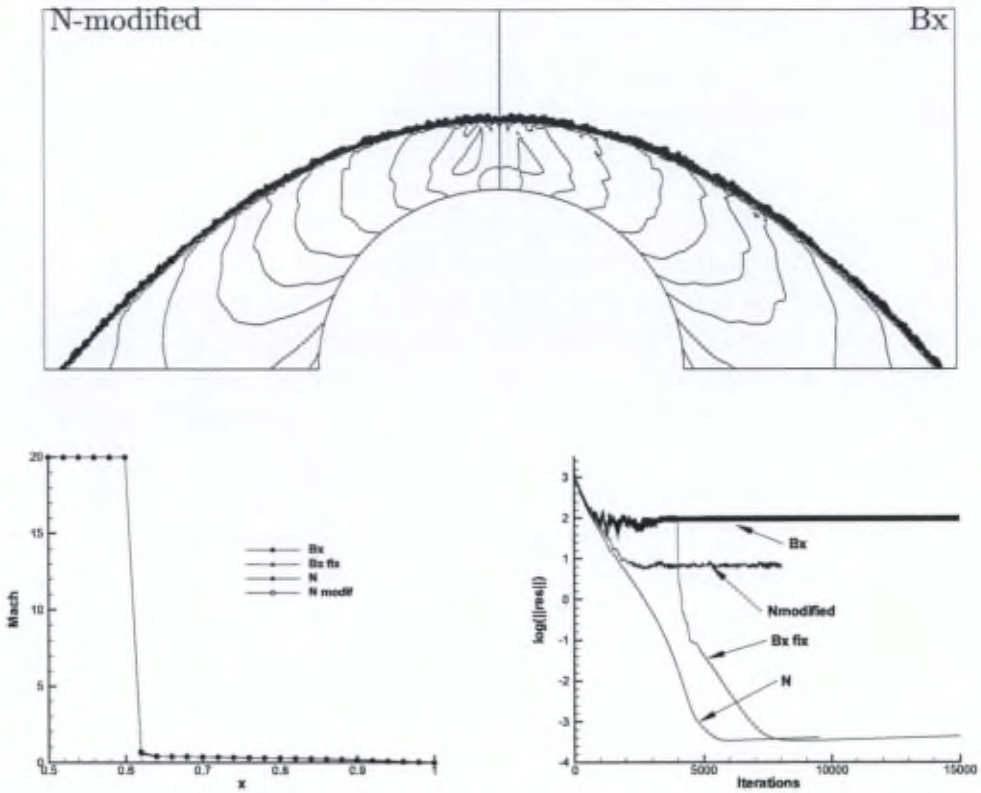


Figure 3.2.: Mach 20 bow shock. Top: isolines of the Mach number, the N-modified scheme is on the left, the Bx scheme on the right. Bottom: cut along the stagnation line and convergence history.

convergence fix, well known from the FV framework [Del96] – after a certain number of iterations $n_0$, when the solution is fully developed, *we don't decrease anymore the blending factor* in the subsequent iterations, i.e.

$$\theta^n = \max(\theta^n, \theta^{n-1}), \qquad \text{for all } n \geq n_0. \tag{3.67}$$

In this case we have chosen $n_0 = 4000$. It is not clear how to apply a similar fix to the N-modified scheme. Note that this definition is opposite of the FV limiter, since $\theta = 1$ gives the non-oscillatory scheme, while in the case of FV $\theta = 0$ reverts to the upwind scheme with constant reconstruction. The scheme recovers convergence to machine accuracy with a possibly slight price of more dissipative solution.

As the last steady case, we present a sub-critical flow around the cylinder [DvLPR89], with $M_\infty = 0.38$. This test examines the behavior of the method in smooth flow regions. We use a much coarser mesh than in reference [DvLPR89], because in that case all the schemes gave very similar, accurate results. Our mesh consists of approximately equilateral triangles with 80 elements along the wall and 40 rows of triangles towards the free stream boundary, see Fig. 3.3. This gives a position of the far-field

boundary approximately 10 diameters away from the cylinder. The exact solution is perfectly symmetric both with respect to $x$ and $y$ axis. The Mach number isolines are plotted in Fig. 3.3 with step of $\Delta M = 0.02$. All the schemes gives reasonably good results. The LDA and present Bx give very similar almost symmetric results, with a small deviation behind the cylinder on the axis of symmetry. The standard formulation of the B scheme gives larger error behind the cylinder, however it still converges to the horizontally symmetric solution. The N-modified scheme did not converge well and wake-like structures appear behind the cylinder. However, unlike the other results in [Pai95], no separation zone develops there. The results suggest that the Bx scheme contains very little unwanted artificial dissipation and it can capture smooth flow regions very well.

The scalar counterpart of the Bx scheme can be easily defined by considering the "shock sensor" as

$$sc = \frac{\int_E \|\nabla u^h\| \, \mathrm{d}\vec{x}}{\delta_u \cdot \mu(E)}. \tag{3.68}$$

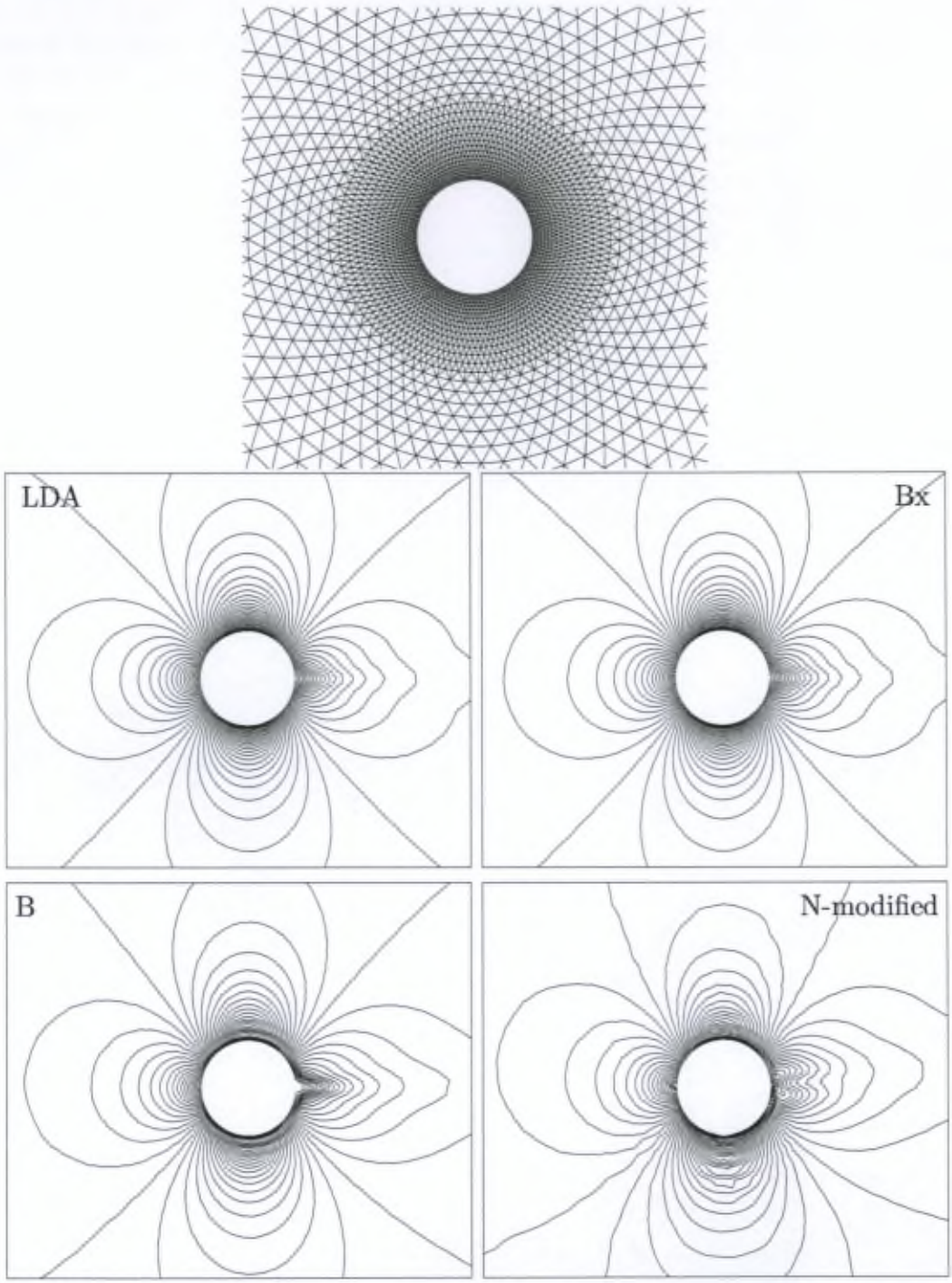


Figure 3.3.: Sub-critical flow past the cylinder. Mach number isolines, $\Delta M = 0.02$.

## 3.6. Schemes for unsteady problems

We start again with the first order N scheme.

### 3.6.1. N scheme

Historically, there are two independently developed versions of the space-time N scheme. One comes from the application of the spatial N scheme to a space-time prismatic element, see [CRD03, RCD05]. The second one was developed as the spatial N scheme equipped with Crank-Nicholson time integration procedure. Both schemes suffer from the same time-step restriction. In the first case the restriction allows time layers decoupling and time marching procedure. The satisfaction of the time step gives positivity of the scheme in the second case. For more discussion and comparison see e.g. [RCD05]. We will omit the first scheme and present only the second scheme.

The unsteady version of the N scheme is a straightforward application of the preferred time integrator to the steady version of the scheme. We shall present the scheme equipped with two different time integrators: Crank-Nicholson (later needed for the N-modified scheme of M. Mezine and R. Abgrall [MRAD03, AM03a]) and the scheme with three points backward (3BDF) time integrator, later needed for the Bx scheme [DD05a, DD06d].

First, we derive the (space-time) nodal contribution for the N scheme with the Crank-Nicholson time integrator. We start from equation (3.20) with the nodal contribution given by (3.35) (taking into account the chosen Crank-Nicholson time integrator)

$$\frac{u_i^{n+1} - u_i^n}{\Delta t} = -\frac{1}{\mu(S_i)} \sum_{E \in \mathcal{D}_i} \frac{1}{2}(\phi_i^{E,n+1} + \phi_i^{E,n}). \tag{3.69}$$

The nodal contribution from the space-time element is obtained by rearranging the terms of (3.69) into space-time contributions

$$\sum_{E \in \mathcal{D}_i} \phi_i^{E^{\mathrm{ST}}} = 0, \qquad \phi_i^{E^{\mathrm{ST}}} = \frac{\mu(E)}{d+1}(u_i^{n+1} - u_i^n) + \frac{1}{2}\Delta t(\phi_i^{E,n+1} + \phi_i^{E,n}), \tag{3.70}$$

with $\phi_i^E$ given by (3.35). The update scheme is then given by (3.26). Space-time element residual $\phi^{E^{\mathrm{ST}}}$ in this case corresponds to use of the trapezoidal integration rule on the space-time prism

$$\phi^{E^{\mathrm{ST}}} = \frac{\mu(E)}{d+1} \sum_{i \in E} (u_j^{n+1} - u_j^n) + \frac{1}{2}\Delta t(\phi^{E,n+1} + \phi^{E,n+1}), \quad \phi^E = \sum_{i \in E} k_i u_i. \tag{3.71}$$

Thanks to the space-time nature of the scheme, we can formulate sub-element positivity for the unsteady space-time RD schemes:

**Definition 13 (Sub-element positivity of the scalar space-time RD scheme).** The fully discrete scheme

$$u_i^{n+1,m+1} = u_i^{n+1,m} - \alpha_i \sum_{E\in\mathcal{D}_i} \phi_i^{E^{\mathrm{ST}}}$$
$$= u_i^{n+1,m} - \alpha_i \sum_{E\in\mathcal{D}_i}\sum_{j\in E} \left[{}^{n+1}c_{ij}^E(u_i^{n+1} - u_j^{n+1}) + {}^{n}c_{ij}^E(u_i^{n+1} - u_j^{n})\right]^m \quad (3.72)$$

is *sub-element positive*, if all coefficients ${}^{n+1}c_{ij}^E$, ${}^{n}c_{ij}^E$ are non-negative and the local relaxation coefficient $\alpha_i$ satisfies

$$0 < \alpha_i \le \left(\sum_{E\in\mathcal{D}_i}\sum_{j\in E}({}^{n+1}c_{ij}^E + {}^{n}c_{ij}^E)\right)^{-1}. \quad (3.73)$$

We now establish sub-element positivity of scheme (3.70) with relaxation procedure (3.26). The fully discrete scheme leads to

$$u_i^{n+1,m+1} = u_i^{n+1,m} - \alpha_i \sum_E \left[\frac{\mu(E)}{d+1}(u_i^{n+1} - u_i^n) + \frac{1}{2}\Delta t(\phi_i^{E,n+1} + \phi_i^{E,n})\right]$$
$$= u_i^{n+1,m} - \alpha_i \sum_E \left[\frac{\mu(E)}{d+1}(u_i^{n+1} - u_i^n)\right.$$
$$\left. + \frac{1}{2}\Delta t[k_i^{+,E}(u_i^{n+1} - u_{\mathrm{in}}^{E,n+1}) + k_i^{+,E}(u_i^n - u_{\mathrm{in}}^{E,n})]\right]. \quad (3.74)$$

The content of the bracket (element superscript $E$ is omitted) is

$$\frac{\mu(E)}{d+1}(u_i^{n+1} - u_i^n) + \frac{1}{2}\Delta t[k_i^{+,E}(u_i^{n+1} - u_{\mathrm{in}}^{E,n+1}) + k_i^{+,E}(u_i^n - u_{\mathrm{in}}^{E,n})]$$
$$= \frac{\mu(E)}{d+1}(u_i^{n+1} - u_i^n) + \frac{1}{2}\Delta t\left[k_i^+(u_i^{n+1} - N\sum_{j\in E}[k_j^- u_j^{n+1}]) + k_i^+(u_i^n - N\sum_{j\in E}[k_j^- u_j^n])\right]$$
$$= \frac{\mu(E)}{d+1}(u_i^{n+1} - u_i^n)$$
$$+ \frac{1}{2}\Delta t\left[k_i^+ N\sum_{j\in E}[k_j^-(-u_i^{n+1} + u_j^{n+1})] + k_i^+ N\sum_{j\in E}[k_j^-(-u_i^n + u_j^n)]\right]$$
$$= \frac{\mu(E)}{d+1}(u_i^{n+1} - u_i^n) + \frac{1}{2}\Delta t k_i^+ N\sum_{j\in E}[k_j^-(-u_i^{n+1} + u_j^{n+1})] + \frac{1}{2}\Delta t k_i^+ N\sum_{j\in E}[k_j^-(-u_i^n + u_j^n)]$$
$$+ \frac{1}{2}\Delta t k_i^+ N\sum_{j\in E}[k_j^- u_i^{n+1}] - \frac{1}{2}\Delta t k_i^+ N\sum_{j\in E}[k_j^- u_i^{n+1}]. \quad (3.75)$$

Now, we can rearrange terms

$$\begin{aligned}
&\frac{\mu(E)}{d+1}(u_i^{n+1}-u_i^n)-\frac{1}{2}\Delta t k_i^+ N\sum_{j\in E}\left[k_j^-(-u_i^{n+1}+u_i^n)\right]\\
&\quad+\frac{1}{2}\Delta t k_i^+ N\sum_{j\in E}\left[k_j^-(-u_i^{n+1}+u_j^{n+1})\right]+\frac{1}{2}\Delta t k_i^+ N\sum_{j\in E}\left[k_j^-(-u_i^{n+1}+u_j^n)\right]\\
&\quad=\left[\frac{\mu(E)}{d+1}-\frac{1}{2}\Delta t k_i^+\right](u_i^{n+1}-u_i^n)+\frac{1}{2}\Delta t k_i^+ N\sum_{j\in E}\left[-k_j^-(u_i^{n+1}-u_j^{n+1})\right]\\
&\qquad\qquad+\frac{1}{2}\Delta t k_i^+ N\sum_{j\in E}\left[-k_j^-(u_i^{n+1}-u_j^n)\right]. \qquad (3.76)
\end{aligned}$$

We check sub-element positivity following definition 13, page 48. The second and third coefficients are always positive. A time-step condition coming from the first term is

$$\Delta t\le\frac{2\mu(E)}{k_i^{+,E}(d+1)},\qquad \forall i,E\in\mathcal{T}^h. \qquad (3.77)$$

The physical time-step condition (3.77) together with the condition (3.73) are sufficient for sub-element positivity of the space-time N scheme (3.70). Condition (3.77) is the same as derived in [AM03a, Ric05, RCD05] started from the implicit method examining properties of the implicit matrices.

Relation (3.73) is satisfied, if the relaxation parameters are bounded by

$$\alpha_i\le\left(\sum_{E\in\mathcal{D}_i}\frac{\mu(E)}{d+1}+\frac{\Delta t}{2}k_i^{+,E}\right)^{-1}. \qquad (3.78)$$

As the second possibility, we consider the 3BDF time integration method

$$\frac{\partial u_i}{\partial t}\approx\frac{\alpha^{n+1}u_i^{n+1}+\alpha^n u_i^n+\alpha^{n-1}u_i^{n-1}}{t^{n+1}-t^n} \qquad (3.79)$$

with coefficients

$$\alpha^{n+1}=\frac{1+2\tau}{1+\tau},\quad \alpha^n=-1-\tau,\quad \alpha^{n-1}=\frac{\tau^2}{1+\tau},\quad \tau=\frac{t^{n+1}-t^n}{t^n-t^{n-1}}, \qquad (3.80)$$

i.e.

$$\frac{1}{t^{n+1}-t^n}\left(\alpha^{n+1}u_i^{n+1}+\alpha^n u_i^n+\alpha^{n-1}u_i^{n-1}\right)=-\frac{1}{\mu(S_i)}\sum_{E\in\mathcal{D}_i}\phi_i^{E,n+1}. \qquad (3.81)$$

The space-time nodal contribution is given by

$$\phi^{E^{\mathrm{ST}}}=\frac{\mu(E)}{d+1}\left(\alpha^{n+1}u_i^{n+1}+\alpha^n u_i^n+\alpha^{n-1}u_i^{n-1}\right)+(t^{n+1}-t^n)\phi_i^{E,n+1}. \qquad (3.82)$$

Positivity cannot be ensured for 3BDF time integration scheme. The system is solved in dual time again. Positivity cannot be ensured for this scheme.

The system scheme with Crank-Nicholson time integration can be written in terms of a space-time nodal contribution

$$\begin{aligned}\mathbf{u}_i^{n+1,m+1} &= \mathbf{u}_i^{n+1,m} - \alpha_i \sum_E \left[ \frac{\mu(E)}{d+1}(\mathbf{u}_i^{n+1} - \mathbf{u}_i^n) + \frac{1}{2}\Delta t(\phi_i^{E,n+1} + \phi_i^{E,n}), \right] \\ &= \mathbf{u}_i^{n+1,m} - \alpha_i \sum_E \left[ \frac{\mu(E)}{d+1}(\mathbf{u}_i^{n+1} - \mathbf{u}_i^n) \right. \\ &\quad \left. + \frac{1}{2}\Delta t[\bar{\mathbf{k}}_i^{+,E}(\bar{\mathbf{u}}_i^{n+1} - \mathbf{u}_{\text{in}}^{E,n+1}) + \bar{\mathbf{k}}_i^{+,E}(\bar{\mathbf{u}}_i^n - \mathbf{u}_{\text{in}}^{E,n})] \right], \quad (3.83)\end{aligned}$$

with $\mathbf{u}_{\text{in}}$ defined by (3.38). Note the difference between $\mathbf{u}_i$ and $\bar{\mathbf{u}}_i$ (equation (3.15)). We would like to mention, that in the original work [AM01, Mez02, MRAD03] a different linearization is used for the discretization of the time derivatives. The 3BDF time integration scheme is extended in a similar manner as the Crank-Nicholson scheme.

The N scheme is a linear, positive scheme, therefore it is first order accurate only.

Two different extension of the second order LDA scheme will be considered. The LDA scheme of Ferrante and Deconinck [FD97], section 3.6.2, was developed using the finite element framework, while the LDA scheme of Caraeni [Car00, CCF01, CF05], section 3.6.3, simply distributes the unsteady residual with a "steady" version of the LDA distribution coefficients.

## 3.6.2. LDA scheme of Ferrante and Deconinck

This version of the LDA scheme was developed by Ferrante and Deconinck, see [FD97]. We start from the conservative formulation of the governing equation (2.1). Multiply the equation by the Petrov-Galerkin test function $\varphi_i$ and integrate over the region $\Omega$

$$\int_\Omega \varphi_i \frac{\partial u}{\partial t} \mathrm{d}\vec{x} + \int_\Omega \varphi_i \nabla_x \cdot \vec{f} \, \mathrm{d}\vec{x} = 0 \quad \text{with} \quad \nabla_x \cdot \vec{f} = \vec{\lambda} \cdot \nabla_x u. \quad (3.84)$$

The integral over domain $\Omega$ is written as the sum of the integrals over simplex elements $E \in \mathcal{D}_i$ adjacent to the node $i$. The solution is approximated on each element using the linear trial functions as

$$u^h = \sum_{j \in E} u_j \psi_j. \quad (3.85)$$

Note that $\nabla_x u^h$ is a constant function per element.

The second integral of equation (3.84) is rewritten in the quasi-linear form and constant terms are taken out

$$\int_E \varphi_i \nabla_x \cdot \vec{f}^h \,\mathrm{d}\vec{x} = \int_{E_t} \varphi_i \vec{\lambda} \cdot \nabla_x u^h \,\mathrm{d}\vec{x} = \overline{\vec{\lambda}} \cdot \nabla_x u^h \int_E \varphi_i \,\mathrm{d}\vec{x} = \beta_i \phi^E. \tag{3.86}$$

with residual $\phi^E$ defined by (3.17), upwind parameters (3.14) and distribution coefficients $\beta_i$ (3.40).

The first integral is approximated as

$$\int_\Omega \varphi_i \frac{\partial u^h}{\partial t} \,\mathrm{d}\vec{x} = \sum_{E \in \mathcal{D}_i} \sum_{j \in E} \frac{\partial u_j}{\partial t} \int_E \varphi_i \psi_j \,\mathrm{d}\vec{x} = \sum_{E \in \mathcal{D}_i} \sum_{j \in E} \frac{\partial u_j}{\partial t} m_{ij}^E. \tag{3.87}$$

Term $m_{ij}^E = \mu(E) \tilde{m}_{ij}^E = \int_E \varphi_i \psi_j \,\mathrm{d}\vec{x}$ is the element contribution to the mass matrix. Equation (3.86) is satisfied for the test function defined as

$$\varphi_i(\vec{x}) = \varphi_i^{\text{Galerkin}}(\vec{x}) + \sum_{E \in i} \left( \beta_i^E - \frac{1}{d+1} \right) \Pi^E(\vec{x}), \tag{3.88}$$

where $\Pi^E(\vec{x})$ is the characteristic function of the element; it is unit for $\vec{x}$ in $E$ and zero outside. Hence, with this test function one can evaluate the element contribution to the mass matrix explicitly

$$m_{ij}^E = \mu(E) \tilde{m}_{ij}^E, \qquad \tilde{m}_{ij}^E = \frac{1}{d+1} \left( \frac{1+\delta_{ij}}{d+2} + \beta_j - \frac{1}{d+1} \right). \tag{3.89}$$

Since the mass matrix is taken into account, any second order time discretization can be used. Here we concentrate on the three point backward differentiation formula (3BDF) (3.79) with coefficients (3.80). The contribution from element $E$ is then

$$\begin{aligned} \frac{\phi_i^{E^{\mathrm{ST}}}}{t^{n+1} - t^n} = {} & \frac{\mu(E)}{d+1} \left( k_i^+ N + \frac{2}{d+2} - \frac{1}{d+1} \right)^{n+1} \frac{\partial u_i}{\partial t} \\ & + \frac{\mu(E)}{d+1} \sum_{\substack{j \in T \\ j \neq i}} \left[ \left( k_j^+ N + \frac{1}{d+2} - \frac{1}{d+1} \right) \frac{\partial u_j}{\partial t} \right]^{n+1} + \beta_i \phi^{E,n+1}. \end{aligned} \tag{3.90}$$

The LDA scheme is formally extended to the system of equations as the other schemes. For the scalar case, the scheme corresponds to the Petrov-Galerkin formulation of the finite element method. In the system case the correspondence is not so clear, since the test functions would have to be matrices.

The element contribution to the mass matrix is in this case sub-matrix

$$m_{ij}^E = \frac{\mu(E)}{d+1} \left( \frac{1+\delta_{ij}}{d+2} \mathbf{I} + \beta_j - \frac{1}{d+1} \mathbf{I} \right) = \frac{\mu(E)}{d+1} \left( \frac{1+\delta_{ij}}{d+2} \mathbf{I} + \bar{\mathbf{k}}_j^+ \mathbf{N} - \frac{1}{d+1} \mathbf{I} \right), \tag{3.91}$$

where matrix $\mathbf{N}$ is given by (3.39). The nodal contribution is

$$\frac{\phi_i^{E^{\mathrm{ST}}}}{t^{n+1}-t^n} = \frac{\mu(E)}{d+1}\left(\bar{\mathbf{k}}_i^+\mathbf{N} + \frac{2}{d+2}\mathbf{I} - \frac{1}{d+1}\mathbf{I}\right)^{n+1}\frac{\partial \mathbf{u}_i}{\partial t} + \frac{\mu(E)}{d+1}\sum_{\substack{j\in E\\ j\neq i}}\left[\left(\bar{\mathbf{k}}_j^+\mathbf{N} + \frac{1}{d+2}\mathbf{I} - \frac{1}{d+1}\mathbf{I}\right)\frac{\partial \mathbf{u}_j}{\partial t}\right]^{n+1} + \bar{\mathbf{k}}_i^+\mathbf{N}\phi^{E,n+1}, \quad (3.92)$$

where $\phi^{E,n+1}$ is given by (3.13). The scheme is equipped with the three point backward differentiation formula (3BDF) for the time discretization.

### 3.6.3. LDA scheme of Caraeni

The space-time scheme of Caraeni [Car00, CCF01, CF05, MRAD03] was developed in a second and third order version. The second order version distributes the space time residual

$$\frac{\phi^{E^{\mathrm{ST}}}}{t^{n+1}-t^n} = \int_E\left(\frac{\partial u^h}{\partial t} + \nabla\cdot\vec{f}^h\right)\mathrm{d}\vec{x} = \mu(E)\sum_{i\in E}\frac{\alpha^{n+1}u_i^{n+1} + \alpha^n u_i^n + \alpha^{n-1}u_i^{n-1}}{t^{n+1}-t^n} + \sum_{i\in E}k_i^{n+1}u_i^{n+1} \quad (3.93)$$

using LDA distribution coefficients (3.40). The time derivative is discretized using 3BDF scheme, but other discretizations can be also considered. For a system of equations, the scheme is extended in the standard manner, i.e. the unsteady residual is distributed using the distribution matrices (3.41).

This scheme is simpler than the LDA scheme of Ferrante and Deconinck from section 3.6.2, but it is also more oscillatory in the vicinity of steep gradients. The version for the system of equations was successfully used for large eddy simulations [Car00].

### 3.6.4. One layer space-time scheme of Mezine and Abgrall

The LDA scheme is a linear second order scheme. A second order, positive scheme must be non-linear, as is known from the Godunov theorem. We will describe the construction of the nonlinear, N-modified scheme of Mezine and Abgrall [AM03a, Mez02] in section 3.6.4. This scheme is positive under a time-step restriction. A (two-layer) second order positive scheme without a time-step restriction is described in section 3.6.5.

The space-time N scheme from section 3.6.1 is linear and sub-element positive with unbounded distribution coefficients. We can apply nonlinear mapping (3.52)

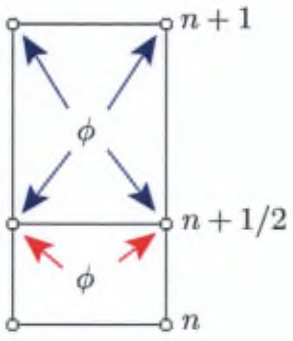


Figure 3.4.: Two layer space-time scheme

to get uniformly bounded coefficients, yet with the unchanged signs of $c_{ij}^E$. Then, the scheme is second order accurate.

The (unlimited) nodal residual is given by the equation (3.70). The modified distribution coefficients are computed according to (3.59). The resulting scheme is sub-element positive under a time-step given by (3.77). The resulting system of algebraic equations is solved in dual time. This scheme was published in [AM01, MA02, AM03a, MRAD03]. The system scheme is obtained in a similar manner.

### 3.6.5. Two layer space-time scheme of Mezine and Abgrall

The two-layer approach was developed as a cure for the time-step restriction of the implicit space-time schemes [CRDP01, Ric01, CD01, CD02, CRD03, Csí02]. Always two layers of elements are solved, see Fig. 3.4. The lower layer, between time levels $n$ and $n+1/2$ is the N-modified scheme from section 3.6.4. The time-step $\Delta t^{\text{Lower}} = t^{n+1/2} - t^n$ obeys restriction (3.77). The scheme in the upper layer is similar to the lower layer scheme, however part of the space-time residual is distributed to nodes in $n+1/2$ level and part to the level $n+1$, such that the scheme is sub-element positive under arbitrary time step $\Delta t^{\text{Upper}}$. The second order accuracy is achieved by the mapping (3.59).

The full scheme is given after assembly of the nodal contributions from the lower layer $[t^n, t^{n+1/2}]$ of elements

$$\phi_i^{E^{\text{ST}},n+1/2,\text{Lower}} = \frac{\mu(E)}{d+1}(u_i^{n+1/2} - u_i^n) + \frac{1}{2}\Delta t_1(\phi_i^{E,n+1/2} + \phi_i^{E,n}), \tag{3.94}$$

with the contribution from the upper layer of elements $[t^{n+1/2}, t^{n+1}]$ to the $n+1/2$ level

$$\phi_i^{E^{\text{ST}},n+1/2,\text{Upper}} = \frac{1}{2}\Delta t_2 \phi_i^{E,n+1/2} \tag{3.95}$$

and the contribution from the upper elements to the $n+1$ level

$$\phi_i^{E^{\text{ST}},n+1,\text{Upper}} = \frac{\mu(E)}{d+1}(u_i^{n+1} - u_i^{n+1/2}) + \frac{1}{2}\Delta t_2 \phi_i^{E,n+1}. \tag{3.96}$$

Note that the element residual at the upper layer given by

$$\phi^{E^{\mathrm{ST}},\mathrm{Upper}} = \sum_{i \in E} \phi_i^{E^{\mathrm{ST}},n+1,\mathrm{Upper}} + \phi_i^{E^{\mathrm{ST}},n+1/2,\mathrm{Upper}}, \tag{3.97}$$

is the same approximation of the space-time residual as for the lower layer scheme. The modification procedure (3.59) is applied on each element in the lower and upper level separately.

This scheme is positive and second order accurate. Unfortunately, it has problems with iterative convergence in dual time. Some reasoning can be found in a recent article [Abg06]. As an alternative without the iterative convergence problems the time accurate Bx scheme was proposed [DD05a].

### 3.6.6. Bx scheme

The basis for the Bx scheme is the LDA scheme of Ferrante and Deconinck [FD97] with 3BDF time integration, see section 3.6.2 and the N scheme with the same time integration procedure, see section 3.6.1. The 3BDF procedure is preferred over the Crank-Nicholson method, because the later does not include dissipation in time, as it corresponds to the central time discretization. It renders Crank-Nicholson scheme not enough robust for technical type of computations.

The change in the pressure due to the traveling pressure wave can be locally approximated as a change due to pure convection of the pressure wave and the change due to its expansion or compression. Pure convection obeys the equation

$$\frac{\partial p}{\partial t} + \vec{v}_c \cdot \vec{\nabla} p = 0, \tag{3.98}$$

where $\vec{v}_c$ is the speed of the wave. This effect is dominant e.g. in the convection of an inviscid vortex. Pure expansions or compressions happen with respect to the frame of reference moving with velocity $\vec{v}_c$. We define $\vec{v}_r = \vec{v} - \vec{v}_c$, where $\vec{v}$ is the velocity of the flow and $\vec{v}_r$ is relative velocity with respect to the frame of reference. The shock sensor has to be constructed *using the relative velocity*, i.e.

$$\begin{aligned} sc = \frac{1}{\delta_{pv}}(\vec{\nabla} p \cdot \vec{v}_r)^+ = \frac{1}{\delta_{pv}}(\vec{\nabla} p \cdot \vec{v}_r + \underbrace{\frac{\partial p}{\partial t} + \vec{v}_c \cdot \vec{\nabla} p}_{=0})^+ \\ = \frac{1}{\delta_{pv}}(\frac{\partial p}{\partial t} + \vec{\nabla} p \cdot (\vec{v}_r + \vec{v}_c))^+ = \frac{1}{\delta_{pv}}(\frac{\partial p}{\partial t} + \vec{\nabla} p \cdot v)^+, \end{aligned} \tag{3.99}$$

with scaling $\delta_{pv}$ defined in section 3.5.5, page 41. If the shock sensor is positive, the flow experiences compression, while if the argument of the shock sensor is negative, the flow is expanding with respect to the relative frame of reference. The operator is scaled in the same manner as for steady problems (3.65) to define the blending

coefficient, which retains the second order of accuracy of the LDA scheme together with non-oscillatory behavior.

Due to the unconditional stability of the underlying N and the LDA schemes with the three points backward time integration formula, the resulting unsteady Bx scheme is expected to be robust for high CFL number simulations.

Since this scheme is novel, we present some numerical results showing its performance in comparison with the performance of the other schemes. We have chosen a smooth convection of a vortex as the first unsteady test case, see [DD05a]. The problem is solved on the square domain $[-0.5, 0.5] \times [-0.5, 0.5]$ filled with a Weatherill type triangulation with 41 points along each side. The flow velocity is given by the main stream velocity $\vec{v}_m = (6, 0)$ and the circumferential perturbation

$$(v_x, v_y)_\theta = (-y, x) \cdot \omega, \quad \omega = 15 \cdot (\cos 4\pi r + 1), \quad r = \sqrt{x^2 + y^2} \tag{3.100}$$

for $r < 0.25$, $(v_x, v_y)_\theta = \vec{0}$ elsewhere. Density is chosen constant $\rho = 1.4$ and the pressure from the balance in the radial direction $p = p_m + \Delta p$, where

$$\Delta p = \frac{15^2 \rho}{(4\pi)^2} \left( 2\cos(4\pi r) + 8\pi r \sin(4\pi r) + \frac{\cos(8\pi r)}{8} + \frac{4\pi r \sin(8\pi r)}{4} + 12\pi^2 r^2 \right) + C. \tag{3.101}$$

The constant $C$ is such that $p|_{r=0.25} = p_m = 100$. This setup gives maximal Mach number in the domain $M \doteq 0.8$. The free stream values are prescribed on the boundaries $y = \pm 0.5$ and periodic boundaries are used for $x = \pm 0.5$. The simulation stops after one period, i.e. $t_{\max} = 1/6$. This test case was first presented in [DD05a].

In Fig. 3.5 the isolines of the pressure for the different schemes are shown. The computation was performed with $CFL = 1$. Distribution of the pressure in the core of the vortex shows that the Bx scheme performs essentially as the LDA scheme for the smooth regions. The performance of the N-limited scheme is noticeably worse. We have performed the same test with several other schemes. The minimal pressure in the vortex core is given in Table 3.2. The finite volume method is cell centered with the three points backward time integration scheme formulated in dual time and with, or without Barth's limiter, see section 4.2. Note, that the Finite Volume scheme performs worse even in the case with no limiter and it uses approximately twice more unknowns than the RD scheme.

As a test to examine the scheme on flow with complex features, we present results for a 2D Riemann problem [MRAD03]. The problem is symmetric along $y = x$ with the initial conditions given by

$$(\rho, v_x, v_y, p) = \begin{cases} (\ 1.5, & 0, & 0, & 1.5\ ) & y < 0.8,\ y > x \\ (\ 0.1379928, & 1.2060454, & 1.2060454, & 0.0290323\ ) & x > 0.8,\ y > x \\ (\ 0.5322581, & 1.2060454, & 0, & 0.3\ ) & y > x \text{ elsewhere,} \end{cases} \tag{3.102}$$

see Fig. 3.6. The simulation stops at $t_{\max} = 0.8$.

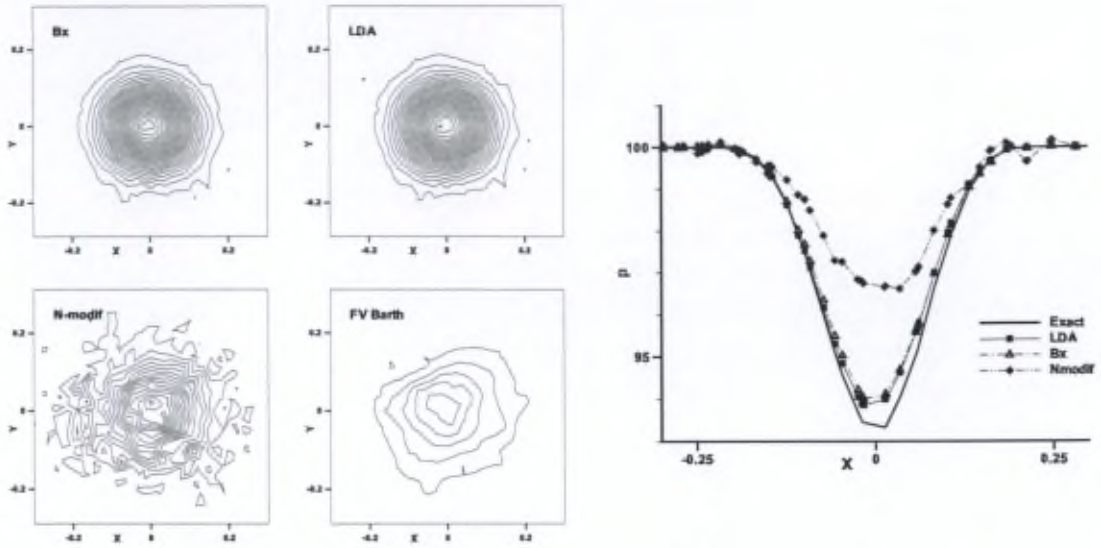


Figure 3.5.: Advection of the vortex, $t = 1/6$. Isolines of the pressure for different schemes. Distribution of the pressure in the core of the vortex for different schemes.

| Scheme: | Bx | LDA | N-limited | LDA [CCF01] | FV nolim | FV Barth | Exact |
|---|---|---|---|---|---|---|---|
| $p_{\max}$ | 100.11 | 100.12 | 100.42 | 100.12 | 100.04 | 100.11 | 100 |
| $p_{\min}$ | 94.00 | 93.84 | 96.27 | 93.88 | 94.35 | 98.76 | 93.213 |

Table 3.2.: The maximal and the minimal pressure in the vortex core for the vortex advection problem, $t = 1/6$. FV is the cell centered Finite Volume scheme with the linear reconstruction and with or without Barth's [BJ89] limiter and the three point backward scheme formulated in dual time.

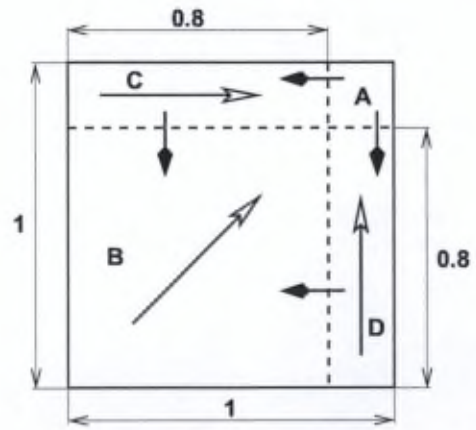


Figure 3.6.: Two-dimensional Riemann problem. Sketch of the situation.

In Fig. 3.7 comparison of the Bx scheme with the N-modified is presented on meshes with spatial resolution 1/200 and 1/400. Both computations with the Bx scheme show much higher resolution. It can be observed on pronounced Kelvin-Helmholtz instabilities along the slip lines, where the Bx scheme gives a richer structure, which is seen from the growth of the rollers along the instability. The N-modified scheme captures the instabilities well, however it clearly gives lower resolution. To show that the scheme captures the discontinuities without spurious oscillations we make a cut along the diagonal for the mesh 1/400, see Fig. 3.7. The solution obtained by the Bx scheme shows non-oscillatory capturing of the smooth regions as well as discontinuities. On the other hand, there are undamped high frequency modes on the solution given by the N-modified scheme, which causes oscillations in the smooth regions of the solution.

A natural question arises: why not use the N scheme with the Euler backward time integration procedure, which has better stability properties (it can be shown positive) than the 3BDF method. However, in this case the scheme would not be conservative, because there is no continuous approximation of the flux $\vec{\mathbf{f}}^h$ except if the blending coefficient $\theta$ is constant in the domain.

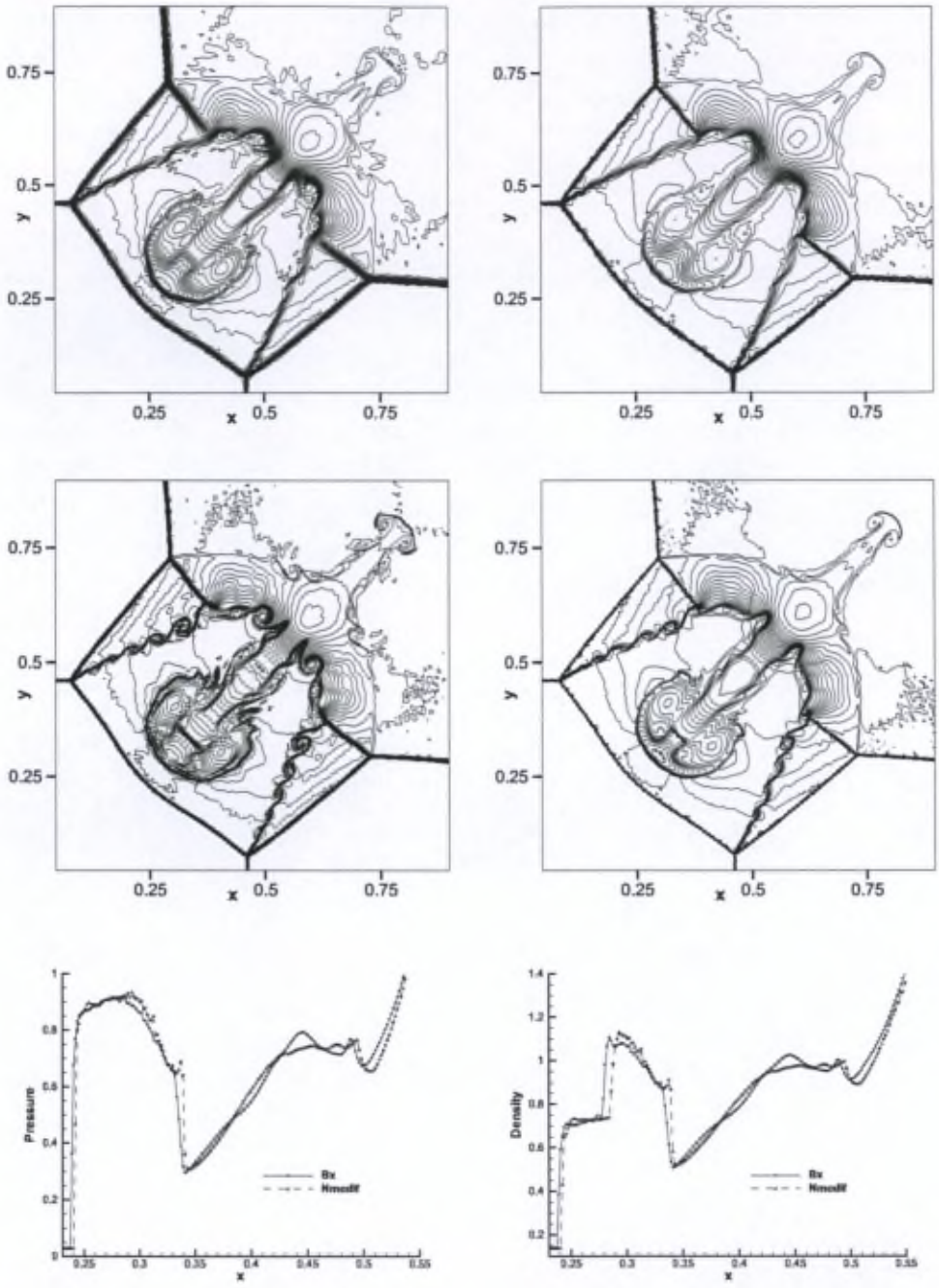


Figure 3.7.: Two-dimensional Riemann problem, density contours ($\Delta\rho = 0.05$) at $t = 0.8$. Left figures show the solution obtained by the Bx scheme, while right figures show the results of the N-modified scheme. Top row: spatial resolution 1/200, middle row 1/400. Bottom: solution along the diagonal for the mesh 1/400 for the pressure and the density.

## 3.7. Extension of the schemes for moving mesh computations

In this section we will extend all the considered schemes from section 3.6, starting from first order and second order linear schemes upto nonlinear schemes.

### 3.7.1. N scheme + Crank-Nicholson

The N scheme with the Euler explicit time integrator was already extended to moving meshes in [Mic00, MSD03]. Extension for the Crank-Nicholson time integrator was published in [DD05b].

We start from the quasi-linear form of the equation (2.27). Similarly to the space-time N scheme, section 3.6.1, the discretization of the time derivative corresponds to the discretization on the medial dual grid

$$\phi_i^{\text{time}} = \frac{1}{t^{n+1} - t^n} \frac{\mu(E^{n+1})u_i^{n+1} - \mu(E^n)u_i^n}{d+1}. \tag{3.103}$$

The convective term including $\vec{w} \cdot \vec{\nabla}_x u$ is discretized as (3.35) with the upwind parameters defined as

$$k_i^{n,n+1} = \overline{(\vec{\lambda} - \vec{w})}^{n,n+1} \cdot \frac{\vec{n}_j^{n,n+1}}{d}, \tag{3.104}$$

where $\vec{\lambda}$ and $\vec{w}$ are the averaged advection vector and mesh velocity in the element at time levels $n$ and $n+1$. For the precise definition of the averaged state see section 3.7.8, page 66. Normals $\vec{n}_j^{n+1}$ and $\vec{n}_j^n$ are taken from the geometric position at time levels $n$ and $n+1$ respectively. The last, geometrical term is discretized in accordance with the time discretization using the identity (2.12). In [Mic00, MSD03] the authors compute the integral of the geometric term over element $E$

$$\int_E u \nabla_x \cdot \vec{w} \, \mathrm{d}\vec{x} \approx \frac{\sum_{j \in E} u_j^n}{d+1} \frac{\mu(E^{n+1}) - \mu(E^n)}{t^{n+1} - t^n} \tag{3.105}$$

and then distribute it with the LDA distribution coefficient $\beta_i^{\text{LDA}}$ (3.40). That discretization spoils the positivity of the scheme. Instead of this, we discretize the last term on the dual mesh, (as it is usual for pointwise treatment of source terms in the vertex centered finite volume schemes). The full nodal contribution is then

$$\begin{aligned} \phi_i^{E^{\text{ST}}} = & \frac{\mu(E^{n+1})u_i^{n+1} - \mu(E^n)u_i^n}{d+1} \\ & + \frac{\Delta t}{2} \left( \left( k_i^+ (u_i - u_{\text{in}}) \right)^{n+1} + \left( k_i^+ (u_i - u_{\text{in}}) \right)^n \right) \\ & - \frac{u_i^n + u_i^{n+1}}{2} \frac{\mu(E^{n+1}) - \mu(E^n)}{d+1}. \end{aligned} \tag{3.106}$$

Note, that the contribution was multiplied by $\Delta t$ for a correspondence to the space-time approach of the unsteady RD schemes. The scheme is sub-element positive under the time-step restriction

$$\Delta t \leq \frac{\mu(E^{n+1}) + \mu(E^n)}{k_i^{+,E}(d+1)}, \qquad \forall i, E \in \mathcal{T}^h. \tag{3.107}$$

The full nodal contribution for the system of equations is

$$\begin{aligned}\phi_i^{E^{\mathrm{ST}}} = &\frac{\mu(E^{n+1})\mathbf{u}_i^{n+1} - \mu(E^n)\mathbf{u}_i^n}{d+1} \\ &+ \frac{\Delta t}{2}\left(\left(\bar{\mathbf{k}}_i^+(\bar{\mathbf{u}}_i - \mathbf{u}_{\mathrm{in}})\right)^{n+1} + \left(\bar{\mathbf{k}}_i^+(\bar{\mathbf{u}}_i - \mathbf{u}_{\mathrm{in}})\right)^{n}\right) \\ &- \frac{\mathbf{u}_i^n + \mathbf{u}_i^{n+1}}{2}\frac{\mu(E^{n+1}) - \mu(E^n)}{d+1}.\end{aligned} \tag{3.108}$$

### 3.7.2. N scheme + 3BDF

The extension of the N scheme with the 3BDF time integrator differs mainly in the treatment of the time derivatives and the geometric source term. The time derivative is discretized as

$$\frac{1}{t^{n+1} - t^n}\frac{\alpha^{n+1}\mu(E^{n+1})u_i^{n+1} + \alpha^n\mu(E^n)u_i^n + \alpha^{n-1}\mu(E^{n-1})u_i^{n-1}}{d+1}. \tag{3.109}$$

The geometrical term is discretized in accordance with the time discretization using the identity (2.12), on the dual mesh with pointwise treatment

$$\frac{1}{t^{n+1} - t^n}u_i^{n+1}\frac{\alpha^{n+1}\mu(E^{n+1}) + \alpha^n\mu(E^n) + \alpha^{n-1}\mu(E^{n-1})}{d+1}, \tag{3.110}$$

where the first fraction is the arithmetic average of the solution over the element and in the second denominator term $d+1$ accounts for the part belonging to node $i$. The full nodal contribution is then

$$\begin{aligned}\frac{\phi_i^{E^{\mathrm{ST}}}}{t^{n+1} - t^n} = &\frac{1}{t^{n+1} - t^n}\frac{\alpha^{n+1}\mu(E^{n+1})u_i^{n+1} + \alpha^n\mu(E^n)u_i^n + \alpha^{n-1}\mu(E^{n-1})u_i^{n-1}}{d+1} \\ &+ k_i^+(u_i^{n+1} - u_{\mathrm{in}}^{n+1}) - \frac{1}{t^{n+1} - t^n}u_i^{n+1}\frac{\alpha^{n+1}\mu(E^{n+1}) + \alpha^n\mu(E^n) + \alpha^{n-1}\mu(E^{n-1})}{d+1}.\end{aligned} \tag{3.111}$$

Similar expression is obtained for a system of equations.

### 3.7.3. LDA scheme of Ferrante and Deconinck

This section was published in [DDF05a, DD06a, DD06b]. We start from the conservative ALE formulation (2.26). Multiply the equation by the Petrov-Galerkin test function from the current configuration $\varphi_i$ and integrate over the time dependent region $\Omega_t$

$$\int_{\Omega_t} \frac{\varphi_i}{J_{\mathcal{A}_t}} \frac{\partial J_{\mathcal{A}_t} u}{\partial t}\bigg|_{\vec{Y}} \mathrm{d}\vec{x} + \int_{\Omega_t} \varphi_i \nabla_x \cdot (\vec{f} - \vec{w}u)\, \mathrm{d}\vec{x} = 0 \quad \text{with} \quad \nabla_x \cdot \vec{f} = \vec{\lambda} \cdot \nabla_x u. \tag{3.112}$$

The integral over domain $\Omega_t$ is written as the sum of the integrals over simplex elements $E \in \mathcal{D}_i$ adjacent to the node $i$. The solution and the mesh velocity are approximated on each element using the linear trial functions as

$$u^h = \sum_{j \in E} u_j \psi_j, \qquad \vec{w}^h = \sum_{j \in E} \vec{w}_j \psi_j. \tag{3.113}$$

Note that $\nabla_x \cdot \vec{w}^h$ and $\nabla_x u^h$ are constant functions per element and the approximation of Jacobian $J^h_{\mathcal{A}_t}$ is constant in space over each element. The trial functions $\psi_j$ as function of the ALE coordinate $\vec{Y}$ are constant in time and can be taken in front of the time derivative

$$\begin{aligned}\int_{\Omega_t} \frac{\varphi_i}{J^h_{\mathcal{A}_t}} \frac{\partial J^h_{\mathcal{A}_t} u^h}{\partial t}\bigg|_{\vec{Y}} \mathrm{d}\vec{x} &= \sum_{E \in \mathcal{D}_i} \frac{1}{J^h_{\mathcal{A}_t}} \sum_{j \in E} \frac{\partial J^h_{\mathcal{A}_t} u_j}{\partial t}\bigg|_{\vec{Y}} \int_{E_t} \varphi_i \psi_j \, \mathrm{d}\vec{x} \\ &= \sum_{E \in \mathcal{D}_i} \frac{1}{J^h_{\mathcal{A}_t}} \sum_{j \in E} \frac{\partial J^h_{\mathcal{A}_t} u_j}{\partial t}\bigg|_{\vec{Y}} m^E_{ij}. \end{aligned} \tag{3.114}$$

Term $m^E_{ij} = \mu(E_t)\bar{m}^E_{ij} = \int_{E_t} \varphi_i \psi_j \, \mathrm{d}\vec{x}$ is the element contribution to the mass matrix.

The second integral of equation (3.112) is rewritten in the quasi-linear form and constant terms are taken out

$$\begin{aligned}\int_{E_t} \varphi_i \nabla_x \cdot (\vec{f}^h - \vec{w}^h u^h)\, \mathrm{d}\vec{x} &= \int_{E_t} \varphi_i (\vec{\lambda} \cdot \nabla_x u^h - \vec{w}^h \cdot \nabla_x u^h - u^h \nabla_x \cdot \vec{w}^h)\, \mathrm{d}\vec{x} \\ &= \overline{(\vec{\lambda} - \vec{w})} \cdot \nabla_x u^h \int_{E_t} \varphi_i \, \mathrm{d}\vec{x} - \nabla_x \cdot \vec{w}^h \int_{E_t} \varphi_i u^h \, \mathrm{d}\vec{x} \\ &= \overline{(\vec{\lambda} - \vec{w})} \cdot \nabla_x u^h \int_{E_t} \varphi_i \, \mathrm{d}\vec{x} - \sum_{j \in E} \left( u_j \nabla_x \cdot \vec{w}^h \int_{E_t} \varphi_i \psi_j \, \mathrm{d}\vec{x} \right) \\ &= \beta_i \phi^E - \nabla_x \cdot \vec{w}^h \sum_{j \in E} \left( u_j m^E_{ij} \right). \end{aligned} \tag{3.115}$$

The ALE element residual $\phi^E$ is defined as

$$\phi^E = \mu(E) \overline{(\vec{\lambda} - \vec{w})} \cdot \sum_{j \in E} u_j \nabla_x \psi_j = \mu(E) \sum_{j \in E} \overline{(\vec{\lambda} - \vec{w})} \cdot \nabla_x \psi_j u_j = \sum_{j \in E} k_j u_j, \tag{3.116}$$

where $\mu(E)$ is the measure of the element and the upwind parameter $k_j$ with respect to the relative speed is given by

$$k_j = \overline{(\vec{\lambda} - \vec{w})} \cdot \nabla_x \psi_j = \overline{(\vec{\lambda} - \vec{w})} \cdot \frac{\vec{n}_j}{d}, \tag{3.117}$$

and $\vec{n}_j$ is the normal to the surface opposite to the node $j$ scaled by its surface.

The distribution coefficient is chosen using the LDA scheme (3.40). The divergence of the mesh velocity is expressed as a time derivative using the identity (2.12). The time derivative (2.12) is discretized by the three point backward differentiation formula (3BDF), i.e.

$$\begin{aligned}
\int_{E_t} \varphi_i u \vec{\nabla}_x \cdot \vec{w} \, \mathrm{d}\vec{x} &= \int_{E_t} \varphi_i u \frac{1}{J_{\mathcal{A}_t}} \frac{\partial J_{\mathcal{A}_t}}{\partial t}\bigg|_{\vec{Y}} \mathrm{d}\vec{x} \approx \int_{E_t} \varphi_i u^h \frac{1}{J^h_{\mathcal{A}_t}} \frac{\partial J^h_{\mathcal{A}_t}}{\partial t}\bigg|_{\vec{Y}} \mathrm{d}\vec{x} \\
&= \int_{E_t} \left( \varphi_i \sum_{j \in E} [\psi_j u_j] \frac{1}{J^h_{\mathcal{A}_t}} \frac{\partial J^h_{\mathcal{A}_t}}{\partial t}\bigg|_{\vec{Y}} \right) \mathrm{d}\vec{x} \\
&= \frac{\alpha^{n+1}\mu(E^{n+1}) + \alpha^n \mu(E^n) + \alpha^{n-1}\mu(E^{n-1})}{t^{n+1} - t^n} \sum_{j \in E} \tilde{m}^E_{ij} u_j,
\end{aligned} \tag{3.118}$$

with coefficients (3.80) and $\tilde{m}^E_{ij}$ defined in (3.89). The scheme respects the discrete geometric conservation law.

The precise averaging of the terms $\overline{(\vec{\lambda} - \vec{w})}$ will be specified later in the chapter 3.7.8. Finally, the fully discrete scheme is given by nodal contribution

$$\begin{aligned}
\frac{\phi_i^{E^{\mathrm{ST}}}}{t^{n+1} - t^n} = \sum_{j \in E} \Bigg[ & \frac{1}{d+1} \left( \frac{\delta_{ij} + 1}{d+2} + \beta_j^{n+1} - \frac{1}{d+1} \right) \\
& \cdot \frac{\alpha^{n+1}\mu(E^{n+1})u_j^{n+1} + \alpha^n \mu(E^n) u_j^n + \alpha^{n-1}\mu(E^{n-1})u_j^{n-1}}{t^{n+1} - t^n} \Bigg] + \beta_i^{n+1} \sum_{j \in E} k_j^{n+1} u_j^{n+1} \\
+ \frac{\alpha^{n+1}\mu(E^{n+1}) + \alpha^n \mu(E^n) + \alpha^{n-1}\mu(E^{n-1})}{t^{n+1} - t^n} & \sum_{j \in E} \left[ \frac{1}{d+1} \left( \frac{1 + \delta_{ij}}{d+2} + \beta_j^{n+1} - \frac{1}{d+1} \right) u_j \right].
\end{aligned} \tag{3.119}$$

The nodal contribution for system of equations is

$$\frac{\phi_i^{E^{\mathrm{ST}}}}{t^{n+1}-t^n} = \underbrace{\frac{1}{d+1}\left(\bar{\mathbf{k}}_i^+\mathbf{N}+\frac{2}{d+2}\mathbf{I}-\frac{1}{d+1}\mathbf{I}\right)}_{\tilde{m}_{ii}^E}\frac{\partial\mu(E)\mathbf{u}_i}{\partial t}$$
$$+\sum_{\substack{j\in E\\ j\neq i}}\left[\underbrace{\frac{1}{d+1}\left(\bar{\mathbf{k}}_j^+\mathbf{N}+\frac{1}{d+2}\mathbf{I}-\frac{1}{d+1}\mathbf{I}\right)}_{\tilde{m}_{ij,j\neq i}^E}\frac{\partial\mu(E)\mathbf{u}_j}{\partial t}\right]+\bar{\mathbf{k}}_i^+\mathbf{N}\sum_{j\in E}\bar{\mathbf{k}}_j\bar{\mathbf{u}}_j$$
$$+\frac{\partial\mu(E)}{\partial t}\sum_{j\in E}\left[\underbrace{\frac{1}{d+1}\left(\frac{1+\delta_{ij}}{d+2}\mathbf{I}+\bar{\mathbf{k}}_j^+\mathbf{N}-\frac{1}{d+1}\mathbf{I}\right)}_{\tilde{m}_{ij}^E}\mathbf{u}_j\right]. \quad (3.120)$$

The time derivatives are discretized by 3BDF scheme (3.79) and (3.80).

### 3.7.4. Galerkin (central) scheme

The Galerkin finite element scheme itself is unstable for hyperbolic problem (2.1). However, it is possible to write an RD scheme as the perturbation of the Galerkin scheme plus dissipation

$$\phi_i = \theta\phi_i^{\mathrm{Galerkin}} + (1-\theta)(\phi_i^{\mathrm{RD}} - \phi_i^{\mathrm{Galerkin}}), \quad (3.121)$$

with coefficient $\theta = 0$. This can be useful later e.g. for the extension of the RD schemes for problems with viscosity [RVAD05, DRAD06]. Once the extension of the LDA scheme for moving meshes (3.119) is known, the Galerkin scheme can be constructed by removing all the terms related to the upwinding (or equivalently dropping the second part of the test function (3.88)). The scheme[2] is given by

$$\frac{\phi_i^{E^{\mathrm{ST}}}}{t^{n+1}-t^n} = \sum_{j\in E}\frac{1+\delta_{ij}}{(d+1)(d+2)}\frac{\partial\mu(E)\mathbf{u}_j}{\partial t}$$
$$+\frac{1}{d+1}\sum_{j\in E}\bar{\mathbf{k}}_j\bar{\mathbf{u}}_j+\frac{\partial\mu(E)}{\partial t}\sum_{j\in E}\frac{1+\delta_{ij}}{(d+1)(d+2)}\mathbf{u}_j. \quad (3.122)$$

[2]This development is strictly valid only for linear flux function.

### 3.7.5. LDA scheme of Caraeni

For the extension of the scheme on the moving meshes the integral of the equation (2.27) over the element is considered. Then, the element residual is

$$\begin{aligned}\frac{\phi^{E^{\mathrm{ST}}}}{t^{n+1}-t^n} &= \int_E \left( \frac{1}{J^h_{\mathcal{A}_t}} \frac{\partial J^h_{\mathcal{A}_t} u^h}{\partial t}\bigg|_{\vec{Y}} + \vec{\nabla}_x \cdot \vec{f}^h - \vec{w}^h \cdot \vec{\nabla}_x u^h - u^h \vec{\nabla}_x \cdot \vec{w}^h \right) \mathrm{d}\vec{x} \\ &= \sum_{i\in E} \frac{\alpha^{n+1}\mu(E^{n+1})u_i^{n+1} + \alpha^n \mu(E^n) u_i^n + \alpha^{n-1}\mu(E^{n-1})u_i^{n-1}}{t^{n+1}-t^n} \\ &+ \sum_{i\in E} k_i^{n+1} u_i^{n+1} + \frac{\alpha^{n+1}\mu(E^{n+1}) + \alpha^n\mu(E^n) + \alpha^{n-1}\mu(E^{n-1})}{t^{n+1}-t^n} \frac{\sum_{i\in E} u_i^{n+1}}{d+1}, \end{aligned} \tag{3.123}$$

with the upwind parameters given by (3.117). The residual is subsequently distributed with LDA distribution coefficients (3.40).

For the system of equations, the integral of the equation (2.27) over the element is considered. Then, the element residual is

$$\begin{aligned}\frac{\phi^{E^{\mathrm{ST}}}}{t^{n+1}-t^n} &= \sum_{i\in E} \frac{\alpha^{n+1}\mu(E^{n+1})\mathbf{u}_i^{n+1} + \alpha^n \mu(E^n) \mathbf{u}_i^n + \alpha^{n-1}\mu(E^{n-1})\mathbf{u}_i^{n-1}}{t^{n+1}-t^n} \\ &+ \sum_{i\in E} \bar{\mathbf{k}}_i^{n+1} \bar{\mathbf{u}}_i^{n+1} + \frac{\alpha^{n+1}\mu(E^{n+1}) + \alpha^n\mu(E^n) + \alpha^{n-1}\mu(E^{n-1})}{t^{n+1}-t^n} \frac{\sum_{i\in E} \mathbf{u}_i^{n+1}}{d+1}, \end{aligned} \tag{3.124}$$

with the upwind parameters given by (3.117). The residual is subsequently distributed with LDA distribution coefficients (3.40).

### 3.7.6. One and Two layer space-time scheme of Mezine and Abgrall

This section was published in [DD06c]. The sub-element positive extension of the N scheme with the Crank-Nicholson time integration method is described in section 3.6.1. As it was noted in section 3.6.5, the upper layer scheme is similar to the lower layer scheme, with the residual distributed to the nodes in $n+1/2$ and $n+1$ levels. We use the similar extension for the upper layer as for the lower layer, i.e. nodal contribution from the lower layer $[t^n, t^{n+1/2}]$ elements is

$$\begin{aligned}\phi_i^{E^{\mathrm{ST}},n+1/2,\mathrm{Lower}} &= \frac{1}{d+1}(\mu(E^{n+1/2})u_i^{n+1/2} - \mu(E^n)u_i^n) \\ &+ \frac{\Delta t^{\mathrm{Lower}}}{2}\left( \left( k_i^+(u_i - u_{\mathrm{in}}) \right)^{n+1/2} + \left( k_i^+(u_i - u_{\mathrm{in}}) \right)^n \right) \\ &- \frac{\sum_{j\in E}(u_j^{n+1/2} + u_j^n)}{2(d+1)} \frac{\mu(E^{n+1/2}) - \mu(E^n)}{d+1}. \end{aligned} \tag{3.125}$$

The contribution from upper elements $[t^{n+1/2}, t^{n+1}]$ to the $n+1/2$ layer is

$$\phi_i^{E^{\mathrm{ST}},n+1/2,\mathrm{Upper}} = \frac{\Delta t^{\mathrm{Upper}}}{2}\left(k_i^+(u_i - u_{\mathrm{in}})\right)^{n+1/2} \tag{3.126}$$

and the contribution from upper elements to the $n+1$ layer is

$$\phi_i^{E^{\mathrm{ST}},n+1,\mathrm{Upper}} = \frac{1}{d+1}(\mu(E^{n+1})u_i^{n+1} - \mu(E^{n+1/2})u_i^{n+1/2}) + \frac{\Delta t^{\mathrm{Upper}}}{2}\left(k_i^+(u_i - u_{\mathrm{in}})\right)^{n+1} - \frac{\sum_{j\in E}(u_j^{n+1} + u_j^{n+1/2})}{2(d+1)}\frac{\mu(E^{n+1}) - \mu(E^{n+1/2})}{d+1}. \tag{3.127}$$

After application the limiting procedure (3.59), the scheme is positive and second order accurate under arbitrary time step $\Delta t = \Delta t^{\mathrm{Lower}} + \Delta t^{\mathrm{Upper}}$.

The scheme is extended for the system of equations in the standard manner. The element contribution is given by

$$\phi_i^{E^{\mathrm{ST}},n+1/2,\mathrm{lower}} = \frac{1}{d+1}(\mu(E^{n+1/2})\mathbf{u}_i^{n+1/2} - \mu(E^n)\mathbf{u}_i^n) + \frac{\Delta t_1}{2}\left(\left(\bar{\mathbf{k}}_i^+(\bar{\mathbf{u}}_i - \mathbf{u}_{\mathrm{in}})\right)^{n+1/2} + \left(\bar{\mathbf{k}}_i^+(\bar{\mathbf{u}}_i - \mathbf{u}_{\mathrm{in}})\right)^{n}\right) - \frac{\sum_{j\in E}(\mathbf{u}_j^{n+1/2} + \mathbf{u}_j^n)}{2(d+1)}\frac{\mu(E^{n+1/2}) - \mu(E^n)}{d+1}. \tag{3.128}$$

The contribution from upper elements $[t^{n+1/2}, t^{n+1}]$ to the $n+1/2$ layer is

$$\phi_i^{E^{\mathrm{ST}},n+1/2,\mathrm{Upper}} = \frac{\Delta t_2}{2}\left(\bar{\mathbf{k}}_i^+(\bar{\mathbf{u}}_i - \mathbf{u}_{\mathrm{in}})\right)^{n+1/2} \tag{3.129}$$

and the contribution from the upper elements to the $n+1$ layer

$$\phi_i^{E^{\mathrm{ST}},n+1,\mathrm{Upper}} = \frac{1}{d+1}(\mu(E^{n+1})\mathbf{u}_i^{n+1} - \mu(E^{n+1/2})\mathbf{u}_i^{n+1/2}) + \frac{\Delta t_2}{2}\left(\bar{\mathbf{k}}_i^+(\mathbf{u}_i - \mathbf{u}_{\mathrm{in}})\right)^{n+1} - \frac{\sum_{j\in E}(\mathbf{u}_j^{n+1} + \mathbf{u}_j^{n+1/2})}{2(d+1)}\frac{\mu(E^{n+1}) - \mu(E^{n+1/2})}{d+1}. \tag{3.130}$$

The limiting procedure (3.63) is applied.

### 3.7.7. Bx scheme

The scheme is a simple blend of the LDA scheme (3.119) and the N scheme (3.111) with blending coefficient defined as (3.99) and (3.65).

### 3.7.8. Conservativity of the schemes on moving meshes

The ALE element residual $\phi^E$ and geometric source term $\phi^{GS}$ are defined using quasilinear form (3.115). For the conservativity the argument of the contour integral has to be continuously approximated in the domain,

$$\phi^E + \phi^{GS} = \oint_{\partial E_t} (\vec{\mathbf{f}}^h - \vec{w}\mathbf{u}^h) \cdot \mathrm{d}\vec{n} = \int_{E_t} \nabla_x \cdot (\vec{\mathbf{f}}^h - \vec{w}\mathbf{u}^h)\, \mathrm{d}\vec{x}, \tag{3.131}$$

i.e. the contour integral over the edge has to be equal for the elements on both sides of the edges. We follow the approach of [DRS93, Mic00, MSD03] and section 3.1. For smooth solutions one has

$$\phi^E + \phi^{GS} = \int_{E_t} \nabla_x \cdot (\vec{\mathbf{f}}^h - \vec{w}\mathbf{u}^h)\, \mathrm{d}\vec{x} = \int_{E_t} [\nabla_x \cdot \vec{\mathbf{f}}^h - \vec{w} \cdot \nabla_x \mathbf{u}^h - \mathbf{u}^h \nabla_x \cdot \vec{w}]\, \mathrm{d}\vec{x}. \tag{3.132}$$

In the first term of the contour integral, we assume linear variation of Roe's parameter vector $\mathbf{z}$, denoted by single hat $\widehat{(\cdot)}$, in the second term linear variation of the domain velocity $\vec{w}^h$ and the solution $\mathbf{u}^h$, denoted by double hat $\widehat{\widehat{(\cdot)}}$.

We have

$$\int_{E_t} \nabla_x \cdot \vec{\mathbf{f}}^h\, \mathrm{d}\vec{x} = \lambda(\bar{z}) \cdot \widehat{\nabla \mathbf{u}}\, \mu(E) \tag{3.133}$$

$$\int_{E_t} \vec{w} \cdot \nabla_x \mathbf{u}^h\, \mathrm{d}\vec{x} = \bar{\vec{w}} \cdot \widehat{\widehat{\nabla_x \mathbf{u}^h}}\, \mu(E). \tag{3.134}$$

The element residual is then

$$\begin{aligned} \phi^E &= \mu(E)\lambda(\bar{\mathbf{z}}) \cdot \widehat{\nabla \mathbf{u}} - \mu(E)\bar{\vec{w}} \cdot \widehat{\widehat{\nabla_x \mathbf{u}^h}} \\ &= \mu(E)[(\lambda(\bar{\mathbf{z}}) - \bar{\vec{w}}) \cdot \widehat{\nabla \mathbf{u}}] - \mu(E)[\bar{\vec{w}} \cdot (\widehat{\widehat{\nabla_x \mathbf{u}^h}} - \widehat{\nabla_x \mathbf{u}^h})]. \end{aligned} \tag{3.135}$$

Both terms are to be distributed with distribution coefficient (matrix) $\beta_i$, implicitly defined for some schemes. The first term is the ALE element residual and the second term is a so called conservative correction [Mic00, MSD03]. Authors [Mic00, MSD03] have found "minimal" importance of this term. However, in all the schemes for computations on moving grid, this term has to be added to the nodal contribution.

Second, we focus on the geometric source term. With above stated assumptions (linear variation of domain velocity $\vec{w}$ and solution $\mathbf{u}^h$ over the element) we have

$$\phi^{GS} = \int_{E_t} \mathbf{u}^h \nabla_x \cdot \vec{w}\, \mathrm{d}\vec{x} = \bar{\mathbf{u}}^h \cdot \widehat{\widehat{\nabla_x \cdot \vec{w}}}\, \mu(E_t). \tag{3.136}$$

Let us recall under which assumption the terms are derived:

- Linear variation of Roe's [DRS93, Roe81] parameter vector: $\lambda(\bar{\mathbf{z}})$, $\widehat{\nabla_x \mathbf{u}^h}$
- Linear variation of the solution: $\bar{\mathbf{u}}^h$, $\widehat{\widehat{\nabla_x \mathbf{u}^h}}$
- Linear variation of the domain velocity: $\bar{\vec{w}}$

The discrepancy between the assumption of linear variation of Roe's parameter vector and the assumption of linear variation of the solution has to be corrected by the conservative correction

$$\mu(E)\bar{\vec{w}} \cdot (\widehat{\widehat{\nabla_x \mathbf{u}^h}} - \widehat{\nabla_x \mathbf{u}^h}), \tag{3.137}$$

and distributed to nodes by the distribution coefficient $\beta_i$.

## 3.8. Implicit time-stepping, dual time approach and parallelization

The time stepping procedure for RD schemes for steady problems (3.19) can be regarded as a general iteration procedure to solve the set of algebraic equations. All the considered RD schemes for unsteady problems are formulated in dual time. Hence, the solution procedure for the unsteady problems (3.26) can be also regarded as an iteration procedure. Both types of schemes can be written as

$$U^{m+1} = U^m - \alpha R, \tag{3.138}$$

where $U^{m+1}$ and $U^m$ are algebraic vectors of solution variables for iterations $m$ and $m+1$; $R$ is the vector of right hand sides and $\alpha$ is a diagonal matrix of positive relaxation coefficients (also regarded as time-steps). The task is to find a stationary point of the system of equations

$$U^{m+1} = U^m = U^* \tag{3.139}$$

as efficient as possible.

To be efficient, we use the highest possible time-step in each node, i.e. we always use *local time-stepping*. The time step limit is given by the CFL condition [CFL28, CFL67, LeV99] for explicit relaxation procedure. The problems considered are non-linear and the time-step restriction usually denoted by $CFL = 1$ is relaxed to a somewhat lower value, e.g. $CFL = 0.9$, depending on the problem. For the higher time-steps, the implicit relaxation procedure has to be used. Since we would like to march as fast as possible towards the stationary solution, we use Euler backward method with linearization

$$U^{m+1} = U^m - \alpha \left[ R^m + \left.\frac{\partial R}{\partial U}\right|_m \left(U^{m+1} - U^m\right) \right], \tag{3.140}$$

giving the system

$$\left(\alpha^{-1} + \left.\frac{\partial R}{\partial U}\right|_m\right) \Delta U = -R^m, \qquad \Delta U = U^{m+1} - U^m. \tag{3.141}$$

For an efficient iteration procedure only an approximation of the Jacobian $\partial R/\partial U$ is needed [Iss97]. We use a one-sided numerical approximation

$$\frac{\partial r}{\partial u} \approx \frac{r(u+\varepsilon) - r(u)}{\varepsilon}, \tag{3.142}$$

because of its conveniency for the code development together with its reasonably good efficiency [Iss97].

System (3.141) is a large set of linear equations with general sparse matrix. We use GMRES method with ILU(0) preconditioning for the solution of the system. In parallel computations, we use block Jacobi preconditioning, where each block is located on one processor and ILU(0) preconditioner on each block.

For a discussion about implicit and explicit iteration procedures we refer to the PhD thesis [Iss97] and work [Dob02, DRD03a].

### 3.8.1. Parallelization

CFD in general is known to be very computationally demanding. In order to increase computational power available, one has to use some kind of parallel computer. Nowadays, most readily available parallel computers are clusters of personal computers running GNU/Linux operating system. This is what we have chosen as the target architecture. The nature of this computer system is most suitable for the domain decomposition approach: the problem domain is divided into distinct subdomains, each sub-domain is solved on a separate processor and data are exchanged on interprocessor boundaries. As the communication software we use MPI [MPI06]. For the solution of linear system, we use PETSc library [PET07].

The mesh is decomposed into non-overlapping regions with the METIS [Met06] software. The computation and the communication has to overlap for higher efficiency. Moreover, we setup communication such that one partition does not exchange data with more than one other partition at the same time. This is achieved by the graph coloring and suitable numbering of the interprocessor boundaries.

The problem of parallelization for RD schemes and FV schemes is very similar, it can be abstracted as an operation on graphs. For additional discussion see section 4.4.

## 3.9. Boundary conditions

In this section we will examine different treatments of the boundary conditions. According to [Pai95], the boundary condition treatment can be differentiated in

*strong boundary condition*, and *weak boundary condition*.

For the strong boundary condition, the residual in the node is changed such that, in the next time level the solution obeys a prescribed value in the boundary node. For the weak boundary condition the value for the nodal update is modified such that the integral of the flux along the boundary line satisfies a prescribed value.

## 3.9.1. Scalar problem

We prescribe all the boundary conditions strongly, i.e. in equation (3.19) or (3.26) a correction is added to the update formula

$$u_i^{h,n+1} = u_i^{h,n} - \alpha_i \left( \sum_{E \in i} \phi_i^E + \phi_i^{\text{corr}} \right), \tag{3.143}$$

with $\phi_i^{\text{corr}}$ chosen such that $u_i^{h,n+1} = u^{\text{BC}}$.

## 3.9.2. Euler equations

### 3.9.2.1. Wall – Petrov-Galerkin formulation

For internal aerodynamic problems it can be very important that no mass or energy escapes/enters the domain through the walls. We call this property *conservativity of the wall boundary condition*. It corresponds to the fact, that the integral of the mass and energy flux through the (rigid) wall has to be zero, i.e. in 2D

$$\int_{\text{wall}} \vec{\mathbf{f}}(\mathbf{u}) \cdot \vec{n} \, \mathrm{d}l = l \cdot (0, \bar{p}n^x, \bar{p}n^y, 0)^T. \tag{3.144}$$

To the knowledge of the author, none of the boundary conditions routinely used with RD schemes strictly respect this conservativity requirement. Among other important properties are accuracy and (at least linear) stability of the boundary conditions. We would also prefer boundary conditions with the same theoretical formulation in 1, 2 and 3D.

One of the possibilities is to take the Petrov-Galerkin (PG) formulation of RD schemes for the derivation of the boundary condition treatment. The PG formulation [Pai95, DRS03, Dob02, DRD03a, DD05b] reads: find $\mathbf{u} = \sum_i \mathbf{u}_i \psi_i$ such that

$$\int_\Omega \varphi_i \left( \frac{\partial \mathbf{u}}{\partial t} + \nabla \cdot \vec{\mathbf{f}}(\mathbf{u}) \right) \mathrm{d}\Omega = 0, \tag{3.145}$$

for every PG weight function

$$\varphi_i = \psi_i + \alpha_i^T \Pi^T, \tag{3.146}$$

where $\psi_i$ is the linear Galerkin test function, $\alpha_i^T = \beta_i - 1/(d+1)$ and $\Pi^T$ is the characteristic function of the element: $\Pi(x)^T = 1$ if $x \in T$, 0 elsewhere. We can split the integral and integrate by parts

$$\int_\Omega \varphi_i \frac{\partial \mathbf{u}}{\partial t} \,\mathrm{d}\Omega = \sum_{E \in T^h} \left[ \int_E \vec{\nabla}\psi_i \cdot \vec{\mathbf{f}}(\mathbf{u}) \,\mathrm{d}\Omega - \int_E \alpha^T \vec{\nabla} \cdot \vec{\mathbf{f}}(\mathbf{u}) \,\mathrm{d}\Omega - \oint_{\partial E} \psi_i \vec{\mathbf{f}}(\mathbf{u}) \cdot \mathrm{d}\vec{n} \right], \quad (3.147)$$

where $\vec{n}$ is the external normal. For a linear flux, the first integral on the RHS gives for element $E$

$$\frac{\mathbf{k}_i}{d+1} \sum_{j \in E} \mathbf{u}_j, \quad (3.148)$$

the second integral is

$$-\beta_i \sum_{j \in E} \mathbf{k}_j \mathbf{u}_j + \frac{1}{d+1} \sum_{j \in E} \mathbf{k}_j \mathbf{u}_j, \quad (3.149)$$

while the third is a sum of fluxes through the boundary of the element. If the point $i$ is an internal point in the computational domain, all the contributions of (3.148) and (3.149) sum to

$$-\sum_{E \in \mathcal{D}_i} \beta_i \left( \sum_{j \in E} \mathbf{k}_j \mathbf{u}_j \right), \quad (3.150)$$

while the sum of the boundary integrals vanishes. However, if $i$ is a boundary point, contributions both from the volume and boundary integrals remain. Without loss of generality, consider a 2D element with points on the wall $i$, $l$ and point $j$ inside the domain. The contribution to the node $i$ is

$$-\phi_i^{\text{wall}} = \underbrace{-\beta_i \sum_{j \in T} \mathbf{k}_j \mathbf{u}_j}_{\phi_i^E} \underbrace{- \mathbf{k}_j \left( \frac{2}{3}\mathbf{u}_i + \frac{1}{3}\mathbf{u}_l \right)}_{\int \psi_i \vec{\mathbf{f}}^{\text{old}} \cdot \mathrm{d}\vec{n}} - \int_{\text{wall}} \psi_i \vec{\mathbf{f}}(u) \cdot \mathrm{d}\vec{n}, \quad (3.151)$$

where $\vec{n}$ denote the external normal and terms which vanish after the element summation are omitted. In the last integral, the imposed flux $\vec{\mathbf{f}} \cdot \vec{n} = (0, pn_x, pn_y, 0)^T$, where linear variation of Roe parameters along the wall is prescribed. This treatment of boundary conditions meets all the above stated requirements.

In scheme (3.151) the first term is the contribution from the inner scheme, the second corresponds to the portion of an "old" flux and the last integral is the imposed flux (3.144) distributed with Galerkin weights. Hence, the whole procedure is a correction of the residual coming from the inner scheme using the boundary flux. From the implementation point of view, to compute the "old" flux, one has to know the solution on all the nodes of the element adjacent to the wall to determine $\mathbf{k}_j$ from the conservative linearization. An easier computer implementation is to compute

the "old" flux using the known linear variation of Roe parameters as a line integral along the wall.

Note the similarity of the PG treatment of boundary conditions with the procedure of van der Weide [vdW98]. The non-conservativity of the treatment [vdW98] lies in the mismatch between the flux integral seen by the inner scheme, i.e. linear variation of Roe parameters, and the boundary integral – linear variation of the solution. Another difference is in the distribution weights – 1/4 and 3/4 vs. 1/3 and 2/3.

For unsteady problems, namely problems involving moving meshes, a consistent space-time treatment of the moving wall boundary conditions is needed. As will be shown later in this section, a simple treatment using boundary conditions developed for spatial schemes introduces an error into the solution. In particular, it is clear that the flux trough the boundary of the element has the form

$$(\vec{\mathbf{f}}(\mathbf{u}) - \mathbf{u}\vec{w}) \cdot \vec{n}. \tag{3.152}$$

For a solid wall the velocity in the direction perpendicular to the boundary has to be clearly equal to the velocity of the wall $\vec{w} \cdot \vec{n}$. E.g. for a 1D problem it is

$$\mathbf{f}(\mathbf{u})^{\text{wall}} = (\rho v, \rho v^2 + p, v(E+p)) - w(\rho, \rho v, E) = (0, p, vp). \tag{3.153}$$

We proceed as above. We compute a boundary corrective flux in the intermediate state, i.e. in the middle between nodes at level $n$ and $n+1$ as the arithmetic average. Then we distribute the boundary correction to the nodes of the face. Finally, the conservative correction flux is added.

This method can be easily extended for the 3BDF time integrator. In this case, the solution is taken from $n+1$ time layer and the mesh velocity is computed by the procedure described later in section 4.3.2.

#### 3.9.2.2. Wall – Weak boundary condition of Paillere

In this formulation, the boundary conditions are implemented using ghost nodes, see [Pai95]. Consider the situation depicted in Fig. 3.8. Ghost nodes $1^*$ and $3^*$ are created, triangles $i, 1, 2$ and $i, 4, 3$ become interior and they are treated as inside of the domain. Variables from node 1 and 3 are mirrored into their counterparts $1^*$ and $3^*$. Then the scheme in the limit of diminishing distance between boundary nodes and their star counterparts is taken. The residual of triangle $E^{1^*,i,2}$ is

$$\phi^{E^{1^*,i,2}} = \mu(E)\, \nabla \vec{\mathbf{f}}^h = \mu(E)\, \frac{\partial \vec{\mathbf{f}}^h}{\partial \mathbf{u}^h} \nabla \cdot \vec{\mathbf{u}}^h = \sum_{j \in E} \bar{\mathbf{k}}_j \bar{\mathbf{u}}_j \tag{3.154}$$

Since $\vec{n}_i = -\vec{n}_{1^*}$ and $\vec{n}_2 = \vec{0}$, recalling definition of the upwind matrix (3.14), we have

$$\bar{\mathbf{k}}_{1^*} = -\bar{\mathbf{k}}_i, \qquad \bar{\mathbf{k}}_2 = \mathbf{0}. \tag{3.155}$$

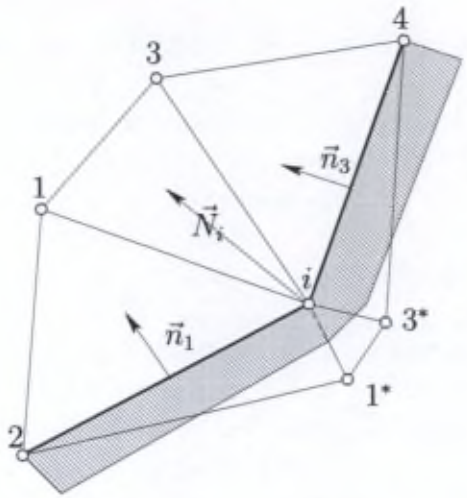


Figure 3.8.: Situation in the vicinity of the wall – Paillere's boundary condition

Therefore, the ghost element residual can be expressed as

$$\phi^{1^*,i,2} = \bar{\mathbf{k}}_i \bar{\mathbf{u}}_i + \bar{\mathbf{k}}_{1^*} \bar{\mathbf{u}}_{1^*} \tag{3.156}$$

Element residual is then distributed with the same distribution scheme as for the inner elements to the node $i$, the distribution matrix $\beta_i$ is determined by the scheme

$$\phi_i = \beta_i \phi^{1^*,i,2}. \tag{3.157}$$

Since the RD scheme for the boundary correction is the same as for the interior domain, this formulation also includes the case with moving meshes.

#### 3.9.2.3. Wall – 2D characteristic strong boundary conditions

In this section 2D characteristic strong boundary conditions are considered. They are included here only for completeness, because they are difficult to extend to three dimensions. For more details about this formulation of the boundary condition, see [Dob02, DRD03a].

Consider the state on the wall in the coordinate system perpendicular to the wall, oriented such that the normal is a unit inner normal $(n_x, n_y)$. We project the residual on the eigenvectors of the flux Jacobian in the direction normal to the wall. In this case the only characteristic entering corresponds to the eigenvalue (where $a$ is sound-speed and $un_x + vn_y$ the normal velocity)

$$\lambda_3 = a + un_x + vn_y \tag{3.158}$$

The corresponding right eigenvector is

$$\mathbf{r}^3 = \left[\frac{\rho}{a}, \rho\left(\frac{u}{a} + n_x\right), \rho\left(\frac{v}{a} + n_y\right), \rho\left(\frac{u^2+v^2}{2a} + un_x + vn_y + \frac{a}{\gamma - 1}\right)\right] \tag{3.159}$$

Consider the update scheme (at the point $i$, index is dropped)

$$\mathbf{u}^{n+1} = \mathbf{u}^{n+1} - \alpha\mathbf{R} = \mathbf{u}^{n+1} - \alpha(\mathbf{R}^{\mathrm{I}} + \mathbf{R}^{\mathrm{BC}}) \tag{3.160}$$

The $\mathbf{R}^{\mathrm{I}}$ residual is computed by the scheme from the interior of the domain and $\mathbf{R}^{\mathrm{BC}}$ is corrective residual. The corrective residual can be expressed as the component corresponding to the ingoing characteristic

$$\mathbf{R}^{\mathrm{BC}} = \beta\mathbf{r}^3, \tag{3.161}$$

where $\beta$ is the unknown amplitude. The solution at level $n+1$ must satisfy

$$\vec{u} \cdot \vec{n} = \vec{w} \cdot \vec{n}. \tag{3.162}$$

Therefore with $\mathbf{u} = (\rho, \rho u, \rho v, E)^T$,

$$\left(\frac{\mathbf{u}_2^{n+1}}{\mathbf{u}_1^{n+1}}\right) n_x + \left(\frac{\mathbf{u}_3^{n+1}}{\mathbf{u}_1^{n+1}}\right) n_y = \vec{w} \cdot \vec{n} \tag{3.163}$$

$$\mathbf{u}_2^{n+1} n_x + \mathbf{u}_3^{n+1} n_y = \mathbf{u}_1^{n+1} \vec{w} \cdot \vec{n} \tag{3.164}$$

$$[\mathbf{u}_2^n - \alpha(\mathbf{R}_2^{\mathrm{I}} + \mathbf{R}_2^{\mathrm{BC}})] n_x + [\mathbf{u}_3^n - \alpha(\mathbf{R}_3^{\mathrm{I}} + \mathbf{R}_3^{\mathrm{BC}})] n_y = [\mathbf{u}_1^n - \alpha(\mathbf{R}_1^{\mathrm{I}} + \mathbf{R}_1^{\mathrm{BC}})] \vec{w} \cdot \vec{n} \tag{3.165}$$

$$[\mathbf{u}_2^n - \alpha(\mathbf{R}_2^{\mathrm{I}} + \beta\mathbf{r}_2^3)] n_x + [\mathbf{u}_3^n - \alpha(\mathbf{R}_3^{\mathrm{I}} + \beta\mathbf{r}_3^3)] n_y = [\mathbf{u}_1^n - \alpha(\mathbf{R}_1^{\mathrm{I}} + \beta\mathbf{r}_1^3)] \vec{w} \cdot \vec{n}, \tag{3.166}$$

from which, we can easily compute the strength $\beta$

$$[\mathbf{u}_2^n - \alpha\mathbf{R}_2^{\mathrm{I}}] n_x + [\mathbf{u}_3^n - \alpha\mathbf{R}_3^{\mathrm{I}}] n_y - [\mathbf{u}_1^n - \alpha\mathbf{R}_1^{\mathrm{I}}] \vec{w} \cdot \vec{n} = \alpha\beta\mathbf{r}_2^3 n_x + \alpha\beta\mathbf{r}_3^3 n_y - \alpha\beta\mathbf{r}_1^3 \vec{w} \cdot \vec{n} \tag{3.167}$$

$$\beta = \frac{[\mathbf{u}_2^n - \alpha\mathbf{R}_2^{\mathrm{I}}] n_x + [\mathbf{u}_3^n - \alpha\mathbf{R}_3^{\mathrm{I}}] n_y - [\mathbf{u}_1^n - \alpha\mathbf{R}_1^{\mathrm{I}}] \vec{w} \cdot \vec{n}}{\alpha\mathbf{r}_2^3 n_x + \alpha\mathbf{r}_3^3 n_y - \alpha\mathbf{r}_1^3 \vec{w} \cdot \vec{n}}. \tag{3.168}$$

#### 3.9.2.4. Wall – Numerical results in 1D

A comparison of the numerical results obtained with different boundary formulations is plotted in Fig. 3.9. The test case is described in section 5.6.1, but here we solve the problem in one spatial dimension. The dependence of the Mach number on the coordinate is shown. The characteristic and van der Weide's [vdW98] formulation are simple extensions of their steady counterparts, where the approximation of the mesh velocity in node $i$ is given by $\vec{w}_i = (\vec{x}_i^{n+1} - \vec{x}_i^n)/\Delta t$ and the solution it taken from the $n+1$ time layer. It corresponds to Euler backward time integration method. The Petrov-Galerkin formulation uses the Crank-Nicholson time integration method, while Paillere's [Pai95] formulation uses the same RD scheme as for the interior elements. In Fig. 3.9 left, the computation using the one layer N-modified scheme described in section 3.6.4 is shown. If the boundary condition does not use the same

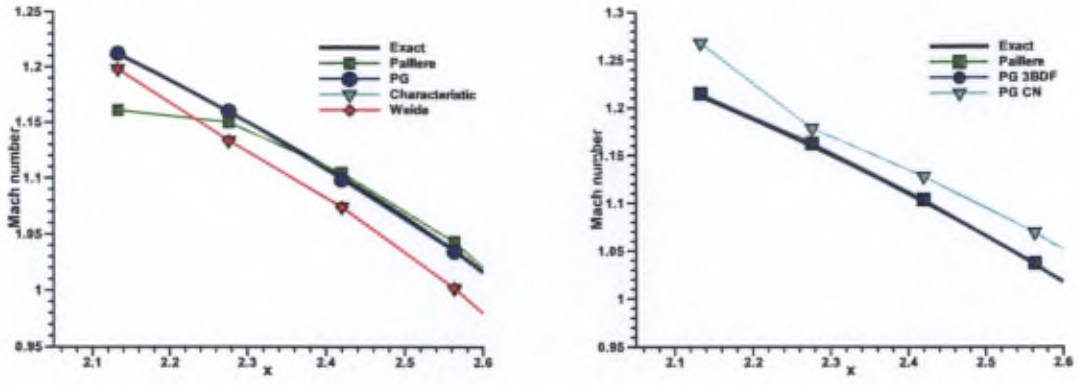


Figure 3.9.: 1D piston problem: Mach number in the vicinity of the piston at $t = 4$. Influence of the different formulation of boundary conditions. Left: One layer N-modifies scheme. Right: LDA scheme with mass matrix and 3BDF time integration.

time integration method as the interior scheme, i.e. Crank-Nicholson, a systematic error is introduced. In Fig. 3.9 right, results given by LDA scheme from section 3.6.2 with mass matrix and 3BDF time integration are shown. Also in this case, if the time integration method for boundary conditions and inner scheme does not match, the numerical results do not agree with the theoretical solution.

The formulation of boundary conditions has to be still improved. We have shown the importance of the choice of the discretization of the mesh velocity and the flux evaluation.

#### 3.9.2.5. Free stream

For the free stream boundary conditions nodal values of

$$\mathbf{u}_{i_\infty} = (\rho, \rho\vec{v}, E)_{i_\infty} \tag{3.169}$$

are prescribed. The boundary correction is computed as

$$\mathbf{R}^{\mathrm{BC}} = \mathbf{k}^{+}_{ii_\infty}(\mathbf{u} - \mathbf{u}_{i_\infty}), \tag{3.170}$$

with the usual definition. The $\mathbf{k}$ matrix is evaluated in the direction of the normal to the boundary. For more details about the free stream boundary conditions see [Dob02, DRD03a].

# Chapter 4.

# Finite volume scheme

Idea behind the finite volume schemes, i.e. approximating integral of the divergence terms as a contour integral, has contributed to the development of many numerical methods, see e.g. [SdBH04]. This part of the work is devoted to the finite volume methods as defined in [Krö97], i.e. discretization based on eq. (4.8). This discretization will be referred as the *finite volume method*.

## 4.1. Introduction

In this section finite volume methods will be considered, which are widely used as the current state of the art approach [Bar94, Bar03, BO04] for the given problem. Among the main advantages we can mention:

**Accuracy:** Second order of accuracy is routinely observed for the method with a piecewise linear reconstruction of unknowns.

**Shock capturing properties:** The use of limiters [Bar94] or the WLSQR [FK02b, Für04, Für06, FK02a] method gives a non-oscillatory solution even in presence of strong shock waves and discontinuities.

**Conservativity:** The method can converge to the proper weak solution of the conservation law (the shock waves are located in the correct position).

**Unstructured mesh:** The use of an unstructured mesh greatly simplifies treatment of complex geometries.

**Efficiency and parallel implementation:** The method is quite efficient in terms of spent CPU time and proper implementation gives high parallel speed-up.

For survey of current research on finite volume methods we refer to [Bar94, Bar03, BO04, Bla01, LeV02, Krö97].

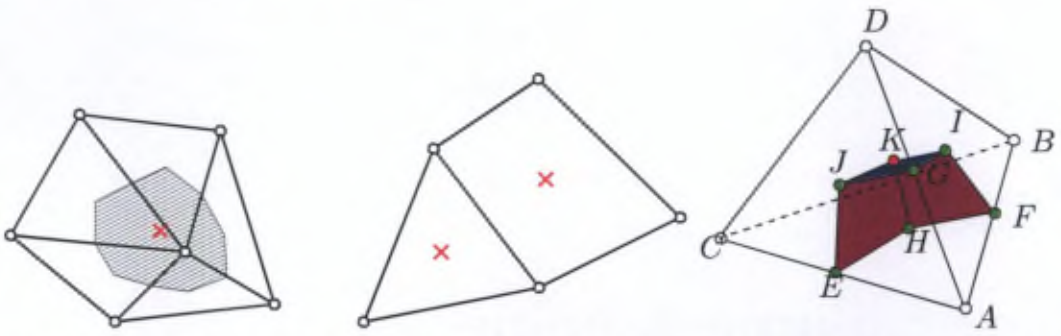


Figure 4.1.: Finite volume scheme. Computational mesh, the cross denotes location of variables. Left: vertex centered (VC) scheme with dual finite volume. Center: cell centered (CC) scheme. Right: Detail of mesh element for 3D vertex centered FV scheme. Part of the finite volume inside the element $ABCD$ surrounding the node $A$. The nodes $EFG$ are at the mid-sides of the edges, nodes $HIJ$ at the centroids of the faces and node $K$ at the centroid of the element.

## 4.2. Finite volume scheme

The domain of solution $\Omega$ is covered by a mesh consisting of elements. We consider two classes of FV schemes: cell centered (CC) and vertex centered (VC), see [BO04, Krö97]. For the CC method the (finite) volumes used to satisfy the integral form of the equation are the mesh elements itself, while for the VC method the finite volumes are cells of the dual mesh. Dual cells are constructed in two dimensions by connecting the centroids of the mesh elements with the centers of the edges. A similar construction applies in 3D. Note that the location of the variables does not necessarily coincide with the mesh vertices, as discussed later, see Fig. 4.1.

We will consider a linear variation of the approximation of the solution $\mathbf{u}^h$ over each finite volume $E_i$, continuity of the numerical solution on the boundary of the volume is not required. The system of conservation laws (2.1) is to be satisfied for every finite volume in the integral sense

$$\int_{E_i} \left( \frac{\partial \mathbf{u}^h}{\partial t} + \vec{\nabla} \cdot \vec{\mathbf{f}}^h \right) \mathrm{d}\vec{x} = 0, \tag{4.1}$$

where $\vec{\mathbf{f}}^h$ is an approximation of the flux tensor. The application of Gauss-Ostrogradski theorem to the convective terms results in

$$\int_{E_i} \frac{\partial \mathbf{u}^h}{\partial t} \mathrm{d}\vec{x} + \oint_{\partial E_i} \vec{\mathbf{f}}^h \cdot \mathrm{d}\vec{n} = 0. \tag{4.2}$$

Let us focus on the treatment of the first term. The solution varies linearly inside the finite volume at a given time instant, i.e. $\mathbf{u}^{h,E} = \mathbf{u}_i + (\vec{x} - \vec{x}_i) \cdot \vec{\nabla} \mathbf{u}_i$. The

coordinate $\vec{x}_i$ is the position, where $\mathbf{u}(x) = \mathbf{u}_i$. The first integral is

$$I_t = \int_{E_i} \frac{\partial \mathbf{u}^h}{\partial t} \, \mathrm{d}\vec{x} = \int_{E_i} \left( \frac{\partial \mathbf{u}_i}{\partial t} + \frac{\partial (\vec{x} - \vec{x}_i) \cdot \vec{\nabla} \mathbf{u}_i}{\partial t} \right) \mathrm{d}\vec{x}$$
$$= \int_{E_i} \left( \frac{\partial \mathbf{u}_i}{\partial t} + (\vec{x} - \vec{x}_i) \cdot \frac{\partial \vec{\nabla} \mathbf{u}_i}{\partial t} \right) \mathrm{d}\vec{x}. \quad (4.3)$$

Both $\mathbf{u}_i$ and $\vec{\nabla} \mathbf{u}_i$ do not depend on $\vec{x}$ inside the element, the latter due to the linearity of $\mathbf{u}^{h,E}$. Hence

$$I_t = \frac{\partial \mathbf{u}_i}{\partial t} \int_{E_i} \mathrm{d}\vec{x} + \frac{\partial \vec{\nabla} \mathbf{u}_i}{\partial t} \cdot \int_{E_i} (\vec{x} - \vec{x}_i) \, \mathrm{d}\vec{x}$$
$$= \mu(E_i) \frac{\partial \mathbf{u}_i}{\partial t} + \frac{\partial \vec{\nabla} \mathbf{u}_i}{\partial t} \cdot \int_{E_i} (\vec{x} - \vec{x}_i) \, \mathrm{d}\vec{x} = \mu(E_i) \frac{\partial \mathbf{u}_i}{\partial t} + \frac{\partial \vec{\nabla} \mathbf{u}_i}{\partial t} \cdot \vec{S}_i, \quad (4.4)$$

where $\vec{S}_i$ is a vector of static moments of the finite volume with respect to $\vec{x}_i$ and $\mu(E_i)$ is the measure of the element $E_i$, i.e. surface or volume of the element. The gradient of the solution inside the finite volume can be expressed as

$$\vec{\nabla} \mathbf{u}_i = \sum_{\forall j} \vec{c}_{ij} (\mathbf{u}_i - \mathbf{u}_j). \quad (4.5)$$

The summation is performed for all $j$ within the stencil of a linear reconstruction. The integral is then

$$I_t = \mu(E_i) \frac{\partial \mathbf{u}_i}{\partial t} + \vec{S}_i \cdot \frac{\partial (\mathbf{u}_i \sum_{\forall j} c_{ij})}{\partial t} - \vec{S}_i \cdot \sum_{\forall j} \frac{\partial \mathbf{u}_j c_{ij}}{\partial t}. \quad (4.6)$$

If the reconstruction coefficients $c_{ij}$ do not depend on the solution, e.g. for the linear scheme, the mass matrix can be introduced

$$I_t = \left( \mu(E_i) + \vec{S}_i \cdot \sum_{\forall j} c_{ij} \right) \frac{\partial \mathbf{u}_i}{\partial t} - \vec{S}_i \cdot \sum_{\forall j} c_{ij} \frac{\partial \mathbf{u}_j}{\partial t} = \sum_{\forall j} m_{ij} \frac{\partial \mathbf{u}_j}{\partial t}. \quad (4.7)$$

However, if the reconstruction coefficients depend on the solution, as is the case for schemes with nonlinear weights in the reconstruction or limiters, the mass matrix is not constant in time and the time dependence has to be considered.

For steady problems the existence of the mass matrix is not important [Bar94] and the mass matrix can be replaced by the diagonal matrix with $\mu(E_i)$ terms on diagonal. However, for unsteady problems, the full mass matrix has to be taken into account. The matrix is global and connects all the elements involved in the

reconstruction stencil. The existence of a non-diagonal mass matrix renders the method implicit even if explicit time stepping is used. The mass matrix for vertex centered finite volume method is discussed e.g. in [VM95, Ven95b, VM96, Bar94, Bla01]. In [VM96] the authors propose a treatment of the mass matrix for the unsteady problems with a Runge-Kutta method.

We will adopt a different approach. It is well known, that the static moment with respect to the gravity center is zero. Hence, in eq. (4.4) if $\vec{x}_i$ are centroids of the finite volumes, all the static moments $\vec{S}_i$ are zero. The mass matrix becomes diagonal with the measure of the volume $\mu(E_i)$ on the diagonal. For cell centered FV $\vec{x}_i$ are the centroids of the mesh elements, for vertex centered FV $\vec{x}_i$ are the centroids of the dual volumes, which generally do not coincide with the position of the mesh nodes (see Fig. 4.1).

The contour integral in eq. (4.2) involves the flux on the boundary of the finite volume. The integral is approximated using the numerical flux evaluated in Gauss points. For the second order approximation, one Gauss point in the centroid of each face of the finite volume is needed.

$$\mu(E_i)\frac{\partial \mathbf{u}_i}{\partial t} + \sum_{\forall j} \mathbf{F}(\mathbf{u}_{L,j}, \mathbf{u}_{R,j}, \vec{n}_j) = \mathbf{0}, \tag{4.8}$$

where the index $j$ goes over the faces of the finite volume $E_i$ and $\vec{n}_j$ is the normal of the face scaled by the the measure (surface) of the face $j$. The $\mathbf{u}_{L,j}$ and $\mathbf{u}_{R,j}$ are values of the approximation of the solution at the Gauss point from the left and right side of the face of the finite volume. A modification of Roe's approximated Riemann solver [Roe81] is used to compute the numerical flux $\mathbf{F}(\mathbf{u}_{L,j}, \mathbf{u}_{R,j}, \vec{n}_j)$. For this we refer to the references, since it is a very standard approach given in many textbooks, e.g. [Roe81, Tor97, LeV02, GR96].

### 4.2.1. Linear reconstruction and monotonicity enforcement

The gradient of the numerical solution $\nabla \mathbf{u}_i$ in each finite volume is estimated using the weighted least square method [Bar94, Bar03]. In 3D it has the form

$$\begin{pmatrix} \sum_k w_{ik}x_k^2 & \sum_k w_{ik}x_k y_k & \sum_k w_{ik}x_k z_k & \sum_k w_{ik}x_k \\ \sum_k w_{ik}x_k y_k & \sum_k w_{ik}y_k^2 & \sum_k w_{ik}y_k z_k & \sum_k w_{ik}y_k \\ \sum_k w_{ik}x_k z_k & \sum_k w_{ik}y_k z_k & \sum_k w_{ik}z_k^2 & \sum_k w_{ik}z_k \\ \sum_k w_{ik}x_k & \sum_k w_{ik}y_k & \sum_k w_{ik}z_k & \sum_k w_{ik} \end{pmatrix} \begin{bmatrix} a \\ b \\ c \\ d \end{bmatrix} = \begin{bmatrix} \sum_k w_{ik}x_k u_k \\ \sum_k w_{ik}y_k u_k \\ \sum_k w_{ik}z_k u_k \\ \sum_k w_{ik}u_k \end{bmatrix}, \qquad \nabla u_i = \begin{bmatrix} a \\ b \\ c \end{bmatrix} \tag{4.9}$$

either with linear weight

$$w_{ik} = \frac{1}{|\vec{x}_i - \vec{x}_k|^2}, \tag{4.10}$$

or nonlinear weight (WLSQR or WENO method) [FK02b, Für04, Für06, FK02a]

$$w_{ik} = \frac{1}{\|\mathbf{u}_i - \mathbf{u}_k\|^2 + |\vec{x}_i - \vec{x}_k|^2}. \tag{4.11}$$

Unfortunately, the system of algebraic equations (4.9) is not necessary well posed, and a suitable method of solution has to be chosen [Bar94, Lep04]. We simply discard the solution and set the gradient to zero for the matrix with (almost) zero determinant, otherwise we use Cramer's rule.

In the case of weight (4.10), the monotonicity of the solution has to be enforced using so called limiters. We use Barth's limiter [BJ89]. The value of the limiter is the largest $\Phi_0$ for which the following holds

$$\Phi_0 = \begin{cases} \min(1, \frac{U^{\max} - u_i}{U_L - u_i}) & \text{if } U_L - u_i > 0, \\ \min(1, \frac{U^{\min} - u_i}{U_L - u_i}) & \text{if } U_L - u_i < 0, \\ 1 & \text{if } U_L - u_i = 0, \end{cases} \tag{4.12}$$

where $U^{\max}$ and $U^{\max}$ are maximal and minimal values at centroids of the finite volumes neighboring the element $E_i$ and $U_L$ is the reconstructed value from the volume $E_i$ to the Gauss points (before application of the limiter). The gradient given by the least square method is then multiplied by the value of the limiter. For the system of equations, we apply the least square procedure component by component and use the minimal value of the limiter for all the components of the vector of conserved variables.

The schemes using Barth's limiter have considerable convergence problems [Ven95a, Bar03]. However, one can apply a simple convergence fix [Del96]. After a certain number of iterations $n_0$, when the solution is fully developed, *we don't increase anymore the value of the limiter* in the subsequent iterations

$$\Phi^n = \min(\Phi^n, \Phi^{n-1}), \qquad \text{for all } n \geq n_0. \tag{4.13}$$

The same fix is applied during the dual time iteration procedure.

### 4.2.2. Time integration procedure

The numerical scheme after the semi-discretization can be written as

$$\frac{\partial \mathbf{u}_i}{\partial t} = -\mathbf{r}, \tag{4.14}$$

where $\mathbf{r}$ is the approximation of the convective terms. This is a set of ordinary differential equations. We use different strategies to solve the problem. For steady problems we use either Euler explicit forward

$$\frac{\mathbf{u}_i^{n+1} - \mathbf{u}_i^n}{\Delta t} = -\mathbf{r}(U^n), \tag{4.15}$$

or implicit backward (with linearization), see equation (3.140), and always local time-stepping. For unsteady problems we use either a two or three step Runge-Kutta method [GS98, GST01, Shu99]. The optimal (in the sense of the largest allowed time step) second order TVD Runge-Kutta method is given by

$$\mathbf{u}^{(1)} = \mathbf{u}^n + \Delta t\, \mathbf{r}(U^n) \tag{4.16}$$

$$\mathbf{u}^{n+1} = \frac{1}{2}\mathbf{u}^n + \frac{1}{2}\mathbf{u}^{(1)} + \frac{1}{2}\Delta t\, \mathbf{r}(U^{(1)}) \tag{4.17}$$

with the stability limit $CFL = 1$. The optimal third order TVD Runge-Kutta method is given by

$$\mathbf{u}^{(1)} = \mathbf{u}^n + \Delta t\, \mathbf{r}(U^n) \tag{4.18}$$

$$\mathbf{u}^{(2)} = \frac{3}{4}\mathbf{u}^n + \frac{1}{4}\mathbf{u}^{(1)} + \frac{1}{4}\Delta t\, \mathbf{r}(U^{(1)}) \tag{4.19}$$

$$\mathbf{u}^{n+1} = \frac{1}{3}\mathbf{u}^n + \frac{2}{3}\mathbf{u}^{(2)} + \frac{2}{3}\Delta t\, \mathbf{r}(U^{(2)}) \tag{4.20}$$

with the same stability limit. For the simulations with larger time step we use the three point backward method (3BDF)

$$\frac{1}{t^{n+1} - t^n} \sum_{i \in E} \left( \alpha^{n+1}\mathbf{u}_i^{n+1} + \alpha^n \mathbf{u}_i^n + \alpha^{n-1}\mathbf{u}_i^{n-1} \right) = -\mathbf{r}(U^{n+1}), \tag{4.21}$$

with coefficients (3.80). For the comparison with the RD schemes with the Crank-Nicholson integration schemes the same scheme was also implemented for the FV method

$$\frac{\mathbf{u}_i^{n+1} - \mathbf{u}_i^n}{\Delta t} = -\frac{1}{2}\left( \mathbf{r}(U^n) + \mathbf{r}(U^{n+1}) \right). \tag{4.22}$$

Both the 3BDF and CN schemes are solved in dual time in the same manner as for the RD schemes, see section 3.8.

### 4.2.3. Stability criterion

For explicit time-integration the time step restriction is governed by a CFL condition. In fact, it is very easy to derive in 1D for a scalar linear advection equation. The following derivation will be based on positivity of the first order upwind scheme.

Consider a scalar advection equation

$$\frac{\partial u}{\partial t} + \vec{\lambda}(\vec{x}) \cdot \nabla u = 0. \tag{4.23}$$

The finite volume scheme with constant reconstruction and with explicit Euler time integration reads

$$\mu(E_i)\frac{u_i^{n+1} - u_i^n}{\Delta t} + \sum_{k=1}^{m} S_k f^h(u_i^n, u_{k_e}^n, \vec{n}_k) = 0, \tag{4.24}$$

where $k$ is the index of surrounding faces, $S_k$ is the surface of face $k$ and $k_e$ is the index of elements at the other side of face $k$. The numerical flux in this case is

$$f^h(u_i, u_{k_e}, \vec{n}_k) = \begin{cases} u_i \vec{\lambda}_k \cdot \vec{n}_k & \text{if } \vec{\lambda}_k \cdot \vec{n}_k > 0 \\ u_{k_e} \vec{\lambda}_k \cdot \vec{n}_k & \text{if } \vec{\lambda}_k \cdot \vec{n}_k < 0. \end{cases} \tag{4.25}$$

This flux can be written as

$$f^h(u_i, u_{k_e}, \vec{n}_k) = \frac{1}{2}(u_i + u_{k_e})\vec{\lambda}_k \cdot \vec{n}_k + \frac{1}{2}(u_i - u_{k_e})|\vec{\lambda}_k \cdot \vec{n}_k| \tag{4.26}$$

Plugging this numerical flux into equation (4.24) one get

$$\mu(E_i)\frac{u_i^{n+1} - u_i^n}{\Delta t} + \sum_{k=1}^{m} \left( S_k \frac{1}{2}(u_i^n + u_{k_e}^n)\vec{\lambda}_k \cdot \vec{n}_k + \frac{1}{2}(u_i^n - u_{k_e}^n)|\vec{\lambda}_k \cdot \vec{n}_k| \right) = 0 \tag{4.27}$$

Gathering terms containing $u_i$ and joining summations we obtain

$$u_i^{n+1} = \left[ 1 - \frac{\Delta t}{\mu(E_i)} \sum_{k=1}^{m} S_k (\vec{\lambda}_k \cdot \vec{n}_k)^+ \right] u_i^n - \sum_{k=1}^{m} \left[ \frac{\Delta t S_k}{\mu(E_i)} (\vec{\lambda}_k \cdot \vec{n}_k)^- u_{k_e}^n \right]. \tag{4.28}$$

The terms in the second bracket are all positive. The first term on the RHS is positive

$$1 - \frac{\Delta t}{\mu(E_i)} \sum_{k=1}^{m} S_k (\vec{\lambda}_k \cdot \vec{n}_k)^+ \geq 0 \tag{4.29}$$

under the time-step restriction

$$\Delta t \leq \frac{\mu(E_i)}{\sum_{k=1}^{m} S_k (\vec{\lambda}_k \cdot \vec{n}_k)^+}. \tag{4.30}$$

The TVD Runge-Kutta schemes used in this work have the same stability limit as the Euler forward scheme [Shu99, GS98, GST01]. The Crank-Nicholson scheme is positive for $CFL \leq 2$. The stability condition for higher order schemes with linear reconstruction is more restrictive [Bar03], see Tab. 4.1.

| Element shape | dimension | CFL number |
|---|---|---|
| Segment | 1 | 1/2 |
| Triangle | 2 | 1/3 |
| Parallelogram | 2 | 1/2 |
| Tetrahedron | 3 | 1/4 |

Table 4.1.: Stability restriction for Euler forward time integration with linear reconstruction for different element shapes [Bar03].

## 4.3. Extension of the scheme for computations on moving meshes

We start from the combination of the equations (2.22) and (2.25),

$$\int_{\Omega_0} \left.\frac{\partial J_{\mathcal{A}_t}\mathbf{u}}{\partial t}\right|_{\vec{Y}} \mathrm{d}\vec{Y} + \oint_{\partial\Omega_t} [\vec{\mathbf{f}}(\mathbf{u}) - \mathbf{u}\vec{w}] \cdot \mathrm{d}\vec{n} = 0. \tag{4.31}$$

In agreement with the development described in section 3 and equation (4.8), the semi-discrete equation is

$$\left.\frac{\partial \mu(E)\mathbf{u}_i}{\partial t}\right|_Y + \sum_{\forall j} \mathbf{F}(\mathbf{u}_{L,j}, \mathbf{u}_{R,j}, \vec{n}_j^{\alpha}, \vec{w}^{\alpha}) = \mathbf{0}. \tag{4.32}$$

The numerical flux is given by Roe's Riemann solver [Roe81]

$$\mathbf{F}(\mathbf{u}_L, \mathbf{u}_R, \vec{n}, \vec{w}) = \frac{1}{2}\left(\bar{\mathbf{f}}(\mathbf{u}_L) + \bar{\mathbf{f}}(\mathbf{u}_R) - \bar{\mathbf{A}}(\mathbf{u}_R - \mathbf{u}_L)\right). \tag{4.33}$$

The extension for the ALE flux is rather simple, the eigenvalues of Jacobian $\bar{\mathbf{A}}$ are given by

$$\lambda^{\mathrm{ALE}} = \lambda^{\mathrm{orig}} - \vec{w} \cdot \vec{n} \tag{4.34}$$

and the flux $\bar{\mathbf{f}}$ is replaced by its ALE counterpart (2.21).

A question is, which value of the approximation of the mesh velocity $\vec{w}^{\alpha}$ and the geometry (normal and surface of the mesh face, $\vec{n}_j^{\alpha}$) shall be taken, the time-level $\alpha = n$, $\alpha = n+1$ or between? All schemes presented in this thesis are chosen such that the approximation of the solution exactly obeys equation (2.29), i.e. the geometric conservation law, see section 3.4.5, is exactly satisfied. Therefore, the choice has to be made in accordance with the time integration scheme.

### 4.3.1. Crank-Nicholson time integration scheme

The simplest extension is such that the geometry is taken as the average between time level $n$ and $n+1$ and the mesh velocity as the mean velocity between the two

levels

$$\vec{n}_j^{n+1/2} = \frac{1}{2}(\vec{n}_j^n + \vec{n}_j^{n+1}) \tag{4.35}$$

$$\vec{w}^{n+1/2} = \frac{\vec{x}^{n+1} - \vec{x}^n}{\Delta t}. \tag{4.36}$$

### 4.3.2. Three points backward scheme – Scheme A

This scheme was introduced by [KF99] and after being proven as robust and accurate, it is presented in many publications of the group of C. Farhat [FGG01, GGF02, GGF03, GF03, FGB03, Far04]. The scheme is an extension of the three point backward scheme. The mesh velocity is computed from time layers $n-1$, $n$ and $n+1$, where within each time slab $[t^{n-1}, t^n]$, $[t^n, t^{n+1}]$ two Gauss points are used. The geometry is taken such that the scheme respects the geometric conservation law.

$$c_+ = \frac{1}{2}\left(1 + \frac{1}{\sqrt{3}}\right) \tag{4.37}$$

$$c_- = \frac{1}{2}\left(1 - \frac{1}{\sqrt{3}}\right) \tag{4.38}$$

$$c_1 = c_2 = \frac{\alpha^{n+1}}{2} \tag{4.39}$$

$$c_3 = c_4 = -\frac{\alpha^{n-1}}{2\tau} \tag{4.40}$$

$$\vec{n}_1 = c_- S^{n+1}\,\vec{n}^{n+1} + c_+ S^n\,\vec{n}^n \tag{4.41}$$

$$\vec{n}_2 = c_+ S^{n+1}\,\vec{n}^{n+1} + c_- S^n\,\vec{n}^n \tag{4.42}$$

$$\vec{n}_3 = c_- S^{n-1}\,\vec{n}^n + c_+ S^{n-1}\,\vec{n}^{n-1} \tag{4.43}$$

$$\vec{n}_4 = c_+ S^n\,\vec{n}^n + c_- S^{n-1}\,\vec{n}^{n-1} \tag{4.44}$$

$$\vec{n}_j = c_{12}(\vec{n}_1 + \vec{n}_2) + c_{34}(\vec{n}_3 + \vec{n}_4) \tag{4.45}$$

$$S = \|\vec{n}_j\| \tag{4.46}$$

$$\tag{4.47}$$

and

$$\vec{w}\cdot\vec{n}_j = c_1\frac{(\vec{x}^{n+1} - \vec{x}^n)\cdot\mathbf{n}_1}{\Delta t^n} + c_2\frac{(\vec{x}^{n+1} - \vec{x}^n)\cdot\mathbf{n}_2}{\Delta t^n} + c_3\frac{(\vec{x}^n - \vec{x}^{n-1})\cdot\mathbf{n}_3}{\Delta t^{n-1}} + c_4\frac{(\vec{x}^n - \vec{x}^{n-1})\cdot\mathbf{n}_4}{\Delta t^{n-1}} \tag{4.48}$$

with $\alpha$ and $\tau$ given in (3.79), where $S$ is the surface of the face. For two dimensions only one Gauss point would be needed for the evaluation of the velocity, however we use always this form of the scheme.

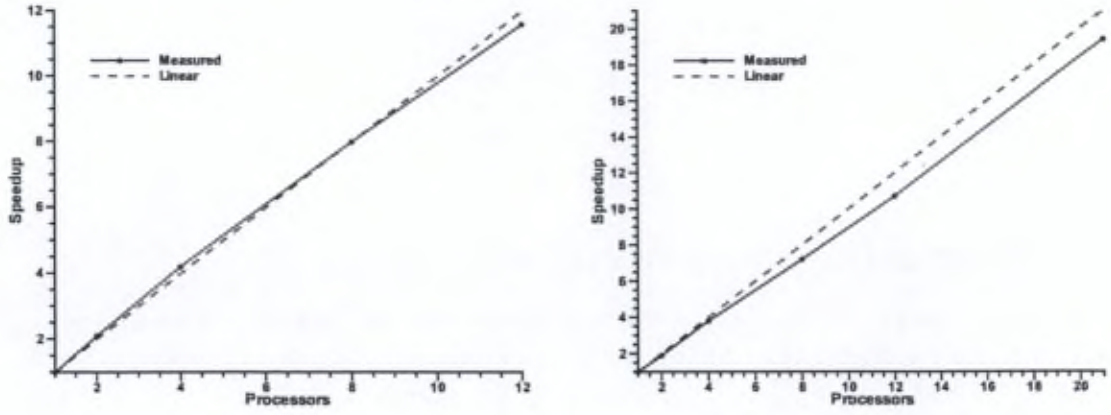


Figure 4.2.: Parallel speed-up. Onera M6 wing. WLSQR (WENO) reconstruction. Left: explicit scheme. Right: implicit scheme, $CFL = 1000$.

| No. of processors | Explicit | | Implicit | |
|---|---|---|---|---|
| | Speedup | Efficiency | Speedup | Efficiency |
| 1 | 1 | 100 % | 1 | 100 % |
| 2 | 2.1 | 105 % | 1.9 | 96 % |
| 4 | 4.2 | 105 % | 3.8 | 96 % |
| 8 | 8.0 | 100 % | 7.2 | 91 % |
| 12 | 11.6 | 96 % | 10.7 | 89 % |
| 21 | | | 19.4 | 92 % |

Table 4.2.: Parallel performance for Onera M6 test case. FV CC scheme, WLSQR reconstruction. For implicit method $CFL = 1000$.

## 4.4. Parallel implementation

The computational domain is split in (almost) equal size sub-domains. The problem is then distributed to different processors in the computational cluster. The data are interchanged with help of the MPI library. Attention must be paid to overlap computations and data exchange.

To achieve a good parallel scalability of the linear solver, entries in the matrix have to be suitably numbered. The numbering of the matrix entries can lower the bandwidth and contribute to higher accuracy of the block ILU preconditioner. Subsequently, the GMRES method converges faster.

The problem of the reduction of the matrix band is known to be NP complete. Hence, only approximate algorithms are used. The conclusive solution is still an open problem [Meu99, Bar94, Ski98]. We have tested the Cuthill-McKee [CM69] algorithm (also in its reverse version [Geo71]) and the multilevel nested dissection al-

| Mesh ordering method | efficiency |
|---|---|
| Cuthill-McKee [CM69] | 91 % |
| Reverse Cuthill-McKee[Geo71] | 90 % |
| Mesh generator (original numbering) | 86 % |
| METIS [Met06, KK99] | 67 % |
| Random | 64 % |

Table 4.3.: Impact of the mesh numbering on parallel performance of the implicit solver, 12 processors. FV2 WENO scheme, $CFL = 1000$.

gorithm [KK99]. The latter is implemented in the METIS [Met06] software package. For comparison, we have also numbered data randomly and as they were numbered originally by the mesh generator.

The parallel efficiency is defined as

$$\xi = \frac{t^1_{\mathrm{CPU}}}{n\, t^n_{\mathrm{CPU}}}, \tag{4.49}$$

where $t^1_{\mathrm{CPU}}$ is the CPU time for solving the problem for sequential computation and $t^n_{\mathrm{CPU}}$ is the CPU time spend to solve the same problem in parallel on $n$ processors. The time is measured with the standard `MPI_Wtime()` routine.

The matrix fill patterns are plotted in Fig. 4.3. The Cuthill-McKee (CM) and Reverse Cuthill-McKee (RCM) gives the same filling patten, while the RCM has lower fill-in for the LU decomposition. The performance results are plotted in Tab. 4.3. One can observe relatively high dependence of the parallel scalability on the mesh numbering. Using the RCM algorithm on a 12 processor cluster one gains a speedup of 11 compared with 8 for the multilevel nested dissection algorithm. The advantage of a proper choice of the mesh renumbering algorithms is clear.

To solve the sparse linear system, we use the PETSc library [PET07]. Unfortunately, a node renumbering algorithm for distributed matrices is not implemented there, at least in the current version 2.3.1.

## 4.5. Boundary conditions

The far field boundary conditions are implemented using the ghost cell approach. The cell next to the boundary face is created and all the components of the vector of unknowns are prescribed. A higher number of prescribed variables than can be determined from the theory of characteristics does not pose problems, because relevant values are selected by the Riemann solver.

For the wall boundary conditions the ALE flux (2.21) is prescribed on the wall boundary, i.e. the velocity perpendicular to the wall is equal to the normal wall

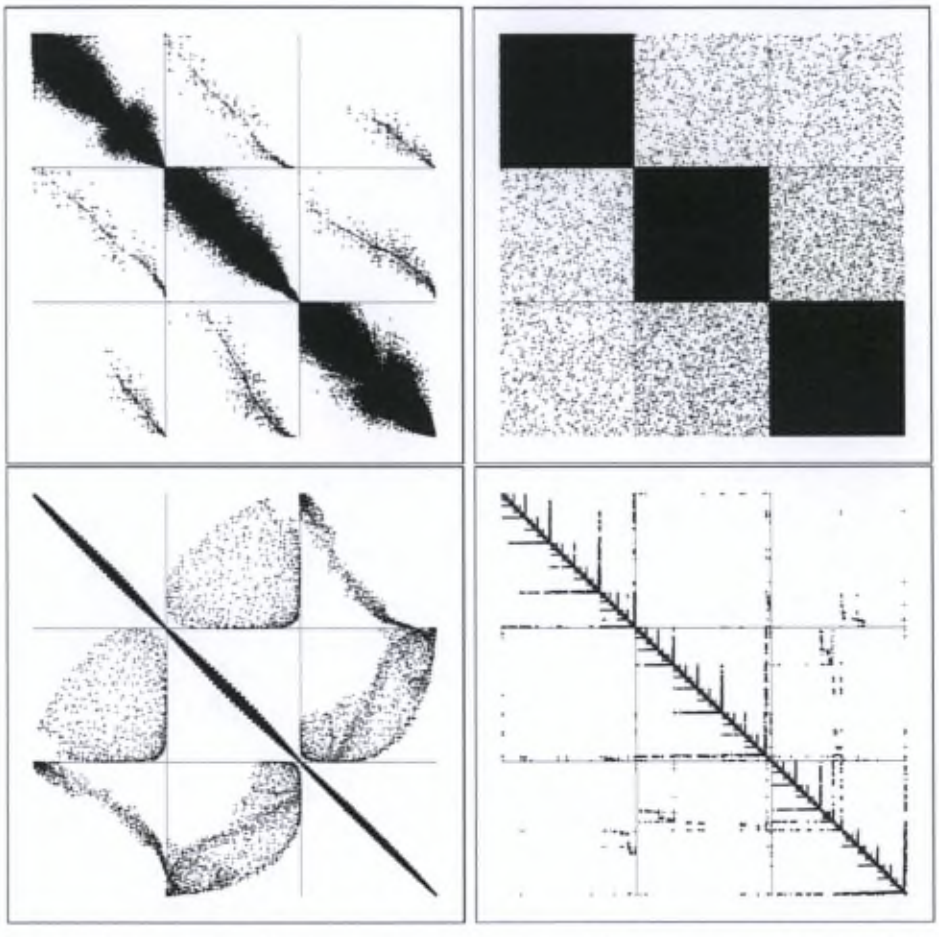

Figure 4.3.: Fill patterns of the matrix for Onera M6 wing $5 \times 306843$ DOF, 3 processors. Top left: natural ordering, right: random reorder. Bottom left: reverse Cuthill-McKee [Geo71], right: multilevel nested dissection algorithm [KK99].

velocity and the pressure, the density and the velocity parallel to the wall are extrapolated from the adjacent cell.

# Chapter 5.

# Comparison of some FV and RD schemes

In the course of this thesis we shall develop and test various numerical schemes. The different tests cases will be presented in this chapter. All the tests are relatively simple to examine specific aspects of the numerical scheme.

In this section we shall investigate Finite Volumes (FV) schemes both in vertex centered (VC) and cell centered (CC) settings in comparison with Residual Distribution (RD) schemes. Some comparisons of CC FV, VC FV and RD were published in [Csí02, PPRN05, Abg01, WK98, SR95, Roe90, Pai95, vdW98, DD05b, DD05a, CDP02, Woo01, MW04]. To perform such a comparison one has to overcome a number of technical problems

- Cell and vertex centered methods employ different number degrees of freedom for the same mesh.
- The methods can significantly differ in the computational complexity.
- The methods have to be available with similar level of development (i.e. both state–of–the–art FV and RD codes).
- Formulation and implementation of the boundary conditions can significantly affect the solution.

Up-to now, there is no wide agreement on the definite superiority of one type of method.

In the first part of this chapter we will compare theoretically the finite volume and residual distribution schemes using a 1D modified equation. We will illustrate the properties derived from the modified equation on a simple numerical test case. In the subsequent chapters we will systematically examine different aspect of the numerical schemes on a carefully chosen set of test cases. The test cases are sorted from easy to more complex: scalar linear equation, then scalar nonlinear equation up-to the system of nonlinear equations; from steady to unsteady flow; from smooth solution to discontinuous solution. We will start with simple, steady scalar linear

equation with smooth data (section 5.3.1). We perform convergence studies for all the schemes appearing in this thesis to check its accuracy and rate of convergence. The study is performed in two and three spatial dimensions to examine differences. Then, the schemes are tested on 2D inviscid Burgers equation to examine their behavior in shocks, see section 5.3.2. Preservation of maximum properties (under and over-shoots) is summarized in table 5.4. This completes *scalar steady* test cases. Accuracy of the unsteady schemes is tested on a 2D circular advection problem in section 5.3.3. Extensive study of the influence of the scheme and time discretization is performed. The convergence rates are plotted in Tab. 5.5. The main topic of the first part of the thesis is the extension of the residual distribution schemes for computations on moving meshes. The accuracy of the schemes is examined in section 5.3.4. The second order of accuracy of the LDA scheme is confirmed, as well as the higher accuracy in comparison with state of the art finite volume schemes. This set of test cases examine the behavior of the schemes for scalar equations, both for steady and unsteady problems and the behavior in shocks. Next, the schemes are examined for the system of Euler equations. Considering steady problems, we first focus on the accuracy of the scheme in smooth parts of the solution and near the wall. Sub-critical flow past circular cylinder was selected, see section 5.4.1. This allows to check also higher order linear schemes, which might fail to compute flows with strong shocks. The section related to the steady solution of the Euler equations is concluded by a well known and technically important test case, inviscid flow past Onera M6 wing, see section 5.4.2. This test case nicely demonstrates the ability to capture weak shock waves on a simple 3D geometry and examines the accuracy of the scheme for flow with a stagnation line (on the leading edge of the wing). Finally, a vortex convection test case gives an idea of the performance of the schemes for smooth unsteady flow, for the system of Euler equations. To conclude, we test the schemes on a set of test cases involving moving meshes. We have selected a test case involving compression of gas inside a piston cylinder. We start again with a smooth solution (see section 5.6.1) and then test the schemes on flow with shocks (see section 5.6.2).

## 5.1. 1D modified equations

In this section we compare the finite volume scheme with linear reconstruction and the LDA scheme of Ferrante and Deconinck [FD97], both equipped with the Crank-Nicholson time integration procedure. We consider 1D unsteady scalar advection equation

$$\frac{\partial u}{\partial t} + a\frac{\partial u}{\partial x} = 0, \tag{5.1}$$

with $a = 1$.

### 5.1.1. Finite volume scheme

The upwind finite volume scheme with Crank-Nicholson time integrator has the form

$$\frac{u_i^{n+1}-u_i^n}{\Delta t}+\frac{1}{2}\frac{a}{\Delta x}\left(f_{i+1/2}-f_{i-1/2}\right)^n+\frac{1}{2}\frac{a}{\Delta x}\left(f_{i+1/2}-f_{i-1/2}\right)^{n+1}=0. \tag{5.2}$$

The numerical flux for the method with linear reconstruction is

$$f_{i+1/2}=au_{i+1/2,L}, \qquad u_{i+1/2,L}=u_i+\left.\frac{\partial u^h}{\partial x}\right|_i\frac{\Delta x}{2} \tag{5.3}$$

with

$$\left.\frac{\partial u^h}{\partial x}\right|_i\approx\frac{u_{i+1}-u_{i-1}}{2\Delta x}. \tag{5.4}$$

The numerical flux is then

$$f_{i+1/2}=a\left(u_i+\frac{1}{4}(u_{i+1}-u_{i-1})\right). \tag{5.5}$$

The whole scheme is

$$\begin{aligned}\frac{u_i^{n+1}-u_i^n}{\Delta t}&+\frac{1}{2}\frac{a}{\Delta x}\left[u_i^n-u_{i-1}^n+\frac{1}{4}(u_{i+1}^n-u_i^n-u_{i-1}^n+u_{i-2}^n)\right]\\&+\frac{1}{2}\frac{a}{\Delta x}\left[u_i^{n+1}-u_{i-1}^{n+1}+\frac{1}{4}(u_{i+1}^{n+1}-u_i^{n+1}-u_{i-1}^{n+1}+u_{i-2}^{n+1})\right]=0,\end{aligned} \tag{5.6}$$

which is Fromm's space discretization combined with Crank-Nicholson time integration. We take the Taylor expansion up to the fourth order

$$\begin{aligned}u(t,x)\Big|_{x_i,t^n}&=u(t^n,x_i)+(t-t^n)u_t+(x-x_i)u_x\\&\quad+\frac{1}{2}(t-t^n)^2u_{tt}+(t-t^n)(x-x_i)u_{tx}+\frac{1}{2}(x-x_i)^2u_{xx}\\&\quad+\frac{1}{6}(t-t^n)^3u_{ttt}+\frac{1}{2}(t-t^n)^2(x-x_i)u_{ttx}+\frac{1}{2}(t-t^n)(x-x_i)^2u_{txx}+\frac{1}{6}(x-x_i)^3u_{xxx}\\&\quad+\frac{1}{24}(t-t^n)^4u_{tttt}+\frac{1}{6}(t-t^n)^3(x-x_i)u_{tttx}+\frac{1}{4}(t-t^n)^2(x-x_i)^2u_{ttxx}\\&\quad+\frac{1}{6}(t-t^n)(x-x_i)^3u_{txxx}+\frac{1}{24}(x-x_i)^4u_{xxxx}+\mathcal{O}(\Delta t^5,\Delta x^5)\end{aligned} \tag{5.7}$$

and plug it into the scheme. In the subsequent computation, the terms $\mathcal{O}(\Delta t^5,\Delta x^5)$ are dropped. After simplification we get

$$\begin{aligned}u_t+au_x&+\frac{1}{2}\Delta t\,u_{tt}+\frac{1}{2}\,a\Delta t\,u_{tx}+1/6\,\Delta t^2\,u_{ttt}+\frac{1}{4}\,a\Delta t^2u_{ttx}-\frac{1}{12}\,a\Delta x^2u_{xxx}\\&+\frac{1}{24}\,\Delta t^3u_{tttt}+\frac{1}{12}\,a\Delta t^3u_{tttx}-\frac{1}{24}\,a\Delta x^2\Delta t\,u_{txxx}+\frac{1}{8}\,a\Delta x^3u_{xxxx}=0.\end{aligned} \tag{5.8}$$

Now, the higher order time derivatives have to be removed. We follow the procedure of [WH74]. To remove $u_{tt}$ term, we derive the equation (5.8) by $t$ and subtract from the equation (5.8) its $\Delta t/2$ multiple. Note, that we don't remove the higher order derivatives using equation (5.1), but equation (5.8). The result is truncated to the fourth order derivatives. The procedure is repeated, until all the higher order time derivatives are removed. The modified equation is then

$$u_t + au_x = \left(\frac{1}{12}a\Delta x^2 - \frac{1}{12}\Delta t^2 a^3\right)u_{xxx} - \frac{1}{8}a\Delta x^3 u_{xxxx}, \tag{5.9}$$

which can be written as

$$u_t + au_x = \frac{a\Delta x^2}{12}\left(1 - CFL^2\right)u_{xxx} - \frac{1}{8}a\Delta x^3 u_{xxxx}, \tag{5.10}$$

where

$$CFL = \frac{a\Delta t}{\Delta x} \tag{5.11}$$

is the CFL number.

### 5.1.2. LDA scheme of Ferrante and Deconinck

The 1D LDA scheme after summation of all the contributions (3.90) is

$$\left(\frac{5}{12\Delta t} - \frac{1}{2}\frac{a}{\Delta x}\right)u_{i-1}^{n+1} + \left(\frac{2}{3\Delta t} + \frac{1}{2}\frac{a}{\Delta x}\right)u_i^{n+1} - \frac{1}{12\Delta t}u_{i+1}^{n+1} + \left(-\frac{5}{12\Delta t} - \frac{1}{2}\frac{a}{\Delta x}\right)u_{i-1}^{n} + \left(-\frac{2}{3\Delta t} + \frac{1}{2}\frac{a}{\Delta x}\right)u_i^{n} + \frac{1}{12\Delta t}u_{i+1}^{n} = 0. \tag{5.12}$$

We take Taylor expansion (5.7) and insert it to the scheme. After simplification we get

$$u_t + au_x + \frac{1}{2}\Delta t\, u_{tt} + \left(-\frac{1}{2}\Delta x + \frac{1}{2}\Delta t\, a\right)u_{tx} - \frac{1}{2}\Delta x\, a u_{xx} + \frac{1}{6}\Delta t^2 u_{ttt} + \left(-\frac{1}{4}\Delta t\,\Delta x + \frac{1}{4}\Delta t^2 a\right)u_{ttx} + \left(-\frac{1}{4}\Delta x\,\Delta t\, a + \frac{1}{6}\Delta x^2\right)u_{txx} + \frac{1}{6}\Delta x^2 a u_{xxx} + \frac{1}{24}\Delta t^3 u_{tttt} + \left(-\frac{1}{12}\Delta t^2\Delta x + \frac{1}{12}\Delta t^3 a\right)u_{ttt x} + \left(\frac{1}{12}\Delta t\,\Delta x^2 - \frac{1}{8}\Delta t^2\Delta x\, a\right)u_{ttxx} + \left(-\frac{1}{12}\Delta x^3 + \frac{1}{12}\Delta x^2\Delta t\, a\right)u_{txxx} - \frac{1}{24}\Delta x^3 a u_{xxxx} = 0. \tag{5.13}$$

Again, we remove the high order time derivatives adding a linear combination of the derivatives of *this equation*. After simplification and truncating the higher order derivatives, we get

$$u_t + au_x = -\frac{1}{12}\Delta t^2 a^3 u_{xxx} - \frac{1}{24} a\Delta x^3 u_{xxxx}. \tag{5.14}$$

This can be written similarly to (5.10)

$$u_t + au_x = a\Delta x^2 \left(-\frac{1}{12} CFL^2\right) u_{xxx} - \frac{1}{24} a\Delta x^3 u_{xxxx}. \tag{5.15}$$

### 5.1.3. Comparison and conclusions

The both schemes are clearly second order accurate, since the leading term in front of the higher order derivatives is of order $\Delta x^2$. Both schemes contain only fourth order dissipation ($u_{xxxx}$), where the LDA scheme has three times lower dissipation than the FV. The dissipation error is of order $\Delta x^3$.

The dispersion error for the LDA scheme is

$$a\Delta x^2 \left(-\frac{1}{12} CFL^2\right), \tag{5.16}$$

while for the FV scheme is

$$a\Delta x^2 \left(\frac{1}{12} - \frac{1}{12} CFL^2\right). \tag{5.17}$$

The absolute value of the dispersion coefficient $|CFL^2/12|$ and $|(1 - CFL^2)/12|$ depending on the CFL number is plotted in Fig. 5.1. For $CFL < \sqrt{1/2} \approx 0.7$ the LDA scheme has lower dispersion error than FV scheme. For the CFL number $CFL = 1$ the FV scheme has zero third order dispersion. Since the coefficient in front of the dissipation is $\Delta x^3$, the scheme become third order accurate.

The problem is solved on a domain of unit length for time $t \in [0, 1]$. Periodic boundary conditions are considered. Hence, the initial condition consisting of a sine pulse or top hat is equal to the solution at time $t = 1$. It is plotted by the full line in Fig. 5.2. The numerical solution obtained by the above-described schemes for a mesh consisting of 100 nodes and time-step corresponding to $CFL = 0.8$ and $CFL = 1.5$, is plotted in Fig. 5.2. Looking at the FV solution for $CFL = 0.8$, the dispersion coefficient is positive and the wiggles appear right to the discontinuity. The dispersion coefficient for the LDA scheme is negative for arbitrary CFL number, which corresponds to the presence of the wiggles left to the discontinuity. For the CFL number $CFL = 1.5$ the dispersion coefficients of both the schemes are negative and comparable magnitude ($-0.187$ for the LDA scheme and $-0.104$ for the FV

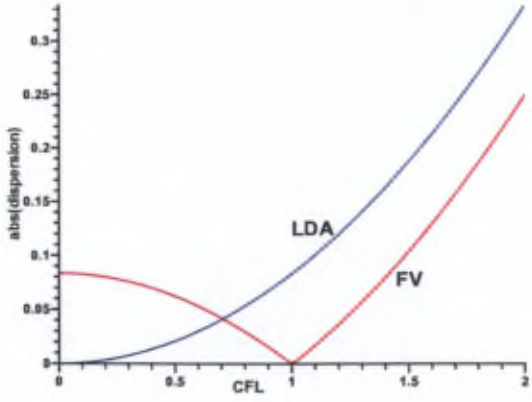


Figure 5.1.: Absolute value of the dispersion coefficient depending on the CFL number for FV scheme with linear reconstruction and no limiter and LDA scheme with mass matrix [FD97]. Both schemes uses the Crank-Nicholson time integration.

scheme), which clearly corresponds to the shift of the wiggles to the left of the discontinuity. The higher absolute value for the LDA scheme places the peak of the wiggle for the LDA scheme left to the peak for the FV scheme.

We can conclude, that both the schemes have dispersion error scaling as $\Delta x^2$ giving the second order of accuracy. For the LDA scheme, the dispersion coefficient is negative and of the same order of magnitude for the higher CFL numbers, rendering the group velocity lower than the advection velocity. For time-step $CFL = 1$ the FV scheme has zero dispersion error and the scheme is third order accurate; for lower CFL numbers the dispersion coefficient is positive. The dissipation error scales as $\Delta x^3$ and the dissipation term is fourth order derivative. The dissipation of the LDA scheme is three times lower than for the FV scheme.

## 5.2. Meshes for common test cases

The numerical methods developed and evaluated in this thesis are intended for 3D industrial-type simulations in complex configurations. The automatic and reliable mesh generation is today biggest bottleneck for this kind of computations [Ath05]. It is still difficult to obtain uniform mesh quality and optimal mesh connectivity, especially in the 3D case [Ath05, DDA00, Ric05]. The tests of the numerical schemes should use similar meshes as those available for the industrial simulations. For this reason, Weatherill [WH94] type of meshes are used. This kind of triangulation has roughly the same size of elements, but the connectivity of the mesh is changing (see Fig. 5.3). The meshes in two dimensions are generated by the mesh generation plug-in of Tecplot [Tec06] or the software developed in the AMeGOS project [AMVD00].

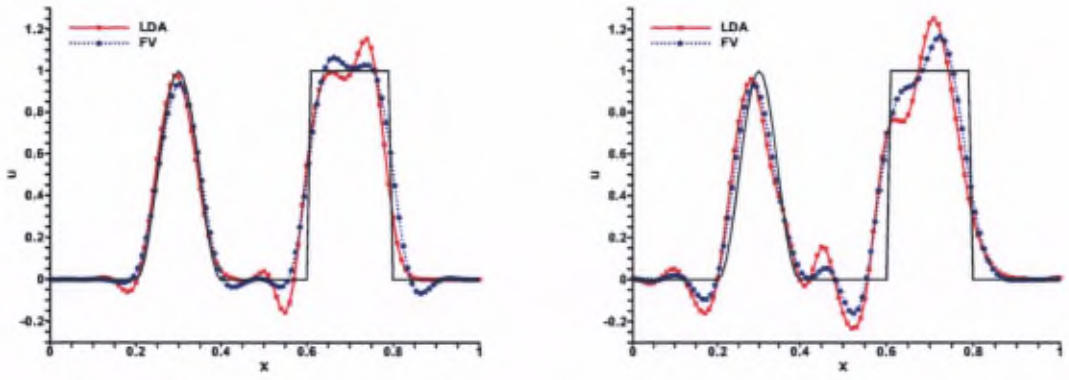


Figure 5.2.: 1D advection equation, $a = 1$, periodic boundary conditions, solution at $t = 1$. FV scheme with linear reconstruction without limiter; LDA scheme with mass matrix [FD97]. Both schemes uses Crank-Nicholson time integration. Left: $CFL = 0.8$, Right: $CFL = 1.5$.

Meshes generated by the ICEM CFD software [ICE06] are used in three dimensions. The latter package is considered today's state of the art software for industrial mesh generation.

For the scalar test in 2D we use a square domain, triangulated with Weatherill type of triangulation, as in Fig. 5.3. One can see the nodes with different connectivity in the figure. The reference size is one over the number of elements along the side, in this case $h = 1/7$. To enable comparison of the methods with different number of degrees of freedom, i.e. cell centered and vertex centered methods, we define equivalent mesh spacing

$$h^{\text{ball}} = 2\sqrt{\frac{S_i}{\pi}}, \tag{5.18}$$

where $h^{\text{ball}}$ is the diameter of circle with surface $S_i$, with

$$S_i = \frac{\mu(\Omega)}{\text{DOF}}. \tag{5.19}$$

Surface of the whole computational domain is denoted by $\mu(\Omega)$ and DOF is the number of degrees of freedom in the domain. Equation (5.18) is modified to

$$h^{\text{ball}} = \sqrt[3]{\frac{3}{4}\frac{S_i}{\pi}}, \tag{5.20}$$

in three spatial dimensions.

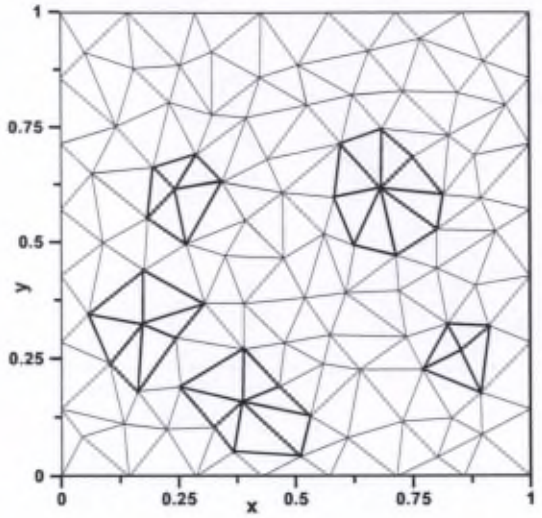


Figure 5.3.: A unit square domain triangulated with Weatherill type mesh used for test problems, $h = 1/7$. One can observe nodes of different degree. Nodes of degree 4, 5, 6, 7 and 8 are emphasized. (See [Ric05].)

## 5.3. Scalar problems

This set of tests is chosen to examine different aspects of the numerical schemes, namely accuracy in smooth parts of the solution (estimated by the convergence studies) and the behavior in the shock. First, we test steady schemes, then unsteady schemes and finally the schemes for computations on moving meshes.

### 5.3.1. 2D and 3D steady circular advection

As the first test we will show performance of the schemes on the 2D steady circular advection problem introduced in section 2.3.1.2, page 25, with four periods of a sinus function on the $y = 0$ boundary. We shall study the cell-centered (CC) finite volume schemes with constant and linear reconstruction with or without limiter, vertex centered (VC) schemes with the same reconstructions and the RD N, LDA and N-modified schemes. Part of this section was published in [DDF06].

The domain of solution is the unit square and we solve the equation (2.1) with flux given by (2.30). For $y = 0$ Dirichlet boundary condition are prescribed

$$u(x) = \sin^2(4\pi x), \tag{5.21}$$

and for $x = 1$ condition $u(y) = 0$. For the other two boundaries no boundary condition is used, as it is given by theory of characteristics [GR96, LeV99, LeV02, Fei93, FFS03]. As the initial condition, we prescribe $u^0(x, y) = 0$.

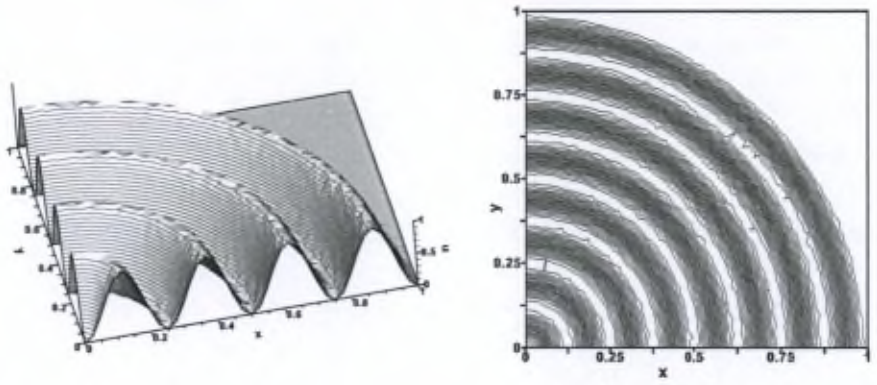


Figure 5.4.: Approximation of the exact solution of the 2D circular advection problem on grid $h = 1/40$.

The analytical solution is the function prescribed as the Dirichlet boundary condition rotated around coordinate origin, i.e.

$$u(x, y) = \sin^2(4\pi \min(1, r)), \quad r = \sqrt{x^2 + y^2} \tag{5.22}$$

The exact solution approximated by the piecewise linear function is depicted in Fig. 5.4.

Once the analytical solution is known, we can perform convergence studies for all the schemes. The $L^p$ norm of error is computed as

$$\|err\|_{L^p} = \sqrt[p]{\int_\Omega |u - u^h|^p \, \mathrm{d}\vec{x}} \approx \sqrt[p]{\sum_{E \in \mathcal{T}^h} \mu(E) |u(\vec{x}_i) - u_i|^p}. \tag{5.23}$$

for the CC FV scheme and

$$\|err\|_{L^p} \approx \sqrt[p]{\sum_{i \in \mathcal{T}^h} \mu(S_i) |u(\vec{x}_i) - u_i|^p}. \tag{5.24}$$

for the VC FV and RD schemes.

As the first result, we plot the solution and the error along the outlet of the domain (for the boundary $x = 0$), for the equivalent mesh with spacing $h^{\text{ball}} = 1/95$ (Fig. 5.5, 5.7, 5.9), i.e. $h = 1/55$ for the cell centered finite volume and $h = 1/77$ for vertex centered finite volume and residual distribution schemes. The N scheme is clearly more accurate than both finite volume schemes with constant reconstruction, see Fig. 5.5, 5.6, and the cell centered scheme is more accurate than the vertex centered scheme. The order of accuracy lower than first for the FV schemes, see Tab. 5.1, is expected, as it is shown in [KRW96, Krö97]. In the case of finite volume schemes with

linear reconstruction, the accuracy is similar in terms of the $L^1$ and $L^2$ norm, see Fig. 5.8. The error in the maximal norm is higher for the cell centered FV scheme than the vertex centered schemes. The LDA scheme is clearly the most accurate in all the norms. The order of accuracy estimated from the $L^1$ and $L^2$ norms is almost two for all the schemes. The LDA scheme shows almost second order accurate behavior even in the $L^\infty$ norm, see Tab. 5.1, while the rate of decrease of the maximal error is closer to one for the finite volume schemes. The situation is quite different for the nonlinear schemes, see Fig. 5.9, 5.10. The vertex centered scheme is more accurate than the cell centered FV, it gives second order of accuracy in $L^1$ and $L^2$ norms. This could be explained by the better behavior of the limiter on dual volume than on the triangular element. The N-modified scheme is the least accurate. However, the order of accuracy estimated from the $L^1$ and $L^2$ norms for cell centered FV and N-modified scheme is similar. The convergence studies were performed also for the B scheme. The error is *very* close to the error of the N-modified scheme, we don't plot convergence study here.

| Scheme | $L^1$ order | $L^2$ order | $L^\infty$ order |
|---|---|---|---|
| CC FV Const. | 0.76 | 0.72 | 0.60 |
| VC FV Const. | 0.58 | 0.54 | 0.40 |
| N | 0.75 | 0.71 | 0.59 |
| CC FV Linear | 2.04 | 1.92 | 0.90 |
| VC FV Linear | 1.99 | 1.95 | 1.39 |
| LDA | 2.16 | 2.11 | 1.79 |
| CC FV Barth | 1.64 | 1.60 | 0.96 |
| VC FV Barth | 2.00 | 1.95 | 1.47 |
| N-mod | 1.66 | 1.54 | 1.21 |

Table 5.1.: Comparison of orders of accuracy for 2D steady circular advection problem

| Scheme | $L^1$ order | $L^2$ order | $L^\infty$ order |
|---|---|---|---|
| CC FV Const. | 0.87 | 0.80 | 0.72 |
| VC FV Const. | 0.65 | 0.57 | 0.44 |
| N | 0.75 | 0.67 | 0.56 |
| CC FV Linear | 2.21 | 2.10 | 1.05 |
| VC FV Linear | 1.51 | 1.38 | 1.20 |
| LDA | 2.45 | 2.30 | 1.90 |
| CC FV Barth | 2.33 | 2.29 | 1.14 |
| VC FV Barth | 1.52 | 1.37 | 1.21 |
| N-mod | 1.74 | 1.64 | 1.37 |

Table 5.2.: Comparison of orders of accuracy for 3D steady circular advection problem

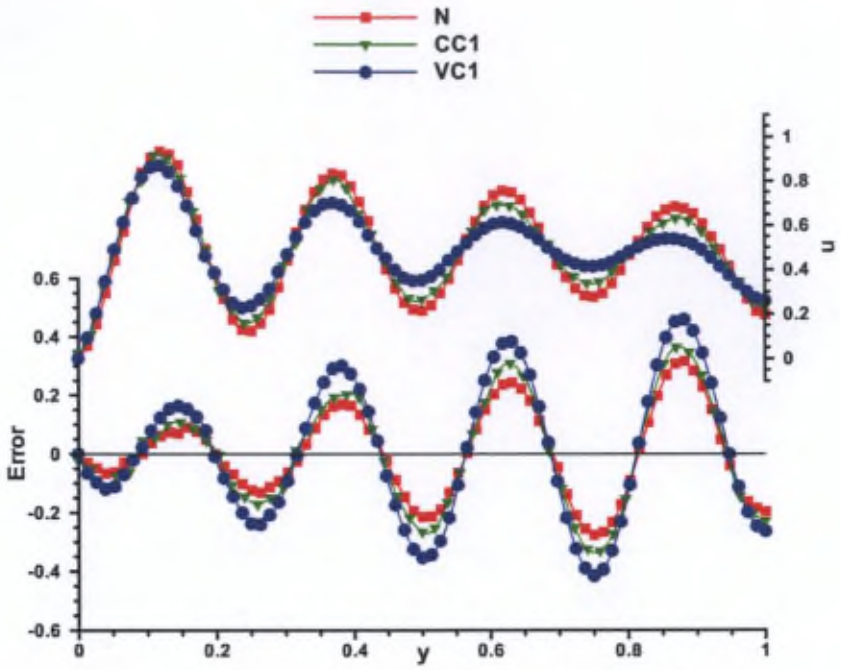


Figure 5.5.: 2D steady circular advection problem. The solution along boundary $x = 0$ and the error for N scheme and the schemes with constant reconstruction.

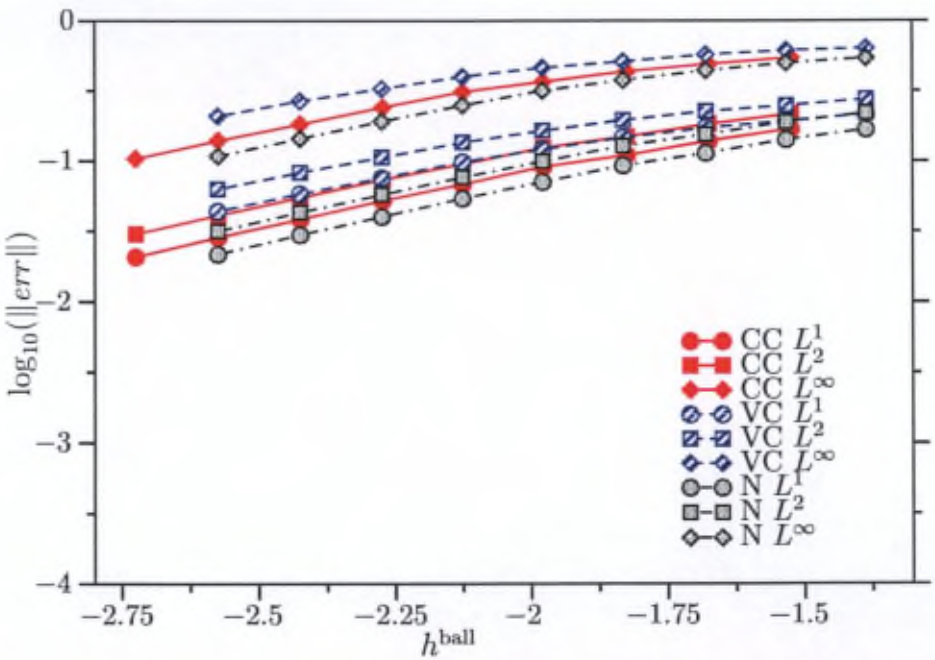


Figure 5.6.: 2D steady circular advection problem. Schemes with constant reconstruction and the N scheme. Norm of error vs. mesh spacing.

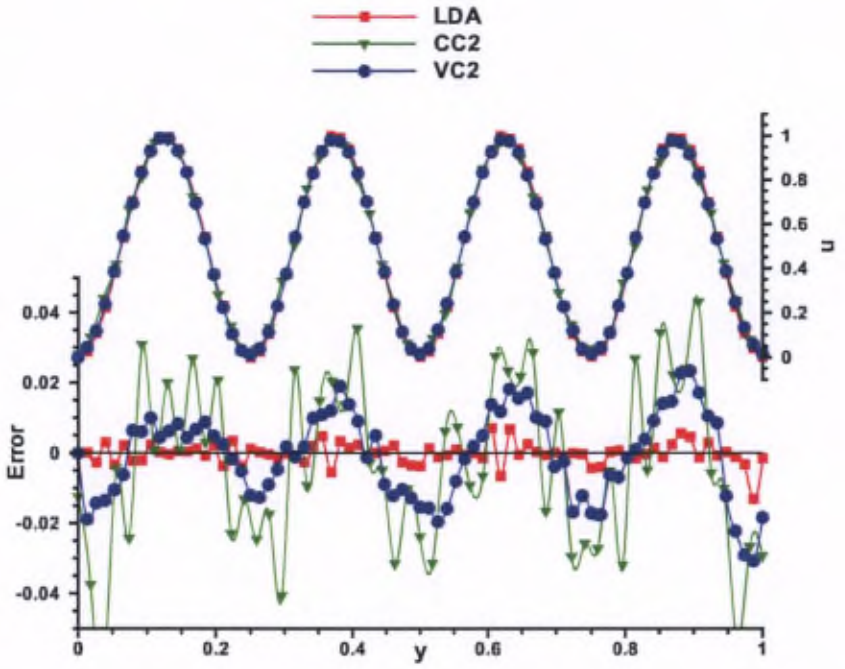


Figure 5.7.: 2D steady circular advection problem. The solution along boundary $x = 0$ and the error of FV schemes with the linear reconstruction and LDA RD scheme.

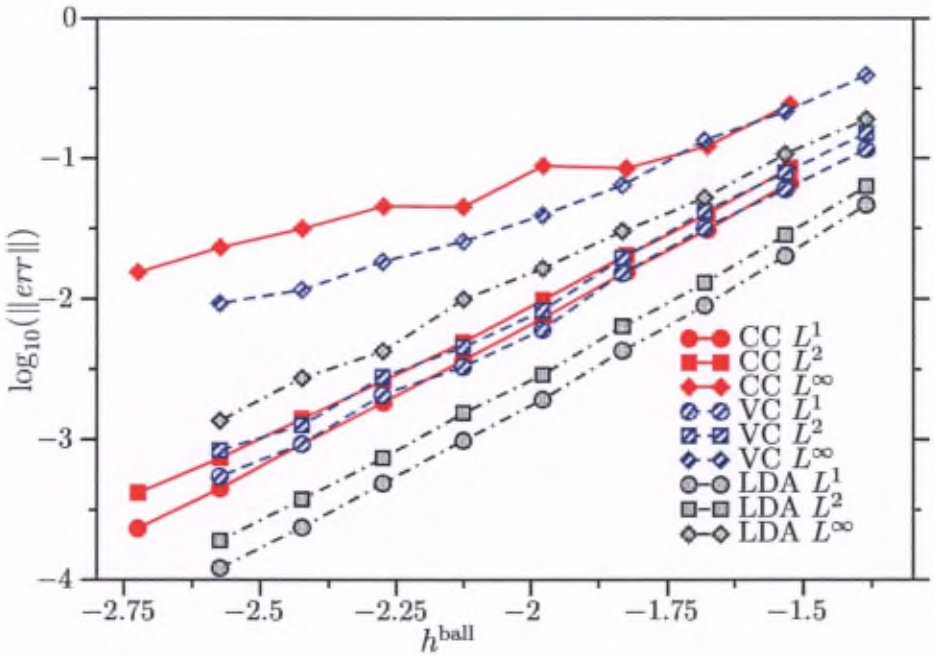


Figure 5.8.: 2D steady circular advection problem. Schemes with linear reconstruction without limiter and LDA scheme. Norm of error vs. mesh spacing.

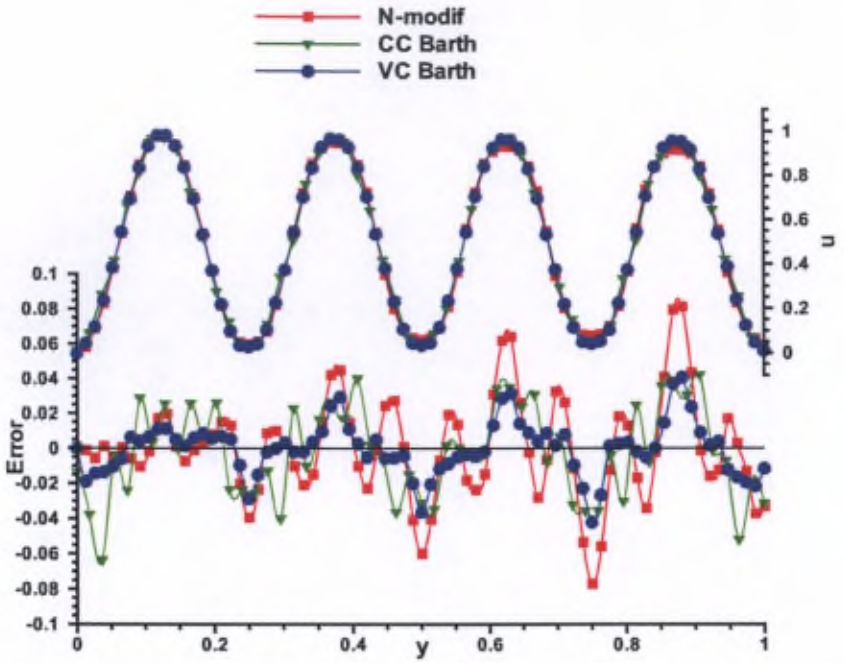


Figure 5.9.: 2D steady circular advection problem. The solution along boundary $x = 0$ and the error of FV schemes with Barth's limiter and N-modified RD scheme.

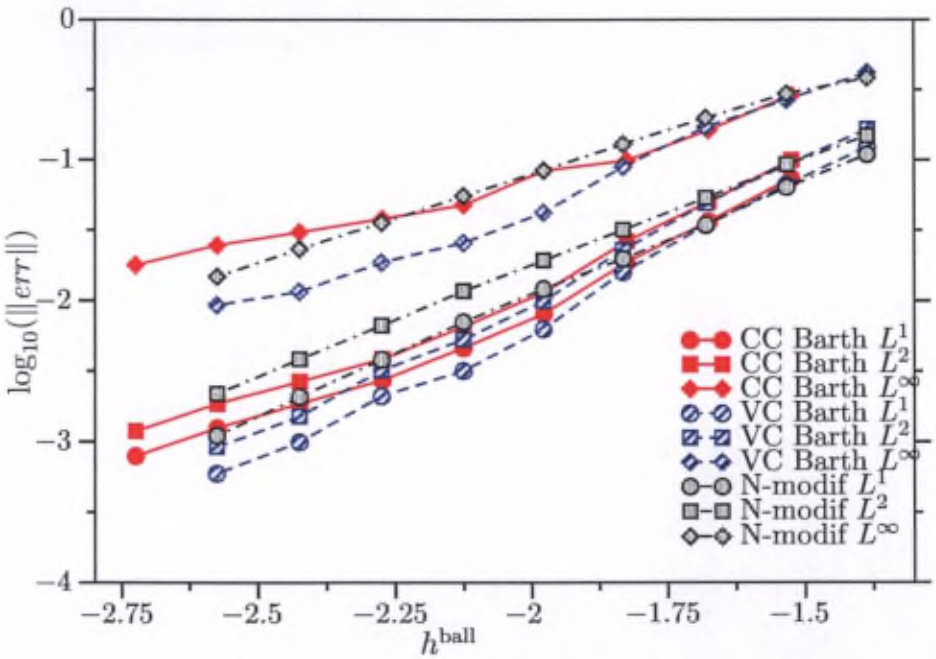


Figure 5.10.: 2D steady circular advection problem. Finite volume schemes with limiter and N-modified scheme. Norm of error vs. mesh spacing.

For the second test, we solve scalar equation

$$u_t + (-y, x, 0) \cdot \vec{\nabla} u = 0 \tag{5.25}$$

on a domain $\Omega = [-1, 1] \times [0, 1] \times [0, 1]$, with the initial conditions $u^0 = 0$ and boundary conditions

$$u = \begin{cases} \cos^2[\pi \min(0.5, 1.4 \|\vec{x} - (0.5, 0, 0.5)\|)] & \text{on } x > 0,\ y = 0, \\ 0 & \text{on the rest of inflow boundary.} \end{cases} \tag{5.26}$$

The similar problem was solved in [Lep04]. The difference between 2D and 3D case lies in the fact, that there is roughly 6 times more elements than nodes for 3D, while only twice more elements in 2D and bigger variations in the mesh connectivity. A sequence of meshes was generated, with the mesh parameters given in Tab. 5.3.

The solution using the FV schemes with constant reconstruction and the N scheme is plotted in Fig. 5.12. The situation is different than for the 2D case: the cell centered finite volume is slightly more accurate than the N scheme. As in the 2D case, the vertex centered finite volume is the least accurate scheme. The finite volume schemes with linear reconstruction exhibits similar behavior, see Fig. 5.13. The cell centered scheme is more accurate than the vertex centered. The LDA scheme is clearly most accurate considered scheme. The convergence order of the LDA scheme estimated from the $L^1$ and $L^2$ norm of error substantially exceeds second order accuracy, while in the $L^\infty$ norm is almost second order accurate, see Tab. 5.2, pg. 99. The cell centered finite volume scheme exhibits second order accuracyin the $L^1$ and $L^2$ norm, while the estimated order for the vertex centered scheme is somewhat lower. Finally, the N-modified scheme is more accurate than the vertex centered finite volume, while the cell centered finite volume gives the most accurate results, see Fig. 5.14. Estimation of convergence order is reported in Tab. 5.2.

The conclusions from the 2D and 3D circular advection test case: the LDA is the most accurate among all the considered schemes. The advantage of the other RD schemes is not so well pronounced – N scheme performs similarly to the cell centered scheme in the 3D case and the N-modified scheme is the least accurate among the nonlinear schemes in the 2D case. In 3D case the vertex centered finite volume scheme is the least accurate in all modifications.

| Id | # nodes | # elements | cell centered $h^{\text{ball}}$ | vertex centered $h^{\text{ball}}$ |
|---|---|---|---|---|
| m1000 | 5248 | 27781 | 0.0258 | 0.0449 |
| m0820 | 9735 | 52004 | 0.0209 | 0.0366 |
| m0670 | 16612 | 91962 | 0.0173 | 0.0306 |
| m0544 | 29984 | 168565 | 0.0141 | 0.0251 |
| m0444 | 55823 | 317535 | 0.0114 | 0.0204 |
| m0369 | 96714 | 555022 | 0.0095 | 0.0170 |
| m0303 | 175959 | 1010467 | 0.0077 | 0.0139 |

Table 5.3.: 3D rotation problem: mesh parameters.

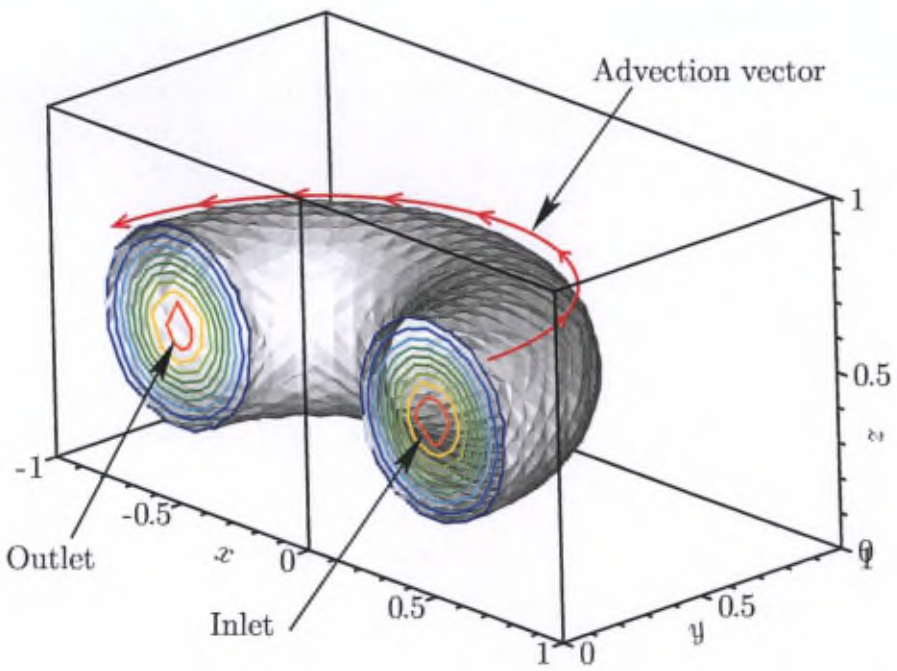


Figure 5.11.: Steady 3D circular advection problem. Sketch of the situation.

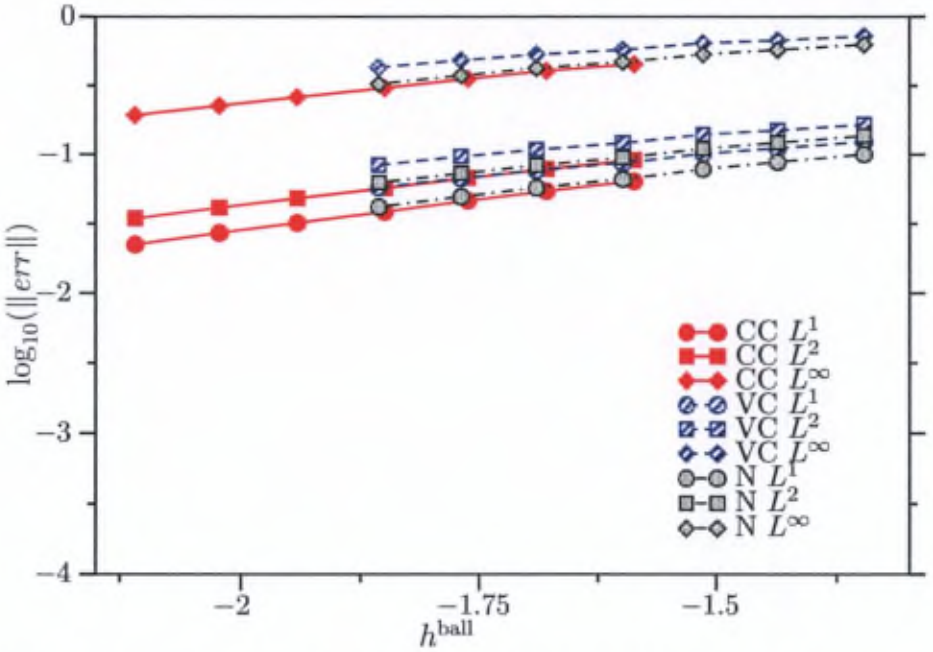


Figure 5.12.: 3D steady circular advection problem. Schemes with constant reconstruction and the N scheme. Norm of error vs. mesh spacing.

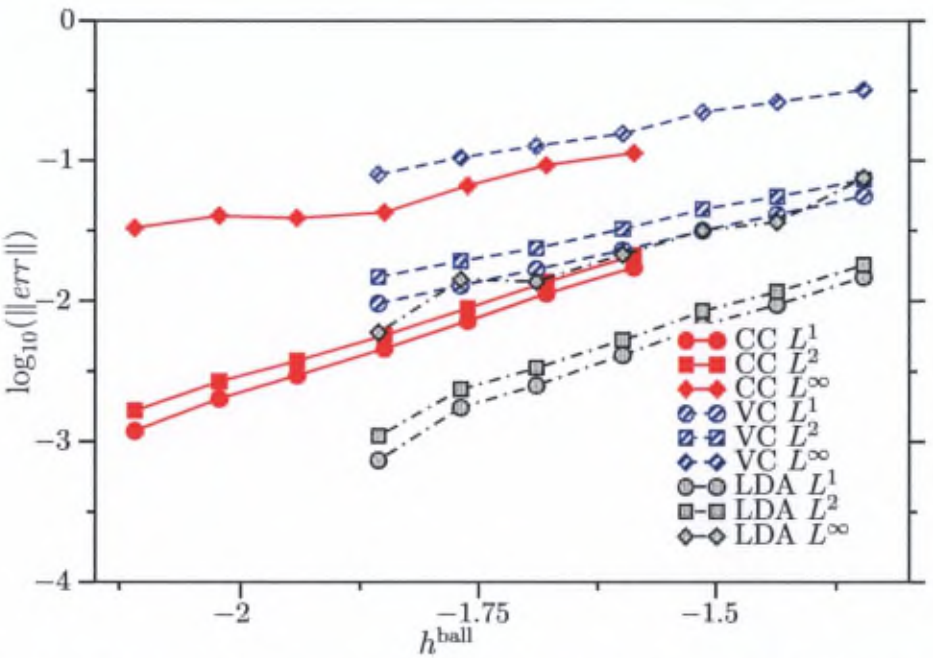


Figure 5.13.: 3D steady circular advection problem. Schemes with linear reconstruction without limiter and LDA scheme. Norm of error vs. mesh spacing.

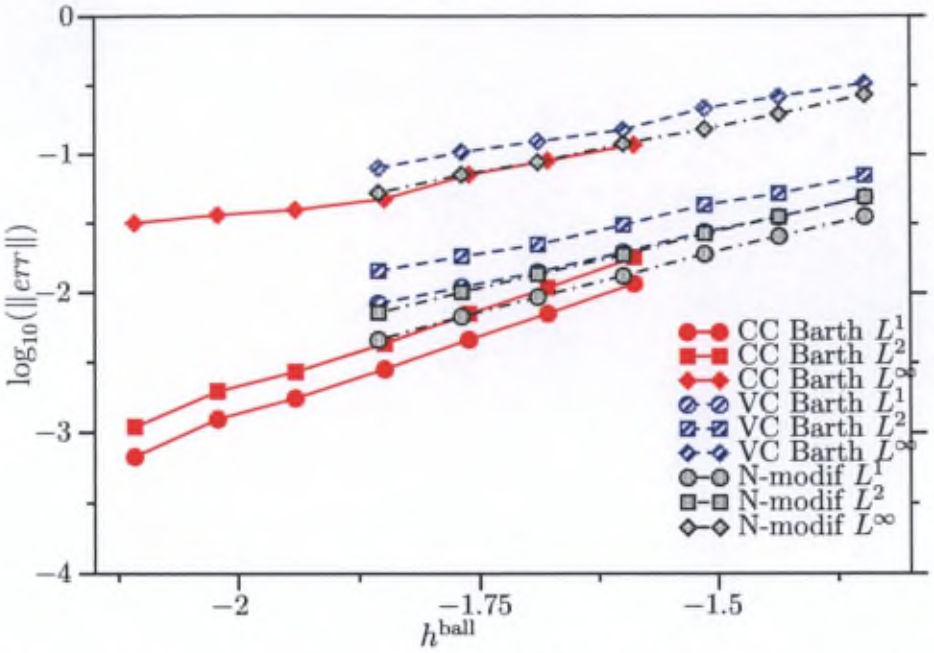


Figure 5.14.: 3D steady circular advection problem. Finite volume schemes with limiter and N-modified scheme. Norm of error vs. mesh spacing.

### 5.3.2. 2D Burgers equation

We solve the 2D inviscid Burgers equation

$$\frac{\partial u}{\partial t} + \frac{1}{2}\frac{\partial u^2}{\partial x} + \frac{\partial u}{\partial y} = 0 \tag{5.27}$$

on the square domain $\Omega = [0, 1.5]\times[0, 1.5]$ with boundary conditions on the boundary $y = 0$

$$u = \begin{cases} 1.5 & \text{for } x \leq 0 \\ -0.5 & \text{for } x \geq 1 \\ 1.5 - 2x & \text{elsewhere} \end{cases} \tag{5.28}$$

and $u = 1.5$ for $x = 0$ and $u = -0.5$ for $x = 1.5$.

The problem was solved on a mesh with 2900 DOF (giving $h = 1/39$ for VC FV and RD schemes and $h = 1/28$ for CC FV schemes). The solution isolines and cut along lines $y = 0.1$ and $y = 1$ are plotted. The symbols on the lines correspond to the cross-section of cuts with the mesh lines. All the FV schemes with constant reconstruction and the N scheme give a strictly monotone solution. Among the linear positive schemes, the N scheme clearly gives the most accurate results, see Fig. 5.15, 5.16, 5.17. The resolution of the CC and VC schemes with constant reconstruction is comparable, with CC results slightly more accurate than the VC. The cell centered scheme with linear reconstruction without limiter gives

| Scheme | Maximum | Minimum | Overshoot | Undershoot |
|---|---|---|---|---|
| Exact | 1.5 | −0.5 | | |
| CC FV Const. | 1.5 | −0.5 | | |
| VC FV Const. | 1.5 | −0.5 | | |
| N | 1.5 | −0.5 | | |
| CC FV Linear | 1.8611 | −0.9657 | 0.3611 | −0.4657 |
| VC FV Linear | 1.8240 | −0.88325 | 0.3240 | −0.3832 |
| LDA | 1.8813 | −0.7385 | 0.3813 | −0.2385 |
| CC FV Barth | 1.5 | −0.5 | | |
| VC FV Barth | 1.50043 | −0.50004 | 0.000439 | $-4.99 \cdot 10^{-5}$ |
| N-modif | 1.5 | −0.5 | | |

Table 5.4.: Maximal and minimal values in the domain for the 2D Burgers problem

less accurate results than the VC and LDA scheme, see Fig. 5.18, 5.19, 5.20. The higher accuracy of the LDA scheme can be observed namely on the region of steep gradient, where the shock forms. The solution is comparable in terms of overshoots and undershoots. Finally, the nonlinear schemes, see Fig. 5.21, 5.22, 5.23: the N-modified scheme gives solution similar to the VC FV scheme with Barth's limiter. The difference lies mainly in the wiggles in the fan region, for discussion see e.g. [Abg06]. The CC scheme with Barth's limiter gives the least accurate results. The monotonicity of the results can be judged from Tab. 5.4 and the cut plots.

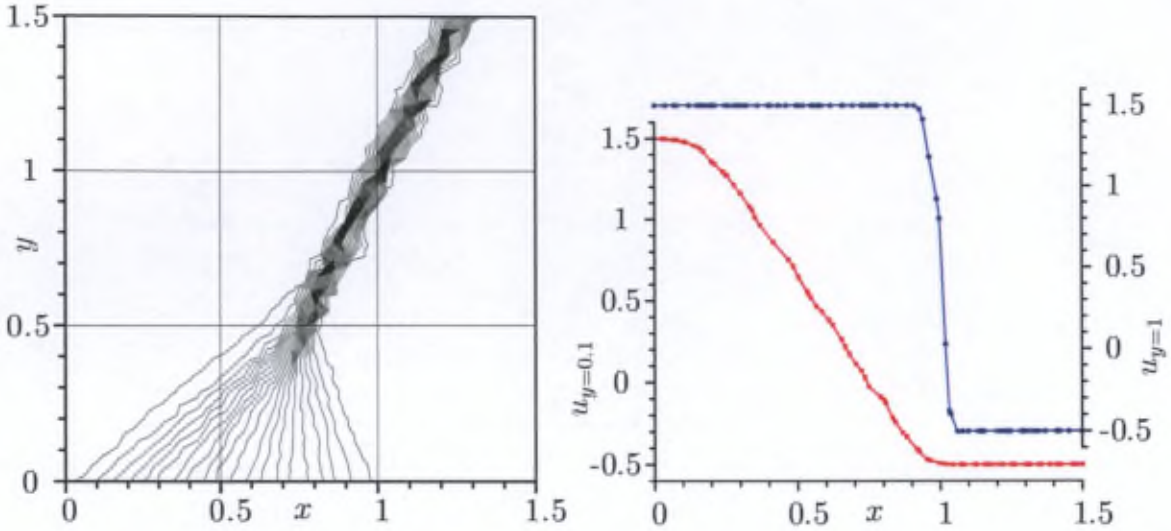


Figure 5.15.: 2D Burgers equation. CC FV with constant reconstruction. Isolines of the solution and the cut along $y = 0.1$ and $y = 1$ lines.

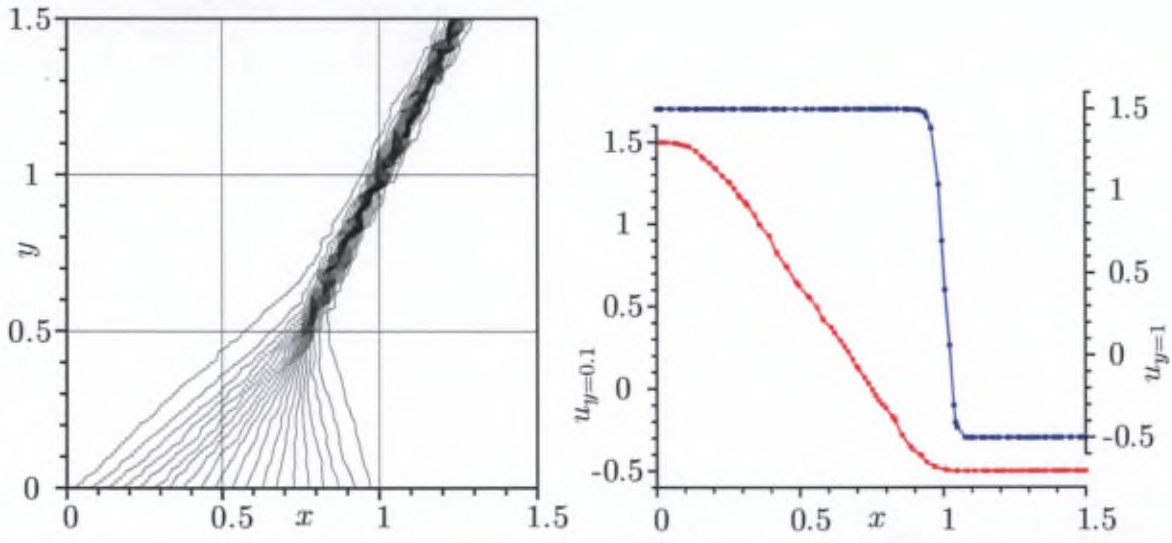


Figure 5.16.: 2D Burgers equation. VC FV with constant reconstruction. Isolines of the solution and the cut along $y = 0.1$ and $y = 1$ lines.

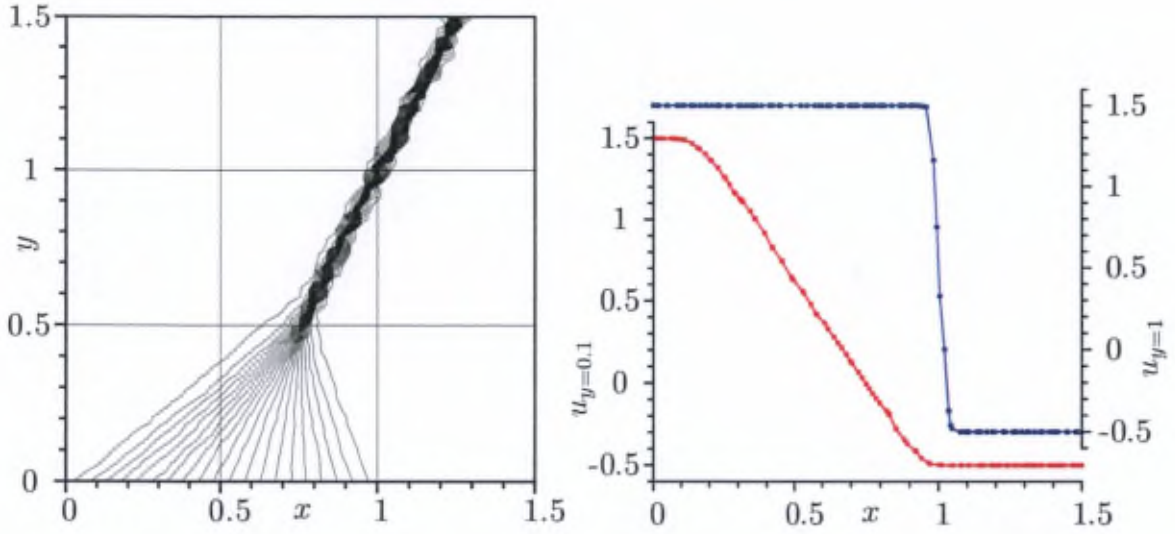


Figure 5.17.: 2D Burgers equation. RD N scheme. Isolines of the solution and the cut along $y = 0.1$ and $y = 1$ lines.

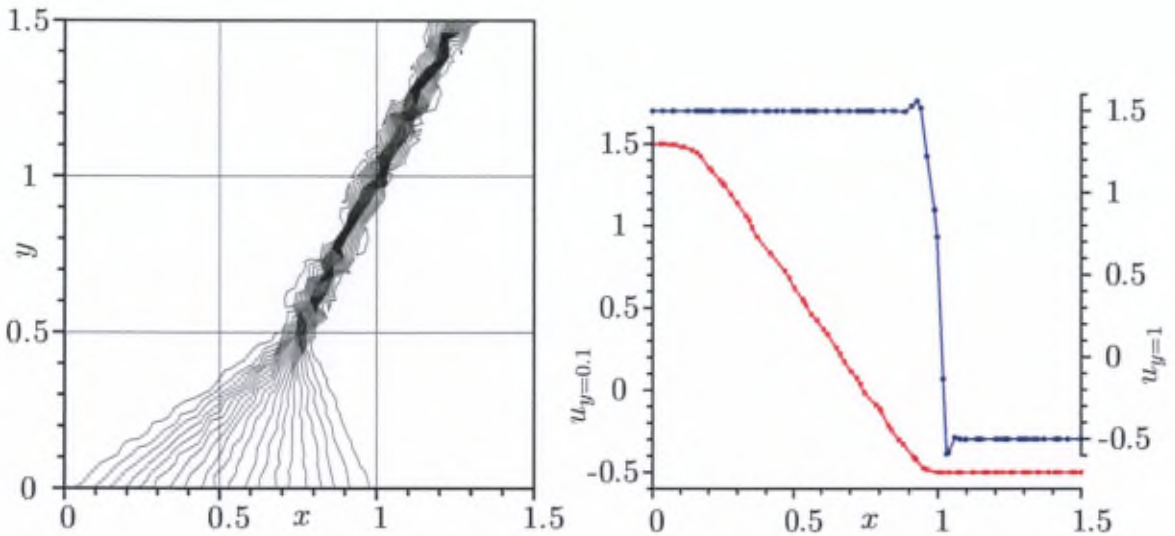


Figure 5.18.: 2D Burgers equation. CC FV with linear reconstruction without limiter. Isolines of the solution and the cut along $y = 0.1$ and $y = 1$ lines.

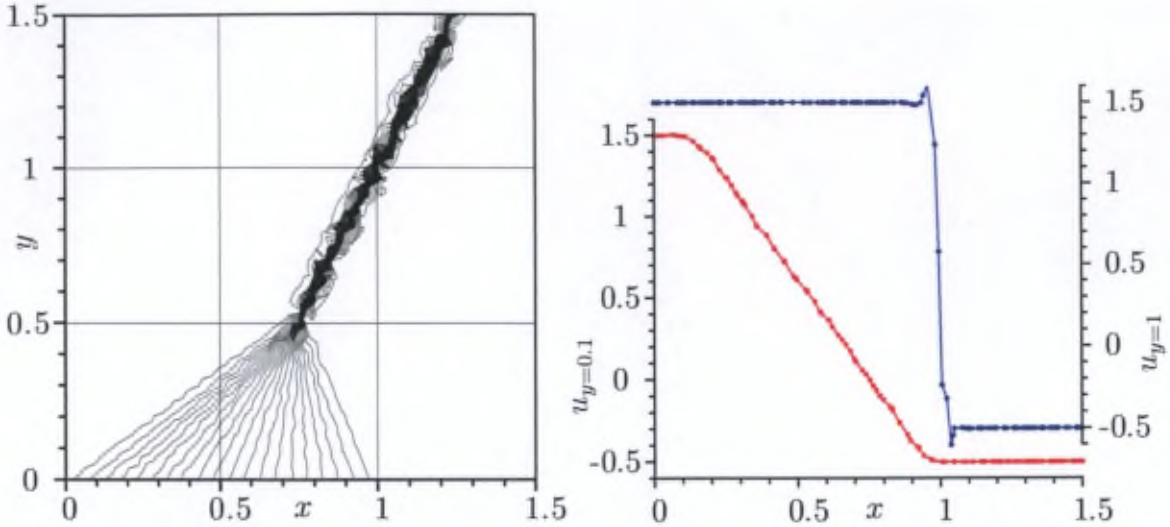


Figure 5.19.: 2D Burgers equation. VC FV with linear reconstruction without limiter. Isolines of the solution and the cut along $y = 0.1$ and $y = 1$ lines.

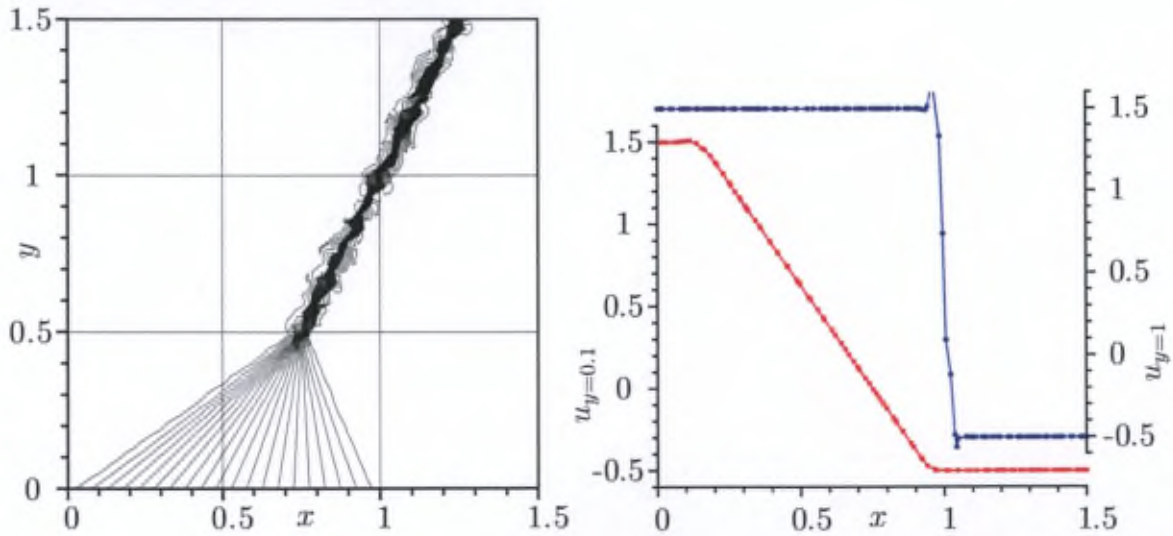


Figure 5.20.: 2D Burgers equation. RD LDA scheme. Isolines of the solution and the cut along $y = 0.1$ and $y = 1$ lines.

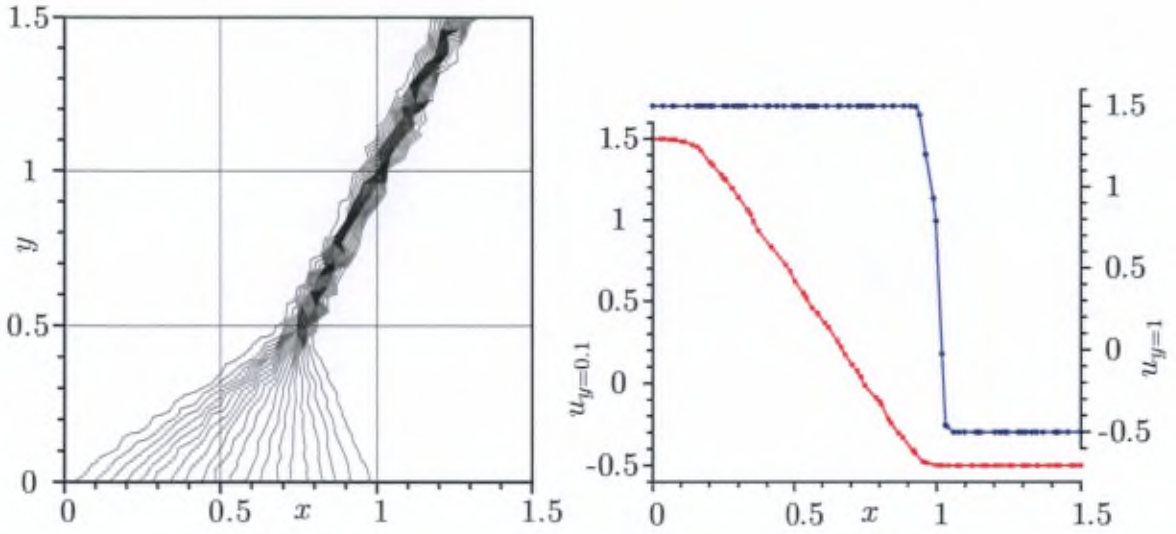


Figure 5.21.: 2D Burgers equation. CC FV with linear reconstruction and Barth's limiter. Isolines of the solution and the cut along $y = 0.1$ and $y = 1$ lines.

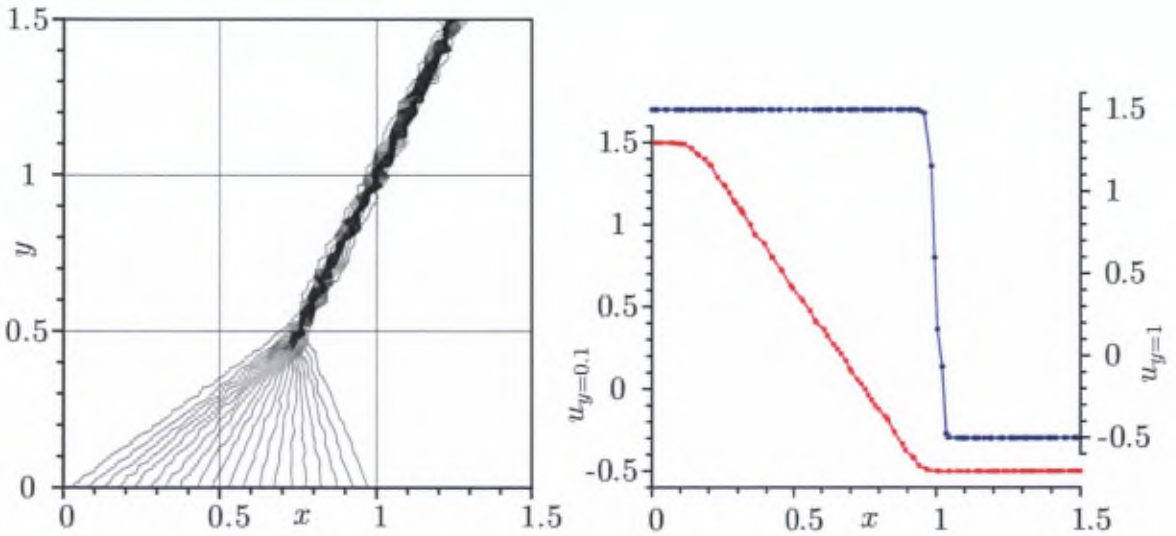


Figure 5.22.: 2D Burgers equation. VC FV with linear reconstruction and Barth's limiter. Isolines of the solution and the cut along $y = 0.1$ and $y = 1$ lines.

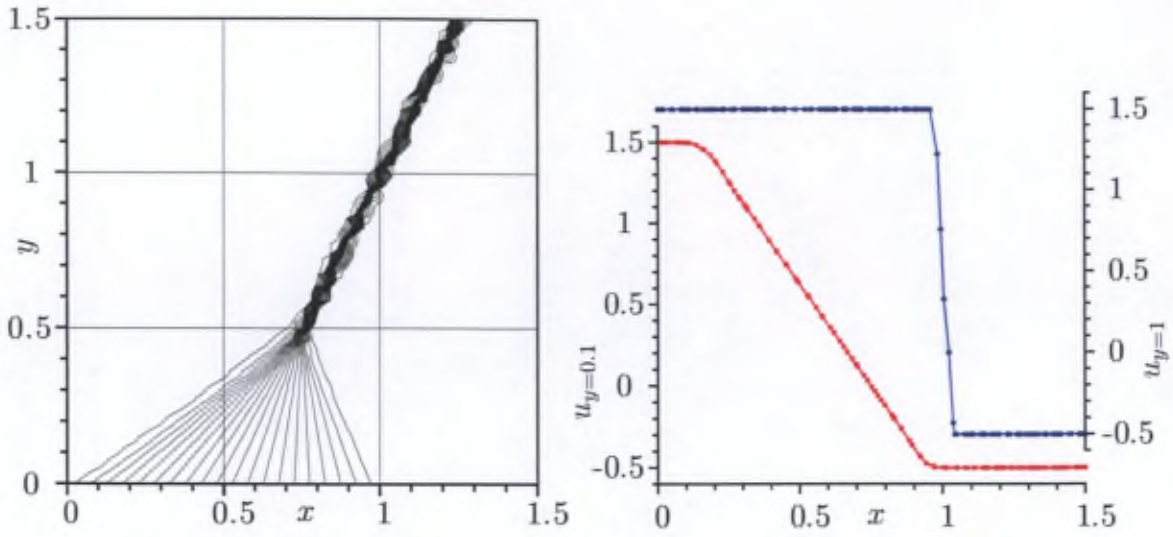


Figure 5.23.: 2D Burgers equation. RD N-modified scheme. Isolines of the solution and the cut along $y = 0.1$ and $y = 1$ lines.

### 5.3.3. 2D unsteady circular advection

As the first test case involving time dependent simulation, the circular advection is considered. The problem is solved in space-time domain $\Omega \times I$, $\Omega = [-1, 1] \times [-1, 1]$, $I = [0, 2\pi]$. As the initial condition the cosinus profile was prescribed

$$u^0(\vec{x}) = 1 + \frac{\cos(4\pi \min(d, 1/4))}{2}, \qquad d = \|\vec{x} - (-0.5, 0)\|. \tag{5.29}$$

The problem was solved on a sequence of grids with spacing $h = 1/20$, $h = 1/28$, $h = 1/39$, $h = 1/55$, $h = 1/77$, $h = 1/108$, $h = 1/152$, $h = 1/214$ and $h = 1/302$. The time-step was chosen $\Delta t = 0.005h$, giving the maximal CFL number in the domain about one. We have performed the convergence studies, with the norm of the error in space–time domain

$$\begin{aligned} \|err\|_{L^p(\Omega \times t)} &= \sqrt[p]{\int_0^{2\pi} \int_\Omega [u(\vec{x}, t) - u^h(\vec{x}, t)]^p \, \mathrm{d}\vec{x} \, \mathrm{d}t} \\ &\approx \sqrt[p]{\sum_n \sum_i \Delta t^n \mu(V_i) [u(\vec{x}_i, t^n) - u^h(\vec{x}_i, t^n)]^p}, \end{aligned} \tag{5.30}$$

where $\mu(V_i)$ is the measure of the volume associated with the point $i$, i.e. surface of the triangle for cell centered FV and surface of the dual volume for vertex centered FV and RD schemes. The $L^\infty$ norm is the maximal error in the *whole space-time domain*.

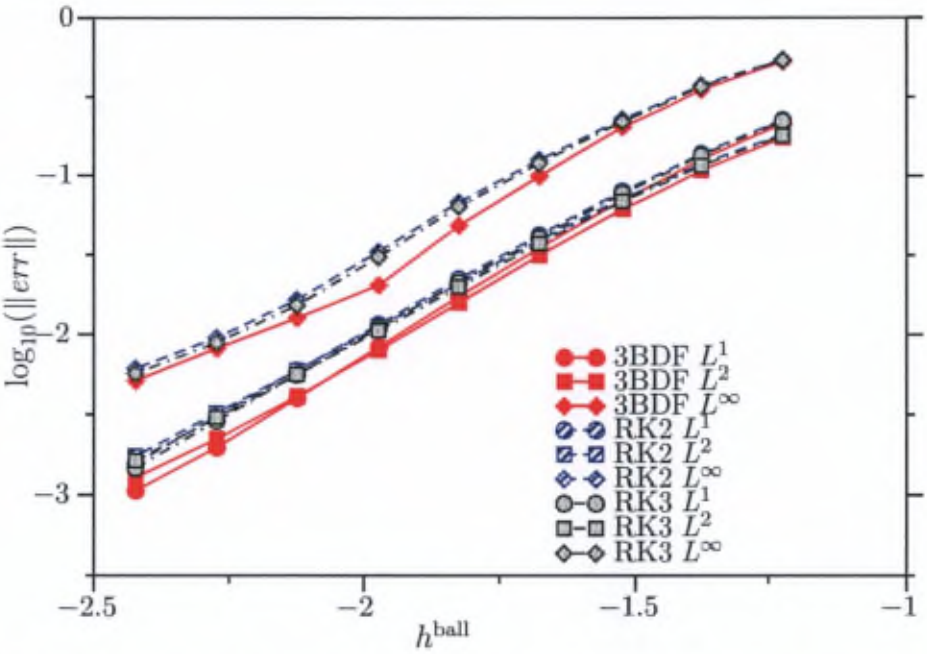


Figure 5.24.: 2D unsteady circular advection problem. CC FV scheme with linear reconstruction without limiter; comparison of time-stepping schemes

First, we examine different time-stepping schemes, see Fig. 5.24. Both second and third order Runge-Kutta (RK) methods gives similar accuracy, slightly higher for the third order RK scheme. The implicit 3BDF time stepping scheme gives much higher accuracy than both Runge-Kutta schemes. Comparison of the schemes with linear reconstruction and the LDA scheme is plotted in Fig. 5.24. The LDA is again the most accurate scheme. The VC is about the same accurate as the CC scheme; different time integration procedure also has to be taken into the account. Finally for nonlinear schemes, see Fig. 5.26, the VC is less accurate than the CC scheme, the N-modified is the least accurate one. Similar conclusions can be drawn from Tab. 5.5.

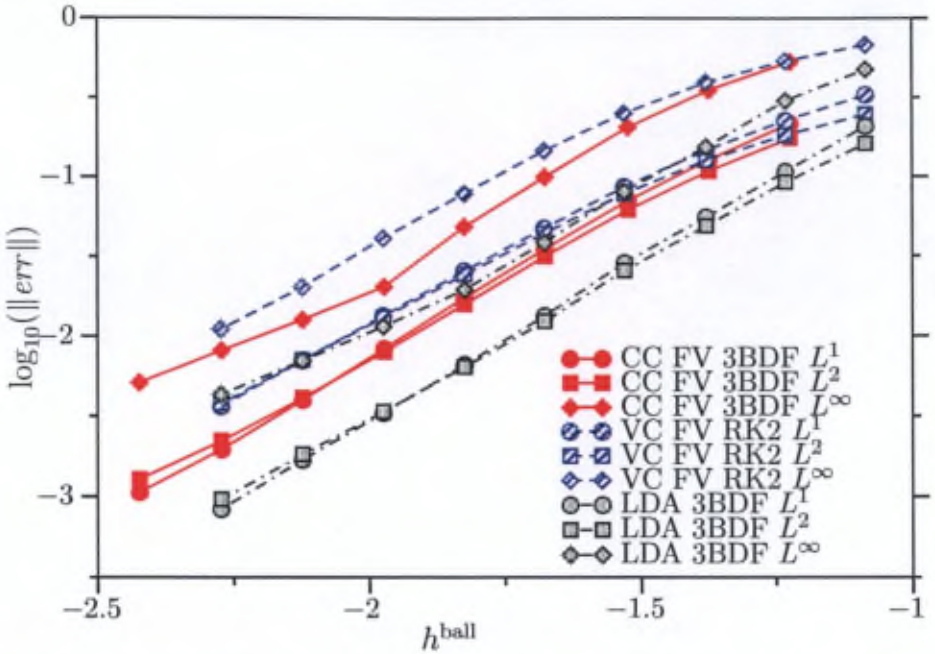


Figure 5.25.: 2D unsteady circular advection problem. CC FV scheme with linear reconstruction without limiter 3BDF time integration scheme; VC FV scheme with linear reconstruction without limiter RK2 time integration scheme; LDA with mass matrix and 3BDF time integration scheme.

| Scheme | $L^1$ order | $L^2$ order | $L^\infty$ order | $\max_{\vec{x}\in\Omega} u^h(\vec{x}, t = 2\pi)$ |
|---|---|---|---|---|
| CC FV2 nolim 3BDF | 2.010 | 1.883 | 1.883 | 0.987 |
| CC FV2 nolim RK2 | 1.865 | 1.775 | 1.850 | 0.987 |
| CC FV2 nolim RK3 | 1.875 | 1.785 | 1.864 | 0.987 |
| VC FV2 nolim RK2 | 1.701 | 1.604 | 1.609 | 0.977 |
| LDA 3BDF | 2.022 | 1.905 | 1.848 | 0.994 |
| CC FV2 Barth 3BDF | 1.871 | 1.850 | 1.498 | 0.965 |
| VC FV2 Barth RK2 | 1.656 | 1.619 | 1.612 | 0.948 |
| N-mod CN | 1.354 | 1.304 | 1.150 | 0.885 |

Table 5.5.: Comparison of orders of accuracy for 2D unsteady circular advection problem and maximal value of the solution on grid $h = 2/150$.

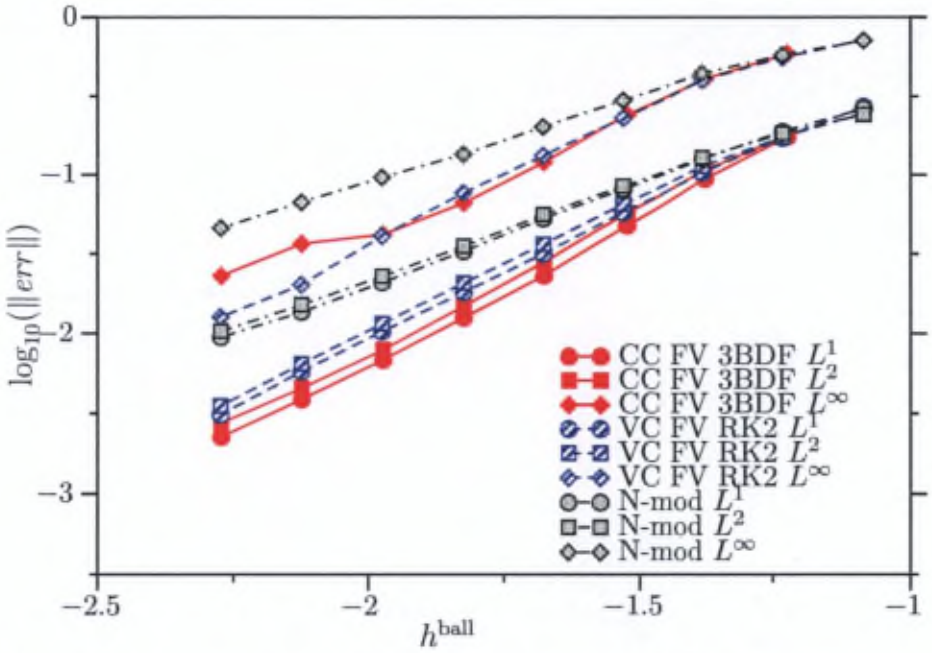


Figure 5.26.: 2D unsteady circular advection problem. CC FV scheme with linear reconstruction with Barth's limiter 3BDF time integration scheme; VC FV scheme with linear reconstruction with Barth's limiter RK2 time integration scheme; one layer N-modified scheme.

### 5.3.4. 2D unsteady circular advection on deforming meshes

This test examine accuracy of the numerical methods on deforming meshes. It is probably the most important test case in this thesis, because proper extension of unsteady schemes for moving mesh computations always raise accuracy concerns [MY06, Far04]. The LDA scheme, see section 3.7.3, is compared with the FV scheme, see section 4.3.2. The FV scheme uses linear reconstruction and no limiter. Both schemes are equipped with the 3BDF time integrator.

The setup of the test-case is similar as for the previous test, see section 5.3.3. We also use the same set of meshes as in the previous test case, while the mesh coordinates depends on time with formula

$$\vec{x}(t) = \frac{3 - \cos t}{2}\vec{Y}, \tag{5.31}$$

where $\vec{Y}$ is the original mesh coordinate and $\vec{x}(t)$ is the current configuration mesh coordinate. This setup gives us the original mesh size for the start $t = 0$ and for the final time $t = 2\pi$ and double size of the original mesh at time $t = \pi$.

The error was measured in the same manner as for the previous test case. Convergence is plotted in Fig. 5.27 and the rate of convergence is computed from the least square fit in Tab. 5.6. The higher accuracy of the LDA scheme in comparison with

| Scheme | $L^1$ order | $L^2$ order | $L^\infty$ order |
|---|---|---|---|
| LDA | 2.02 | 1.91 | 1.94 |
| FV2 nolim | 1.71 | 1.64 | 1.73 |

Table 5.6.: Comparison of orders of accuracy for 2D unsteady circular advection problem on deforming mesh.

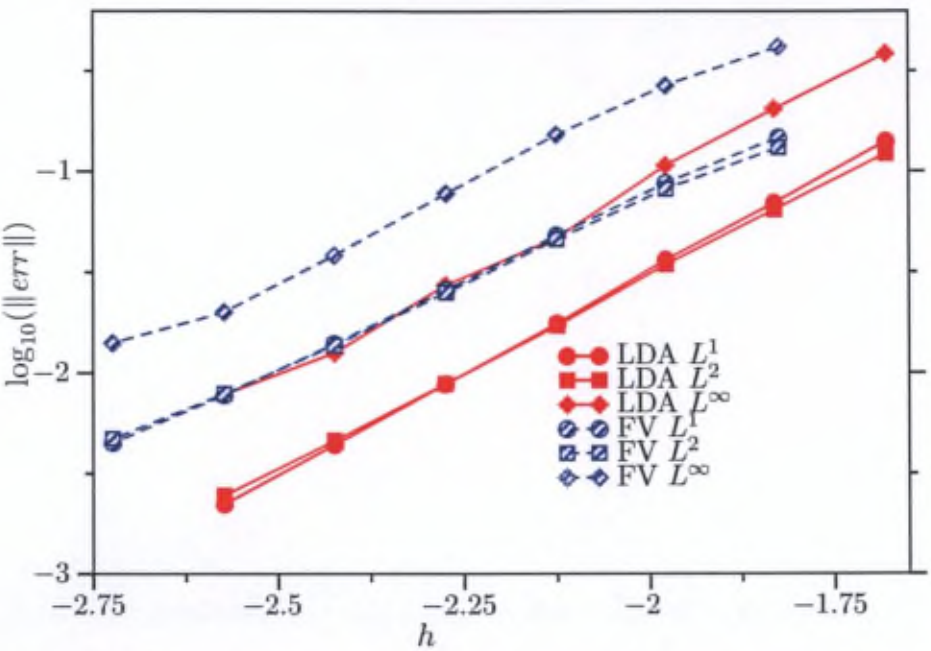


Figure 5.27.: 2D unsteady circular advection problem of deforming mesh. LDA scheme and FV scheme with linear reconstruction without limiter. Norm of error vs. mesh spacing.

the FV scheme is clear, both from the lower error and from the higher convergence rate.

## 5.3.5. Conclusions

The developed methods were tested on 2D and 3D linear, non-linear, steady and unsteady scalar problems. From the linear schemes, the LDA is consistently the best in the class. The CC and VC formulation of the FV scheme gives similar results, the CC scheme gave more often better results than the VC one. The N-modified scheme gives superior results for the Burgers equation with shock wave, while the accuracy for smooth solution is lower, often lower than the finite volume scheme.

## 5.4. Euler equations – steady problems

We examine behavior of the schemes for the case of Euler equations in this section. Note that some results were already presented in section 3.5.5. We start again with the smooth steady solution, the next case is a steady solution involving the shocks. Then we test the schemes for unsteady problems. This section conclude with test cases involving computations on moving meshes.

### 5.4.1. Sub-critical flow past a cylinder

The test case is introduced in section 3.5.5, page 41. Recall the free stream Mach number $M_\infty = 0.38$. Here we present some additional results. The computational mesh is shown in Fig. 5.28. We have generated two meshes, the one used for the cell centered finite volume has 676 nodes and 1269 triangular elements with 61 elements along the wall boundary and the one used for the vertex centered finite volumes and RD schemes has 1247 nodes and 2386 triangular elements with 79 element along the wall boundary. This ensures that all the methods uses similar number of degrees of freedom. The meshes are even coarser then in section 3.5.5, to amplify the differences between the schemes. We do not compare only the schemes, but also different formulations of boundary conditions, as they are given in section 3.9.2, page 69.

The solution of the FV schemes with constant reconstruction and RD N scheme are given in Fig. 5.29. In all cases, the solution is more-less symmetric with respect to the horizontal axis. One can observe spurious wake-like structure behind the cylinder, which is given by the high dissipativity and relatively low accuracy of the schemes. All the formulations of the boundary conditions gave similar results.

The results for the LDA scheme and FV scheme with linear reconstruction without the limiter are shown in Fig. 5.30. We don't plot the results from the vertex centered FV scheme without the limiter, since negative pressure has always been obtained during the convergence and the method has failed. Surprisingly large differences are caused by the formulation of the boundary conditions for the LDA scheme. The Paillere's formulation, see sec. 3.9.2.2, page 71, gave spurious separation, very different from the other boundary conditions formulation. For the characteristic formulation and Weide's formulation the solution is roughly symmetric and looks similar to the cell centered finite volume scheme, presented on the bottom left figure. For the CC FV schemes gradient at the first cell next to the wall is often set to zero to prevent obtaining negative pressure at the wall. Since this is a wide-spread approach, we have it included to the numerical results to show, how significantly it can change the solution. With uncorrected linear reconstruction in the element next to the wall the solution looks symmetric with respect to the horizontal axis, while if the gradient is set to zero the solution become non-symmetric, as it can be observed in the right bottom Fig. 5.30.

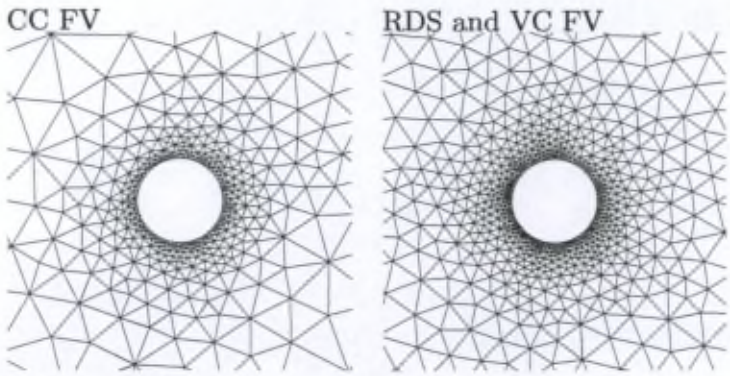


Figure 5.28.: Sub-critical flow past a cylinder. Computational meshes. Left: CC FV, right RD schemes and VC FV.

Results obtained with the nonlinear schemes with Barth's limiter and N-modified scheme are plotted in Fig. 5.31. The differences between the formulation of the boundary conditions are striking. On the other hand, it can be surprising, that for the VC finite volume scheme the formulation of the boundary conditions almost does not affect the solution. Unlike for the LDA scheme, where the Weide's and characteristic formulation of the BC gave almost the same result, here the characteristic formulation gave the best results and the Weide's formulation is slightly worse. The Paillere's formulation is the worst again, moreover it gave the worst results in this class of scheme. If we compare results between the schemes, the N-modified scheme gave the most symmetric results. The VC FV scheme gives more pronounced the spurious wake-like region and on the top and bottom of the cylinder the scheme produced non-symmetricity in the flow with respect to the vertical axis. The CC FV scheme gave the most wiggly results, while the accuracy seems to be similar to the VC scheme.

Finally, we present the results obtained with the Bx scheme and the FV scheme with WLSQR reconstruction, as defined in section 4.2.1, page 78. The results given by the Bx scheme are substantially the same as for the LDA scheme, which point to the high accuracy of the scheme. The results of the CC FV with WLSQR reconstruction are very similar to the CC FV scheme without limiter and quantitatively similar to the Bx scheme. The computations using the VC FV scheme with WLSQR reconstruction has failed due to the negative pressure obtained during the iterative procedure.

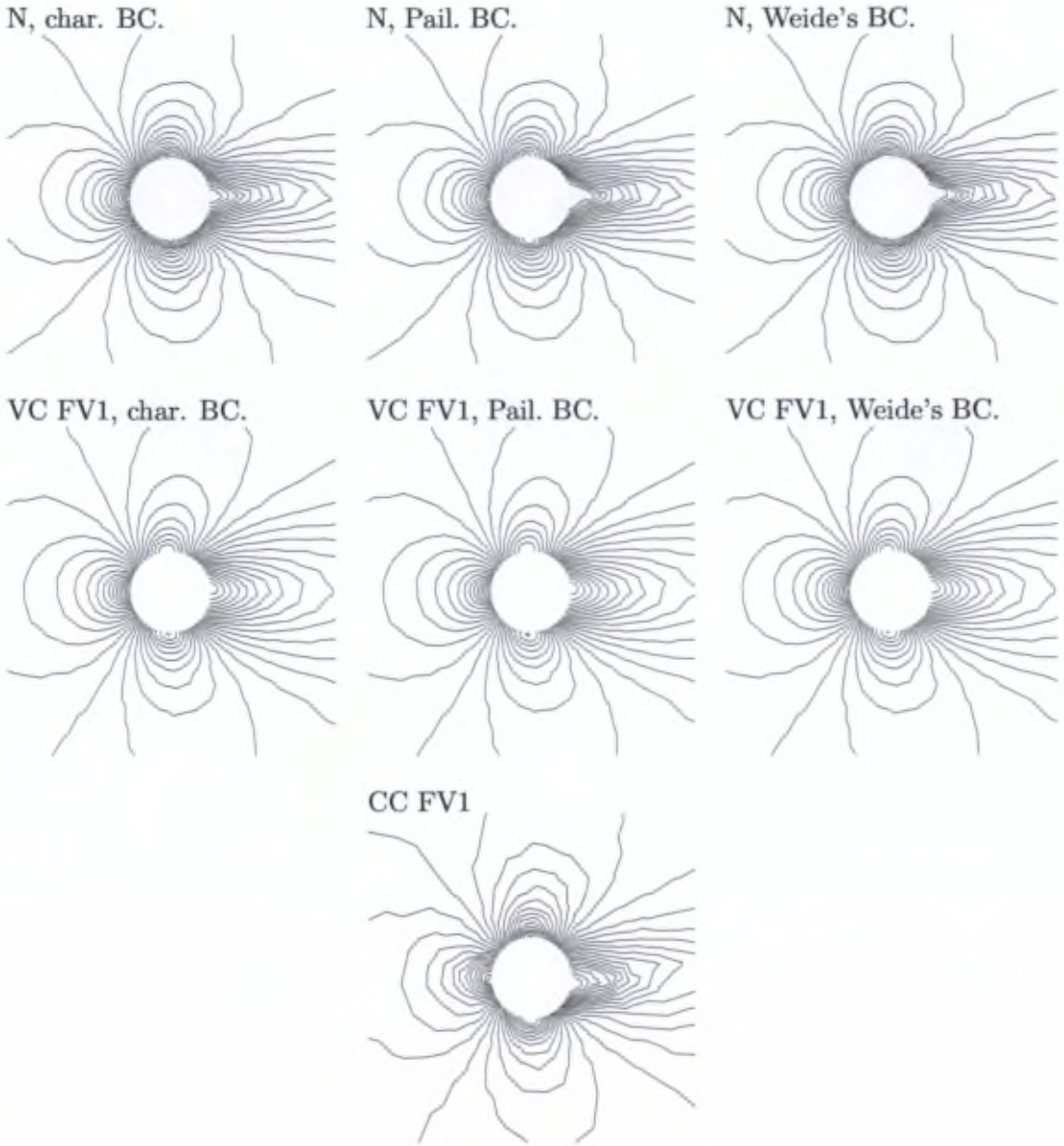


Figure 5.29.: Sub-critical flow past a cylinder. FV schemes with constant reconstruction and the N scheme.

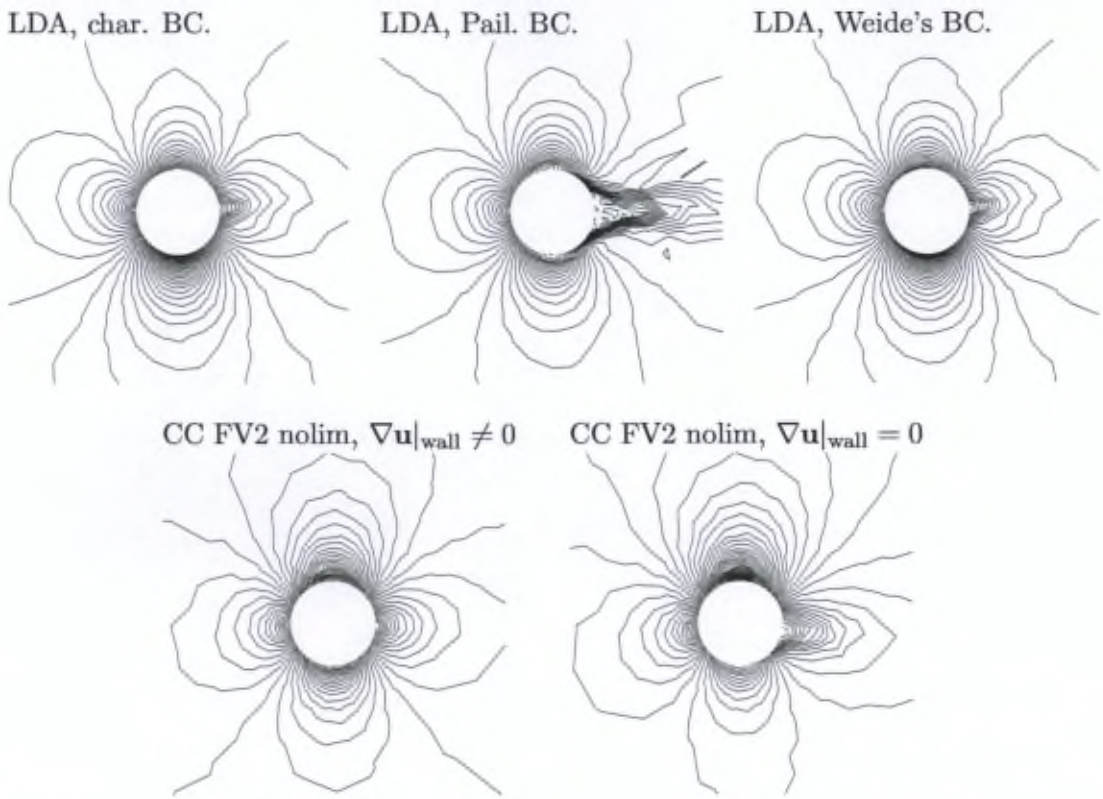


Figure 5.30.: Sub-critical flow past a cylinder. Linear FV schemes with linear reconstruction and LDA scheme.

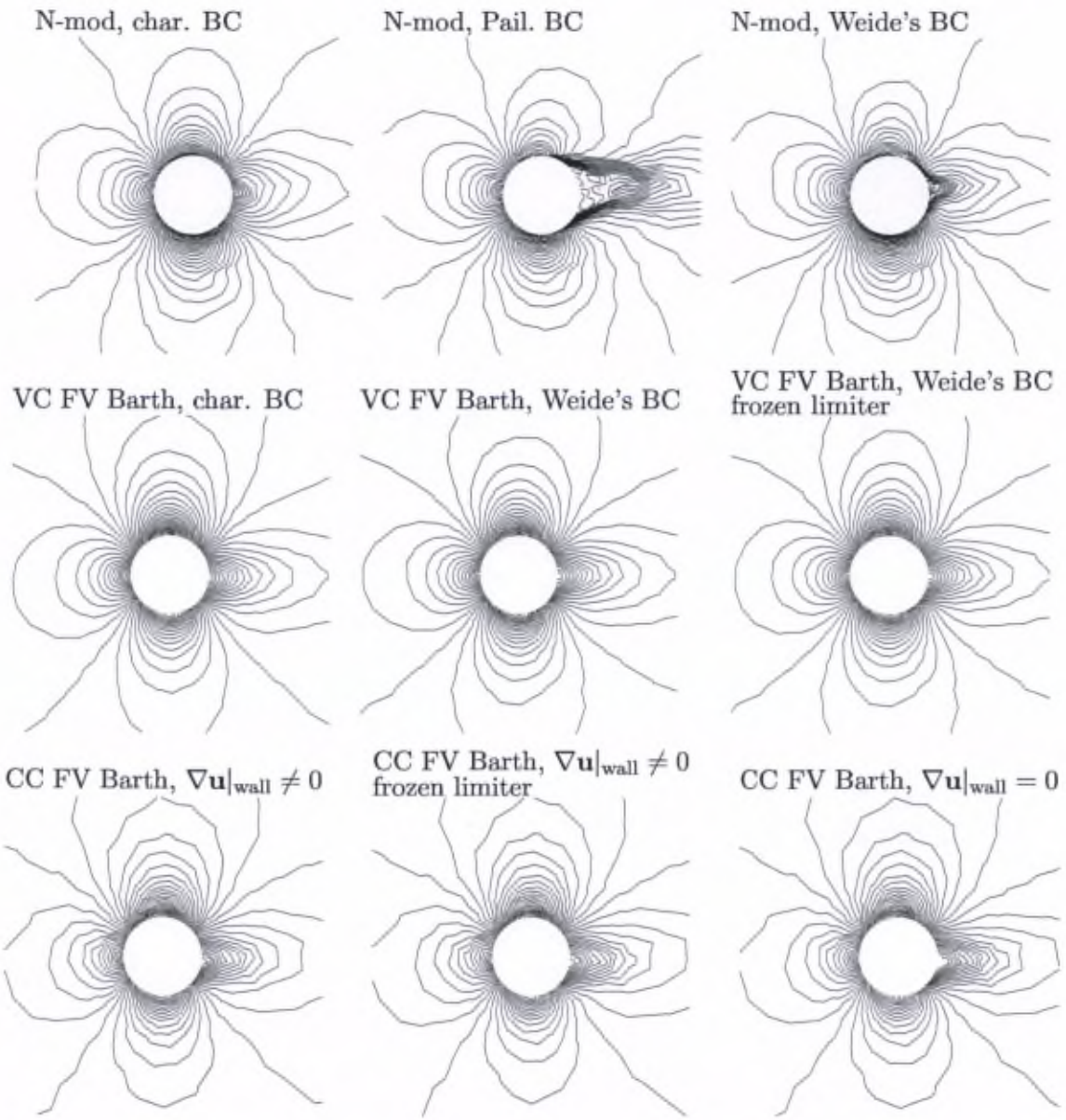


Figure 5.31.: Sub-critical flow past a cylinder. Nonlinear FV schemes with linear reconstruction and N-modified scheme.

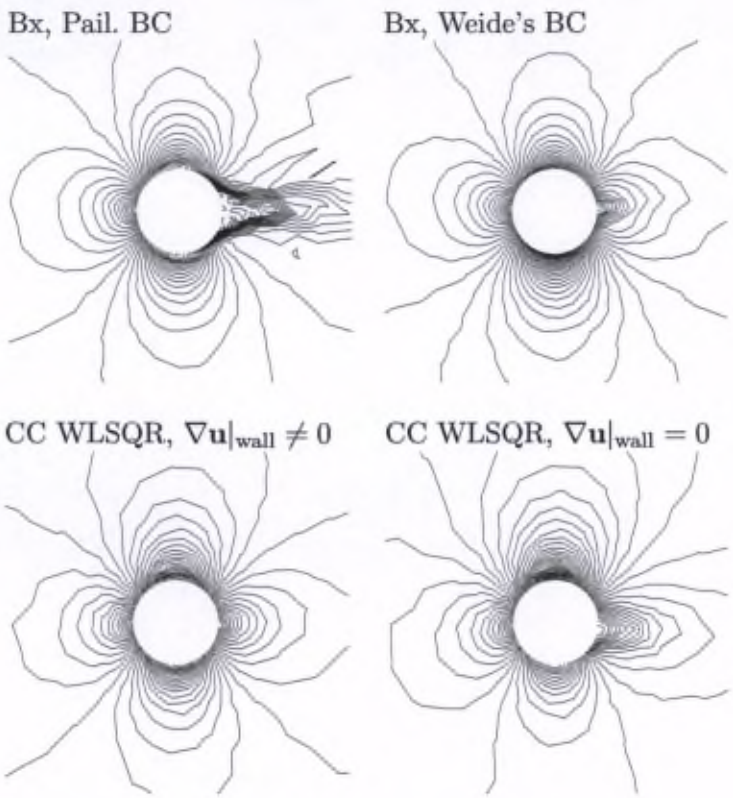


Figure 5.32.: Sub-critical flow past a cylinder. Nonlinear FV schemes with linear reconstruction and Bx scheme scheme.

### 5.4.2. 3D inviscid flow around the Onera M6 wing

This is a well known test case, measurements were published in [SC79]. We have chosen data from Test 2308, i.e. with free stream Mach number $Ma_\infty = 0.8395$ and angle of attack $\alpha = 3.06°$ . We use an unstructured mesh consisting of 57041 nodes and 306843 tetrahedral elements. It means that the CC FV scheme cannot be directly compared to the VC FV and RD schemes, since CC FV uses about 6 times more unknowns. Isolines of the Mach number are presented in Fig. 5.34, 5.35, 5.36. The $\lambda$-shock pattern is clearly visible for the more accurate schemes. The N scheme is about the same accurate as the VC FV scheme with constant reconstruction. One can see a big improvement of the method with linear reconstruction compared to the constant reconstruction. For the nonlinear schemes, the RD B scheme and CC FV with Barth's limiter perform similarly, still with RD schemes using 6 times less unknowns. A similar situation occurs for the comparison of WENO schemes with the Bx RD scheme. Differences between the schemes are even more clear in Fig. 5.37, 5.38 and 5.39. The figures show the distribution of the lift coefficient $c_p$ at cuts in the 44 %, 90 % and 99 % of the span. In all cases, the RD schemes gives better results than the VC FV schemes. Only the RD N scheme gives similar results as the VC FV1 scheme. The solution with the Barth's limiter and the B scheme features monotonous shock capturing. The WLSQR (WENO) method and the Bx scheme gives higher accuracy, while one can observe a small undershoot in the $c_p$ coefficient at in Fig. 5.37, 5.38, bigger for the Bx scheme. Part of this section was published in [DDF06].

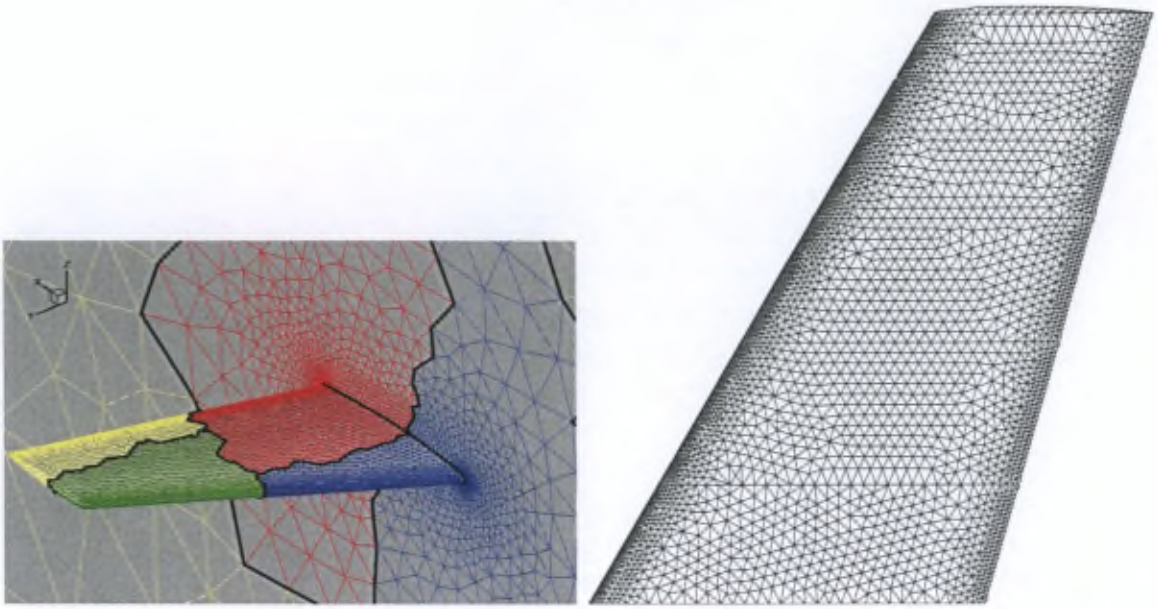

Figure 5.33.: Inviscid flow past Onera M6 wing. Computational mesh with domains for parallel solution. The mesh has 57041 nodes and 306843 tetrahedral elements.

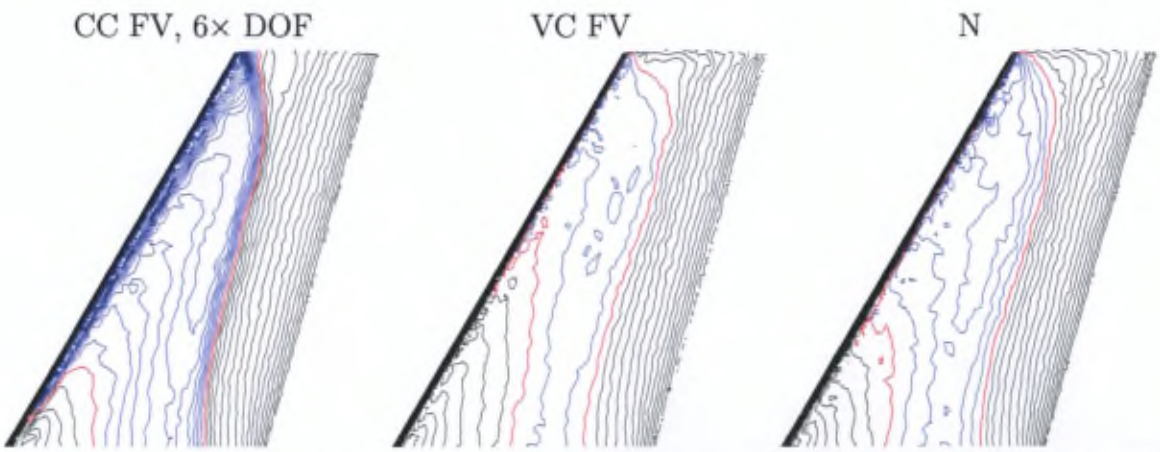


Figure 5.34.: Inviscid flow past Onera M6 wing. Isolines of Mach number. Left: CC FV1 scheme. Middle: VC FV1 scheme. Right RD N scheme.

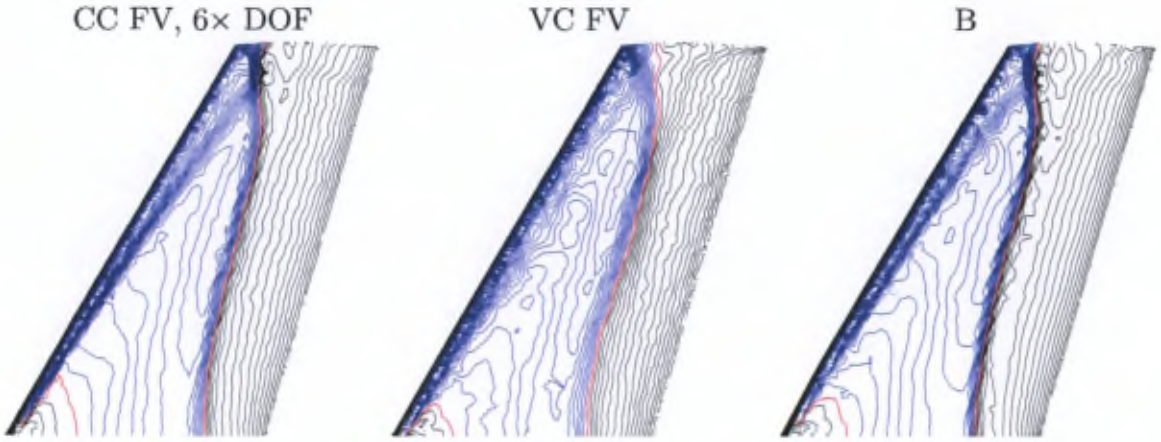


Figure 5.35.: Inviscid flow past Onera M6 wing. Isolines of Mach number. Left: CC FV scheme with Barth's limiter. Middle: VC FV scheme with Barth's limiter. Right RD B scheme.

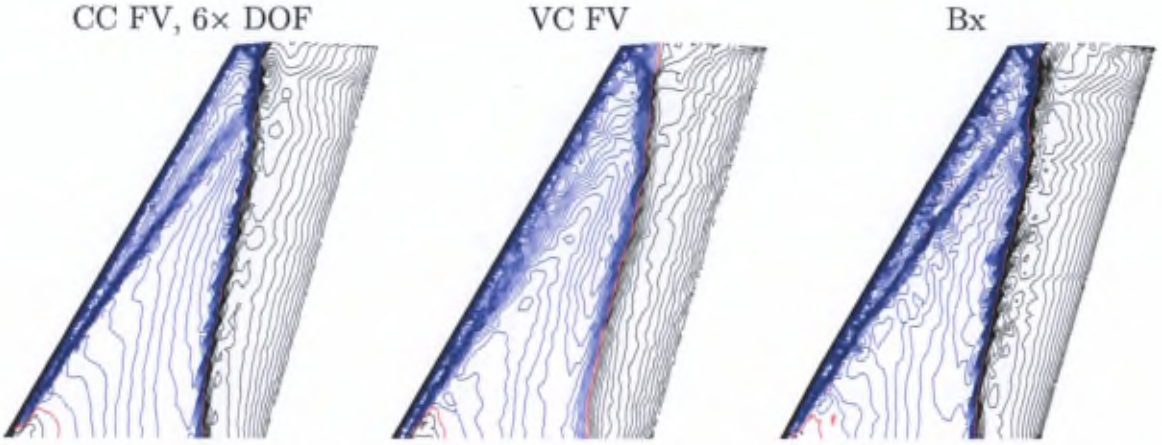


Figure 5.36.: Inviscid flow past Onera M6 wing. Isolines of Mach number. Left: CC FV WENO scheme. Middle: VC FV WENO scheme. Right RD Bx scheme.

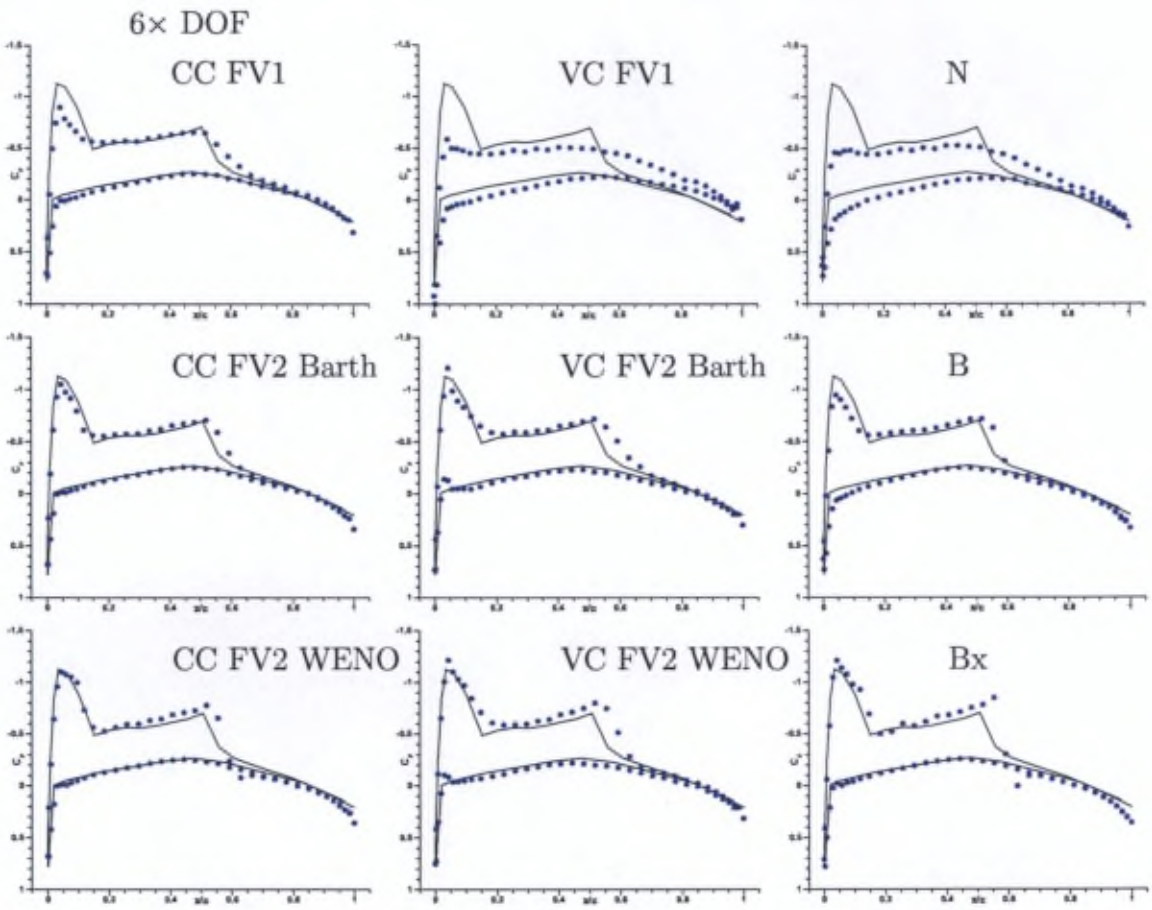


Figure 5.37.: Inviscid flow past Onera M6 wing. Cut at 44 % of span. Full line: experiment, points: numerical solution. Left column: CC FV schemes. Middle column: VC FV schemes. Right column RD schemes. Top row: FV1 and N scheme. Middle row: FV scheme with linear reconstruction and Barth's limiter, B scheme. Bottom row: FV WENO scheme and Bx scheme.

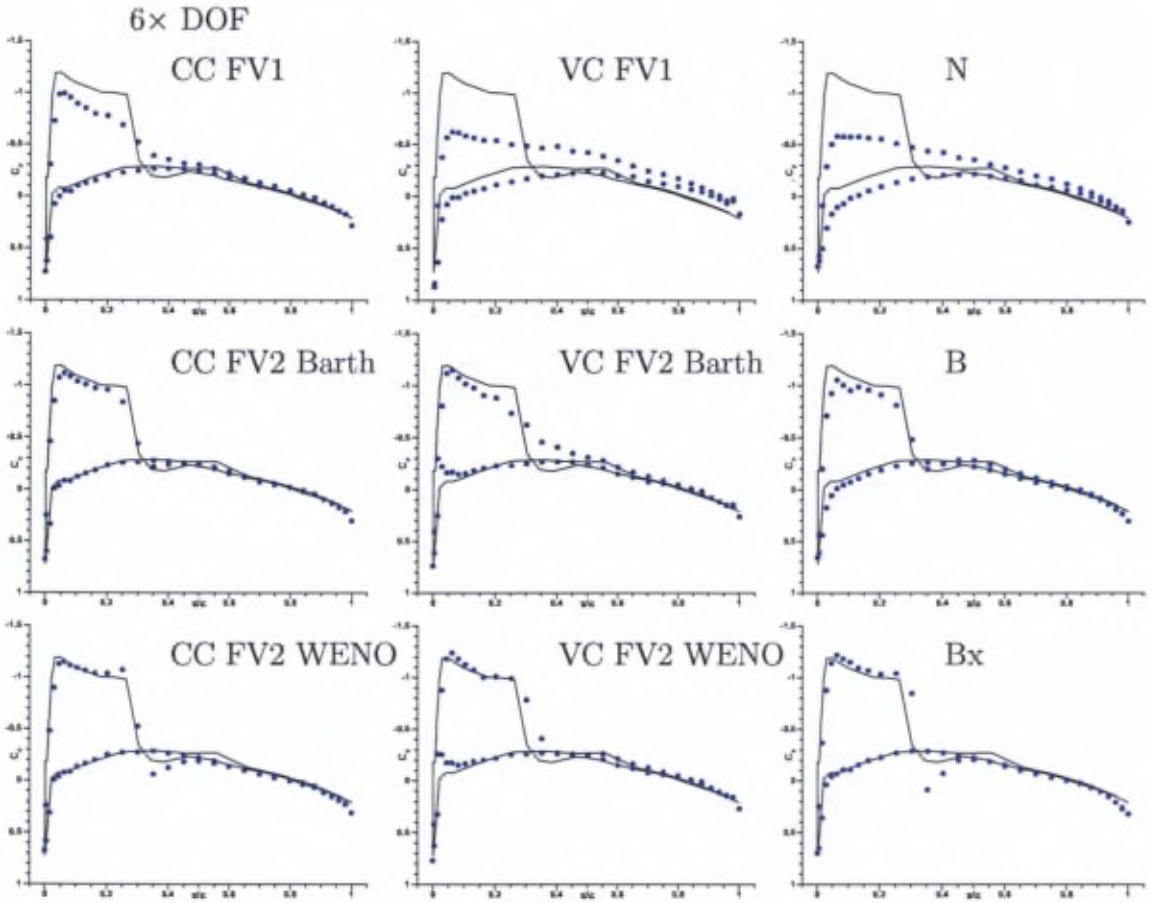


Figure 5.38.: Inviscid flow past Onera M6 wing. Cut at 90 % of span. Full line: experiment, points: numerical solution. Left column: CC FV schemes. Middle column: VC FV schemes. Right column RD schemes. Top row: FV1 and N scheme. Middle row: FV scheme with linear reconstruction and Barth's limiter, B scheme. Bottom row: FV WENO scheme and Bx scheme.

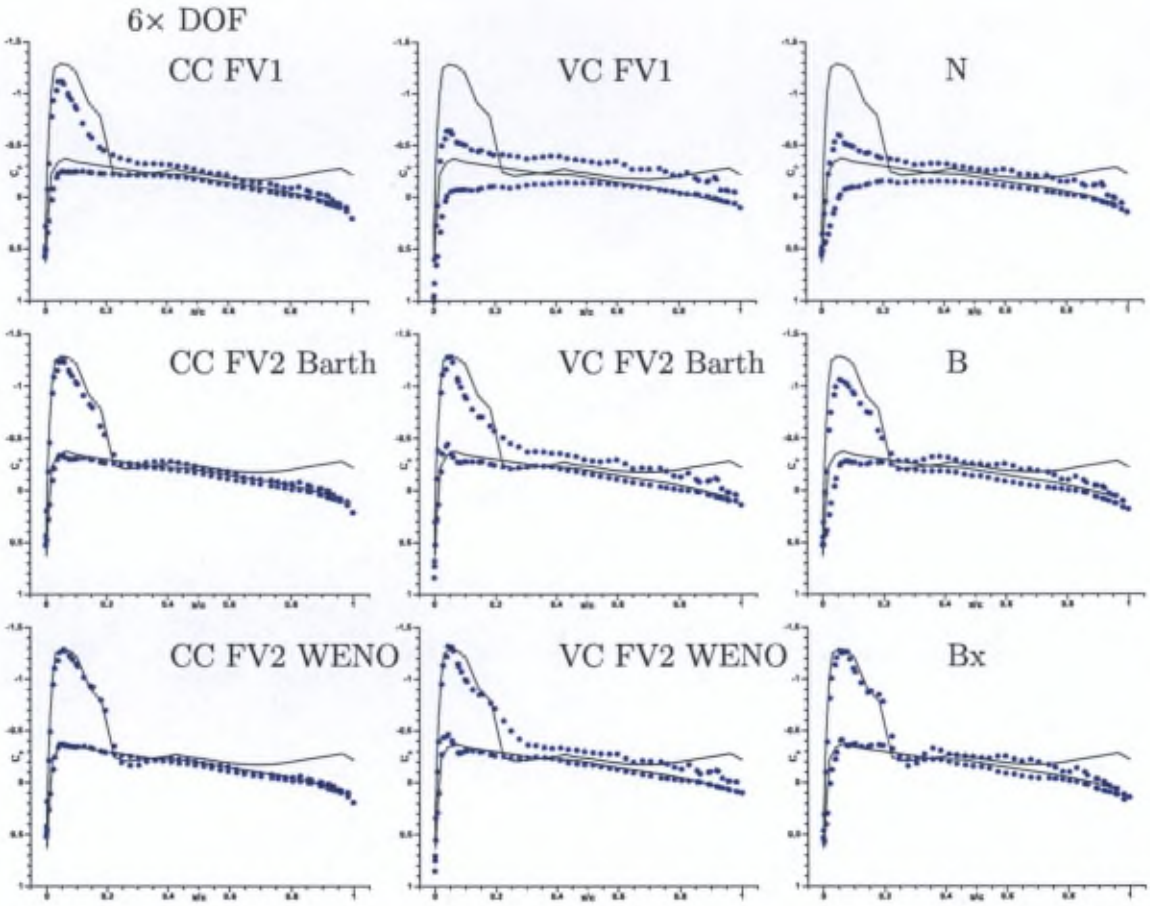


Figure 5.39.: Inviscid flow past Onera M6 wing. Cut at 99 % of span. Full line: experiment, points: numerical solution. Left column: CC FV schemes. Middle column: VC FV schemes. Right column RD schemes. Top row: FV1 and N scheme. Middle row: FV scheme with linear reconstruction and Barth's limiter, B scheme. Bottom row: FV WENO scheme and Bx scheme.

## 5.5. Euler equations – unsteady problems

### 5.5.1. 2D vortex convection

Here we consider the test case from the section 3.6.6, pg. 55, which examines the scheme for the performance in the smooth parts of the flow. Here discuss some additional figures for the comparison. For the FV schemes only cell centered formulation is presented. Cuts along the $x$ direction in the core of the vortex are depicted in Fig. 5.40. For the comparison of the pressure in the core of the vortex, see Table 3.2 on page 56. The superiority of the LDA and Bx scheme is clear, even though the number of DOF is twice smaller. The nonlinear Bx scheme is even better than the unlimited FV scheme. The FV WLSQR (WENO) scheme performs much worse, even worse than the N-modified scheme. In the case of the transonic flow past the Onera M6 wing the performance of the CC WENO FV scheme and Bx scheme were comparable, whereas it is different for this test case. Problem with non-smooth solution can be observed on the solution of the N-modified scheme, as it is analyzed in [Abg06, RA06]. Clearly the worst performance is obtained for the FV scheme with Barth's limiter.

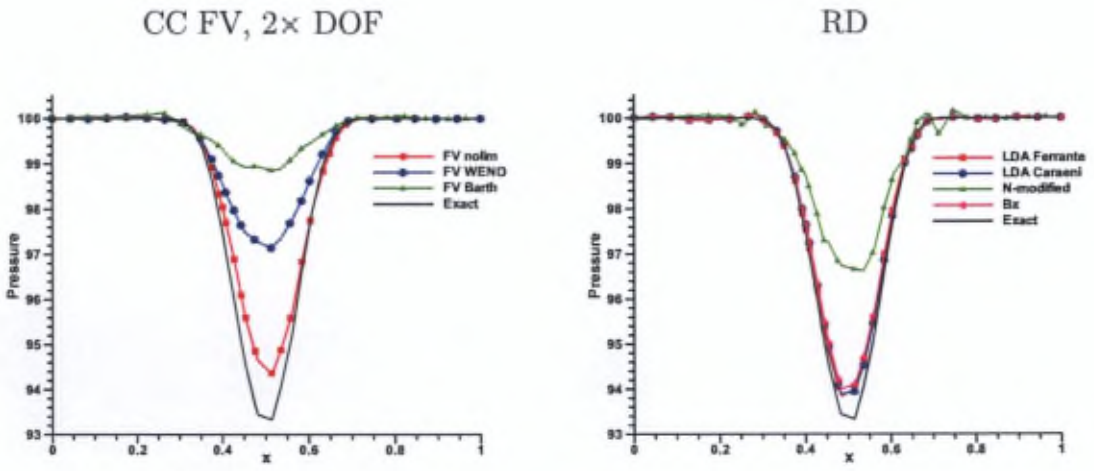


Figure 5.40.: 2D convection of the vortex test case. Cut in the $x$ direction. Left: FV schemes. Right: RD schemes.

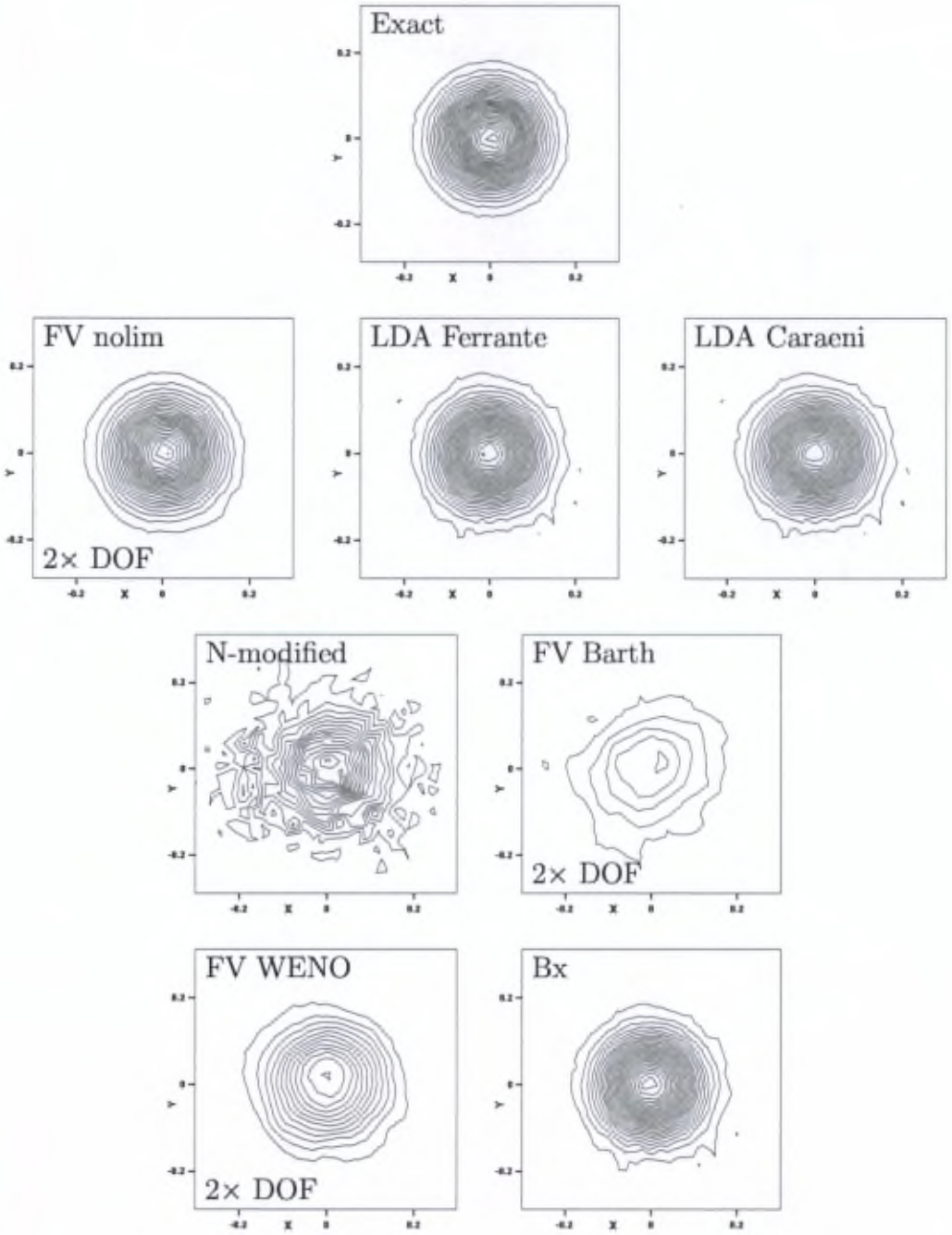


Figure 5.41.: 2D convection of the vortex test case. Isolines of the pressure at $t = 1/6$.

## 5.6. Euler equations – unsteady problems with mesh movement

### 5.6.1. Smooth inviscid flow in a piston (2D)

This case was introduced in [DD05b]. It is motivated by internal aerodynamics problems, namely flow in piston engines. A gas at rest is enclosed between walls. One of the walls slowly starts to move. This problem can be solved by the method of characteristics [ZH76] until the head of the pressure wave reflects from the other wall or a shock is created. We have used a domain of length $l = 5$ and initial conditions $u^0 = 0$, $\rho^0 = 1.4$ and $p^0 = 1$. The piston starts to accelerate with derivative of acceleration $\ddot{x} = 0.2$. The numerical solution is plotted at time $t = 4$, when the piston has reached position $x = 2.13\bar{3}$. The exact solution is included in the appendix A.1, pg. 201.

The mesh consist of 180 nodes and 310 triangular elements for CC FV and 280 nodes and 498 triangular elements for VC FV and RD schemes. The difference in number degrees of freedom is in order of 10 %. The CC1 FV scheme gives similar solution as the N scheme. On the other hand, the LDA scheme gives much better results than the FV scheme with linear reconstruction and no limiter. Two boundary conditions are included, Petrov-Galerkin, section 3.9.2.1, and Paillere's 3.9.2.2 formulation. The both gives almost the same, highly accurate results. The solution using one and two layer N-modified scheme is plotted in Fig. 5.47, 5.48. They both give similar results, much more accurate than the FV scheme with Barth's limiter. There are small wiggles in the vicinity of the moving wall in the very smooth part of the solution. For discussion of this issue we refer again to [Abg06, RA06]. Finally, the Bx scheme and FV scheme with Barth's limited is compared, see Fig. 5.46 and 5.49. Unfortunately, in this case the Bx scheme gives worse result than the FV scheme. It is due to the activation of the N scheme in the compression wave. Better formulation of the blending function would certainly help.

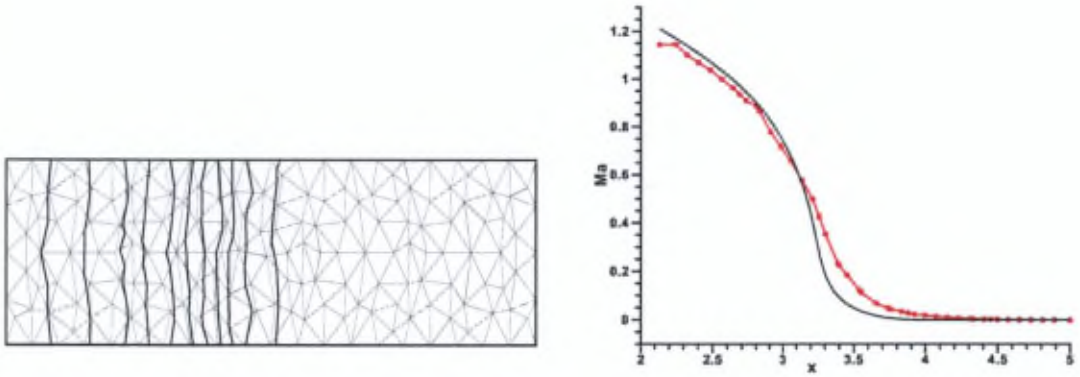


Figure 5.42.: Smooth compression of gas inside a piston cylinder. Mach number isolines and cut along the central line. FV1 scheme, 3BDF time integration procedure.

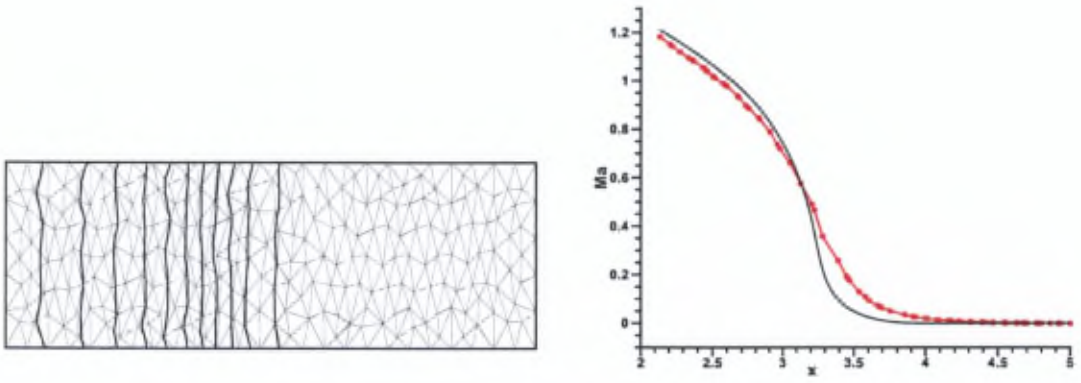


Figure 5.43.: Smooth compression of gas inside a piston cylinder. Mach number isolines and cut along the central line. N scheme 3BDF time integration procedure.

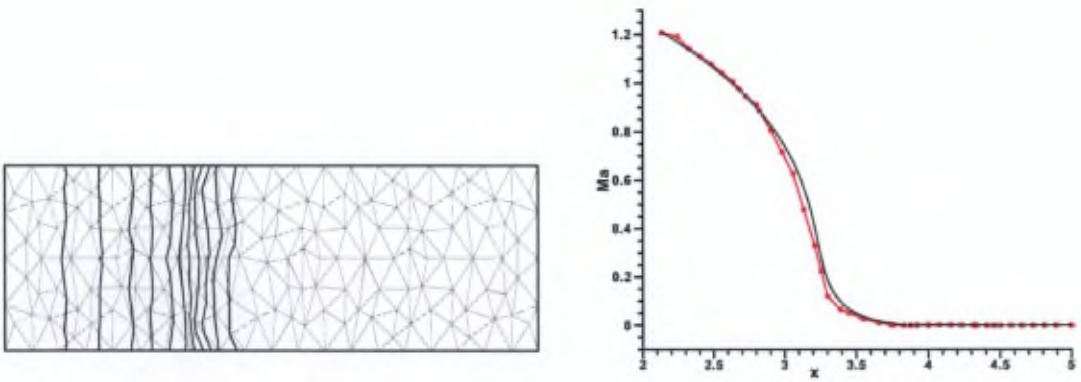


Figure 5.44.: Smooth compression of gas inside a piston cylinder. Mach number isolines and cut along the central line. FV2 scheme, no limiter, 3BDF time integration procedure.

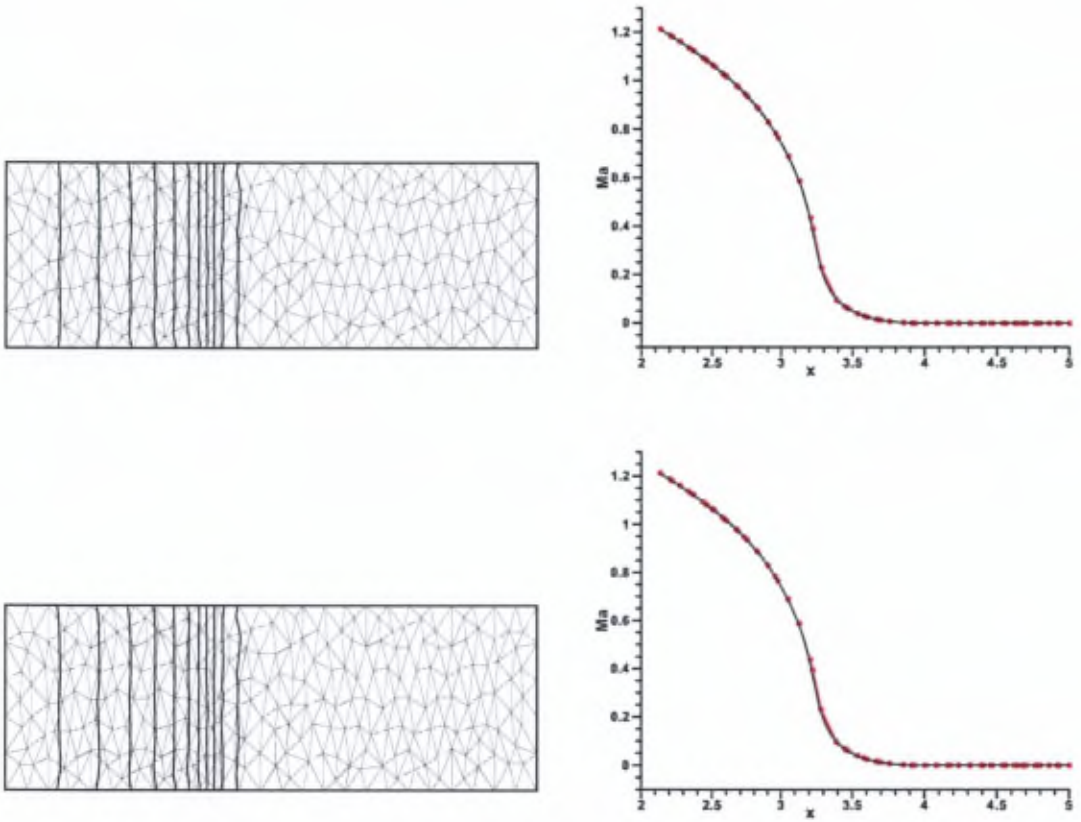


Figure 5.45.: Smooth compression of gas inside a piston cylinder. Mach number isolines and cut along the central line. LDA scheme, 3BDF time integration procedure. Top: Weide's BC, Bottom: Paillere's BC.

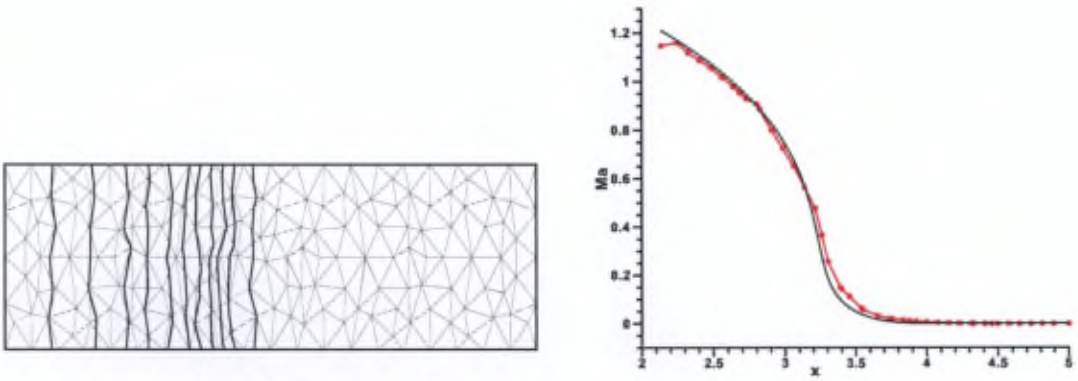


Figure 5.46.: Smooth compression of gas inside a piston cylinder. Mach number isolines and cut along the central line. FV2 scheme, Barth's limiter, 3BDF time integration procedure.

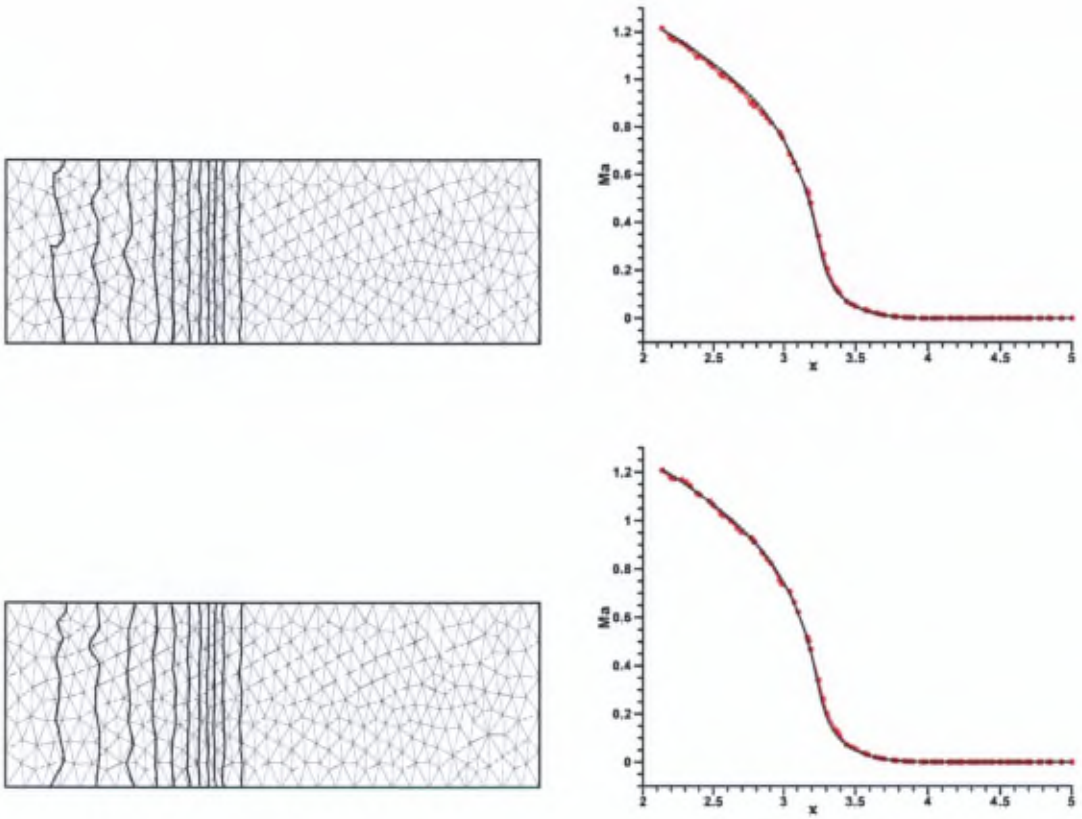


Figure 5.47.: Smooth compression of gas inside a piston cylinder. Mach number isolines and cut along the central line. 1 layer N-modified scheme. Top: Weide's BC, Bottom: Paillere's BC.

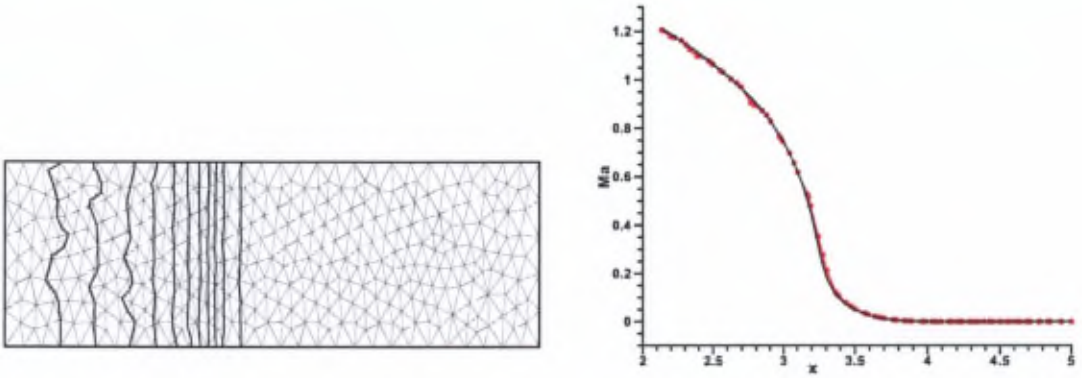


Figure 5.48.: Smooth compression of gas inside a piston cylinder. Mach number isolines and cut along the central line. 2 layer N-modified scheme.

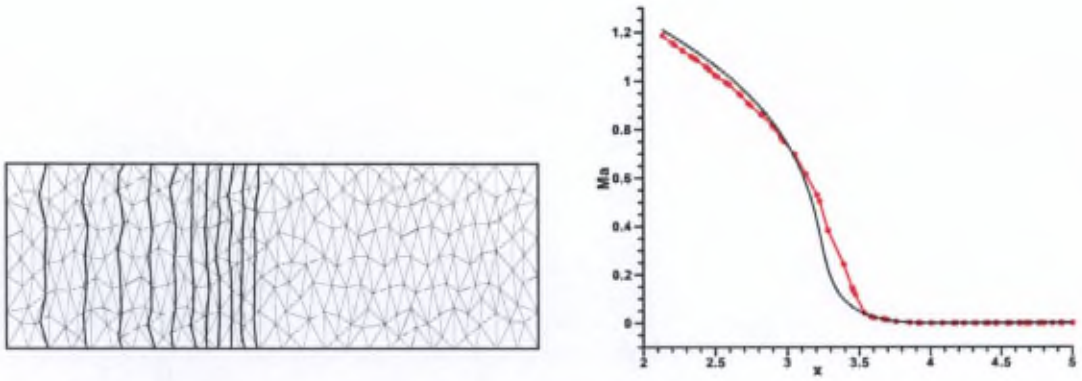


Figure 5.49.: Smooth compression of gas inside a piston cylinder. Mach number isolines and cut along the central line. Bx scheme

### 5.6.2. Inviscid flow in a piston involving a shock (2D)

This problem involves a piston instantaneously accelerated to a uniform speed. From the Rankine-Hugoniot jump conditions we can compute the solution analytically. Piston velocity is chosen 0.8, therefore flow velocity is $u_L = 0.8$, $u_R = 0$, density is $\rho_L = 2.8191$, $\rho_R = 1.4$ and pressure is $p_L = 2.78$, $p_R = 1$. Shock speed is 0.79461. The solution at $t = 2$ is shown. The mesh is the same as in section 5.6.1.

In following figures cuts in the axis of the domain are plotted for Mach number, pressure and Entropy. One can notice a problem with entropic layer in the vicinity of the piston surface. First, compare schemes with constant reconstruction and N scheme. The shock resolution is perfectly monotone. The shock is more smeared for the N scheme than for the FV scheme. There is a slightly higher pressure for the PG formulation of boundary conditions and the shock is in a more advanced position. The spurious entropy generation in the vicinity of the piston is much higher for the Paillere's formulation. In the comparison of the N-modified scheme with the FV scheme with linear reconstruction and Barth's limiter, the N-modified scheme gives sharper resolution of the shock wave. Both the schemes gives monotone resolution of the shock wave. The spurious entropy generation is higher for the Paillere formulation of boundary condition. The two-layer N-modified scheme gives similar results as the one-layer scheme, including the behavior of the spurious entropy layer. Finally, the Bx scheme performs worse than the WLSQR (WENO) scheme, in terms of the shock resolution and also spurious entropy layer. The Bx scheme performs actually the same as the N scheme. The FV scheme performs well, both with Barth's limiter and the WLSQR (WENO) reconstruction. The results obtained with the N scheme and Bx are not so good. Source of relatively poor performance for this type of test case is still has to be investigated. The Paillere formulation of boundary condition depends on the numerical scheme used for the inner element in the domain. As it was noted, for Bx scheme the performance is better than the PG formulation, for the N scheme performs equally, while for the N-modified scheme the performance of the Paillere formulation is substantively worse than the PG formulation.

## 5.7. Conclusions

In this chapter results obtained by the cell centered, vertex centered finite volumes and RD schemes were presented and compared. In all the test cases the LDA scheme was consistently the best. Also the cell centered FV scheme has performed very well. The vertex centered finite volume schemes did not show outstanding result. For the nonlinear schemes, the Bx scheme or the CC FV scheme with linear reconstruction with WLSQR (WENO) weights are among the most accurate. The Barth's limiter appears to be a good choice if a strict monotonicity of the solution is

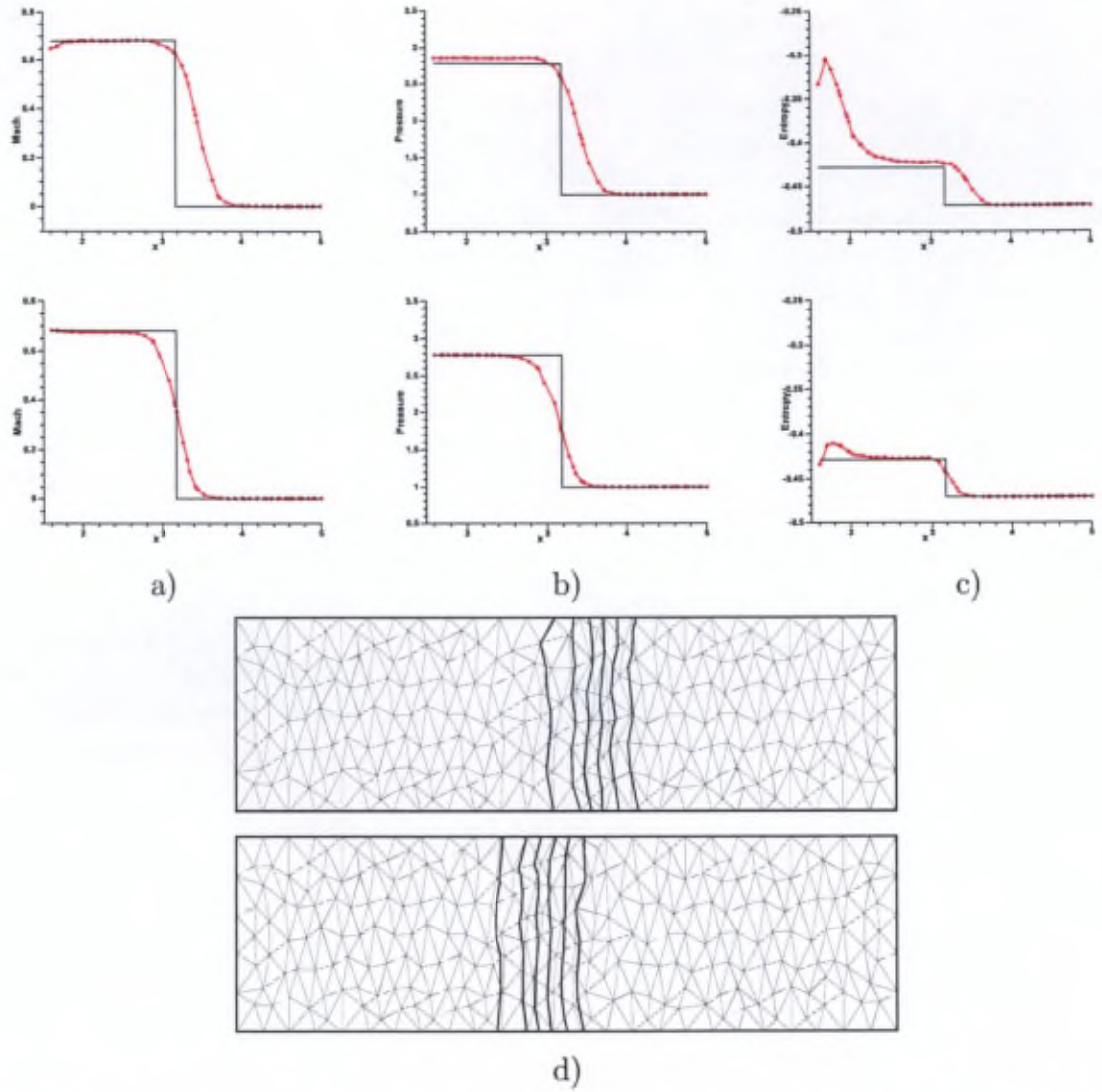


Figure 5.50.: 2D flow near suddenly moving piston. Cuts: a) Mach number, b) static pressure, c) entropy; d) computational mesh and isolines of Mach number. Space-time N scheme. Top: PG boundary conditions, Bottom: Paillere's boundary conditions.

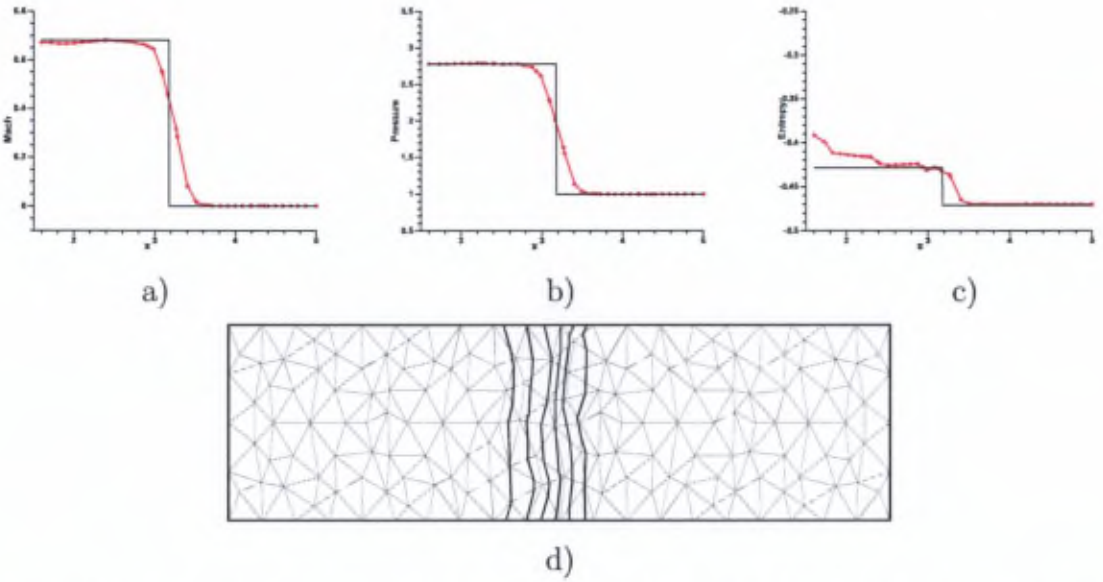


Figure 5.51.: 2D flow near suddenly moving piston. Cuts: a) Mach number, b) static pressure, c) entropy; d) computational mesh and isolines of Mach number. CC FV1 scheme with 3BDF time integration.

needed. Surprisingly, in the opposite to the common findings, the N-modified scheme did not perform very well. It has to be noted, that the nonlinear RD schemes are currently in the focus of intense research.[1]

[1] already for more than 20 years

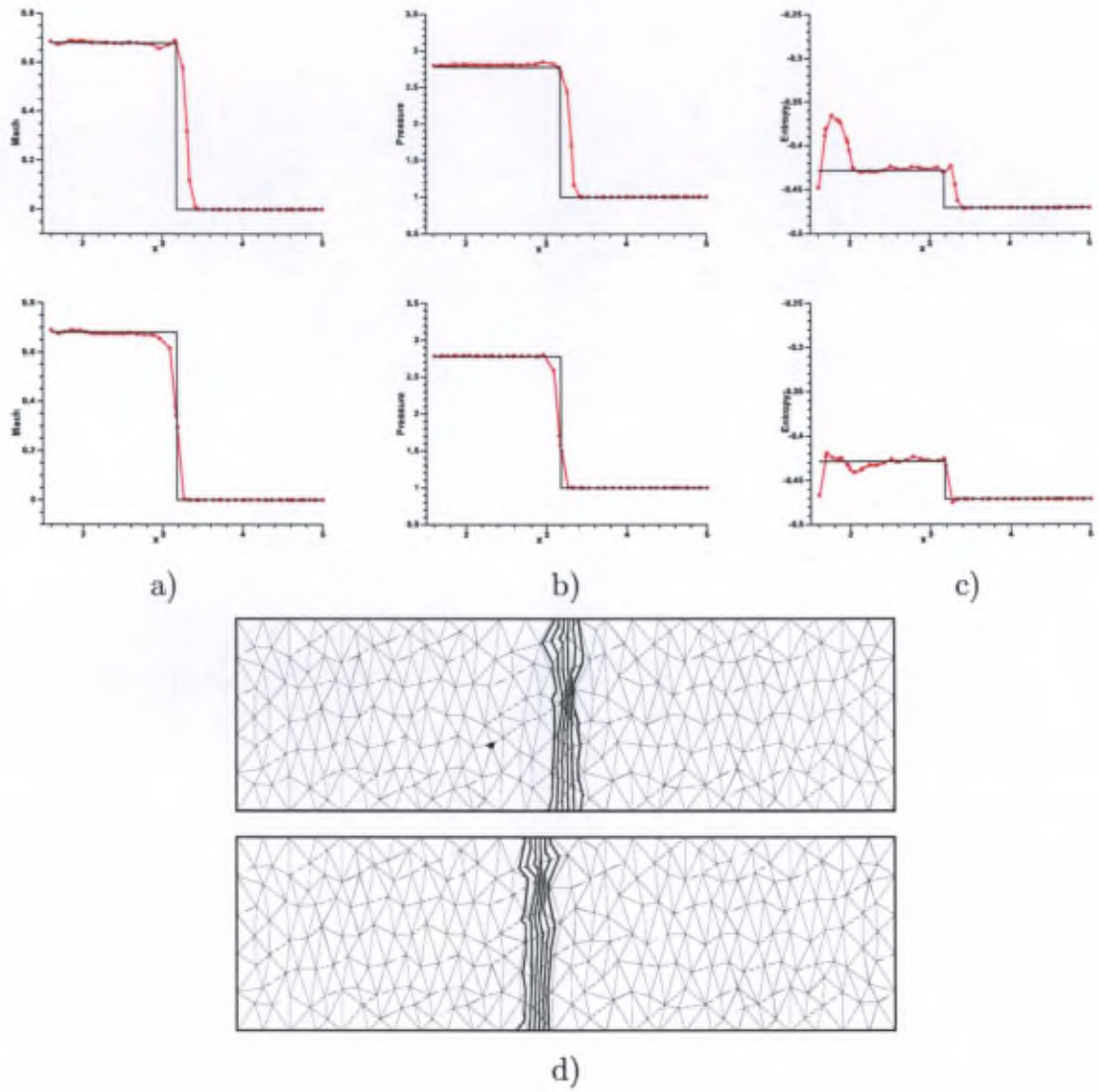


Figure 5.52.: 2D flow near suddenly moving piston. Cuts: a) Mach number, b) static pressure, c) entropy; d) computational mesh and isolines of Mach number. 1 layer space-time N-modified scheme. Top: PG boundary conditions, Bottom: Paillere's boundary conditions.

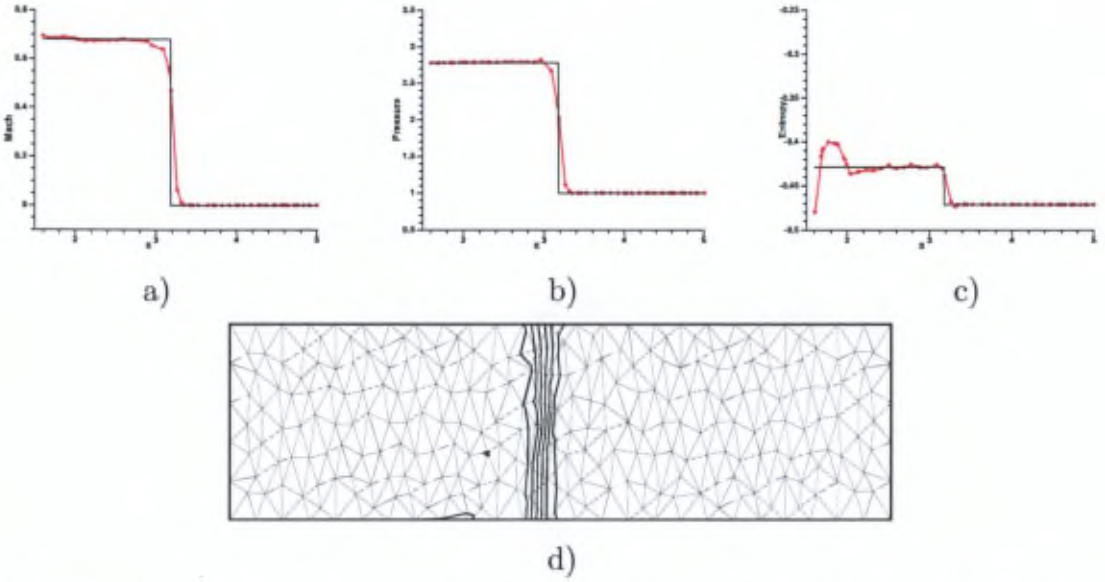


Figure 5.53.: 2D flow near suddenly moving piston. Cuts: a) Mach number, b) static pressure, c) entropy; d) computational mesh and isolines of Mach number. 2 layer space-time N-modified scheme. PG boundary conditions.

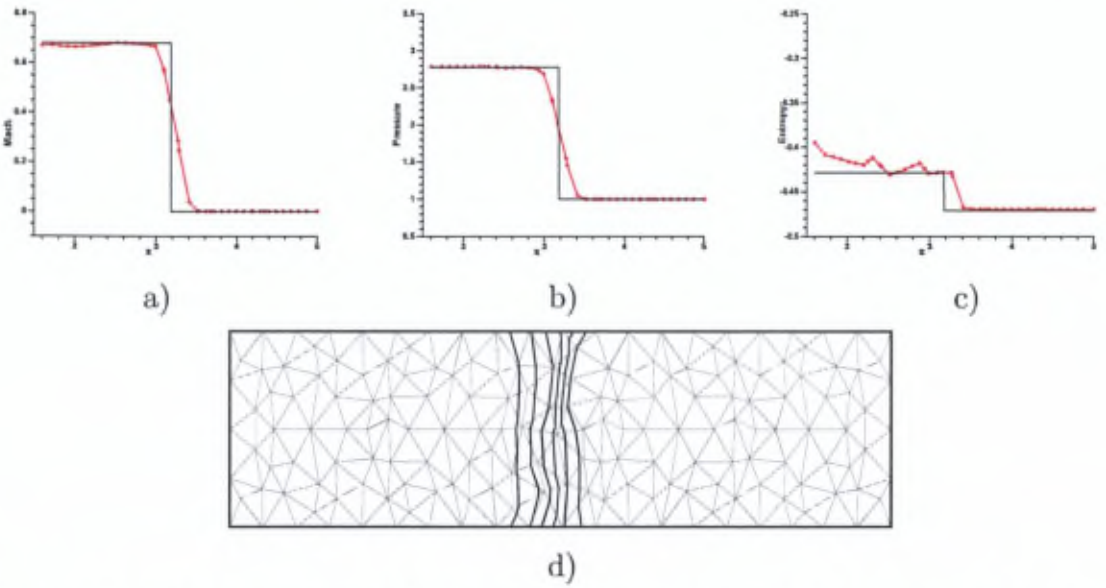


Figure 5.54.: 2D flow near suddenly moving piston. Cuts: a) Mach number, b) static pressure, c) entropy; d) computational mesh and isolines of Mach number. CC FV scheme with Barth's limiter and 3BDF time integration.

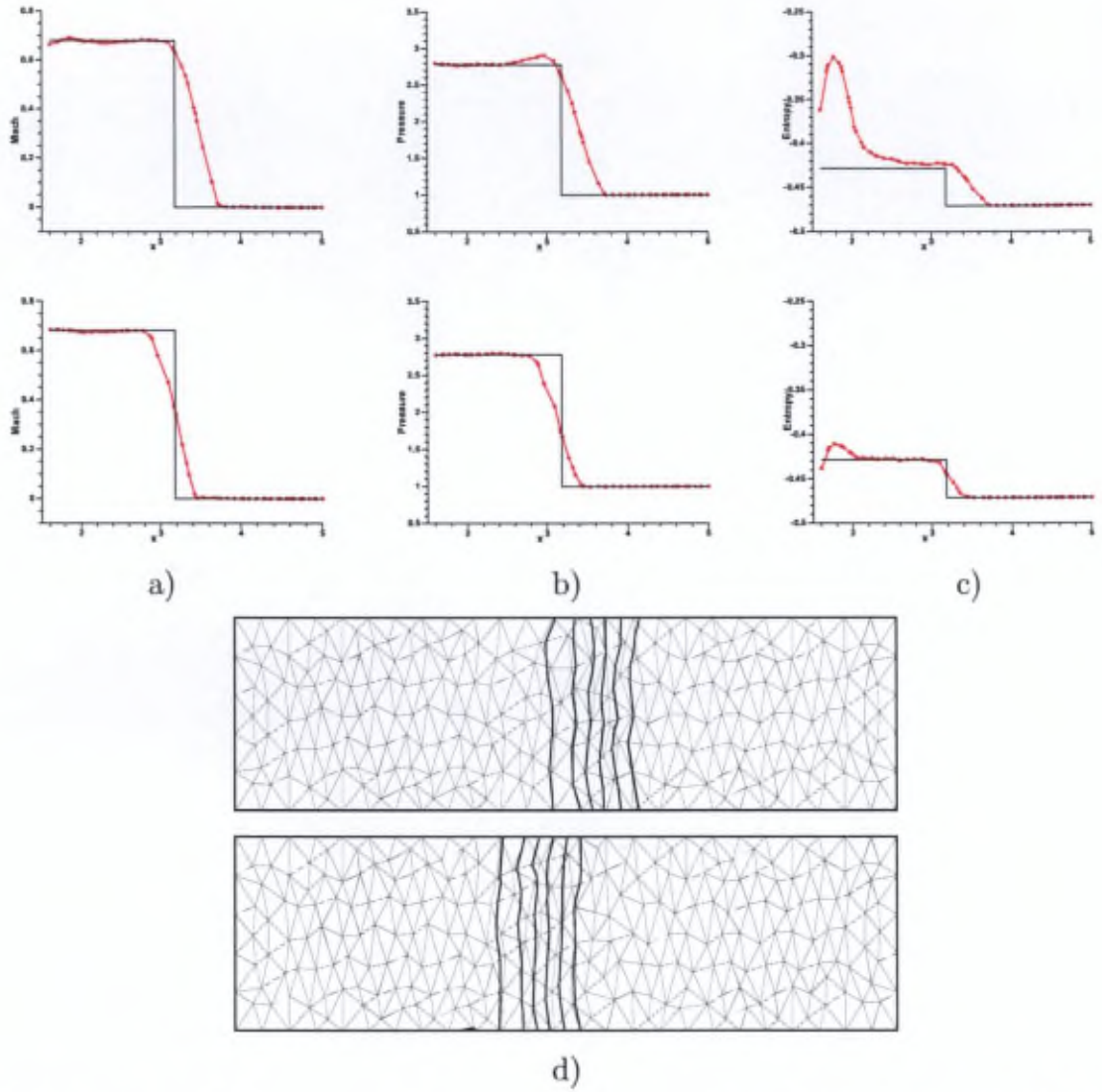


Figure 5.55.: 2D flow near suddenly moving piston. Cuts: a) Mach number, b) static pressure, c) entropy; d) computational mesh and isolines of Mach number. Bx scheme. Top: PG boundary conditions, Bottom: Paillere's boundary conditions.

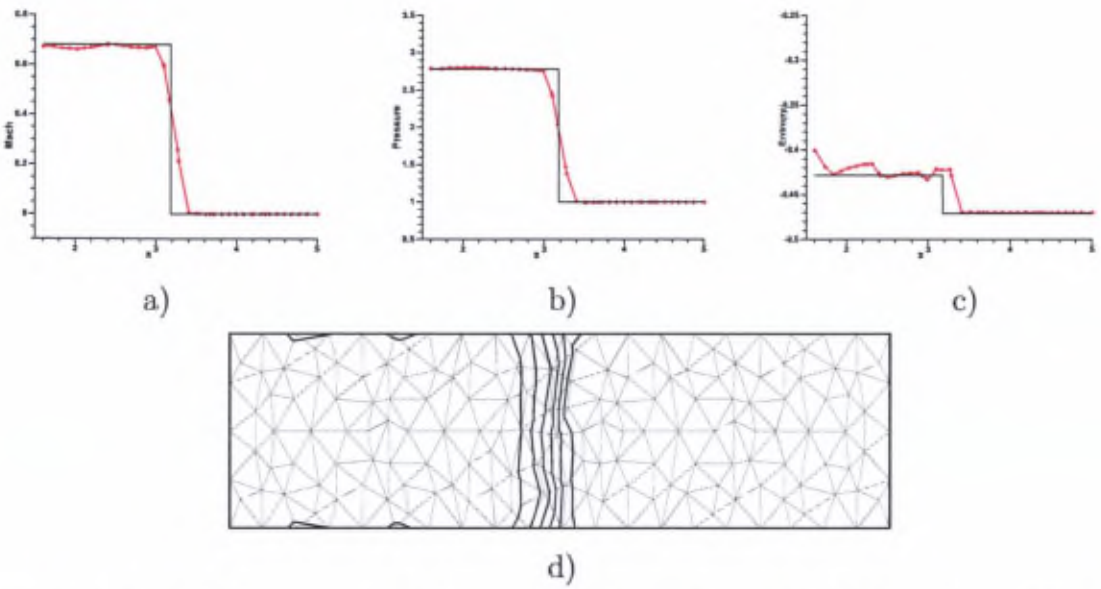


Figure 5.56.: 2D flow near suddenly moving piston. Cuts: a) Mach number, b) static pressure, c) entropy; d) computational mesh and isolines of Mach number. CC FV scheme WENO reconstruction and 3BDF time integration.

# Part II.

# Fluid-structure interaction

# Chapter 6.

# Finite element method for elasticity problems

## 6.1. Introduction

In this section we will derive the equations of elasticity for both small and large displacements. We will start from Newton's law, the stress-strain relation and the generalized Hooke's law, finally leading to second order partial differential equation. Then, we will introduce a finite element method, usually used for the solution of this problem. The chapter concludes with a few examples documenting the performance of the method.

Elastic problems can be also formulated as a set of first order hyperbolic partial differential equations and solved by the method usuallly applied for fluid dynamic problems. However, this formulation is not suitable for the elasticity problems of standard engineering mechanics. It is more usual for the applications, where a shock waves inside the material has to be captured, see e.g. [LeV02]. We will not put forward this approach, although some preliminary test were performed in the framework of RD schemes.

## 6.2. Formulation of the problem

In this section we will derive the general elastic model for finite displacements. We will use a nonlinear finite strain displacement relation. The strain tensor has the form

$$\varepsilon_{ij} = \frac{1}{2}\left(\frac{\partial u_i}{\partial x_j} + \frac{\partial u_j}{\partial x_i} + \frac{\partial u_k}{\partial x_i}\frac{\partial u_k}{\partial x_j}\right), \tag{6.1}$$

where $u_j$ is the displacement in direction $j$ and $k$ is a summation index. The displacement is defined as the difference between the deformed state and the initial state

$$u_i = x_i' - x_i. \tag{6.2}$$

We use a linear relation between the strain $\varepsilon$ and the stress $\sigma$ called (generalized) Hooke's law

$$\sigma_{ij} = c_{ijkl}\varepsilon_{kl}, \tag{6.3}$$

where $c_{ijkl}$ is the elastic tensor. Hooke's law can be expressed for a homogenous isotropic body in the form

$$\sigma_{ij} = \lambda\delta_{ij}\theta + 2\mu\varepsilon_{ij}, \tag{6.4}$$

where $\sigma$ is the stress tensor, $\lambda$ and $\mu$ are Lame parameters, depending on the body material, and $\theta$ is a tensor invariant

$$\theta = \varepsilon_{ii} = \varepsilon_{11} + \varepsilon_{22} + \varepsilon_{33}. \tag{6.5}$$

The dynamic equation for the continuum (Newton's law) is

$$\rho\frac{\partial^2 u_i}{\partial t^2} = \frac{\partial \sigma_{ij}}{\partial x_j} + f_i, \tag{6.6}$$

where $f_i$ is a component of internal (e.g. gravity) force and $\rho$ is material density. Structural damping is not considered.

For the moment, we will consider only homogenous isotropic material. One can substitute the equation for the strain tensor into Hooke's law. We obtain (using Einstein summation convention)

$$\theta = \frac{\partial u_i}{\partial x_i} + \frac{1}{2}\frac{\partial u_i}{\partial x_j}\frac{\partial u_i}{\partial x_j} \tag{6.7}$$

$$\sigma_{ij} = \lambda\delta_{ij}\left[\frac{\partial u_k}{\partial x_k} + \frac{1}{2}\frac{\partial u_k}{\partial x_l}\frac{\partial u_k}{\partial x_l}\right] + \mu\left[\frac{\partial u_i}{\partial x_j} + \frac{\partial u_j}{\partial x_i} + \frac{\partial u_k}{\partial x_i}\frac{\partial u_k}{\partial x_j}\right] \tag{6.8}$$

$$\frac{\partial}{\partial x_j}\left(\lambda\delta_{ij}\left[\frac{\partial u_k}{\partial x_k} + \frac{1}{2}\frac{\partial u_k}{\partial x_l}\frac{\partial u_k}{\partial x_l}\right] + \mu\left[\frac{\partial u_i}{\partial x_j} + \frac{\partial u_j}{\partial x_i} + \frac{\partial u_k}{\partial x_i}\frac{\partial u_k}{\partial x_j}\right]\right) + f_i = \rho\frac{\partial^2 u_i}{\partial t^2}. \tag{6.9}$$

The last equation is in fact a set of second order nonlinear differential equations. One has to note that the equations are nonlinear even though the linear Hooke's law was used, due to the hyphotesis of large deformations.

We now return back to equation (6.6) and derive the weak form of the equation. We have

$$\rho\frac{\partial^2 u_i}{\partial t^2} - \frac{\partial \sigma_{ij}}{\partial x_j} = f_i. \tag{6.10}$$

Multiplying by test function $\varphi$ and integrating over $\Omega$ we obtain

$$\int_\Omega \varphi\rho\frac{\partial^2 u_i}{\partial t^2}\,\mathrm{d}\Omega - \int_\Omega \varphi\frac{\partial \sigma_{ij}}{\partial x_j}\,\mathrm{d}\Omega = \int_\Omega \varphi f_i\,\mathrm{d}\Omega \tag{6.11}$$

$$\int_\Omega \varphi\rho\frac{\partial^2 u_i}{\partial t^2}\,\mathrm{d}\Omega - \oint_{\partial T} \varphi\underbrace{\sigma_{ij}\,\mathrm{d}n_j}_{t_i} + \int_\Omega \frac{\partial \varphi}{\partial x_j}\sigma_{ij}\,\mathrm{d}\Omega = \int_\Omega \varphi f_i\,\mathrm{d}\Omega \tag{6.12}$$

$$\int_\Omega \varphi\rho\frac{\partial^2 u_i}{\partial t^2}\,\mathrm{d}\Omega + \int_\Omega \frac{\partial \varphi}{\partial x_j}\sigma_{ij}\,\mathrm{d}\Omega = \int_\Omega \varphi f_i\,\mathrm{d}\Omega + \oint_{\partial\Omega} \varphi t_i\,\mathrm{d}S, \tag{6.13}$$

where $t_i$ is a traction (load per unit surface) in the direction of the $i$ axis. This formulation leads directly to the matrix representation for the numerical solution. From the first integral a mass matrix arises, from the second a stiffness matrix and the RHS corresponds to the load vector.

Note that the problem is formulated in Lagrangian coordinates, hence no moving mesh is needed.

A fundamental assumption has to be made in two dimensions. Either the strain in the third dimension is zero (and the stress in nonzero) or the stress is nonzero (and the strain is zero). This is called plane stress and plane strain assumption. In a case of plane strain the Lame parameters are related to Young modulus $E$ and Poisson ratio $\nu$ by relations [BSS02]

$$\lambda = \frac{E\nu}{(1+\nu)(1-2\nu)} \qquad \mu = \frac{E}{2(1+\nu)}. \tag{6.14}$$

In case of plane stress the relations are

$$\lambda = \frac{E\,\nu}{1-\nu^2} \qquad \mu = \frac{E}{2(1+\nu)}. \tag{6.15}$$

The Young modulus $E$ and Poisson ratio $\nu$ are tabulated in technical tables for various materials. For the test cases at the end of this chapter, the Poisson ratio will be taken $\nu = 0.3$, as the typical value for steel.

For the 3D orthotropic material Hooke's law has the form

$$\begin{pmatrix}\sigma_{11}\\ \sigma_{22}\\ \sigma_{33}\\ \sigma_{23}\\ \sigma_{31}\\ \sigma_{12}\end{pmatrix} = \begin{pmatrix} c_{11} & c_{12} & c_{13} & 0 & 0 & 0\\ c_{21} & c_{22} & c_{23} & 0 & 0 & 0\\ c_{31} & c_{32} & c_{33} & 0 & 0 & 0\\ 0 & 0 & 0 & 2c_{44} & 0 & 0\\ 0 & 0 & 0 & 0 & 2c_{55} & 0\\ 0 & 0 & 0 & 0 & 0 & 2c_{66}\end{pmatrix}\begin{pmatrix}\varepsilon_{11}\\ \varepsilon_{22}\\ \varepsilon_{33}\\ \varepsilon_{23}\\ \varepsilon_{31}\\ \varepsilon_{12}\end{pmatrix}. \tag{6.16}$$

The constants are related to Young modulus $E_{ij}$, shear modulus $G_{ij}$ and Poisson

ratio $\nu_{ij}$ by the coefficients

$$c_{11} = \frac{1 - \nu_{23}\,\nu_{23}}{E_{22}\,E_{33}\,D} \qquad c_{12} = \frac{\nu_{12} + \nu_{13}\,\nu_{23}}{E_{22}\,E_{33}\,D} \qquad c_{13} = \frac{\nu_{13} + \nu_{12}\,\nu_{23}}{E_{22}\,E_{33}\,D} \tag{6.17}$$

$$c_{22} = \frac{1 - \nu_{13}\,\nu_{13}}{E_{11}\,E_{33}\,D} \qquad c_{23} = \frac{\nu_{23} + \nu_{13}\,\nu_{12}}{E_{11}\,E_{33}\,D} \qquad c_{33} = \frac{1 - \nu_{12}\,\nu_{12}}{E_{11}\,E_{22}\,D} \tag{6.18}$$

$$c_{44} = G_{23} \qquad c_{55} = G_{13} \qquad c_{66} = G_{12} \tag{6.19}$$

with

$$D = \frac{1 - \nu_{12}\,\nu_{12} - \nu_{23}\,\nu_{23} - \nu_{13}\,\nu_{13} - 2\,\nu_{12}\,\nu_{23}\,\nu_{13}}{E_{11}\,E_{22}\,E_{33}}. \tag{6.20}$$

Then, an equation similar to (6.9) is derived.

The two types of boundary conditions are considered – traction and displacement. In the case of displacement, the value on the boundary is prescribed (Dirichlet's boundary condition). In the case of traction, the force per unit length is prescribed, which is term $t_i$ in equation (6.13).

## 6.3. Numerical method for steady problems

The domain of solution is covered by finite elements. The displacement $u_i$ in the $i$-direction is approximated by the trial functions as

$$u_i^h = \sum_{k \in T^h} u_{i,k} \psi_k. \tag{6.21}$$

The trial functions will be specified later. The test functions belong to the same space as the trial functions. Hereafter we will not make a distinction between trial and test functions. The weak formulation (6.13) gives directly the finite element method, where the solution is replaced by its approximation (6.21) and the test functions by the trial functions $\psi$. The problem can be written as

$$\mathbf{M}\ddot{U} + \mathbf{K}U = F, \tag{6.22}$$

where $U$ is the algebraic vector of unknowns (displacements), $\mathbf{M}$ is the mass matrix, $\mathbf{K}$ is the stiffness matrix and $F$ the vector of right hand sides.

### 6.3.1. Selection of elements and spatial integration

The trial function has to be chosen suitably. We use simple Lagrangian elements [ZT00b], with linear, bilinear or quadratic approximation of the solution and linear or bilinear approximation of the geometry. The elements, where the geometry is approximated by the lower order polynomial, while the solution is approximated by the higher order polynomial are called sub-parametric. We have chosen (bi-)linear

Figure 6.1.: Finite elements in 2D. Left: linear TRI3 element. Middle: bilinear QUAD4 element. Right: biquadratic sub-parametric element QUAD9, the solution is approximated with 9 DOF, the geometry with 4 DOF.

approximation of the geometry, since the mesh generation software we use does not support higher order elements[1]. The 2D elements are depicted in Fig. 6.1. Similar elements were used in three spatial dimensions, i.e. 4 node linear TETRA4, 8 node tri-linear HEXA8 and 27 nodes tri-quadratic HEXA27 elements. The method is very general and other types of elements (trial functions) can be simply added.

The contributions to the mass and stiffness matrix have the form of integrals over the elements. The trial function can be expressed directly in the spatial variables, or the element can be transformed to the mother element and integrated in the transformed system of coordinates [ZT00b]. In that case, we use Gauss quadrature with sufficient number of quadrature points. On the bilinear element transformed to the square $[-1,1] \times [-1,1]$ we use four Gauss points located at points with coordinates given by the tensor product of $(-\sqrt{1/3}, \sqrt{1/3})$. For bi-quadratic element we use nine Gauss points identified by the tensor product of $(-\sqrt{0.6}, 0, \sqrt{0.6})$. The procedure is standard, we include it with a reference to [ZT00b] or any other finite element textbook.

For the large displacement formulation, the quadratic terms have to be computed. We use Picard approximation (also called direct iteration method), i.e. quadratic terms are approximated as independent of the solution, and the solution is taken from the previous iteration. The influence of the large displacement vs. small displacement formulation is depicted in Fig. 6.2.

## 6.3.2. Approximations of boundary conditions

The displacement boundary condition corresponds imposing directly the nodal value of the solution. In this case, we discard the corresponding line in the $\mathbf{K}$ matrix and set unit on the diagonal. Then we set the right hand side to the prescribed nodal value.

[1] Although a on purpose code to improve mesh can be easily written.

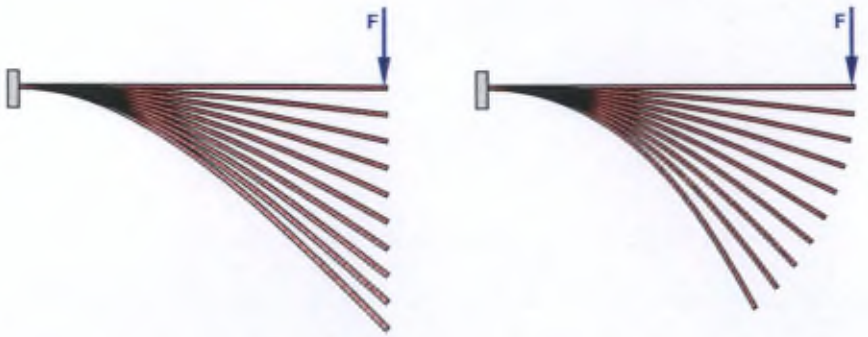


Figure 6.2.: Linear (the left) and nonlinear (right), large deformation formulation. Bending of a beam. Sequence of beams loaded with increasing force is shown.

Consider node $k$. For the prescribed traction $t_i$ in direction of $i$ on the boundary, the line (surface integral in 3D)

$$\int_S \varphi_k t_i \, \mathrm{d}\vec{n}_i \tag{6.23}$$

has to be evaluated. This value is then added to the RHS of the equation.

For steady problems (e.g. static aeroelasticity) the mass and time dependent part of equation (6.22) is omitted ($\mathbf{M} \equiv 0$) and the problem reduces to solving the sparse system of algebraic equations

$$\mathbf{K}U = F. \tag{6.24}$$

For the moment we use GMRES with ILU(0) preconditioning, or block Jacobi preconditioning in parallel, where the ILU(0) preconditioner is applied on each block. A second option is the LU decomposition.

## 6.4. Numerical method for unsteady problems and modal analysis

### 6.4.1. Newmark method

For time dependent (dynamic) problems we have to consider the full system of (6.22). This semi-discrete ODE can be solved by the Newmark family of methods. In this method the function and its first time derivative are approximated according

| $\alpha$ | $\gamma = 2\beta$ | |
|---|---|---|
| 1/2 | 1/2 | the constant-average acceleration method (stable) |
| 1/2 | 1/3 | the linear acceleration method (conditionally stable) |
| 1/2 | 0 | the central difference method (conditionally stable) |
| 3/2 | 8/5 | the Galerkin method (stable) |
| 3/2 | 2 | the backward difference method (stable) |

Table 6.1.: Special case of choice of parameters among the Newmark family of methods.

to

$$U^{n+1} = U^n + \Delta t \dot{U}^n + \frac{1}{2}\Delta t^2 \ddot{U}^{n+\gamma}$$
$$= U^n + \Delta t \dot{U}^n + \frac{1}{2}\Delta t^2 \gamma \ddot{U}^{n+1} + \frac{1}{2}\Delta t^2 (1-\gamma)\ddot{U}^n. \quad (6.25)$$

and

$$\dot{U}^{n+1} = \dot{U}^n + \Delta t \ddot{U}^{n+\alpha} = \dot{U}^n + \alpha \Delta t \ddot{U}^{n+1} + (1-\alpha)\Delta t \ddot{U}^n. \quad (6.26)$$

Different schemes are obtained for special choices of the parameters $\alpha$ and $\gamma$, as summarized in Tab. 6.1. From equation (6.25) we express $\ddot{U}^{n+1}$ and plug it into equation (6.22). When all the terms from the level $n$ are moved to the RHS, one gets

$$\hat{\mathbf{K}} U^{n+1} = \hat{F}, \quad (6.27)$$

with

$$\hat{\mathbf{K}} = \mathbf{K} + a_3 \mathbf{M} \quad (6.28)$$
$$\hat{F} = F + \mathbf{M}(a_3 U^n + a_4 \dot{U}^n + a_5 \ddot{U}^n), \quad (6.29)$$

and

$$a_1 = \alpha \Delta t \qquad a_2 = (1-\alpha)\Delta t \qquad a_3 = \frac{2}{\gamma \Delta t^2} \quad (6.30)$$

$$a_4 = \frac{2}{\gamma \Delta t} \qquad a_5 = \frac{1}{\gamma} - 1. \quad (6.31)$$

Once solution $U^{n+1}$ is obtained, the velocity and acceleration are computed using

$$\ddot{U}^{n+1} = a_3 (U^{n+1} - U^n) - a_4 \dot{U}^n - a_5 \ddot{U}^n \quad (6.32)$$
$$\dot{U}^{n+1} = \dot{U}^n + a_2 \ddot{U}^n + a_1 \ddot{U}^{n+1}, \quad (6.33)$$

these relations are equations (6.25) and (6.26) again. In all the work we use the unconditionally stable constant-average acceleration method ($\alpha = \gamma = 1/2$), which is known to preserve energy of the body.

### 6.4.2. Modal analysis

For the problems of fluid-structure interaction, we are interested in periodic or nearly periodic movement of the elastic bodies. These kind of problems are typically solved by modal analysis. The modal analysis is needed also for the setup of initial conditions for the AGARD 445.6 test case, see section 8.3.2 page 185.

We are looking for a solution in the form

$$U = \sum_m U_m e^{-i\omega_m t} \tag{6.34}$$

of the homogeneous equation

$$\mathbf{M}\ddot{U} + \mathbf{K}U = 0. \tag{6.35}$$

This leads to a generalized eigen-problem

$$\omega_m^2 \mathbf{M}U_m + \mathbf{K}U_m = 0. \tag{6.36}$$

This problem is much easier to solve than the eigen-problem of the matrix $(\mathbf{M}^{-1}\mathbf{K})$, because both mass and stiffness matrices are sparse while $(\mathbf{M}^{-1}\mathbf{K})$ is not. The Arnoldi method [HRV03, HRTV04] is used to solve the problem. The eigenvalues and eigenvectors are real, the frequency of the mode is

$$f_m = \frac{1}{2\pi\sqrt{\lambda_m}}. \tag{6.37}$$

The eigenvectors directly correspond to the displacement. There are as many eigen-pairs as degrees of freedom, but we consider only the first few relevant eigen-modes. For the better performance of the eigen-solver, the mass matrix $\mathbf{M}$ and stiffness matrix $\mathbf{K}$ can be scaled such that the entries are close to one. Of course, the eigenvalues have to be later scaled back.

## 6.5. Numerical results

In this section a few numerical results documenting the performance of the method will be shown.

All the considered elements are able to exactly reproduce pure stretch and shear, in the small and large deformation formulation. The bend is a surprisingly more difficult test case. We consider a beam clamped on one side of length $l = 10$ with uniform thickness $h = 0.1$. The bending force on the other end of the beam is chosen such that the deflection is unit. The small deformation formulation is used. The solution on different meshes and elements is plotted in Fig. 6.3. The results are given in Tab. 6.2. The error of the solution on linear and bilinear elements is

| Mesh (DOF) | TRI3 | QUAD4 | QUAD9 |
|---|---|---|---|
| 2×40 | 0.032 | 0.093 | 0.997 |
| 2×100 | 0.161 | 0.390 | 1 |

Table 6.2.: Linear bending of a beam. Deflection ($z$) of the end of the beam for different elements and meshes. Exact solution is $z = 1$.

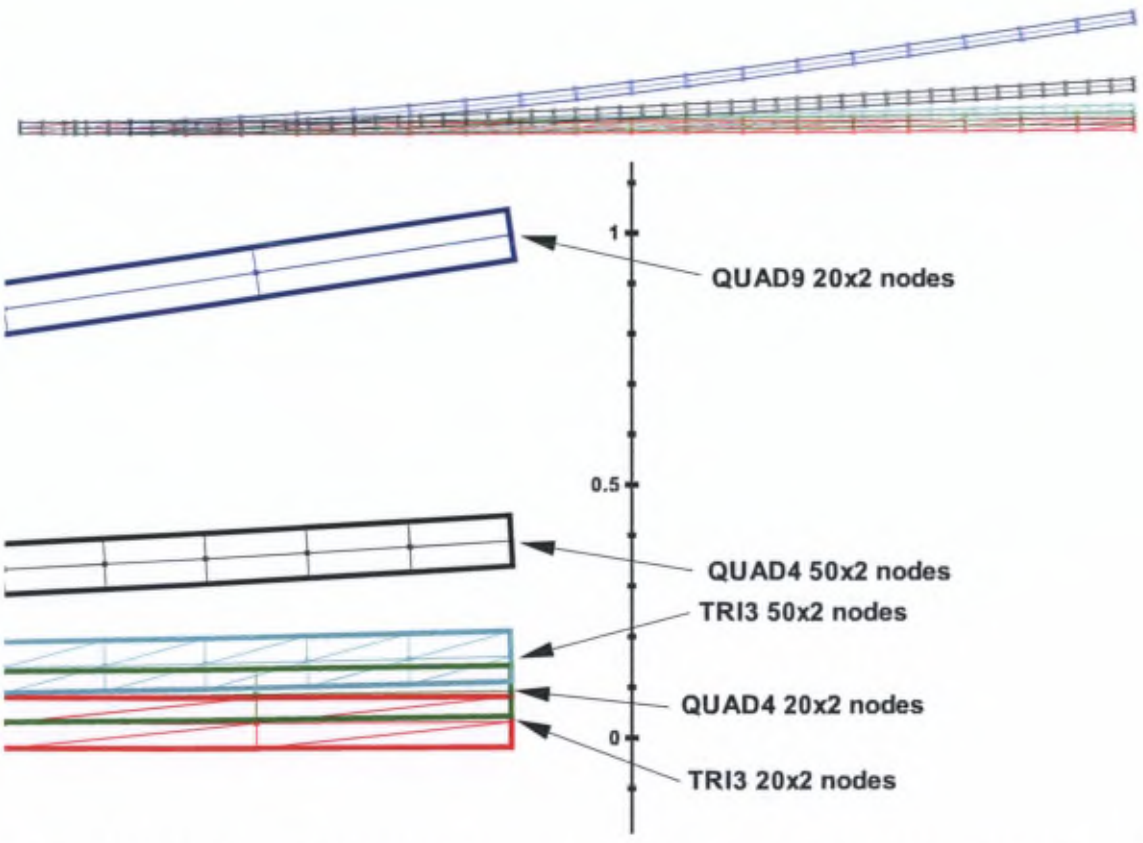


Figure 6.3.: Linear bending of a beam. Plot of the solution and zoom to the end of the beam. Exact solution is $z = 1$. Different elements are considered.

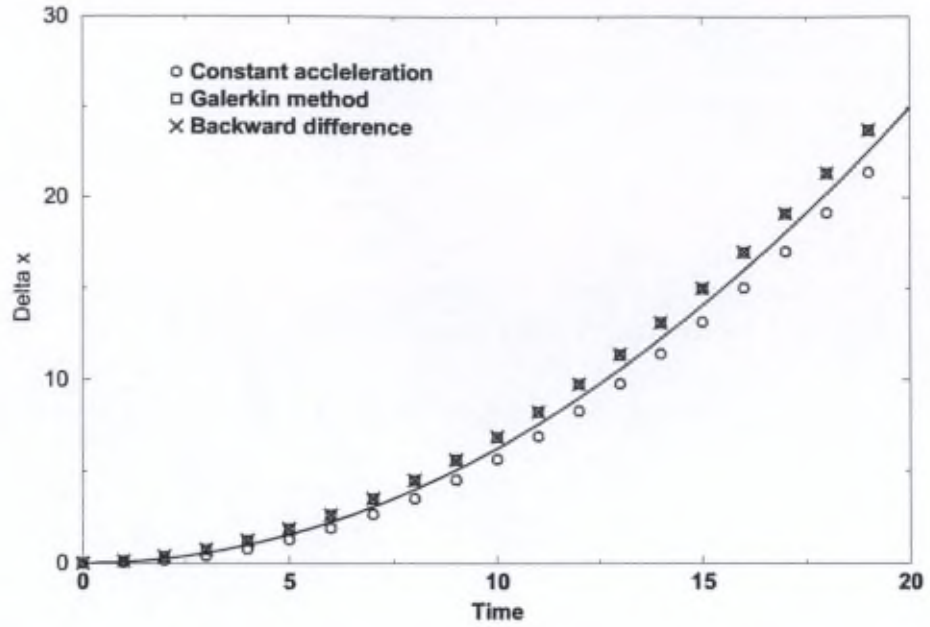


Figure 6.4.: Comparison of the time integration methods. Force accelerating a free body. For definition of schemes see Tab. 6.1.

so high, that the method cannot be used for engineering applications. The method using bi-quadratic elements gives reasonable accuracy for the considered case.

The second test case consist of one element with very large stiffness ($E = 10^{15}$) and unit mass. The unit force starts to accelerate the body according to Newton's law. The numerical solution with different parameters of Newmark's method together with the exact solution is plotted in Fig. 6.4. Only unconditionally stable methods were considered. One can clearly see the discretization error of the scheme and the need for sufficiently small time-steps. In the future, the extension for higher order time integration scheme should be considered.

The last test case involves a modal analysis of a beam. We consider a 3D beam of dimensions $10 \times 0.15 \times 0.1$, clamped on one side and free elsewhere. Young modulus is $E = 2$ and density $\rho = 5$. The mesh is rather coarse consisting of $10 \times 1 \times 1$ tri-quadratic HEX27 elements. Natural frequencies obtained from 1D theory and the modal analysis are compared in Tab. 6.3. The theoretical values [BSS02] are

$$\omega_m = \frac{m_n^2}{l^2}\sqrt{\frac{Eh^2}{12\rho}}, \tag{6.38}$$

where $m_n$ are roots of equation

$$\cos m \cosh m = -1. \tag{6.39}$$

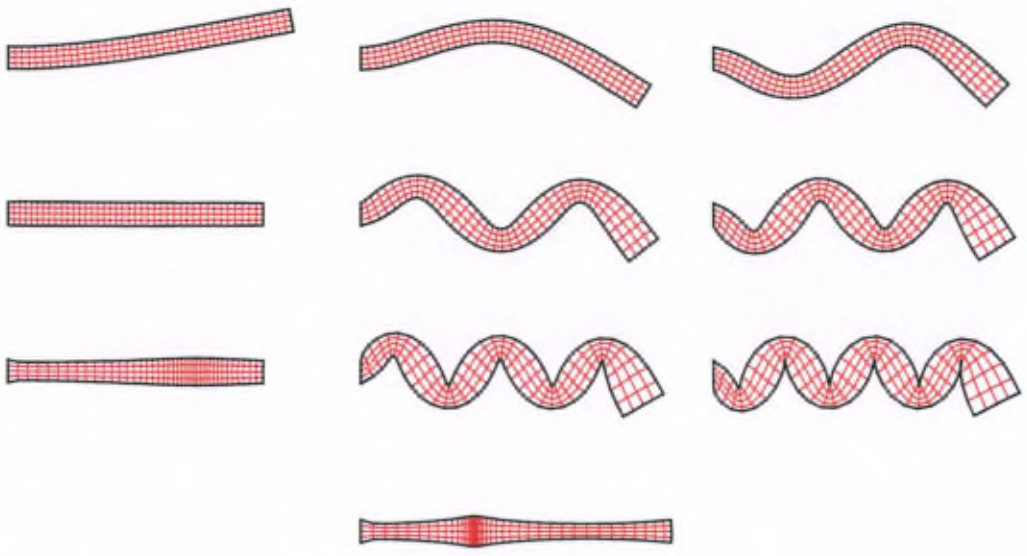

Figure 6.5.: Modal analysis of 2D beam. First 10 modes plotted.

| | From 1D theory | From modal analysis |
|---|---|---|
| 1st bending mode – $y$ | $6.41 \cdot 10^{-4}$ | $6.47 \cdot 10^{-4}$ |
| 1st bending mode – $z$ | $9.62 \cdot 10^{-4}$ | $9.70 \cdot 10^{-4}$ |
| 2nd bending mode – $y$ | $40.24 \cdot 10^{-4}$ | $40.97 \cdot 10^{-4}$ |
| 2nd bending mode – $z$ | $60.36 \cdot 10^{-4}$ | $61.31 \cdot 10^{-4}$ |

Table 6.3.: Modal analysis of a 3D beam. Natural frequencies.

The first three roots are approximately $m_1 = 1.8751$, $m_2 = 4.6941$, $m_3 = 7.8548$. One can see that even on such a coarse mesh, the error is in the order of 1 % for the first mode and less than 2 % for the second mode. Modal shapes for a similar problem in 2D are potted in Fig. 6.5.

# Chapter 7.

# Numerical method for fluid–structure interaction problems

The problem of the interaction of fluids and solid bodies is characterized essentially by two distinct, but intrinsically coupled problems. The numerical methods for problems of fluid dynamic (CFD) were discussed in the first part of this thesis, the numerical methods for elastic bodies (CSM) were discussed in chapter 6. In this chapter a method to couple both problems will be discussed.

## 7.1. Three field formulation

If the amplitude of the structural body movement is small, the coupled problem can be solved using the simple transpiration approach [HKH03, HKH04b, HKH04a]. However, if the deformation is larger, the problem has to be solved on a moving mesh [Far04]. The three field formulation was introduced in [LF93]. The three distinct fields involve CFD, CSM and the fluid mesh deformation as the third field.

- CFD is coupled with the CSM via position and velocity of the computational domain. It is also intrinsically coupled to the mesh dynamics.
- CSM is coupled to CFD by the stress tensor on the surface of the body
- The position and velocity of the mesh boundary is coupled to the position and velocity of the surface of the body.

We will discuss the coupling of CFD and CSM by the movement of the mesh boundary and transfer of the stress tensor in section 7.2. The mesh deformation algorithm for a given position of the nodes on the boundary is treated in section 7.3.

### 7.1.1. Formulation of the FSI problem

Let us recall once again the problem to solve. For the gas, we solve the system of Euler equations in ALE formulation (introduced as (2.26)) in a time dependent

domain $\Omega_{t,\text{fluid}}$,

$$\frac{1}{J_{\mathcal{A}_t}} \frac{\partial J_{\mathcal{A}_t} \mathbf{u}}{\partial t}\bigg|_{\vec{y}} + \vec{\nabla}_x \cdot [\vec{\mathbf{f}}(\mathbf{u}) - \mathbf{u}\vec{w}] = 0, \qquad \forall x \in \Omega_{t,\text{fluid}}, \quad t \in [0, T_{\max}] \tag{7.1}$$

with conserved variables

$$\mathbf{u} = (\rho, \rho\vec{v}, E), \tag{7.2}$$

see section 2.3.2. The determinant of Jacobian $J_{\mathcal{A}_t}$ is defined by (2.8) and the domain velocity $\vec{w}$ by (2.10). The flux is given by

$$\mathbf{f}_i = (\rho v_i, \rho v_i v_j + \delta_{ij} p, [E + p] v_i), \qquad 1 \leq j \leq d. \tag{7.3}$$

The system is closed by the equation for the pressure (introduced as (2.33))

$$E = \frac{p}{\gamma - 1} + \frac{1}{2}\rho \sum_{i=1}^{d} v_i^2 \tag{7.4}$$

with given ratio of specific heats $\gamma$. A standard set of boundary conditions on $\partial\Omega_{t,\text{fluid}}$ is used. Specifically, the velocity of the gas perpendicular to the wall is equal to the normal velocity of the wall.

The other system of equations is the dynamic equation for the continuum in a Lagrangian system of reference

$$\rho \frac{\partial^2 \hat{u}_i}{\partial t^2} = \frac{\partial \sigma_{ij}}{\partial \hat{x}_j} + f_i, \qquad \forall \vec{\hat{x}} \in \Omega_{\text{elastic}}, \quad t \in [0, T_{\max}]. \tag{7.5}$$

The hat ($\hat{\cdot}$) is used to distinguish the Lagrangian coordinate of the elastic body and to prevent conflict in the notation in this section. The displacement is defined as the difference between the deformed state and the initial state

$$\hat{u}_i = \hat{x}'_i - \hat{x}_i. \tag{7.6}$$

The stress is related to the strain tensor by the generalized Hooke's law

$$\sigma_{ij} = c_{ijkl} \varepsilon_{kl}, \tag{7.7}$$

where $c_{ijkl}$ is a given elastic tensor. Tensor of deformation is defined as

$$\varepsilon_{ij} = \frac{1}{2}\left(\frac{\partial \hat{u}_i}{\partial \hat{x}_j} + \frac{\partial \hat{u}_j}{\partial \hat{x}_i} + \frac{\partial \hat{u}_k}{\partial \hat{x}_i}\frac{\partial \hat{u}_k}{\partial \hat{x}_j}\right), \tag{7.8}$$

where $\hat{u}_j$ is the displacement in direction $j$.

The systems (7.1) and (7.5) are connected by the interface conditions relating the displacement of the elastic body with the fluid boundary

$$x_{\text{fluid}} = \hat{x}'_{\text{elastic}}, \tag{7.9}$$

for all the fluid boundaries $\partial\Omega_{t,\text{fluid,wall}}$ immersing the elastic bodies and for all the elastic boundaries $\partial\Omega_{\text{elastic,wet}}$ immersed in the fluid. Similarly, the forces has to be equal from the both sides of the interface

$$p\,\vec{n}_{\text{fluid}} = \vec{f}, \tag{7.10}$$

where $\vec{n}_{\text{fluid}}$ is the outer normal on the fluid boundary and $\vec{f}$ is the normal force acting on the elastic body.

Finally, the ALE mapping $\mathcal{A}_t$ (see equation (2.6)) has to be found, such that the condition (7.9) is satisfied.

The problem is the following: find $\mathbf{u} : \Omega_{t,\text{fluid}} \times [0, T_{\max}] \to \mathbb{R}^q$, $\mathcal{A}_t : \Omega_{0,\text{fluid}} \times [0, T_{\max}] \to \Omega_{t,\text{fluid}}$ and $\vec{\hat{u}} : \Omega_{\text{elastic}} \times [0, T_{\max}] \to \mathbb{R}^d$ such that all the equations in this section are simultaneously satisfied.

## 7.2. Coupling of fluid and structural problems – load and motion transfer algorithm

For the aeroelastic computations, there is a ultimate need to treat non-matching interfaces. A non-matching interface is an interface between fluid and structural computational mesh, where the boundary points do not coincide. The non-matching interface allows to generate the mesh independently for fluid and structural problem and both the meshes can be tailored to their specific needs. Here we follow work of [FLL98, Far04].

The computation of the fluid mesh boundary displacement proceeds as follows (see Fig. 7.1). For each node on the fluid boundary, the projection to the elastic boundary along the normal is found. Then, the displacement of the fluid boundary node is assumed equal to the displacement of the projected node to the solid boundary. The displacement is determined using the trial functions of the finite element method $\psi_i$, which is used in the elastic body solver from the known displacement at the nodes of the solid mesh element. This gives later needed coefficients $c_{ij}$. This approach gives smooth variation of the fluid mesh boundary, since it uses quadratic polynomials for the interpolation (provided the quadratic finite elements for the elastic solver are used). Another advantage is, that the displacement is computed exactly for rigid body motion, which might not be the case for some other methods.

The force on the boundary of the elastic body is prescribed from the equality of virtual works. Virtual work performed by the fluid is

$$\delta W^F = \int_{\Gamma_F} -p\,\vec{n} \cdot \vec{u}_F \,\mathrm{d}s, \tag{7.11}$$

where $\Gamma_F$ is the fluid boundary, $p$ is the pressure, $\vec{n}$ is the normal to the fluid boundary and $\vec{u}_F$ is the virtual displacement of the fluid boundary. The virtual work

performed by the elastic body can be expressed as the sum of the nodal displacements and the nodal forces

$$\delta W^S = \int_{\Gamma_S} \vec{f} \cdot \vec{u}_S \, \mathrm{d}s = \sum_{i=1}^{i=i_S} \vec{f}_i \cdot \vec{u}_{S_i}, \tag{7.12}$$

where $\vec{f}_i$ is the force at node $i$ and $\vec{u}_{S_i}$ is the displacement of the node $i$. Both expressions of the virtual work have to be equal

$$\int_{\Gamma_F} -p\vec{n} \cdot \vec{u}_F \, \mathrm{d}s = \sum_{i=1}^{i=i_S} \vec{f}_i \cdot \vec{u}_{S_i}. \tag{7.13}$$

The fluid boundary displacement depends on the displacement of the boundary nodes

$$\vec{u}_F = \vec{u}_F(\vec{u}_{1,F}, \vec{u}_{2,F}, \ldots, \vec{u}_{n,F}). \tag{7.14}$$

The displacement of the fluid boundary node can be expressed as the linear combination of the elastic boundary node displacements

$$\vec{u}_{i,F} = \sum_j c_{ij} \vec{u}_{S_j}. \tag{7.15}$$

Combining equations (7.13), (7.14), (7.15) and eliminating the solid boundary node displacement $u_{S_j}$ we get the expression for the nodal forces $\vec{f}_i$ acting on the elastic body. In our case, the boundary is a polygon and we approximate the integral on the left hand side of equation (7.13) with the trapezoidal integration rule

$$\int_{\Gamma_F} -p\vec{n} \cdot \vec{u}_F \, \mathrm{d}s \approx \sum_e \frac{S_e}{n_e} \sum_{k=1}^{n_e} -p_k \vec{n}_e \cdot \vec{u}_{k,F}, \tag{7.16}$$

where $n_e$ is the number of nodes on boundary face $e$, $S_e$ is the surface of the boundary face $e$, $p_k$ is the pressure at node $k$, $\vec{n}_e$ is a normal to the face $e$ and $\vec{u}_{k,F}$ is the displacement of node $k$. If we plug relation (7.15) into (7.16) and (7.13) we get

$$\sum_e \frac{S_e}{n_e} \sum_{k=1}^{n_e} -p_k \vec{n}_e \cdot \sum_j c_{kj} \vec{u}_{S_j} = \sum_{i=1}^{i=i_S} \vec{f}_i \cdot \vec{u}_{S_i}, \tag{7.17}$$

where the index $e$ loops over all the fluid boundary faces. This has to be valid for any $\vec{u}_{S_i}$, hence

$$\vec{f}_i = \sum_j c_{ij} \sum_e \frac{S_e}{n_e} \sum_{k=1}^{n_e} -p_k \vec{n}_e, \tag{7.18}$$

where the index $j$ loops over all the nodes with nonzero $c_{ij}$ and index $e$ for all boundary faces containing node $j$.

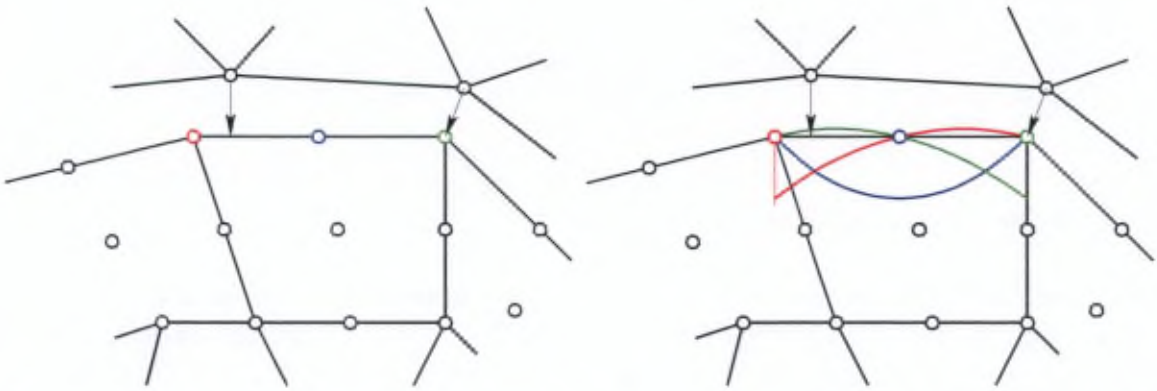

Figure 7.1.: Fluid boundary movement algorithm. Upper mesh is fluid, lower is elastic body.

## 7.3. Mesh deformation algorithm

Many different strategies were developed for the mesh movement [YM05, JT96, JT94, Far04]. The problem reads: given a nodal displacement on the part of the boundary, find a displacement of the remaining nodes in the computational domain. We have chosen the pseudo-elasticity approach, where the mesh moves according to the behavior of the pseudo-elastic body [Far04, YM05]. Displacement of the mesh vertices is described by the equation

$$\mathbf{K}U = F, \tag{7.19}$$

where $\mathbf{K}$ is the fictious stiffness matrix, $U$ is the algebraic vector of nodal displacements and $F$ is the algebraic vector of nodal forces. We omit the time derivative in equation (6.22). Equations (7.19) and (6.22) gives comparable results, while equation (6.22) has more parameters (element masses) and the method is more computationally demanding. We solve the same system as equation (6.24), with the method described in chapter 6. The Young modulus is chosen such that the stiffness increases in the vicinity of problematic regions [YM05, JT96, JT94]. We have chosen the Young modulus in element $T$ as

$$E = \frac{1}{\sqrt{d\,\mu(T)}}, \tag{7.20}$$

where $d$ is the distance of the centroid of the element to the nearest wall and $\mu(T)$ is the volume of the element. For viscous flow simulations, the Young module has to depend also on the aspect ratio of the element to ensure a good behavior of the method in the wake. The stiffness matrix $\mathbf{K}$ is evaluated in each time step based on the deformed state from the previous step, as the algorithm gives better mesh quality [Far04].

The nodal displacement is prescribed on the wall, the zero traction is prescribed at the free stream. The numerical approximation of the boundary conditions is described in section 6.3.2.

## 7.4. The solution procedure

The problem of fluid-structure interaction is coupled and the fluid flow and structural dynamics have to be solved together. One possibility is to make one step by the fluid solver and one step by the structural method, however an error of order $\mathcal{O}(\Delta t)$ is then introduced into the solution. The discussion about different approaches is given by reference [Far04]. We use a very simple sub-iteration approach. For every time–step (i.e. from the solution at time-level $n$ to the solution at time-level $n+1$) we perform the following procedure:

- Compute preliminary nodal forces at the nodes of the elastic boundary, see eq. 7.18, from the CFD solution at time $n$.
- Do until converged:
  - Compute new (preliminary) position of the elastic body at time level $n+1$.
  - Move the CFD mesh to the preliminary position at time level $n+1$.
  - Compute the corresponding flow field solving the CFD problem on the preliminary mesh position at time level $n+1$.
  - Compute the nodal forces at the nodes of the elastic boundary, see eq. 7.18, from the preliminary CFD solution at time $n+1$.
- Advance elastic body position and the flow field ($n \rightarrow n+1$).

The advantage of this approach is the accuracy, the obvious disadvantage is the long computational time and in some cases convergence problems [MvBdB04]. On the other hand, we use the CFD method formulated in dual time, which is solved by the sub-iteration approach anyway. We perform sub-iterations until the residual of the CFD method drops sufficiently low.

We have developed one method to solve the elastic problem, one mesh motion algorithm and one load/motion transfer algorithm. Since this thesis is focused mainly on CFD methods development, we employ several methods for the CFD side of the fluid–structure interaction problem. These CFD methods are specified for each test case separately.

## 7.5. Numerical tests: load/motion transfer algorithm and mesh deformation algorithm

The first test case involves the mesh deformation algorithm. This test documents the behavior of the method near the boundary and also the possibility to get an invalid mesh with negative volumes of the elements. A two-dimensional hybrid mesh was generated around the double circular arc profile, see Fig. 7.2. The chanel width is chosen $d = 1$, with length of $l = 3$ and the 10 % thick profile has chord of $c = 1$. The mesh is used only for this test case, we do not solve the fluid flows on it. In Fig. 7.2 a) the non-deformed mesh is depicted. Fig. 7.2 b) shows the deformation of the mesh for the profile rotated by $\alpha = 20°$ , with zoom of the trailing edge region in 7.2 g). This mesh is valid, i.e. all the element volumes remain positive. Note the behavior of the wake region, the term to increase the stiffness of the elements in the wake is not included. The possibility to obtain mesh with negative volumes of the elements is documented in Fig. 7.2 c). A zoom of the trailing edge region is depicted in 7.2 g). Unfortunately, negative mesh volumes can be obtained also by a simple translation of the profile, as can be seen in Fig. 7.2 e) and f). The zoom of the problematic region is depicted in Fig. 7.2 h). The mesh movement procedure is still an open problem [JT96, JT94] and even the state of the art approaches remesh from time to time in case of very large displacements [SBTP01, TO01b, TO01a, KT00, SBK+00].

We assess the performance of the non-matching load and motion transfer algorithm in two dimensions. A membrane of length $l = 30$ and thickness $h = 0.1$ with Young modulus $E = 2$ is exposed to the pressure difference, created by the fluid in the rest from one side and the prescribed traction from the other side. The pressure from the fluid side is set to $p = 12.4 \cdot 10^{-6}$, while the ambient pressure is set to $p = 6.2 \cdot 10^{-6}$. Plane stress assumption is used. Two lateral thirds of the membrane are rigidly supported and both sides are clamped, see Fig. 7.3. The formulation of the problem is given in Section 6.2, page 149, the computational method in Section 6.3, page 152. The regular fluid mesh contains $250 \times 17$ elements and the elastic mesh contains $100 \times 1$ bi-quadratic QUAD9 elements. The problem is solved in parallel on 22 processors. This is only to test the parallel algorithm, the whole computation takes a few seconds on one processor. The theoretic displacement in the middle of the membrane, computed from the 1D beam theory, is $z = 1$. One can observe a smooth variation of the fluid boundary, as it can be expected. The computed displacement is $z = 1.013$, giving the error of the order of 1 %.

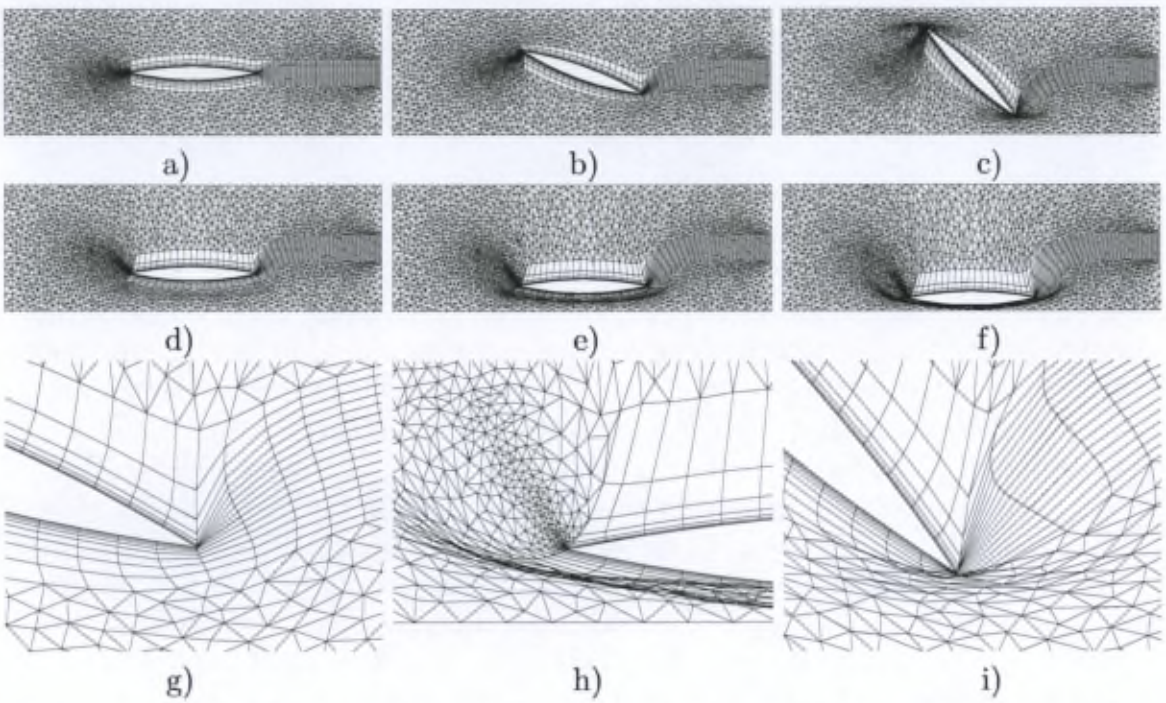


Figure 7.2.: Hybrid mesh deformation test. a) Initial mesh. b) $\alpha = 20°$ , c) $\alpha = 45°$ . d) $\Delta z = 20$ %, e) $\Delta z = 30$ %, f) $\Delta z = 40$ % of the chanel width. g) Detail for $\alpha = 20°$ . h) Detail for $\Delta z = 40$ %. i) Detail for $\alpha = 45°$ . The meshes for cases $\Delta z = 20$ % and $\alpha = 20°$ are valid and the meshes for case $\Delta z = 30$ %, $\Delta z = 40$ % and $\alpha = 45°$ are invalid.

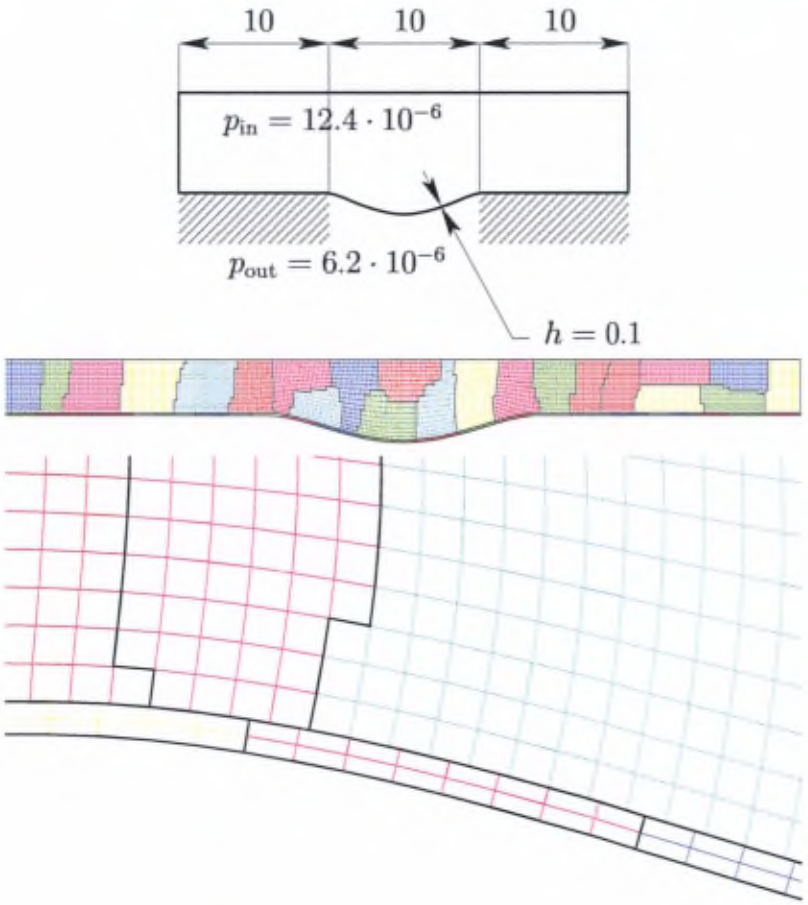


Figure 7.3.: Solution of the membrane problem, solution on 22 processors, interprocessor boundaries are emphasized.

# Chapter 8.

# Numerical results for complex fluid-structure interaction problems

## 8.1. Transonic flutter of NACA 64A010 airfoil

Some parts of this section were published in [DDF05b].

### 8.1.1. Introduction

In this section we present a solution of the interaction of the fluid with a two dimensional airfoil profile. We present results of a well known test case, namely a transient response of the NACA 64A010 profile. The case corresponds to the typical section of a large transport aircraft with swept wings. The problem was investigated in [Iso79, Iso80, Iso81] and later widely used as a test case for fluid-structure interaction problems (see e.g. [AJ94]).

### 8.1.2. Formulation of the problem

We consider a rigid body with two degrees of freedom $h$ and $\alpha$. The following system for large displacements is considered [SFH05, Hor03]

$$m\ddot{h} + k_{hh}h + S_\alpha \ddot{\alpha}\cos\alpha - S_\alpha \dot{\alpha}^2 \sin\alpha = -L(t) \tag{8.1}$$

$$S_\alpha \ddot{h}\cos\alpha + I_\alpha \ddot{\alpha} + k_{\alpha\alpha}\alpha = M(t), \tag{8.2}$$

where

$L(t)$ [N] aerodynamic force (upwards positive),
$M(t)$ [N m] is aerodynamic torsional moment (clockwise positive),
$m$ [kg] mass of the airfoil,
$S_\alpha$ [kg m] static moment around the elastic axis,
$I_\alpha$ [kg m$^2$] inertia moment around the elastic axis,
$k_{hh}$ [N/m] bending stiffness
$k_{\alpha\alpha}$ [N m/rad] torsional stiffness

$\alpha$ [rad] rotational displacement around the elastic axis (clockwise positive), and
$h$ [m] vertical displacement of the elastic axis (downward positive).
Geometric position of the elastic axis is given.
The system is transformed into first order system using $h_d = \dot{h}$ and $\alpha_d = \dot{\alpha}$

$$\begin{pmatrix} m & S_\alpha \cos\alpha & 0 & 0 \\ S_\alpha \cos\alpha & I_\alpha & 0 & 0 \\ 0 & 0 & 1 & 0 \\ 0 & 0 & 0 & 1 \end{pmatrix} \begin{pmatrix} \dot{h}_d \\ \dot{\alpha}_d \\ \dot{h} \\ \dot{\alpha} \end{pmatrix} = \begin{pmatrix} -k_{hh}h + S_\alpha \alpha_d^2 \sin\alpha - L(t) \\ -k_{\alpha\alpha}\alpha + M(t) \\ h_d \\ \alpha_d \end{pmatrix} \tag{8.3}$$

Inverting the matrix, the following system of equation arises

$$\dot{h}_d = \frac{I_\alpha}{D^*} L^* - \frac{S_\alpha \cos\alpha}{D^*} M^* \tag{8.4}$$

$$\dot{\alpha}_d = -\frac{S_\alpha \cos\alpha}{D^*} L^* + \frac{m}{D^*} M^* \tag{8.5}$$

$$\dot{h} = h_d \tag{8.6}$$

$$\dot{\alpha} = \alpha_d \tag{8.7}$$

with

$$D^* = I_\alpha m - S_\alpha^2 \cos^2\alpha \tag{8.8}$$

$$L^* = -k_{hh}h + S_\alpha \alpha_d^2 \sin\alpha - L(t) \tag{8.9}$$

$$M^* = -k_{\alpha\alpha}\alpha + M(t). \tag{8.10}$$

If the deformations are small, the system simplifies to

$$\dot{h}_d = \frac{I_\alpha}{\tilde{D}^*} \tilde{L}^* - \frac{S_\alpha}{\tilde{D}^*} \tilde{M}^* \tag{8.11}$$

$$\dot{\alpha}_d = -\frac{S_\alpha}{\tilde{D}^*} \tilde{L}^* + \frac{m}{\tilde{D}^*} \tilde{M}^* \tag{8.12}$$

$$\dot{h} = h_d \tag{8.13}$$

$$\dot{\alpha} = \alpha_d \tag{8.14}$$

with

$$\tilde{D}^* = I_\alpha m - S_\alpha^2 \tag{8.15}$$

$$\tilde{L}^* = -k_{hh}h - L(t) \tag{8.16}$$

$$\tilde{M}^* = -k_{\alpha\alpha}\alpha + M(t). \tag{8.17}$$

System (8.1), (8.2) can be also written as

$$\mathbf{M}\ddot{y} + \mathbf{K}y = F, \tag{8.18}$$

with

$$\mathbf{M} = \begin{pmatrix} m & S_\alpha \\ S_\alpha & I_\alpha \end{pmatrix}, \quad \mathbf{K} = \begin{pmatrix} k_{hh} & 0 \\ 0 & k_{\alpha\alpha} \end{pmatrix}, \quad y = \begin{pmatrix} h \\ \alpha \end{pmatrix}, \quad F = \begin{pmatrix} -L \\ M \end{pmatrix}, \tag{8.19}$$

where $\mathbf{M}$ is the mass matrix and $\mathbf{K}$ is the stiffness matrix.

The dynamics of the profile is coupled with the fluid flow by lift and moment; the fluid problem is coupled to the profile dynamics by position and velocity of the profile. The problems cannot be solved separately, they are intrinsically coupled.

### 8.1.3. Numerical method

The problem consist of two subproblems: flow field and profile dynamics. The sub-iteration method is used to couple both subproblems.

We use an ALE extension of the FV method with three point backward time integration scheme, see section 4.3.2, with modified Roe's Riemann solver [Roe81] and linear reconstruction with Barth's limiter [BJ89].

The system of first order ODEs (8.4)–(8.7) for the profile dynamics is solved by the standard 4th order Runge-Kutta method

$$k_1 = f(y^n) \qquad k_2 = f(y^n + \Delta t\, k_1/2)$$
$$k_3 = f(y^n + \Delta t\, k_2/2) \qquad k_4 = f(y^n + \Delta t\, k_3)$$

$$y^{n+1} = y^n + \frac{1}{6}\Delta t(k_1 + 2k_2 + 2k_3 + k_4). \tag{8.20}$$

For every time–step (i.e. from solution at time-level $n$ to solution at time-level $n+1$) we perform following procedure:

- Compute the lift $L(\mathbf{u}^n)$ and moment $M(\mathbf{u}^n)$
- Do until converged:
  - Compute new (preliminary) position of the airfoil using RK4 ($h^* = f(L, M, h^n, \alpha^n, L^n, M^n)$, $\alpha^* = f(L, M, h^n, \alpha^n, L^n, M^n)$)
  - Move CFD mesh ($h^*$, $\alpha^*$)
  - Compute corresponding flow field $\mathbf{u}^* = f(h^*, \alpha^*)$
  - Compute lift $L = f(\mathbf{u}^*)$ and moment $M = f(\mathbf{u}^*)$
- Advance airfoil position ($h^{n+1} = h^*$, $\alpha^{n+1} = \alpha^*$) and the flow field ($\mathbf{u}^{n+1} = \mathbf{u}^*$)

The sub-iteration procedure exactly conserves momentum and energy.

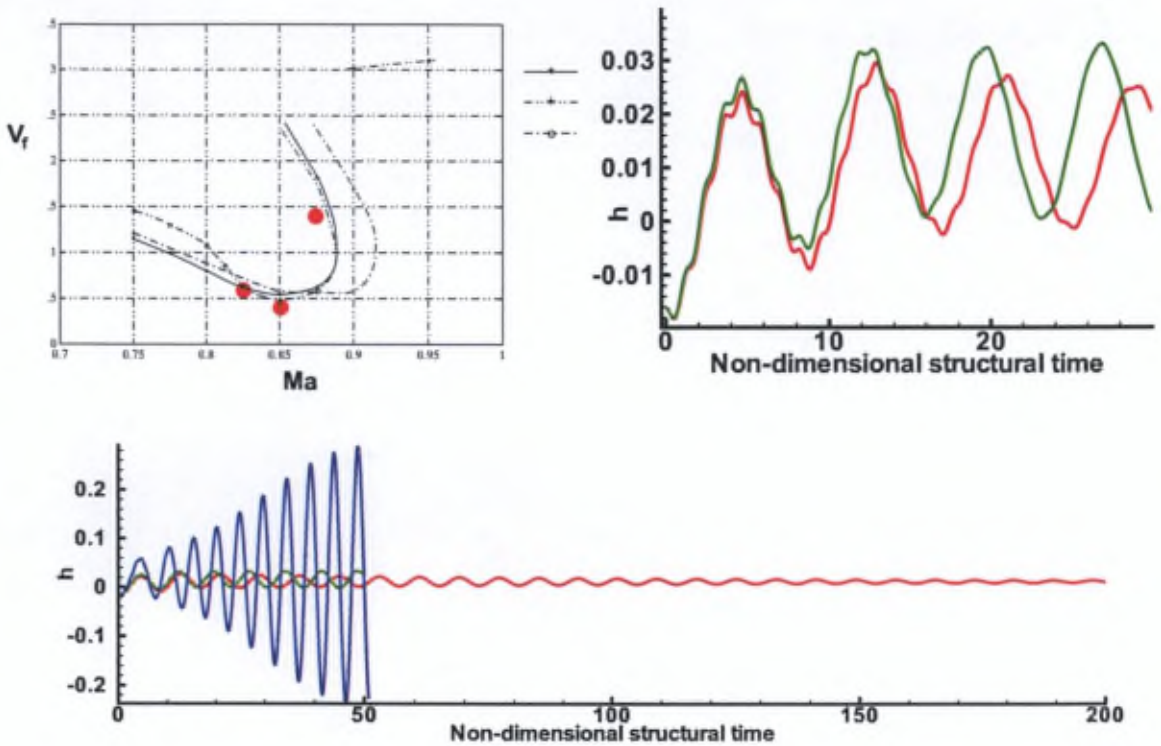


Figure 8.1.: Upper left: trace of zero damping (taken from [AJ94]) with selected cases. Upper right: zoom on indefinite and damped regime. Bottom: dependence of hinge $h$ on time. FV scheme with linear reconstruction and Barth's limiter.

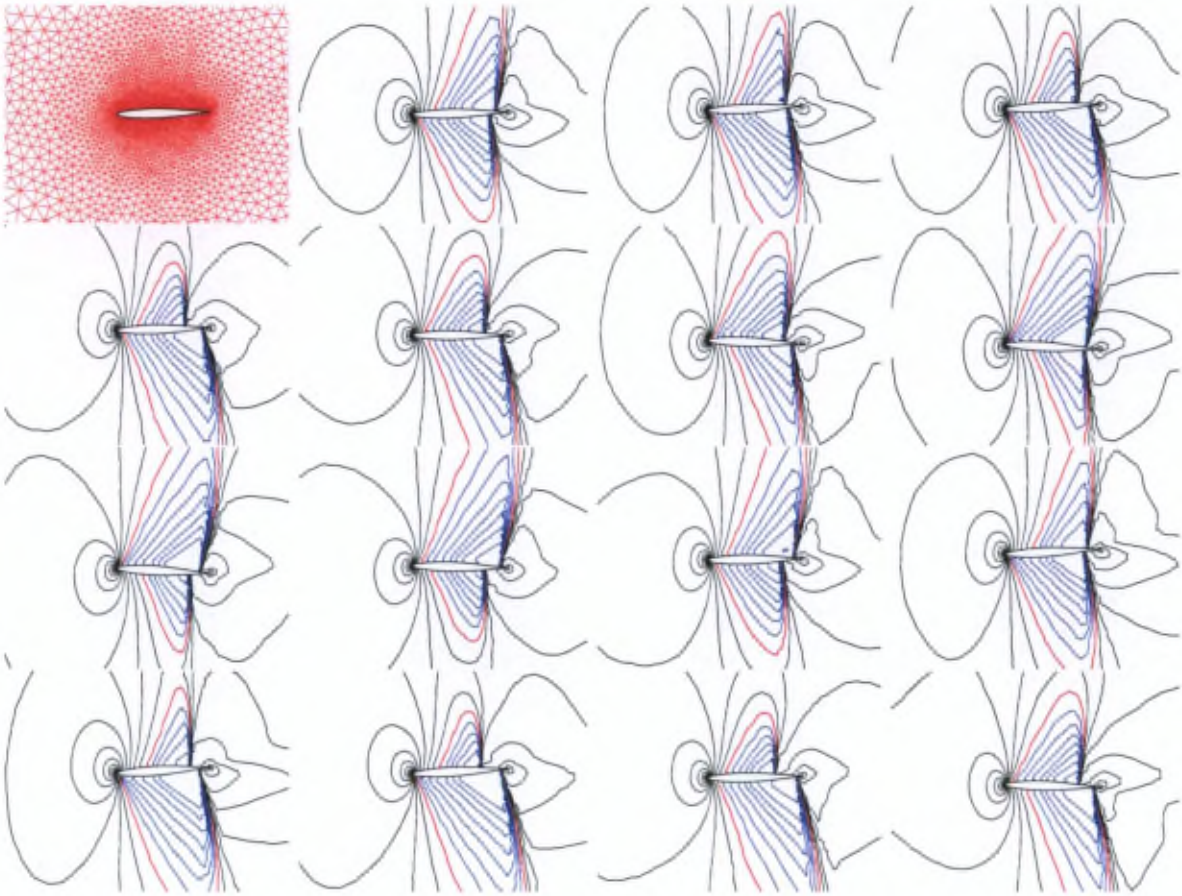

Figure 8.2.: Computational mesh. Mach number isolines ($\Delta Ma = 0.05$) at non-dimensional structural time $\tau = 21.5$ and further with step $\Delta\tau = 5$. FV scheme with linear reconstruction and Barth's limiter.

### 8.1.4. Numerical results

The aeroelastic regime is characterized by the Mach number $Ma$ and the flutter velocity defined as

$$V_f = \frac{u}{b\,\omega_f\sqrt{\mu}}, \qquad \mu = \frac{m}{\pi\rho b^2}, \tag{8.21}$$

where $u$ [m·s$^{-}$1] is the velocity of the air, $\omega_f$ [s$^{-1}$] is the frequency of the forced oscillations, $\mu$ [1] is the airfoil mass ratio and $b$ [m] is the half chord. Common parameters for the tests are following: $m = 18.8495$, $S_\alpha = 33.9292$, $I_\alpha = 65.5964$, $k_{hh} = 188495$, $k_{\alpha\alpha} = 655964$, $\omega_f = 100$, $b = 1$. The formulation for the small displacement is used. These settings give eigenvalues and eigenvectors of matrix

| Case | | | $\rho$ | $u$ | $v$ | $p$ |
|---|---|---|---|---|---|---|
| Indefinite: | $Ma = 0.825$, | $V_f = 0.612$ | 0.1 | 474.053161576 | 0 | 23584.0377804 |
| Damping: | $Ma = 0.85$, | $V_f = 0.439$ | 0.1 | 340.047937797 | 0 | 11431.7943648 |
| Flutter: | $Ma = 0.875$, | $V_f = 1.42$ | 0.1 | 1099.92727032 | 0 | 112871.370262 |

Table 8.1.: Free stream conditions characterizing different cases. The profile is rotated with respect to the Cartesian axes by 1°.

$(\mathbf{M}^{-1}\,\mathbf{K})$

$$\lambda_1 = 5089.309505, \qquad r_1 = (0.881354687, 0.4724551996), \tag{8.22}$$

$$\lambda_2 = 284925.4131, \qquad r_2 = (-0.881354687, 0.4724551996) \tag{8.23}$$

with corresponding natural frequencies $\omega_{1,2} = \sqrt{\lambda_{1,2}} = (71.34, 533.7)$ and periods $T_{1,2} = 2\pi/\omega_{1,2} = (0.08807, 0.01177)$ [s], which fully describes the homogenous solution of equation (8.18). The free stream conditions characterizing different regimes are given in Tab. 8.1. We have chosen three different cases, with negative, zero and positive damping. The curve of zero damping taken from [AJ94] is plotted in Fig. 8.1. The domain of solution is discretized with an unstructured triangular mesh consisting of 5574 nodes and 10950 elements, there are 129 nodes along the profile (see Fig. 8.2).

The computations started from a steady solution with linear combination of the modes $(h, \alpha)_0 = y_0 = 0.02r_1 + 0.002r_2$ of equation (8.22), (8.23). The lift and pitching moments were artificially set to zero, in order to avoid sharp transient response of the profile. Both the moments reached their respective values during the first cycle of the oscillations. The computations were performed with the following physical time-steps: flutter case $CFL = 20$, indefinite case $CFL = 43$, damping case $CFL = 25$.

Dependence of the hinge $h$ on time is shown in Fig. 8.1. Non-dimensional structural time is $\tau = \omega_\alpha t$, where $\omega_\alpha = \sqrt{k_{\alpha\alpha}/I_\alpha} = 100$. One can clearly see the difference between negative, zero and positive damping. There is a zoom to the previous picture on the upper right figure with two different frequencies of the oscillations visible, corresponding to the two eigen-modes of the dynamic system of the airfoil. The faster mode is quickly damped. At the next series of figures the Mach number isolines are shown during one cycle of the oscillation for the flutter case, starting at time $t = 0.215$ ($\tau = 21.5$) and with time-step $\Delta t = 0.05$ ($\Delta\tau = 5$).

## 8.2. Supersonic flutter of 2D flat plate

Supersonic panel flutter has appeared as an important problem in the development of V2 missiles during the Second World War. Since then, the problem was theoretically,

experimentally and numerically investigated, see e.g. [The35, The40, Mar58, BAH96, Dow04] and many other references about fluid-structure interaction. The test case was chosen from reference [PF01].

An elastic panel with infinite aspect ratio is clamped on both edges. Its upper side is exposed to the supersonic airstream, while the lower side resides in the still air with the same pressure as on the upper side. The panel has length $L = 0.5\,\mathrm{m}$, a uniform thickness $h = 1.35 \cdot 10^{-3}\,\mathrm{m}$, Young modulus $E = 7.728 \cdot 10^{10}\,\mathrm{N/m^2}$, Poisson ratio $\nu = 0.33$ and density $\rho_s = 2710\,\mathrm{kg/m^3}$. The flow conditions are given by $p_\infty = 25714\,\mathrm{Pa}$ and $\rho_\infty = 0.4\,\mathrm{kg/m^3}$. The critical Mach number $Ma_\infty^{\mathrm{cr}}$ that is, the lowest free stream Mach number for which an unstable aeroelastic mode of the panel appears, is given in the reference [PF01]. Using theoretical method the authors get $Ma_\infty^{\mathrm{cr}} \approx 2.27$ and using their numerical scheme $Ma_\infty^{\mathrm{cr}} \approx 2.23$, which they consider an "excellent agreement".

First, we test the FSI methods with the FV scheme for different free stream Mach numbers. The computational domain is depicted in Fig. 8.3, together with typical isolines of the pressure for one time instant with the free stream Mach number $Ma_\infty = 2.2$. The domain of solution is rather small, however due to the supersonic nature of the flow possible perturbations resulting from the finite size of the computational domain do not reach the oscillating panel. We have chosen the physical time-step $\Delta t = 1 \cdot 10^{-4}$, giving approx. 150 time-steps for one period.

The CFD method was selected with the following parameters: A uniform Cartesian mesh of $300 \times 100$ elements (giving 100 elements along the profile) was used for the flow domain, hereafter denoted as *fine*. The 3BDF time-stepping procedure was used, together with the implicit dual-time stepping formulation. Linear least square reconstruction with Barth's limiter was employed and the solution of the Riemann problem was approximated with the help of the Roe's Riemann solver.

The panel was discretized by $60 \times 2$ QUAD9 (see Fig. 6.1) elements. The Galerkin FEM method was equipped with the constant average acceleration method ($\gamma = \alpha = 0.5$). The plane strain assumption was used.

The free-stream conditions were prescribed to the flow domain and the panel was deflected with initial deflection

$$\Delta y_0(x) = c \cdot d(2x), \quad d(\bar{x}) = A\cos(\lambda\bar{x}) + B\sin(\lambda\bar{x}) + C\cosh(\lambda\bar{x}) + D\sinh(\lambda\bar{x}) \quad (8.24)$$

with $c = 0.002$ and $A = 1$, $B = -0.982502$, $C = -1$, $D = 0.982502$, $\lambda = 4.73004$, corresponding to the first mode of the panel [BSS02].

The integral of the deflection as a function of time for various Mach numbers around the critical Mach number is plotted in Fig. 8.4. One can see that the critical Mach number is about $Ma_\infty^{\mathrm{cr}} = 2.2$, which corresponds to the results presented in [PF01].

Second, we solve the problem on the fully unstructured grid (see Fig. 8.5) for the free stream Mach number $Ma_\infty = 2.2$. The mesh consists of 3451 nodes and 6722

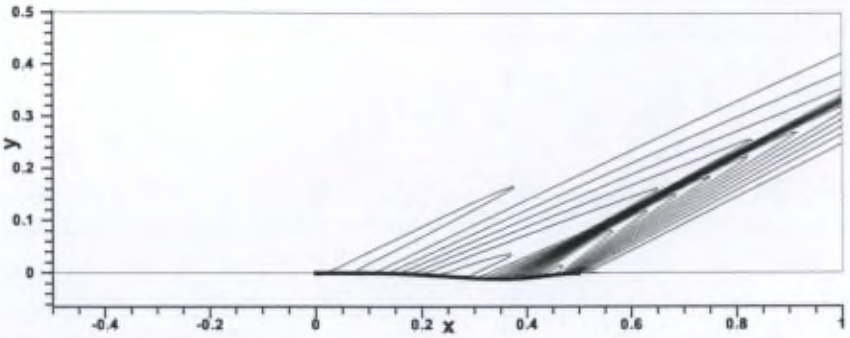


Figure 8.3.: Panel flutter problem. Solution on fine mesh. Isolines of pressure for one time instant, $Ma_\infty = 2.2$.

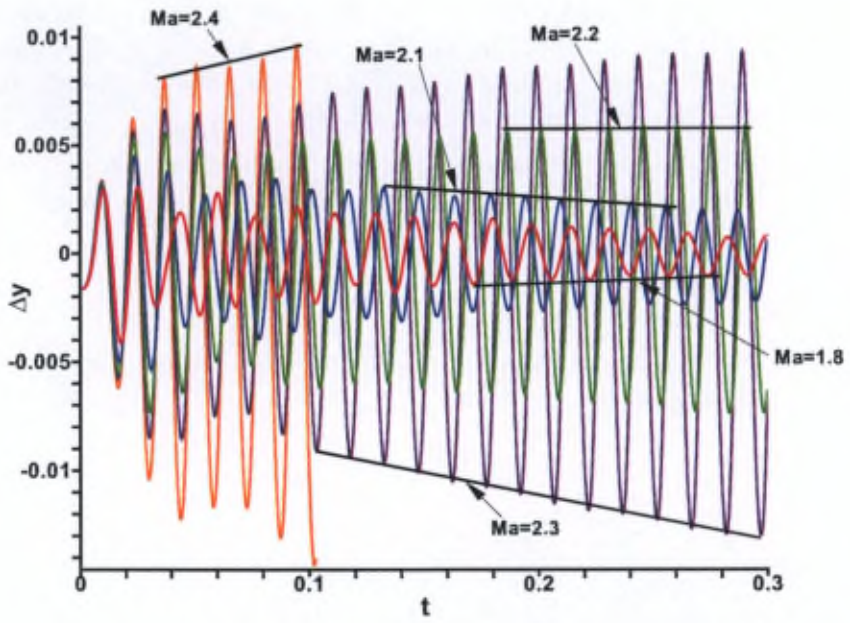


Figure 8.4.: Panel flutter problem. Solution on fine mesh. Dependence of the integral of deflection on time for different free stream Mach numbers.

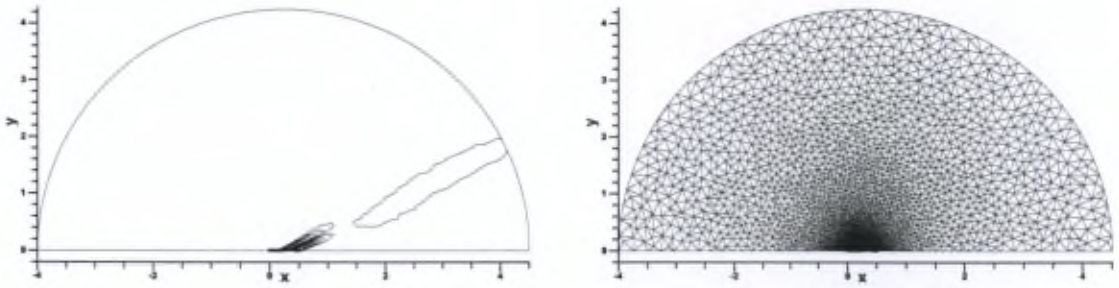

Figure 8.5.: Panel flutter problem. Domain of solution for unstructured mesh. Isolines of pressure for one time instant, $Ma_\infty = 2.2$.

triangular elements, giving 50 elements along the panel. We use CC FV scheme with Barth's limiter, LDA, N and Bx schemes, all with the 3BDF time integration. Even though the flow is supersonic, the shock-waves are relatively weak and we can expect acceptable capture of the shocks with the linear LDA scheme. All the other parameters of the simulation remain the same.

The dependence of the integral of deflection on time is plotted in Fig. 8.6. The results of the FV scheme correspond to the results of the computation on the fine mesh. One can see very good agreement of the second order RD schemes with the FV scheme.

The plotted results show a good agreement between each other and with theoretical investigations, but there are still some open questions. The simulations were repeated with different wall boundary conditions, namely the ones derived from the weak Petrov–Galerkin formulation, marked as PG (see section 3.9.2.1) and the weak boundary conditions due to Paillere [Pai95], marked P (see section 3.9.2.2). Results obtained with these two formulations of the wall boundary conditions are given in Fig. 8.7. First of all, the PG formulation was derived for Petrov–Galerkin schemes, i.e. schemes with bounded distribution coefficients. These are linearity preserving schemes in the RD framework. Neither N, nor Bx schemes belong to this class and the derivation might not be valid. However, the formulation of the PG boundary condition is equivalent (at least for the linear case) to the Van der Weide formulation of wall boundary condition [vdW98], see section 3.9.2.1, (with modified distribution coefficient), and in this case is not clear if the formulation of Weide does work for the non-linearity preserving schemes. For the LDA scheme, being the most accurate scheme, the difference is rather small. It it bigger for Bx the scheme. For N scheme, the two different formulations of the boundary conditions give completely different dynamic response. The suitable formulation of the boundary condition has to be tested and the problem is still not fully solved.

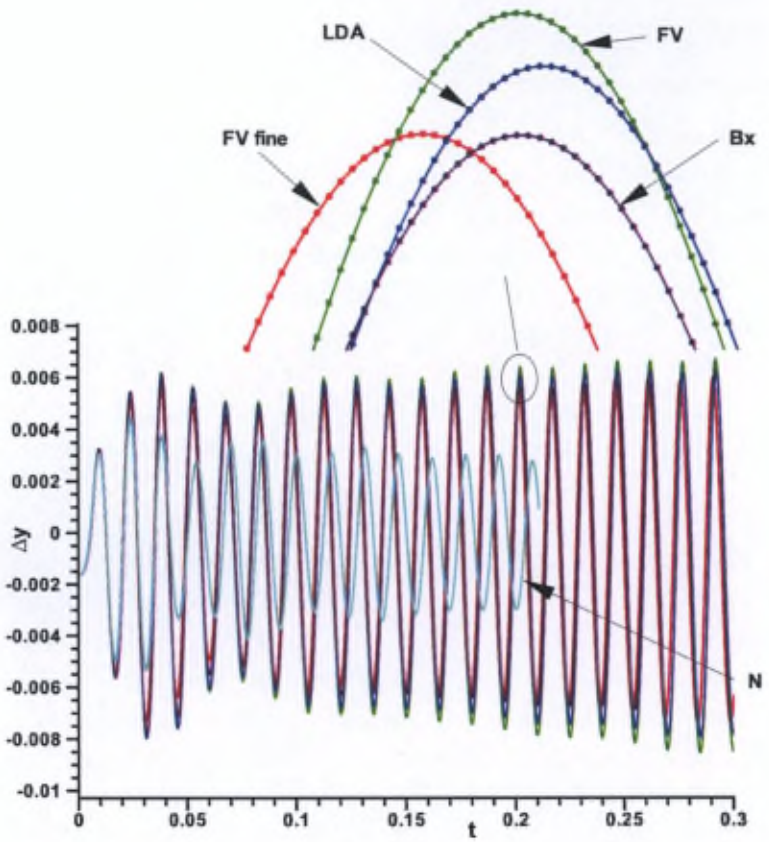


Figure 8.6.: Panel flutter problem. Solution on unstructured mesh. Dependence of the integral of deflection on time for different numerical schemes. $Ma_\infty = 2.2$. Paillere's boundary conditions.

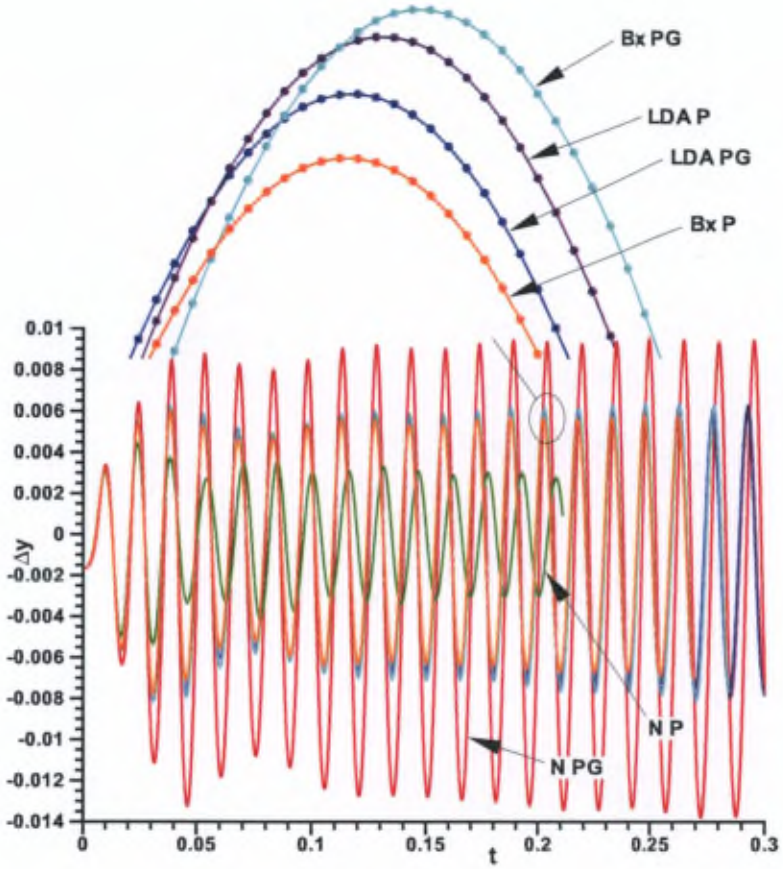


Figure 8.7.: Panel flutter problem. Solution on the unstructured mesh. Dependence of the integral of deflection on time for different implementation of the wall boundary conditions. P stands for boundary conditions due to Paillere, PG stands for Petrov–Galerkin formulation of boundary conditions. $Ma_\infty = 2.2$.

## 8.3. Transonic flutter of AGARD 455.6 wing

As a final test, a flutter computation of the AGARD 445.6 wing is presented. This is a very classical test case, first measured in 1956 [JU56], then measured and computed in 1962 [ECYLJTF63] (report [JU56] includes [ECYLJTF63] as appendix). The finite element computation with modal shapes is later provided in [ECY87]. A number of publications including this test case exist, note the recent book [HWS03], with comparison of several state of the art computations.

We provide all the details regarding the construction of this test case, including origin of used parameters, for the sake of clarity and repeatability. The conversion of units is taken from [Mec73].

Two types of models were built for the experiments, a solid model and a weakened model. There is a lack of detailed material properties of the wing in the references [ECYLJTF63, ECY87]. However, in [YKM+03] it has been found, that the solid model was made of Honduras mahagony (Swietenia macrophylla), see Fig. 8.8, with elastic constants as in the Tab. 8.2. Precisely for this reason we have selected the solid model for our flutter computations, despite the fact the weakened model was more extensively tested and it is more often referred to in the literature.

Geometric data are taken from reference [ECY87]: quarter-chord sweep-back angle of 45° and NACA 65A004 airfoil section in the stream-wise direction. The geometry is presented in Fig. 8.9 together with numerical data. The panel span $s = 2.500\,\text{ft}$ (=0.762 m), root chord $2b_s = 1.833\,\text{ft}$ (=0.5587 m) and tip chord $2b_t = 1.208\,\text{ft}$ (=0.3682 m). The measurements were performed with "solid model 2", measured mass is $\bar{m} = 0.14658\,\text{slugs}$ (=2.1391 kg).

We will investigate stability of the elastic response near a point given by the free stream Mach number $Ma_\infty = 0.92$ and flutter speed index

$$V_f = \frac{V}{b_s \omega_\alpha \sqrt{\bar{\mu}}}, \tag{8.25}$$

given by $V_f = 0.5214$ [ECY87, pg. 50], with $V$ the free stream gas velocity and $\omega_\alpha = 2\pi f_\alpha$ the natural angular frequency of the wing in first uncoupled torsion mode, which we will take from the reference. The measurements were performed for Freon-12 gas, with specific heat ratio $\gamma = 1.14$ [ECY87, pg. 3]. To asses the behavior of the method, we perform computations for different values of the flutter speed index $V_f$, see Tab. 8.4. The last non-dimensional parameter is the mass ratio[ECY87, pg. 38], given by

$$\bar{\mu} = \frac{\bar{m}}{\rho v}, \tag{8.26}$$

for our combination of the wing and the gas it is $\bar{\mu} = 9.300$ [ECY87, pg. 51]. Symbol $\bar{m}$ is the measured mass of the wing given above, $\rho$ is the density of the test medium and $v$ is the volume of the conical frustum having the stream-vise root chord as the

Figure 8.8.: Honduras Mahagony (Swietenia macrophylla) [Mah06b, Mah06a]

| | | |
|---|---|---|
| $E_{11}$ | $192.96 \cdot 10^6$ lbf/ft$^2$ | 9238.9 MPa |
| $E_{22}$ | $12.63 \cdot 10^6$ lbf/ft$^2$ | 604.72 MPa |
| $E_{33}$ | $21.11 \cdot 10^6$ lbf/ft$^2$ | 1010.7 MPa |
| $G_{12}$ | $13.02 \cdot 10^6$ lbf/ft$^2$ | 623.40 MPa |
| $G_{13}$ | $16.59 \cdot 10^6$ lbf/ft$^2$ | 794.33 MPa |
| $G_{23}$ | $5.53 \cdot 10^6$ lbf/ft$^2$ | 264.77 MPa |
| $\nu_{12}$ | 0.034 | |
| $\nu_{13}$ | 0.033 | |
| $\nu_{23}$ | 0.326 | |

Table 8.2.: Elastic constants of Honduras Mahagony (Swietenia macrophylla) taken from [YKM+03]. Indexes 1, 2 and 3 denote longitudinal (fiber), tangential and radial directions

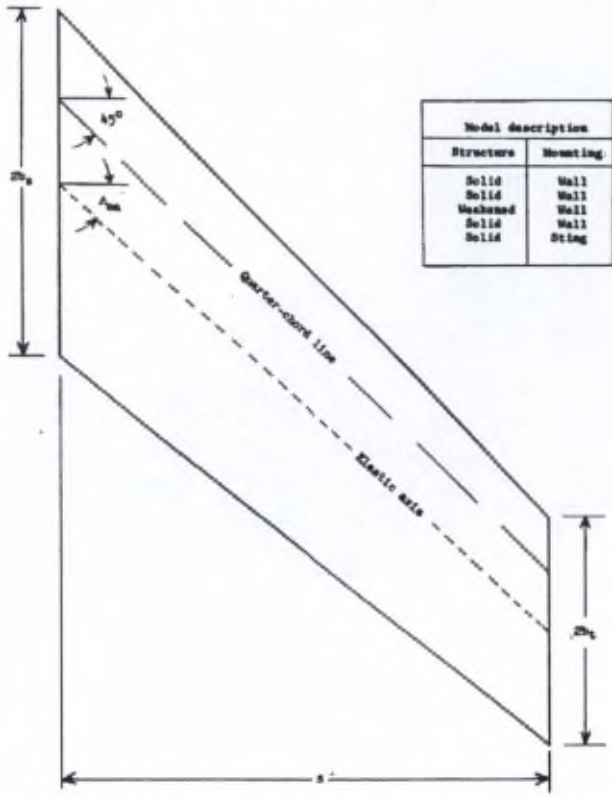


| Model description | | $s$, | $2b_s$, | $2b_t$, | $\Lambda_{ea}$, |
|---|---|---|---|---|---|
| Structure | Mounting | ft | ft | ft | deg |
| Solid | Wall | 1.250 | 0.917 | 0.604 | 43.15 |
| Solid | Wall | 2.500 | 1.833 | 1.208 | 43.15 |
| Machined | Wall | 2.500 | 1.833 | 1.208 | 43.15 |
| Solid | Wall | 3.750 | 2.750 | 1.812 | 43.15 |
| Solid | Sting | 1.167 | .856 | .567 | 43.15 |

Figure 8.9.: Geometry of the AGARD wing, taken from [ECY87, pg. 51].

lower base diameter, stream-vise tip chord as upper base diameter and the panel span as height.

The surface of the cross-section of the half airfoil with unit cord is computed numerically by using trapezoidal rule, giving $P = 0.0135938\,\mathrm{m}^2$. The surface of the cross-section at the root is then $P_1 = 2 \cdot 0.0135938 \cdot 0.5586984^2 = 0.0084864\,\mathrm{m}^2$, at the tip it is $P_2 = 2 \cdot 0.0135938 \cdot 0.3681984^2 = 0.0036858\,\mathrm{m}^2$.

The volume (see e.g. [Rek95, I, pg. 105, eqn. 9]) of the wing is then

$$v_w = \frac{1}{3}s(P_1 + P_2 + \sqrt{P_1 P_2}) = \frac{1}{3} \cdot 0.762 \cdot (0.0084864 + 0.0036858 + \sqrt{0.0084864 \cdot 0.0036858}) = 0.0045123\,\mathrm{m}^3 \quad (8.27)$$

The density of the material is then $\rho = \bar{m}/v_w = 2.1391/0.0045123 = 474.056\,\mathrm{kg/m}^3$

### 8.3.1. Computational mesh

The wing was discretized using 350 tri-quadratic elements, 14 elements are along the span, each element contains 27 nodes, see Fig. 8.10. The unstructured fluid mesh was downloaded from the Internet [BKC00], generated by the group of C. Farhat. It consists of 22014 nodes and 118480 tetrahedral elements.

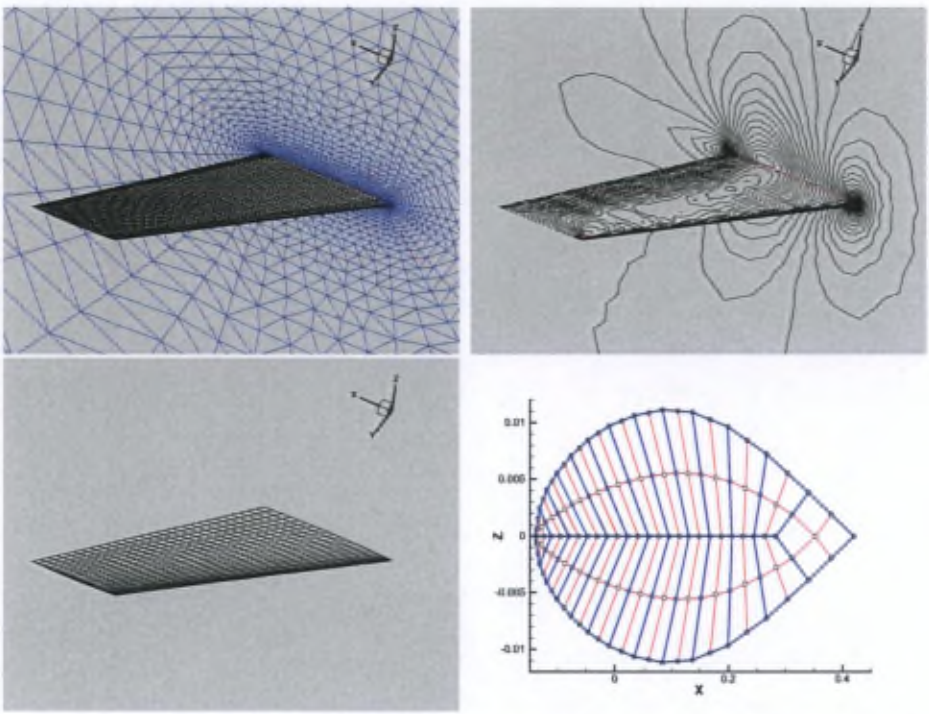

Figure 8.10.: AGARD 445.6 wing. Top: Fluid mesh, Mach number isolines in steady state (initially deformed). Bottom: structural mesh, cross-section of structural mesh with emphasized quadratic elements.

## 8.3.2. Modal analysis

As a first step, a modal analysis of the wing was performed. The direction of the fibers is declined by 45° from the $x$-axis and the elastic tensor has to be transformed in accordance. Frequencies resulting from the analysis are given in Tab. 8.3. The difference from the computation is of order 5%. If a three time denser mesh is used, the first modal frequency slightly increases such that the difference is about 4%. This systematic difference can by caused by the fact that our model uses elastic constants found in reference[YKM+03, Ano44]. These can be significantly different from the material of the constructed wing. Also radial and tangential direction of fibers are uncertain. Note, that we use a 3D anisotropic model, while the authors [ECY87] use a simplified 2D model, moreover the elastic constants taken from [Ano44] were modified: *"Values moduli and Poisson's ratio representing the anisotropic character [...taken from [Ano44]...] were modified slightly in order to duplicate as closely as possible the measured modal frequencies and mode lines"* [ECY87, pg. 2].

The isolines of deflection in $z$-direction for the computed modes are plotted in Fig. 8.11 and 8.12. Although the isolines are not in the same scale, the correspondence is clear. Fig. 8.13 shows an axonometric plot of the modes.

The first four modes were used as the initial deflection for the fluid-structure com-

| | Frequency, [Hz] | | | | |
|---|---|---|---|---|---|
| | $f_1$ | $f_2$ | $f_3$ | $f_4$ | $f_5$ |
| Measured [ECYLJTF63] | 14.10 | 69.30 | 50.70 | 127.10 | |
| 2D FEM [ECY87] | 14.1201 | 50.9125 | 68.9416 | 122.2556 | 160.5292 |
| Present method | 13.3645 | 45.6225 | 64.7223 | 113.513 | 157.599 |

Table 8.3.: AGARD 445.6 wing – solid model 2. Measured and computed modal frequencies [ECY87] and computation by present method.

putation in the ratio 1:0.2:0.04:0.008. Maximal deflection of the wing corresponds to $\Delta z \approx 0.0125$.

### 8.3.3. Steady flow solution – initial condition for FSI

Fluid-structure interaction computation starts from the steady state solution of the flow-field around the wing in the deformed state. The flow regime is sufficiently given by the Mach number and zero angle of attack, however for later use we set correct flow-field parameters with respect to the flutter speed index.

The flutter speed index is given by (8.25). Natural circular frequency $f_\alpha$ was calculated in [ECYLJTF63] using procedure [JU56]. We didn't recompute the value, but we took $f_\alpha = 50.68\,\mathrm{Hz}$ as [ECY87, pg. 48]. Root and tip half-chords $b_s$, $b_t$ are given above and volume of conical frustum is

$$v = \frac{\pi s}{3}(b_s^2 + b_s b_t + b_t^2). \tag{8.28}$$

From the equation (8.26) gas density is

$$\rho = \frac{\bar{m}}{v\bar{\mu}}, \tag{8.29}$$

and from (8.25)

$$V = V_f b_s \omega_\alpha \sqrt{\bar{\mu}}. \tag{8.30}$$

From the definition of the Mach number

$$Ma = \frac{V}{a} = V\sqrt{\frac{\rho}{\gamma p}} \tag{8.31}$$

the pressure is

$$p = \frac{V^2 \rho}{Ma^2 \gamma}. \tag{8.32}$$

The flow parameters are given in Tab. 8.4. The flow solution is self-similar, only one computation is needed, the others are obtained by scaling velocity as $V_f/V_{f\mathrm{ref}}$

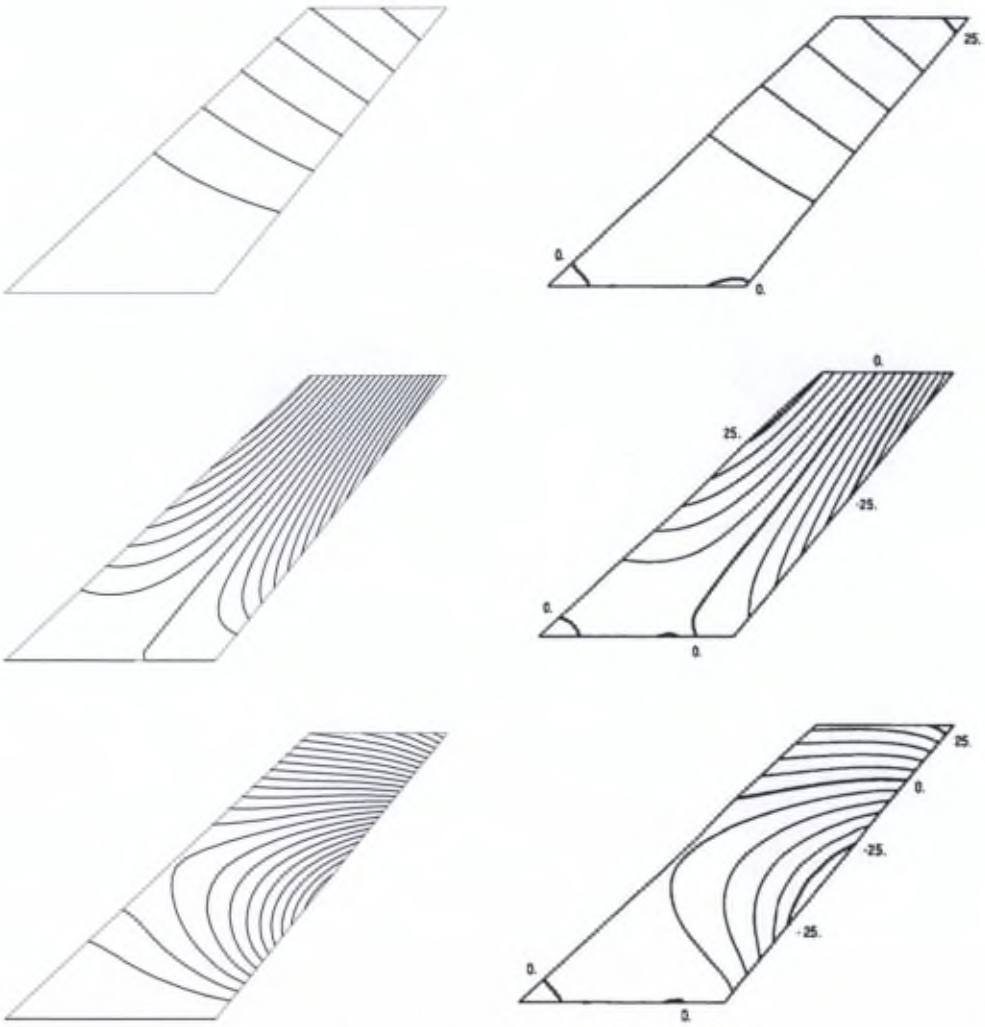


Figure 8.11.: First three modes of AGARD 445.6 wing. Left: present method. Right: calculation from reference [ECY87].

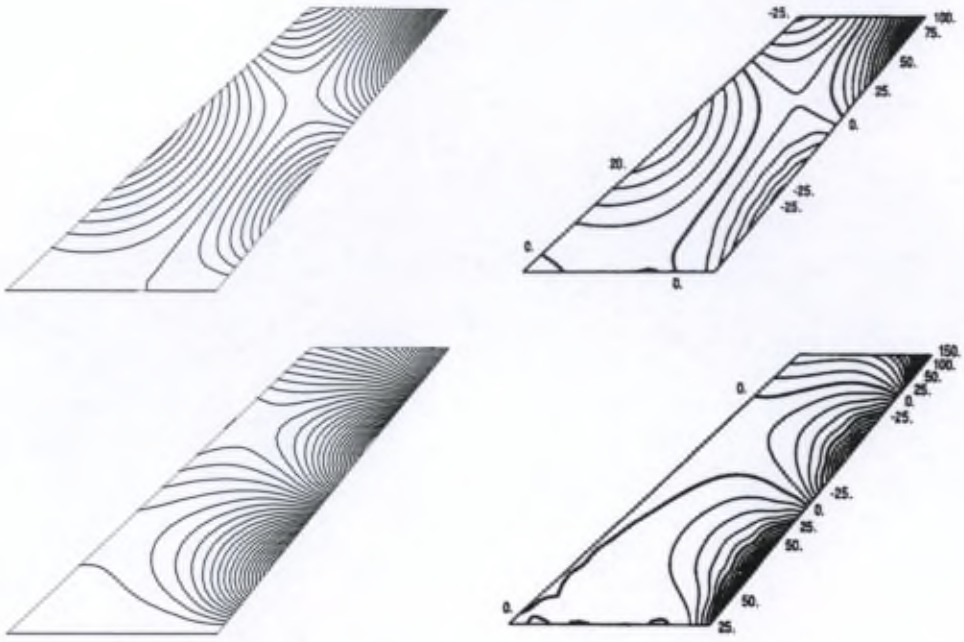

Figure 8.12.: Forth and fifth mode of AGARD 445.6 wing. Left: present method. Right: calculation from reference [ECY87].

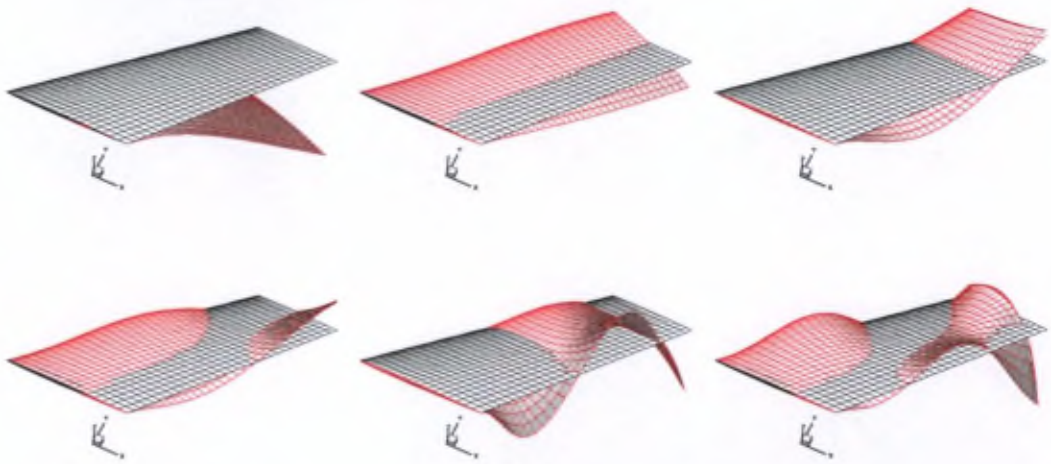

Figure 8.13.: AGARD 445.6 wing. Axonometric plot of the first six modes.

| Regime | Flutter speed index variation | $V_f$ | $\rho$ | $V$ | $p$ |
|---|---|---|---|---|---|
| Neutral | 0% | 0.52140 | 1.764526 | 141.4413 | 36584.789 |
| Damping | -5% | 0.49533 | 1.764526 | 134.3692 | 33017.772 |
| Damping | -8% | 0.47968 | 1.764526 | 130.1260 | 30965.365 |
| Damping | -10% | 0.46926 | 1.764526 | 127.2972 | 29633.679 |

Table 8.4.: Computed regimes for the AGARD 445.6 wing. $Ma_\infty = 0.92$

and the pressure as $V_f^2/V_{f\text{ref}}^2$. The isolines of the Mach number for the steady state solution are depicted in Fig. 8.10. The geometry is in the initially deformed state. The whole flow-field is subsonic, there is a tiny supersonic packet at the front tip of the wing.

### 8.3.4. Transonic flutter calculations

We start computations from the initial conditions described above. We have chosen a time step $\Delta t = 0.0003$, corresponding to about 120 time-steps per oscillation. Dependence of the integral of the deflection on time $t$ is depicted in Fig. 8.14. The neutral response is slightly above 95 % of the measured velocity, corresponding to an error in flutter speed index less than 5 %.

The measured flutter frequency is 172.1 radians/sec [ECY87, pg. 48], corresponding to the period $T_{\text{meas}} = 0.036508$. From Fig. 8.14, the period (computed from the first three cycles) is $T_{0\%} = 0.03866$, $T_{-5\%} = 0.0403333$, $T_{-8\%} = 0.0415333$. The flutter frequency error is then $(T_{-5\%} - T_{\text{meas}})/T_{\text{meas}} = 4.7\%$.

The second method was the LDA scheme from section 3.7.3 with two different boundary conditions, the first due to Paillere (section 3.9.2.2) and the second given by the Petrov-Galerkin formulation, see section 3.9.2.1. The computations were performed for the measured neutral response, see Fig. 8.15. The response in the case of Paillere's boundary conditions is almost perfectly neutral, while the Petrov-Galerkin formulation gives roughly twice bigger growth of the initial perturbation than the finite volume scheme. The flutter frequency obtained from the first three periods from plot 8.15 is given in Tab. 8.5. The error in frequency, computed as above, for the LDA scheme with Paillere's boundary condition is less than 1 %, which can be judged much more accurate than can be expected, taking into account relatively simple method for elastic problems and the uncertainty in the value of the elastic constants. The error in the frequency for the Petrov-Galerkin formulation of the boundary conditions is less than 3 % and for the finite volume scheme about 2 %.

| Method | Period $T$ | Error |
|---|---|---|
| Measured | 0.036508 | |
| LDA Paillere | 0.036265 | 0.66 % |
| LDA Petrov-Galerkin | 0.035436 | 2.93 % |
| FV | 0.035746 | 2.08 % |

Table 8.5.: Flutter frequency for the AGARD 445.6 wing, comparison for the neutral response regime. Influence of the boundary conditions.

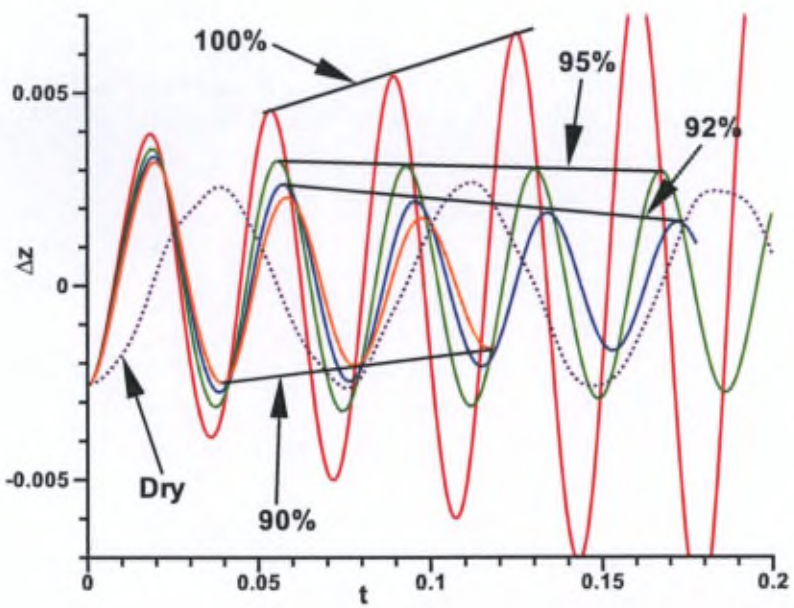


Figure 8.14.: AGARD 445.6 wing. Time dependence of the volume integral of the deflection for the velocity of 100 %, 95 %, 92 % and 90 % of the measured neutral response. Comparison with the dry elastic response.

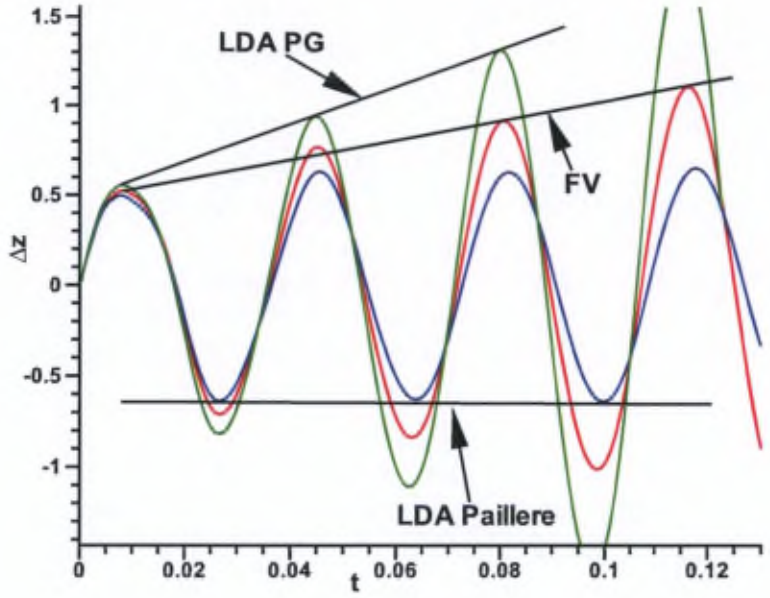


Figure 8.15.: AGARD 445.6 wing. Time dependence of the volume integral of the deflection for the measured neutral response. Comparison of the FV scheme and LDA scheme with different formulations of boundary conditions.

| No. of processors | Speedup | Efficiency |
|---|---|---|
| 1 | 1 | 100 % |
| 2 | 1.77 | 88.5 % |
| 4 | 3.24 | 81.2 % |

Table 8.6.: Parallel performance for the AGARD 445.6 wing.

### 8.3.5. Parallel performance

We have performed the simulations on a parallel cluster up to four processors. The parallel efficiency, as defined in (4.49), together with the speedup is presented in Tab. 8.6. The implementation is far from optimal, however a noticeable speedup can be seen. The parallel efficiency problem is caused by the very coarse structural mesh for the parallel solution in the current implementation.

## 8.4. Conclusions

In this chapter, results from several examples of technically important fluid-structure interaction problems were presented. All selected test cases are well known and widely used as benchmarks. One can compare the performance of the presented methods with own methods or other methods from the references.

The transonic flutter of the profile NACA64A010 was presented. The profile was modeled as a rigid body with two degrees of freedom. The neutral, damped and flutter response was reproduced.

The supersonic flutter of a 2D panel was selected as second test case. The problem was solved on two different meshes, fine and unstructured. Different formulations of numerical schemes and boundary conditions were studied. The critical Mach number estimated from the computations using the finite volume scheme was $Ma_{\infty}^{cr} = 2.2$, while the theoretical value was $Ma_{\infty}^{cr} = 2.27$ and from the reference [PF01] $Ma_{\infty}^{cr} = 2.23$. The case was solved by the novel formulation of the LDA, N and Bx schemes, confirming good performance of the LDA and the Bx schemes. The influence of the boundary conditions was also considered.

As the last ultimate test case, the transonic flutter of the AGARD 445.6 wing was considered. This is probably the most famous transonic flutter test case, partially because lack of flutter data for the other technically relevant test cases. The modal analysis of the wing was performed. The difference between the computed frequency and the measured frequency of the first mode is about 5 %. The computation using the FV scheme was performed. Computed flutter speed index was lower than measured by a difference less than 5 %. Then the computations were performed with the LDA scheme with two different boundary conditions for the case of measured neutral response. In one case, the resulting response was almost exactly neutral, for the second version of the boundary conditions the difference was bigger. The error of the flutter frequency was less than 1 % in one case and about 3 % in the second.

All the presented results can be considered very good. However, it has to be mentioned that for reliable fluid-structure computations the method has to be thoroughly validated.

# Chapter 9.

# Conclusions

The goals stated in the beginning of presented work were successfully fulfilled.

1. A numerical method based on residual distribution schemes was developed and several extensions for moving mesh simulation were proposed. We have analyzed the positivity of first order schemes, showing that the proposed extension satisfies a discrete maximum principle for a scalar conservation law. We have also analyzed the positivity and accuracy requirements of nonlinear schemes constructed as a linear combination of low and high order schemes. We have proposed and tested a new nonlinear scheme built as a convex combination of the LDA and the N scheme, named Bx scheme.

2. We have developed a finite volume method in both cell centered and vertex centered settings, including the capability to handle moving meshes. We have tested the influence of renumbering degrees of freedom for a parallel implicit method, showing its importance for the parallel performance.

3. We have conducted a number of computational experiments, starting from scalar advection problems, Burgers equation up to the Euler equations, including the technically important case of transonic flow past the Onera M6 wing. The tests were performed in two and three spatial dimensions, for steady and unsteady problems, including problems with deforming meshes. A number of convergence studies for scalar cases were performed, also in three dimensions, giving opportunity to directly compare the accuracy of different schemes for the same test case.

4. A finite element method for the structural problem has been developed in two and three dimensions including large displacement formulation and handling of anisotropic material properties. The modal analysis capabilities were included, as they are needed for the validation of the structural model and the prescription of the initial conditions in the fluid–structure interaction problem.

5. A numerical method for fluid–structure interaction was developed and coded. The numerical method for the fluid flow is based on the schemes developed

in the first part of the work. Interface boundary conditions were developed and validated. The mesh motion algorithm uses the finite element method to find a nodal displacement. The method was validated for 2D transonic flow past a NACA 64A010 airfoil, where the structural dynamics is modeled by a system of two ordinary differential equations. The flutter, neutral and damping response were correctly reproduced. A flutter boundary for one selected Mach number of a two-dimensional elastic panel problem was computed and compared with theoretical results and solutions known from the literature. Finally, the method was tested on the 3D AGARD 445.6 wing test case. We have compared the solution using different developed CFD methods, both of the residual distribution and finite volume type.

## 9.1. Original contribution of this thesis

The main achievements of the thesis are summarized below.

- Development of the numerical methods based on residual distribution (RD) schemes and their extension for simulations on moving meshes.

  Chapter 3 is devoted to the development of the residual distribution schemes (RDS). We have shown that a positive multidimensional upwind scheme, which is a convex combination of the N scheme and the LDA scheme, does not exist, see Theorem 11, page 38. We have also proven, that *any* scalar multidimensional upwind scheme in two dimension can be constructed from the blend of two other schemes, e.g. N scheme and LDA scheme, see Theorem 12.

  A new RD scheme has been developed, see Chapter 3.5.5, page 41, based on physical considerations for blending the LDA and N schemes, named Bx scheme. The Bx scheme is constructed such that the LDA scheme is active in smooth parts of the flow and the N scheme introduces higher order error, giving second order accuracy in smooth parts of the flow. The blending coefficient is smooth, leading to superior iterative convergence properties. The Bx scheme is extended for unsteady flow computations, taking into account the mass matrix of the RD schemes.

  We have extended several unsteady versions of the RD schemes for computations on moving meshes, see section 3.7, page 59 and further. Unlike in [MSD03], our extension preserves the positivity of the N scheme, allowing to prove a discrete maximum principle for scalar problems. Then, we have derived the extension of several versions of the space-time RD schemes and the extension of the LDA scheme with mass matrix. We have used the analogy with Petrov-Galerkin formulation of the LDA scheme. Unlike other authors, see e.g. [SFH05], we *do not need to compute the time derivative of the mass matrix*, which could be a prohibitively expensive operation for the RD schemes.

The method was implemented for large scale computations, i.e. the program is written to solve 3D problems in parallel using an implicit time integration procedure.

The connection between the linear, linearity preserving residual distribution schemes and the Petrov-Galerkin formulation allows us to formulate a consistent boundary conditions treatment. In particular, we have shown the connection between the Petrov-Galerkin formulation and van der Weide's formulation, see section 3.9.2.1, page 69. We have also formulated a condition for *conservativity* of wall boundary conditions.

- Development of the state-of-the-art finite volume (FV) methods.

  We have considered the stated-of-the-art finite volume method, which uses unstructured meshes and numerical flux obtained by solving a Riemann problem at each face of the finite volume. We have used linear least square reconstruction with limiter, see [BJ89], or nonlinear weight, called WLSQR (WENO) method, see e.g. [Für06]. The extension of the method for moving mesh computations was done according to [KF99]. The computer implementation allows to solve 3D industrial type flows, again using a parallel implicit time integration procedure.

  We have compared parallel element renumbering strategies and shown a *large influence* of the mesh numbering on the computational speed-up, see section 4.4, page 84.

- Evaluation of the performance and comparison of the schemes for steady and unsteady flow problems.

  The finite volume schemes and residual distribution schemes are first compared in unsteady version via a modified equation approach, see Section 5.1, page 90. We have shown that both methods have a dispersion error term of order $\mathcal{O}(\Delta x^2)$ and fourth order dissipation term scaled as $\mathcal{O}(\Delta x^3)$. Our theoretical results were demonstrated numerically for the solution of a 1D advection problem of smooth profile and top-hat.

  In the subsequent part of Section 5, we have systematically performed numerical experiments to show the behavior of the schemes for a number of problem types. It includes smooth problems and problems with shock waves; scalar and system of equations; and problems involving moving meshes simulations. The RD schemes can be directly compared with cell centered and vertex centered formulations of the FV scheme. When it was possible, we have estimated the accuracy order by convergence study of the error in the appropriate norm. We have shown the definitive superiority of the LDA scheme in its class; and the high accuracy of the cell centered formulation of the finite volume scheme with Barth limiter for non-linear schemes. We have also demonstrated the

unsatisfactory performance of the N-modified scheme and the superiority of the Bx scheme. The vertex centered formulation of the FV scheme was giving consistently worse results than the RD and cell centered FV methods.

- Development of a method for aeroelastic computations and performance test.

  The finite element method was developed for the elastic continuum simulations. The method is simple, however it includes the key ingredients to solve the elastic behavior of the wooden wing: anisotropic elastic material; formulation for small and large displacements; possibility to solve unsteady problems and modal analysis. We have shown the practical necessity to use elements with at least quadratic trial functions, see Section 6.5, page 156. The same method was later used for the computational fluid dynamics (CFD) mesh motion. The CFD mesh is large and our parallel implementation of the algorithm is an advantage.

  The fluid-structure interaction problem was formulated using the three field approach: computation of fluid dynamics on moving meshes, computational structured dynamics in Lagrangian formulation and mesh motion algorithm. The three problems are solved together using a simple sub-iteration approach.

  The performance of the method is demonstrated in Chapter 8, page 171. As the simpler test we solve transonic flutter of the NACA 64A010 airfoil. The airfoil motion is described by the system of ordinary differential equations, we use Runge-Kutta scheme to solve the ODEs. The second test includes the 2D panel flutter problem. We asses the performance of the method in comparison with the theoretical solution.

  As the final test in this thesis, we solve the transonic flutter problem of an AGARD 455.6 wing in three spatial dimensions. We describe the full setup of the problem, including the modal analysis and flow conditions for sake of clarity and repeatability. Then, we have compared the solution obtained with the FV scheme and RD scheme, also with experimental data.

Some of the results obtained during the work were published, the most important publications include:

- Extension of the RD schemes for computations on moving meshes [DD05b, DDF05a, DD06a, DD06c, DD06b].
- Blended (Bx) scheme [DD05a, DD06d].
- Fluid-structure interaction problem of an airfoil with two degrees of freedom [DDF05b].
- Fluid-structure interaction problem of the AGARD 445.6 wing [DFDF07].

- Comparison of cell centered and vertex centered formulation of finite volume scheme [DDF06].

## 9.2. Conclusions and further perspectives

The finite volume method proved to be an accurate and reliable method for fluid flow simulations. The methods developed in the course of this thesis have been validated on a number of test cases, including internal turbomachinery flows (transonic axial and radial turbines) and external flows, i.e. airfoils and wings. Those results are not included in the thesis, for space limitations, but they are published in scientific journals [DFH05, BUK+03, DFF+03a, DFH03, FDHK02, DFF+01], conference proceedings abroad [DFF+04a, DFF+04b, DFH04, DFF+03c, DFF+03d, DFF+03b, DFF+02], conferences in the Czech Republic and internal research reports of the Department of Technical Mathematics. The method was extended for the turbulent flows, which is also not included here. For the references we give [DFH05] and the internal research reports of the Department of Technical Mathematics. For the further extension, we recommend to consider a better approximation of the Jacobian for the implicit method, to improve boundary condition treatment and to include higher order implicit time integration method (higher than two).

The residual distribution schemes are much less developed in comparison to the finite volume methods. The LDA scheme was shown to be superiorly accurate with respect to the finite volume schemes, while keeping enough dissipativity to compute flows with weak shock waves and discontinuities. The N-modified scheme was believed to be superior in terms of accuracy to the finite volume schemes, whereas the comparison presented in chapter 5 has raised doubts about this statement. The Bx scheme was intended as the replacement, however, the shock capturing operator does not stand on solid mathematical basis, it is rather an *ad hoc* solution. A lot of work is still needed for the improvement of the nonlinear schemes. The only nonlinear unsteady shock capturing residual distribution scheme working sufficiently well for large time-steps seems to be the Bx scheme, for the time being. There are iterative convergence problems for the two layer space-time N-modified scheme with large time steps, which effectively prevents its use for fluid-structure interaction problems. The possible extension for viscous problems is described in e.g. [vdW98, DRAD06], or for space-time schemes of [CD02] in [DRD03b, DRD03a, DRD05].

This is a first research on the development of second order accurate RD schemes for aeroelastic simulations, and the proposed second order extensions are the first work known to the author concerning this topic. Although very encouraging results were obtained, it will still take a lot of effort to finish the methods such that routine aeroelastic simulations would be possible.

Considering the method for elastic simulations, a relatively simple formulation was used. For realistic simulations of aircrafts the model has to be extended to

consider internal mechanics of the wings with all the equipment normally modeled, such as rods, bars, springs and honey combs. Contrary to the fluid flow modeling, computational solid mechanics methods are well developed and reliable and commercial software packages are readily available. On side of post-processing of the results, identification of the dynamics parameters has to be improved, one of the proposed methods is the ERA algorithm [JP77].

## Acknowledgments

I would like express my deep acknowledgments to my supervisors prof. Jaroslav Fořt (Czech Technical University) and prof. Herman Deconinck (von Karman Institute), they both gave me the full support during the PhD study. I would like to thank prof. Karel Kozel for all the encouraging discussions and creating an excellent atmosphere at the Department.

I would like to thank all my colleagues and friends who helped me from scientific and personal side, namely Mario Ricchiuto (all the RD stuff, mathematics and everything else), Aristotelis Athanasiadis (computational meshes, C++), Jiří Fürst (mathematics and many other things), Petr Sváček (mathematics, English language), Luděk Beneš (mathematics and the roof at my parent's cabin) and many other people from the Von Karman Institute and the Department of Technical Mathematics.

The biggest thanks go to my family, in particular to my wife Zuzana, who was standing next to me during all the years of work.

Praha, June 2006

# Appendix A.

# Appendix

## A.1. Smooth compression of gas inside the piston cylinder

This test case is motivated by internal aerodynamics problems, namely flow in piston engines. A gas at rest is enclosed between two walls. One of the walls slowly starts to move. This problem can be solved by the method of characteristics [ZH76] until the head of the pressure wave reflects from the other wall or a shock is created. We have used a domain of length $l = 5$ and initial conditions $u^0 = 0$, $\rho^0 = 1.4$ and $p^0 = 1$. The piston starts to accelerate with derivative of acceleration $\ddot{x} = 0.2$. The solution at $t = 4$ from the method of characteristic is given in the table below.

| # | x | Mach | u | rho | p |
|---|---|---|---|---|---|
| 1 | 2.133333e+00 | 1.212121e+00 | 1.600000e+00 | 5.610450e+00 | 6.982606e+00 |
| 2 | 2.185243e+00 | 1.193759e+00 | 1.568160e+00 | 5.476419e+00 | 6.750191e+00 |
| 3 | 2.235394e+00 | 1.175405e+00 | 1.536640e+00 | 5.346270e+00 | 6.526674e+00 |
| 4 | 2.283819e+00 | 1.157062e+00 | 1.505440e+00 | 5.219890e+00 | 6.311705e+00 |
| 5 | 2.330552e+00 | 1.138734e+00 | 1.474560e+00 | 5.097172e+00 | 6.104945e+00 |
| 6 | 2.375627e+00 | 1.120422e+00 | 1.444000e+00 | 4.978009e+00 | 5.906071e+00 |
| 7 | 2.419075e+00 | 1.102130e+00 | 1.413760e+00 | 4.862298e+00 | 5.714772e+00 |
| 8 | 2.460932e+00 | 1.083862e+00 | 1.383840e+00 | 4.749938e+00 | 5.530749e+00 |
| 9 | 2.501229e+00 | 1.065619e+00 | 1.354240e+00 | 4.640835e+00 | 5.353715e+00 |
| 10 | 2.540001e+00 | 1.047406e+00 | 1.324960e+00 | 4.534892e+00 | 5.183397e+00 |
| 11 | 2.577280e+00 | 1.029225e+00 | 1.296000e+00 | 4.432019e+00 | 5.019529e+00 |
| 12 | 2.613100e+00 | 1.011080e+00 | 1.267360e+00 | 4.332127e+00 | 4.861860e+00 |
| 13 | 2.647494e+00 | 9.929733e-01 | 1.239040e+00 | 4.235131e+00 | 4.710146e+00 |
| 14 | 2.680495e+00 | 9.749092e-01 | 1.211040e+00 | 4.140947e+00 | 4.564154e+00 |
| 15 | 2.712137e+00 | 9.568908e-01 | 1.183360e+00 | 4.049493e+00 | 4.423660e+00 |
| 16 | 2.742453e+00 | 9.389214e-01 | 1.156000e+00 | 3.960692e+00 | 4.288449e+00 |
| 17 | 2.771476e+00 | 9.210045e-01 | 1.128960e+00 | 3.874467e+00 | 4.158316e+00 |
| 18 | 2.799240e+00 | 9.031438e-01 | 1.102240e+00 | 3.790744e+00 | 4.033063e+00 |
| 19 | 2.825777e+00 | 8.853426e-01 | 1.075840e+00 | 3.709451e+00 | 3.912499e+00 |
| 20 | 2.851122e+00 | 8.676047e-01 | 1.049760e+00 | 3.630519e+00 | 3.796444e+00 |

```
21 2.875307e+00 8.499336e-01 1.024000e+00 3.553881e+00 3.684722e+00
22 2.898365e+00 8.323331e-01 9.985600e-01 3.479470e+00 3.577165e+00
23 2.920330e+00 8.148069e-01 9.734400e-01 3.407223e+00 3.473614e+00
24 2.941236e+00 7.973587e-01 9.486400e-01 3.337079e+00 3.373912e+00
25 2.961114e+00 7.799924e-01 9.241600e-01 3.268977e+00 3.277913e+00
26 2.980000e+00 7.627119e-01 9.000000e-01 3.202861e+00 3.185474e+00
27 2.997926e+00 7.455209e-01 8.761600e-01 3.138673e+00 3.096458e+00
28 3.014924e+00 7.284234e-01 8.526400e-01 3.076359e+00 3.010736e+00
29 3.031030e+00 7.114234e-01 8.294400e-01 3.015867e+00 2.928180e+00
30 3.046275e+00 6.945248e-01 8.065600e-01 2.957145e+00 2.848672e+00
31 3.060693e+00 6.777317e-01 7.840000e-01 2.900143e+00 2.772094e+00
32 3.074318e+00 6.610480e-01 7.617600e-01 2.844814e+00 2.698337e+00
33 3.087183e+00 6.444779e-01 7.398400e-01 2.791110e+00 2.627293e+00
34 3.099320e+00 6.280254e-01 7.182400e-01 2.738987e+00 2.558861e+00
35 3.110764e+00 6.116947e-01 6.969600e-01 2.688400e+00 2.492942e+00
36 3.121547e+00 5.954898e-01 6.760000e-01 2.639307e+00 2.429443e+00
37 3.131703e+00 5.794149e-01 6.553600e-01 2.591668e+00 2.368273e+00
38 3.141265e+00 5.634743e-01 6.350400e-01 2.545441e+00 2.309346e+00
39 3.150266e+00 5.476720e-01 6.150400e-01 2.500589e+00 2.252579e+00
40 3.158740e+00 5.320122e-01 5.953600e-01 2.457074e+00 2.197891e+00
41 3.166720e+00 5.164993e-01 5.760000e-01 2.414859e+00 2.145208e+00
42 3.174239e+00 5.011373e-01 5.569600e-01 2.373911e+00 2.094454e+00
43 3.181331e+00 4.859305e-01 5.382400e-01 2.334194e+00 2.045561e+00
44 3.188028e+00 4.708832e-01 5.198400e-01 2.295675e+00 1.998460e+00
45 3.194365e+00 4.559995e-01 5.017600e-01 2.258324e+00 1.953086e+00
46 3.200373e+00 4.412837e-01 4.840000e-01 2.222108e+00 1.909379e+00
47 3.206088e+00 4.267400e-01 4.665600e-01 2.186999e+00 1.867277e+00
48 3.211541e+00 4.123726e-01 4.494400e-01 2.152967e+00 1.826725e+00
49 3.216766e+00 3.981858e-01 4.326400e-01 2.119984e+00 1.787666e+00
50 3.221797e+00 3.841836e-01 4.161600e-01 2.088024e+00 1.750050e+00
51 3.226667e+00 3.703704e-01 4.000000e-01 2.057059e+00 1.713824e+00
52 3.231408e+00 3.567502e-01 3.841600e-01 2.027066e+00 1.678942e+00
53 3.236055e+00 3.433272e-01 3.686400e-01 1.998018e+00 1.645356e+00
54 3.240640e+00 3.301055e-01 3.534400e-01 1.969893e+00 1.613023e+00
55 3.245198e+00 3.170893e-01 3.385600e-01 1.942668e+00 1.581899e+00
56 3.249760e+00 3.042825e-01 3.240000e-01 1.916321e+00 1.551945e+00
57 3.254361e+00 2.916893e-01 3.097600e-01 1.890830e+00 1.523120e+00
58 3.259033e+00 2.793136e-01 2.958400e-01 1.866175e+00 1.495388e+00
59 3.263811e+00 2.671594e-01 2.822400e-01 1.842335e+00 1.468713e+00
60 3.268726e+00 2.552306e-01 2.689600e-01 1.819292e+00 1.443060e+00
61 3.273813e+00 2.435312e-01 2.560000e-01 1.797028e+00 1.418396e+00
62 3.279105e+00 2.320649e-01 2.433600e-01 1.775523e+00 1.394690e+00
63 3.284635e+00 2.208356e-01 2.310400e-01 1.754762e+00 1.371912e+00
64 3.290437e+00 2.098470e-01 2.190400e-01 1.734727e+00 1.350033e+00
```

```
 65 3.296543e+00 1.991028e-01 2.073600e-01 1.715402e+00 1.329025e+00
 66 3.302987e+00 1.886066e-01 1.960000e-01 1.696773e+00 1.308862e+00
 67 3.309802e+00 1.783620e-01 1.849600e-01 1.678824e+00 1.289519e+00
 68 3.317021e+00 1.683726e-01 1.742400e-01 1.661540e+00 1.270972e+00
 69 3.324679e+00 1.586416e-01 1.638400e-01 1.644909e+00 1.253197e+00
 70 3.332807e+00 1.491726e-01 1.537600e-01 1.628917e+00 1.236173e+00
 71 3.341440e+00 1.399689e-01 1.440000e-01 1.613551e+00 1.219879e+00
 72 3.350610e+00 1.310336e-01 1.345600e-01 1.598800e+00 1.204294e+00
 73 3.360352e+00 1.223700e-01 1.254400e-01 1.584652e+00 1.189400e+00
 74 3.370697e+00 1.139811e-01 1.166400e-01 1.571095e+00 1.175179e+00
 75 3.381680e+00 1.058698e-01 1.081600e-01 1.558118e+00 1.161613e+00
 76 3.393333e+00 9.803922e-02 1.000000e-01 1.545713e+00 1.148686e+00
 77 3.405691e+00 9.049205e-02 9.216000e-02 1.533869e+00 1.136382e+00
 78 3.418786e+00 8.323106e-02 8.464000e-02 1.522576e+00 1.124686e+00
 79 3.432651e+00 7.625890e-02 7.744000e-02 1.511827e+00 1.113586e+00
 80 3.447320e+00 6.957811e-02 7.056000e-02 1.501612e+00 1.103066e+00
 81 3.462827e+00 6.319115e-02 6.400000e-02 1.491923e+00 1.093115e+00
 82 3.479203e+00 5.710038e-02 5.776000e-02 1.482754e+00 1.083721e+00
 83 3.496484e+00 5.130804e-02 5.184000e-02 1.474097e+00 1.074873e+00
 84 3.514701e+00 4.581629e-02 4.624000e-02 1.465944e+00 1.066560e+00
 85 3.533889e+00 4.062718e-02 4.096000e-02 1.458291e+00 1.058773e+00
 86 3.554080e+00 3.574265e-02 3.600000e-02 1.451131e+00 1.051502e+00
 87 3.575308e+00 3.116454e-02 3.136000e-02 1.444458e+00 1.044739e+00
 88 3.597606e+00 2.689455e-02 2.704000e-02 1.438268e+00 1.038476e+00
 89 3.621007e+00 2.293432e-02 2.304000e-02 1.432555e+00 1.032705e+00
 90 3.645545e+00 1.928533e-02 1.936000e-02 1.427315e+00 1.027421e+00
 91 3.671253e+00 1.594896e-02 1.600000e-02 1.422544e+00 1.022616e+00
 92 3.698164e+00 1.292649e-02 1.296000e-02 1.418238e+00 1.018286e+00
 93 3.726312e+00 1.021907e-02 1.024000e-02 1.414395e+00 1.014424e+00
 94 3.755729e+00 7.827726e-03 7.840000e-03 1.411010e+00 1.011028e+00
 95 3.786450e+00 5.753372e-03 5.760000e-03 1.408083e+00 1.008092e+00
 96 3.818507e+00 3.996803e-03 4.000000e-03 1.405609e+00 1.005613e+00
 97 3.851933e+00 2.558690e-03 2.560000e-03 1.403588e+00 1.003590e+00
 98 3.886762e+00 1.439585e-03 1.440000e-03 1.402017e+00 1.002018e+00
 99 3.923028e+00 6.399181e-04 6.400000e-04 1.400896e+00 1.000896e+00
100 3.960762e+00 1.599949e-04 1.600000e-04 1.400224e+00 1.000224e+00
101 5.000000e+00 0.000000e+00 0.000000e+00 1.400000e+00 1.000000e+00
```

## A.2. Snehurka evolution

Once upon a time, late one evening May 2002, approximately 11 p.m. a time had come to write a new CFD code. The code was intended to replace the overly complex `bob2d` code and work in one, two and three spatial dimensions. The original C

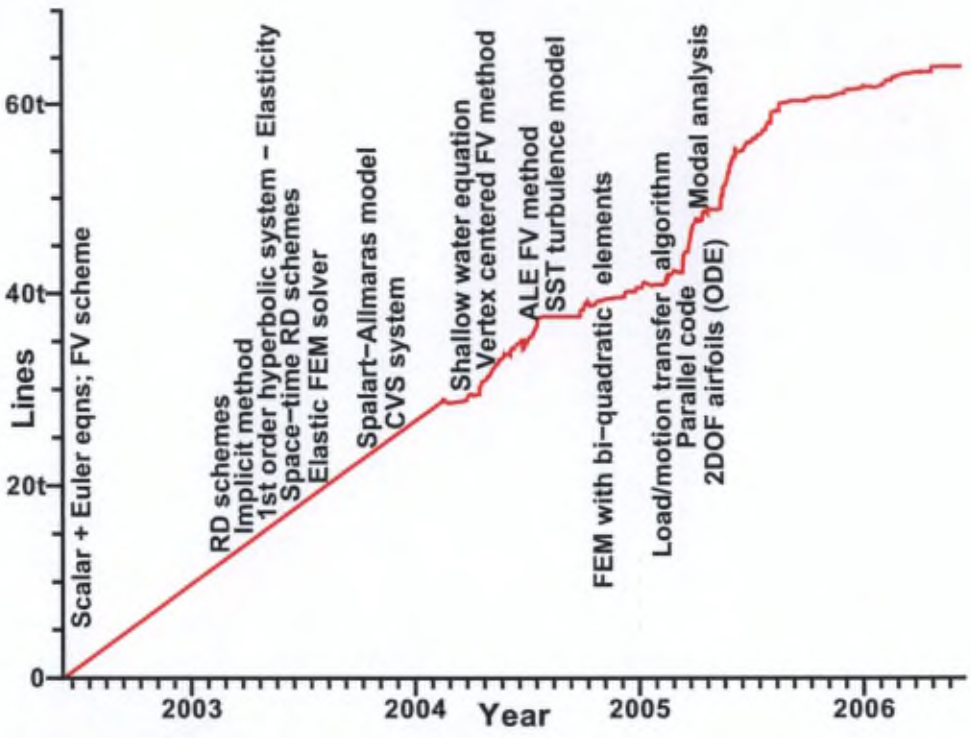


Figure A.1.: Evolution of the ultimate CFD code `Snehurka`. Lines of the code vs. time.

language coding was changed to C++ in the Autumn of 2002 following the advice of Jiří Fürst. The subsequent evolution of Snehurka is shown in Fig. A.1.

# Bibliography

(each reference is followed by the list of the pages where it is cited)


[AB02] R. Abgrall and T. Barth. Residual distribution schemes for conservation laws via adaptive quadrature. *SIAM J. Sci. Comput.*, 24(3):732–769, 2002. 15, 30

[Abg01] R. Abgrall. Toward the ultimate conservative scheme: Following the quest. *JCP*, 167(2):277–315, 2001. 15, 27, 32, 35, 38, 89

[Abg05] R. Abgrall. Construction of high order residual distribution schemes for scalar problems, preliminary results for systems. CFD - High Discretization Methods. VKI Lecture Series 2006–01, Von Karman Institute for Fluid Dynamics, Chausée de Waterloo 72, B-1640 Rhode Saint Genèse, Belgium, 2005. 33

[Abg06] R. Abgrall. Essentially non-oscillatory residual distribution schemes for hyperbolic problems. *Journal of Computational Physics*, 214(2):773–808, 2006. URL `http://www.sciencedirect.com/science/article/B6WHY-4HYD9PY-1/2/e2d40300873ea14bf1e3dd6a1c389aec`. 54, 107, 129, 132

[AJ94] J. J. Alonso and A. Jameson. Fully implicit time-machring aeroelastic solutions. AIAA Paper 94–0056, Jan 1994. 16, 171, 174, 176

[AM01] R. Abgrall and M. Mezine. Construction of second order accurate monotone and stable residual distributive schemes: the unsteady case. RC-MAB Report 2001-33, Universite Bordeaux 1, 2001. 31, 33, 37, 50, 53

[AM03a] R. Abgrall and M. Mezine. Construction of second order accurate monotone and stable residual distribution schemes for unsteady flow problems. *Journal of Computational Physics*, 188:16–55, 2003. 15, 16, 27, 31, 35, 47, 49, 52, 53

[AM03b] R. Abgrall and M. Mezine. Residual distribution scheme for steady problems. 33rd Computational Fluid Dynamics course, VKI Lecture Series 2003–05, Von Karman Institute for Fluid Dynamics, Chausée de Waterloo 72, B-1640 Rhode Saint Genèse, Belgium, 2003. 38, 40

[AM04] R. Abgrall and M. Mezine. Construction of second-order accurate monotone and stable residual distribution schemes for steady problems. *Journal of Computational Physics*, 195(2):474–507, 2004. 15, 16, 27, 33, 34, 35

[AMVD00] A. Athanasiadis, Y. Majewski, P. Vankeirsbilck, and H. Deconinck. Automatic mesh generation and optimization for industrial flow simulations (AMeGOS), surface grid generation and graphical user interface for the 2d hybrid grid approach. Technical Report No. D1.2.1a, ESPRIT, High Performance Computing and Networking (HPCN), Domain 6. Industrial R & D Project 28195, 1. Oct. – 30. Apr. 2000. 94

[Ano44] Anon. Design of wood aircraft structures. Technical Report ANC-18, Army-Navy-Civil Comittee on Aircraft Design Criteria, June 1944. 185

[AR03] R. Abgrall and P. L. Roe. High order fluctuation schemes on triangular meshes. *J. Sci. Comput.*, 19(1–3):3–36, 2003. URL `http://dx.doi.org/10.1023/A:1025335421202`. 15, 33

[Ath05] A. Athanasiadis. *Three-dimensional hybrid grid generation with application to high Reynolds number viscous flows.* PhD thesis, Université Libre de Bruxelles, Von Karman Institute for Fluid Dynamics, 2005. 13, 14, 43, 94

[BAH96] R. L. Bisplinghoff, H. Ashley, and R. L. Halfman. *Aeroelasticity.* Dover Publications, 1996. ISBN 0486691896. 177

[Bar93] T. J. Barth. Recent improvements in high order k-exact reconstruction on unstructured meshes. AIAA Paper 93-0668, AIAA, 1993. 14

[Bar94] T. J. Barth. Aspects of unstructured grids and finite-volume solvers for the Euler and Navier-Stokes equations. In *25th Computational Fluid Dynamics.* von Karman Institute, Mar 1994. 14, 16, 25, 34, 75, 77, 78, 79, 84

[Bar03] T. J. Barth. Numerical methods and error estimation for conservation laws on structured and unstructured meshes. *33rd Computational Fluid dynamics Course, von Karman Institute for Fluid Dynamics*, 2003. 75, 78, 79, 81, 82

[BF90] T. J. Barth and P. O. Frederickson. Higher order solution of the euler equations on unstructured grids using quadratic reconstruction. AIAA Paper 90-0013, AIAA, 1990. 14

[BJ89] T. J. Barth and D. C. Jesperson. The design and application of upwind schemes on unstructured meshes. AIAA Paper 89–0366, AIAA, Jan 1989. 14, 56, 79, 173, 195

[BKC00] J. Blachon, B. Koobus, and R. Carpentier. Multi-physics: Flutter analysis of an AGARD 445.6 wing. URL `http://www-sop.inria.fr/rodeo/personnel/Jean-Antoine.Desideri/FLOWNET/des_agard.html`. 2000. 184

[Bla01] J. Blažek. *Computational Fluid Dynamics: Principles and Applications*. Elsevier, 2001. ISBN 0-08-043009-0. 75, 78

[BO04] T. J. Barth and M. Ohlberger. *Encyclopedia of Computational Mechanics*, volume 1, Fundamentals, chapter Finite Volume Methods: Foundation and Analysis. John Wiley and Sons, Ltd, 2004. ISBN 0-470-84699-2. 13, 14, 75, 76

[BSS02] M. Brdička, L. Samek, and B. Sopko. *Mechanika Kontinua*. Academia, Praha, 2002. ISBN 80-200-0772-5. In Czech. 151, 158, 177

[BUK+03] J. Benetka, J. Ulrych, M. Kladrubský, J. Fořt, and J. Dobeš. Transsonické proudění v přímé lopatkové mříži RS0 - experiment a numerické řešení. *Letecký zpravodaj*, 2:21–26, 2003. 197

[Car00] D. A. Caraeni. *Development of a Multidimensional Residual Distribution Solver for Large Eddy Simulation of Industrial Turbulent Flows*. PhD thesis, Lund Institute of Technology, Sweden, 2000. 15, 50, 52

[CBK06] C. Corre, A. Beccantini, and T. Kloczko. A residual-based compact scheme for computing all-speed flows on unstructured grids. In H. Deconinck and E. Dick, editors, *4th ICCFD Conference*, Ghent, Belgium, July 2006. 15

[CCF01] D. Caraeni, M. Caraeni, and L. Fuchs. A parallel multidimensional upwind algorithm for LES. AIAA paper 2001-2547, AIAA, Anaheim, 2001. 15th AIAA Computational Fluid Dynamics Conference. 31, 50, 52, 56

[CD01] A. Csík and H. Deconinck. Space time residual distribution schemes for hyperbolic conservation laws on unstructured linear finite elements. In M. Baines, editor, *Numerical Methods for Fluid Dynamics VII*, pages 557–564. Oxford University Computing Laboratory, Oxford, 2001. Presented at the ICFD Conference in Oxford, March, 2001. 31, 53

[CD02] A. Csík and H. Deconinck. Space time residual distribution schemes for hyperbolic conservation laws on unstructured linear finite elements. *International Journal for Numerical Methods in Fluids*, 40:573–581, 2002. 31, 53, 197

[CDP01] A. Csík, H. Deconinck, and S. Poedts. Monotone residual distribution schemes for the ideal 2D magnetohydrodynamic equations on unstructured grids. *AIAA Journal*, 39(8):1532–1541, August 2001. xi, 37

[CDP02] A. Csík, H. Deconinck, and S. Poedts. Performance comparison of multidimensional upwind residual distribution and dimensionally split finite volume Roe schemes on the steady solution of conservation laws. In *3rd International Symposium on Finite Volume for Complex Applications, 24-28 June*, Porquerolles, France, 2002. Hermes Penton Ltd, London. 89

[CF05] D. Caraeni and L. Fuchs. Compact third-order multidimensional upwind discretization for steady and unsteady flow simulations. *Computers & Fluids*, 34(4–5):419–441, 2005. URL `http://www.sciencedirect.com/science/article/B6V26-4CB0717-2/2/29bdd33c512a66589275b4ad86cfcf35`. 15, 31, 50, 52

[CFL28] R. Courant, K. O. Friderichs, and H. Lewy. Über die partielen Differenzengleichungen der mathematishen Physik. *Math. Ann.*, 100:32–74, 1928. ix, 67

[CFL67] R. Courant, K. O. Friderichs, and H. Lewy. On the partial differential equations of mathematical physics. *IBM Journal*, 11:215–234, 1967. ix, 67

[CM69] E. Cuthill and J. McKee. Reducing the bandwidth of sparse symmetric matrices. In *Proceedings of the 1969 24th national conference*, pages 157–172, New York, NY, USA, 1969. ACM Press. URL `http://portal.acm.org/citation.cfm?id=805928`. 84, 85

[Coc99] B. Cockburn. Discontinuous Galerkin methods for convection dominated problems. In T. J. Barth and H. Deconinck, editors, *High-Order Methods for Computational Physics*, number 9 in Lecture Notes in Computational Science and Engineering, pages 69–224. Springer, Berlin, 1999. 15

[Coc04] B. Cockburn. *Encyclopedia of Computational Mechanics*, chapter Discontinuous Galerkin Methods for Computational Fluid Dynamics. John Wiley & Sons, Ltd., 2004. 15

[CPNP96] L. A. Catalano, P. D. Palma, M. Napolitano, and G. Pascazio. A critical analysis of multi-dimensional upwinding for the euler equations. *Computers & Fluids*, 25(1):29–38, 1996. 15

[CRD02] A. Csík, M. Ricchiuto, and H. Deconinck. A conservative formulation of the multidimensional upwind distribution schemes for general nonlinear conservation laws. *Journal of Computational Physics*, 179(1):286–312, June 2002. 30

[CRD03] Á. Csík, M. Ricchiuto, and H. Deconinck. Space-time residual distribution schemes for hyperbolic conservation laws over linear and bilinear elements. *33rd Computational Fluid dynamics Course, Von Karman Institute for Fluid Dynamics*, 2003. 31, 47, 53

[CRDP01] A. Csík, M. Ricchiuto, H. Deconinck, and S. Poedts. Space-time residual distribution schemes for hyperbolic conservation laws. In *15th AIAA Computational Fluid Dynamics Conference*, Anaheim, California, June 2001. AIAA 2001-2617. 31, 53

[Csí02] Á. G. Csík. *Upwind Residual Distribution Schemes for General Hyperbolic Conservation Laws and Application to Ideal Magnetohydrodynamics.* PhD thesis, Katholieke Universiteit Leuven, Faculteit Wetenschappen Centrum voor Plasma-Astrofysica, Belgium, October 2002. 15, 27, 30, 31, 35, 53, 89

[DD05a] J. Dobeš and H. Deconinck. Second order blended multidimensional residual distribution scheme for steady and unsteady computations. *Journal of Computational and Applied Mathematics (JCAM)*, 2005. Accepted for publication. Special issue of Third international conference on advanced computational methods in engineering ACOMEN

2005, Ghent, Belgium, May 30 – June 2, 2005. xi, 31, 41, 47, 54, 55, 89, 196

[DD05b] J. Dobeš and H. Deconinck. A second order space-time residual distribution method for solving compressible flow on moving meshes. AIAA Paper 2005-0493, AIAA, 2005. Presented on 43rd AIAA Aerospace Sciences Meeting and Exhibit 10–13 January 2005, Reno, Nevada. 31, 59, 69, 89, 132, 196

[DD06a] J. Dobeš and H. Deconinck. An ALE formulation of the multidimensional RDS for computations on moving meshes. In H. Deconinck and E. Dick, editors, *The Fourth International Conference on Computational Fluid Dynamics, July 10–14*, Ghent, Belgium, July 2006. 61, 196

[DD06b] J. Dobeš and H. Deconinck. Extension of linear second order residual distribution schemes for computations on moving meshes. In J. Příhoda and K. Kozel, editors, *Proceedings of "Topical Problems of Fluid Mechanics 2006"*, pages 27–30. IT CAS CZ, February 2006. ISBN 80-85918-98-6. 61, 196

[DD06c] J. Dobeš and H. Deconinck. A second order unconditionally positive space-time residual distribution method for solving compressible flows on moving meshes. In *Programs and Algorithms of Numerical Mathematics 13, May 28–31.*, pages 60–66, Prague, Czech Republic, 2006. Mathematical Institute, Academy of Sciences. ISBN 80-85823-54-3. 64, 196

[DD06d] J. Dobeš and H. Deconinck. A shock sensor based second order blended (Bx) upwind residual distribution scheme for steady and unsteady compressible flow. In *Eleventh International Conference on Hyperbolic Problems Theory, Numerics, Applications, July 17-21*, Ecole Normale Supérieure de Lyon, Lyon, France, 2006. Springer. To appear. 31, 41, 47, 196

[DDA00] J. Dobeš, H. Deconinck, and A. Athanasiadis. Three-dimensional unstructured grid generation. Stagiaire report, Von Karman Institute for Fluid Dynamics, Belgium, 2000. 94

[DDF05a] J. Dobeš, H. Deconinck, and J. Fořt. Inviscid calculation of a transonic flutter of naca 64a010 profile using a finite volume scheme. In J. Příhoda and K. Kozel, editors, *Proceedings of "Kolokvium Dynamika Tekutin 2005"*, pages 21–24. IT CAS CZ, October 2005. ISBN 80-85918-94-3. 31, 61, 196

[DDF05b] J. Dobeš, H. Deconinck, and J. Fořt. Inviscid calculation of a transonic flutter of NACA 64A010 profile using a finite volume scheme. In J. Příhoda and K. Kozel, editors, *Kolokvium "Dynamika Tekutin 2005"*, pages 21–24. IT CAS CZ, October 2005. ISBN 80-85918-94-3. 171, 196

[DDF06] J. Dobeš, H. Deconinck, and J. Fořt. Comparison of cell centered and vertex centered formulation of finite volume method. *Inženýrská mechanika/Engineering Mechanics*, 13(3):191–200, 2006. ISSN 1210-2717. 96, 123, 197

[DDF07] J. Dobeš, H. Deconinck, and J. Fořt. Design of unsteady nonlinear multidimensional residual distribution schemes – application for moving meshes problems. *Computers and Fluids*, 2007. Submitted. 37

[Dec03] H. Deconinck. Novel methods for convection dominated problems. 33rd Computational Fluid Dynamics course, VKI Lecture Series 2003–05, Von Karman Institute for Fluid Dynamics, Chausée de Waterloo 72, B-1640 Rhode Saint Genèse, Belgium, 2003. 15, 16, 27

[Del96] M. Delanaye. *Polynomial Reconstruction Finite Volume Schemes for the Compressible Euler and Navier-Stokes Equations on Unstructured Adaptive Grids.* PhD thesis, University of Liege, Faculty of Applied Sciences, 1996. 44, 79

[DFD07a] J. Dobeš, J. Fürst, and H. Deconinck. Arbitrary Lagrangian Eulerian formulation: Lax-Wendroff type theorem and convergence study for residual distribution method. *International Journal for Numerical Methods in Fluids*, 2007. Submitted. 35

[DFD07b] J. Dobeš, J. Fürst, and H. Deconinck. Convergence analysis of arbitrary Lagrangian Eulerian formulation for residual distribution schemes. In *ICFD 2007 Conference*, 2007. 35

[DFDF07] J. Dobeš, J. Fürst, H. Deconinck, and J. Fořt. Numerical solution of transonic and supersonic 2d and 3d fluid–elastic structure interaction problems. In *Conference Enumath*, 2007. Submitted. 196

[DFF+01] J. Dobeš, J. Fořt, J. Fürst, J. Halama, and K. Kozel. Comparison of several numerical methods for internal transonic flow problems. *ZAMM*, 81(3):451–452, 2001. ISSN 0044-2267. 197

[DFF+02] J. Dobeš, J. Fürst, J. Fořt, J. Halama, and K. Kozel. Numerical simulation of transonic flow in steam turbine cascades. In H. Sobieczky, editor, *Proceedings of Symposium Transonicum IV*, pages 145–150, Göttingen, September 2002. DLR, Kluwer Academic Publishers. ISBN 1-4020-1608-5. 197

[DFF+03a] J. Dobeš, J. Fořt, J. Fürst, J. Halama, T. Hyhlík, P. Louda, K. Kozel, J. Příhoda, and P. Šafařík. Experimental and numerical analysis of transonic flow through plane turbine cascade. *Engineering Mechanics*, 10(5), 2003. ISSN 1210-2717. 197

[DFF+03b] J. Dobeš, J. Fořt, J. Fürst, J. Halama, and K. Kozel. Numerical solution of transonic flows in a 2D and 3D axial and radial turbine cascades. In J. V. T. Lajos, editor, *Proceedings of "Modelling Fluid Flow" (CMFF'03)*, volume II, pages 1230–1237, Budapest, September 2003. ISBN 96342077740. 197

[DFF+03c] J. Dobeš, J. Fürst, J. Fořt, J. Halama, and K. Kozel. Numerical solution of transonic flows in 2D and 3D axial and radial turbine cascades. In *Proceedings of 5th European conference on Turbomachinery*, pages 1105–1114, Prague, 2003. 197

[DFF+03d] J. Dobeš, J. Fürst, J. Fořt, J. Halama, and K. Kozel. Numerical solution of transonic flows in 2D and 3D axial and radial turbine cascades. In *Proceedings of 12th International conference on fluid flow technologies*, Budapest, 2003. 197

[DFF+04a] J. Dobeš, J. Fořt, J. Fürst, J. Halama, and K. Kozel. Numerical solution of transonic flows in turbine cascades. In *1st International Conference "From Scientific Computing to Computational Engineering"*. University of Patras, 2004. 197

[DFF+04b] J. Dobeš, J. Fořt, J. Fürst, J. Halama, and K. Kozel. Numerical solution of transonic flows in turbine cascades. In *Proceedings of Conference "International Conference "From Scientific Computing to Computational Engineering", 8–10 September, Athens*, 2004. 197

[DFH03] J. Dobeš, J. Fořt, and J. Halama. Numerical solution of transonic turbulent and two-phase flow in turbine cascades. *PAMM*, 3(1):404–405, 2003. 197

[DFH04] J. Dobeš, J. Fořt, and J. Halama. Numerical solution of single- and two-phase transonic flow in axial cascade. In *Proceedings of 4th European Congress on Computational methods in Applied Sciences*

*and Engineering*, volume 1. University of Jyvaskyla, 2004. ISBN 951-39-1868-8. 197

[DFH05] J. Dobeš, J. Fořt, and J. Halama. Numerical solution of single and multiple-phase internal transonic flow problems. *International Journal for Numerical Methods in Fluids*, 48(1):91–97, March 2005. 197

[Dob02] J. Dobeš. Implicit space-time method for laminar viscous flow. Project Report 2002-06, Von Karman Institute for Fluid Dynamics, Belgium, June 2002. 31, 68, 69, 72, 74

[Dow04] E. Dowell, editor. *A Modern Course in Aeroelasticity*. Solid Mechanics and Its Applications. Springer, 4 edition, 2004. ISBN 1402020392. 177

[DR05] H. Deconinck and M. Ricchiuto. Higher order discretization methods. 34rd Computational Fluid Dynamics course, vki lecture series, Von Karman Institute for Fluid Dynamics, Chausée de Waterloo 72, B-1640 Rhode Saint Genèse, Belgium, 2005. 15, 27

[DRAD06] J. Dobeš, M. Ricchiuto, R. Abgrall, and H. Deconinck. Development of residual distribution disretization for viscous problems: extension for scalar unsteady cases and system of navier–stokes equations. Mab report, MAB/Inria Bordeaux, 2006. under preparation. 63, 197

[DRD03a] J. Dobeš, M. Ricchiuto, and H. Deconinck. Implicit space-time residual distribution method for unsteady laminar viscous flow. *33rd Computational Fluid Dynamics Course, Von Karman Institute for Fluid Dynamics*, 2003. 31, 68, 69, 72, 74, 197

[DRD03b] J. Dobeš, M. Ricchiuto, and H. Deconinck. Implicit space-time residual distribution method for unsteady viscous flow. In *16th AIAA Computational Fluid Dynamics Conference, Orlando, Florida*, AIAA-2003-3691, 2003. 31, 197

[DRD03c] J. Dobeš, M. Ricchiuto, and H. Deconinck. Implicit space-time residual distribution method for laminar viscous flow. *6th Belgian National Conference, Gent*, 2003. 31

[DRD05] J. Dobeš, M. Ricchiuto, and H. Deconinck. Implicit space-time residual distribution method for unsteady laminar viscous flow. *Computers and Fluids*, 34:593–615, 2005. ISSN 0045-7930. 31, 197

[DRS93] H. Deconinck, P. L. Roe, and R. Struijs. A multidimensional generalization of Roe's flux difference splitter for the Euler equations. *Computers and Fluids*, 22:215–222, 1993. xi, 27, 30, 66, 67

[DRS03] H. Deconinck, M. Ricchiuto, and K. Sermeus. Introduction to residual distribution schemes and stabilized finite elements. *33rd Computational Fluid dynamics Course, Von Karman Insitute for Fluid Dynamics*, 2003. 15, 69

[DSA00] H. Deconinck, K. Sermeus, and R. Abgrall. Status of multidimensional upwind residual distribution schemes and applications in aeronautics. AAIA Paper 2000-2328, AIAA, 2000. 15, 27, 31

[DSBR93] H. Deconinck, R. Struijs, G. Bourgeois, and P. L. Roe. Compact advection schemes on unstructured meshes. 24th Computational Fluid Dynamics, VKI Lecture Series 1993–04, Von Karman Institute for Fluid Dynamics, Chausée de Waterloo 72, B-1640 Rhode Saint Genèse, Belgium, 1993. 32, 34

[DT85] G. Dhatt and G. Touzot. *The Finite Element Method Displayed.* John Wiley & Sons, 1983, reprinted 1985. ISBN 0-471-90110-5. 16

[DvLPR89] A. Dervieux, B. van Leer, J. Periaux, and A. Rizzi, editors. *Numerical Simulation of Compressible Euler Flows*, Vieweg, Braunschweig, June 1989. GAMM workshop. Proceedings of the GAMM workshop on the Numerical Simulation of Compressible Euler flows, held at INRIA, Rocquencourt, France. 44

[ECY87] J. E. Carson Yates. AGARD standard aeroelastic configurations for dynamic response. Candidate configuration I.-Wing 445.6. Technical Memorandum 100492, NASA, August 1987. 182, 184, 185, 186, 187, 188, 189

[ECYLJTF63] J. E. Carson Yates, N. S. Land, and J. Jerome T. Foughner. Measured and calculated subsonic and transonic flutter characteristics of a 45° sweptback wing planform in air and in freon-12 in the langley transonic dynamics tunnel. Technical Note TN D-1616, NASA, March 1963. 182, 186

[Far04] C. Farhat. *Encyclopedia of Computational Mechanics*, chapter CFD-Based Nonlinear Computational Aeroelasticity. John Wiley & Sons, Ltd., 2004. 15, 16, 34, 35, 83, 115, 161, 163, 165, 166

[FD97] A. Ferrante and H. Deconinck. Solution of the unsteady Euler equations using residual distribution and flux corrected transport. Project Report VKI PR 1997-08, Von Karman Institute for Fluid Dynamics, Belgium, June 1997. 31, 50, 54, 90, 94, 95

[FDHK02] J. Fořt, J. Dobeš, J. Halama, and M. Kladrubský. Upwind and central type schemes applied to internal and external flow problems. *PAMM (Proceedings in Applied Mathematics and Mechanics)*, 1(1):262–263, 2002. ISSN 1617-7061, http://www3.interscience.wiley.com/cgi-bin/abstract/92013333/ABSTRACT. 197

[Fei93] M. Feistauer. *Mathematical Methods in Fluid Dynamics.* Longman Sc & Tech, 1993. ISBN 0582209889. 19, 20, 21, 22, 25, 96

[FFS03] M. Feistauer, J. Felcman, and I. Straškraba. *Mathematical and Computational Methods for Compressible Flow.* Clarendon Press, Oxford, 2003. ISBN 0-19-850588-4. 19, 25, 96

[FGB03] C. Farhat, P. Geuzaine, and G. Brown. Application of a three-field nonlinear fluid-structure formulation to the prediction of the aeroelastic parameters of an f-16 fighter. *Computers and Fluids*, 32:3–29, 2003. 83

[FGG01] C. Farhat, P. Geuzaine, and C. Grandmont. The discrete geometric conservation law and the nonlinear stability of ALE schemes for the solution of flow problems on moving grids. *Journal of Computational Physics*, 174:669–694, 2001. 19, 34, 83

[FK02a] J. Fürst and K. Kozel. Numerical solution of transonic flows through 2D and 3D turbine cascades. *Computing and Visualization in Science*, 4(3):183–189, February 2002. 75, 79

[FK02b] J. Fürst and K. Kozel. Second and third order weighted ENO scheme on unstructured meshes. In *Finite Volumes for Complex Applications*, France, 2002. Hermes. 75, 79

[FLL98] C. Farhat, M. Lesoinne, and P. LeTallec. Load and motion transfer algorithms for fluid/structure interaction problems with non-matching discrete interfaces: Momentum and energy conservation, optimal discretization and application to aeroelasticity. *Computer Methods in Applied Mechanics*, 157:95–114, 1998. 163

[FN99] L. Formaggia and F. Nobile. A stability analysis for the Arbiliary Lagrangian Eulerian formulation with finite elements. *East-West J. of Numerical Mathematics*, 7:105–132, 1999. 19, 35

[FN04] L. Formaggia and F. Nobile. Stability analysis of second-order time accurate schemes for ALE-FEM. *Comput. Methods Appl. Mech Engrg.*, 193:4097–4116, 2004. 19, 21

[Für06] J. Fürst. A weighted least square scheme for compressible flows. *Flow, Turbulence and Combustion*, 76(4):331–342, June 2006. 75, 79, 195

[Für04] J. Fürst. Numerical solution of compressible flows using tvd and eno finite volume methods. Associate Professor Thesis, CTU Prague, 2004. 75, 79

[Geo71] J. A. George. Computer implementation of the finite element method. Technical Report STAN-CS-71-208, Computer Science Departement, Stanford University, 1971. 84, 85, 86

[GF00] H. Guillard and C. Farhat. On the significance of the geometric conservation law for flow computations on moving meshes. *Computer Methods in Applied Mechanics and Engineering*, 190:1467–1482, 2000. 34

[GF03] P. Geuzaine and C. Farhat. Design and time-accuracy analysiss of ALE schemes for inviscid and visocus flow computations on moving meshes. AIAA Paper 2003–3694, June 2003. 21st Applied Aerodynamics Conference, June 23–26, Orlando, Florida. 83

[GGF02] P. Geuzaine, C. Grandmont, and C. Farhat. Design and analysis of ALE schemes with provable second-order time-accuracy for inviscid and viscous flow simulations. Technical Report CU-CAS-02-21, Center for Aerospace Structures. College of Engineering University of Colorado, Campus Box 429, Boulder, Colorado 80309, Nov 2002. 83

[GGF03] P. Geuzaine, C. Grandmont, and C. Farhat. Design and analysis of ALE schemes with provable second-order time-accuracy for inviscid and viscous flow simulations. *Journal of Computational Physics*, 191:206–227, 2003. 34, 83

[GR96] E. Godlewski and P.-A. Raviart. *Numerical Approximation of Hyperbolic Conservation Laws*. Springer, 1996. ISBN 0-387-94529-6. 19, 20, 21, 22, 25, 78, 96

[GS98] S. Gottlieb and C.-W. Shu. Total variational diminishing Runge–Kutta schemes. *Math. Comput.*, 67:73–85, 1998. 15, 80, 81

[GST01] S. Gottlieb, C.-W. Shu, and E. Tadmor. Strong stability-preserving high-order time discretization methods. *SIAM Review*, 43(1):89–112, 2001. ISSN 0036-1445. 15, 80, 81

[GW01] L. Gato and M. Webster. An experimental investigation into the effect of rotor blade sweep on the performance of the variable-pitch wells turbine. *Journal of Power and Energy*, 215:611–622, 2001. 15

[Har83] A. Harten. High resolution schemes for hyperbolic conservation laws. *Journal of Computational Physics*, 49(3):357–393, 1983. URL `http://www.sciencedirect.com/science/article/B6WHY-4DD1XP3-1PC/2/7139ec41e5bce99e04612c431428ead2`. 34

[HFM87] T. J. R. Hughes, L. P. Franca, and M. Mallet. A new finite element formulation for computational fluid dynamics: Vi. convergence analysis of the generalized SUPG formulation for linear time-dependent multidimensional advective-diffusive systems. *Computer Methods in Applied Mechanics and Engineering*, 63(1):97–112, 1987. 14

[HKH03] R. Honzátko, K. Kozel, and J. Horáček. Numerical solution of flow through a cascade and over a profile with dynamical and aeroelastic effects. *PAMM*, 3(1):282–283, 2003. ISSN 1617-7061. URL `www.gamm-proceedings.com`. 161

[HKH04a] R. Honzátko, K. Kozel, and J. Horáček. Flow over a profile in a channel with dynamical effects. *PAMM*, 4(1):322–323, 2004. ISSN 1617-7061. URL `www3.interscience.wiley.com/cgi-bin/abstract/109802044/ABSTRACT`. 161

[HKH04b] R. Honzátko, K. Kozel, and J. Horáček. Numerical solution of flow through a cascade and over a profile with dynamical and aeroelastic effects. In *Flow - Induced Vibration*, volume 2, Paris: École Polytechnique, 2004. ISBN 2-7302-1142-X. 161

[HL05] M. E. Hubbard and A. L. Laird. Achieving high-order fluctuation splitting schemes by extending the stencil. *Computers and Fluids*, 34:443–459, 2005. ISSN 0045-7930. 15

[Hor03] J. Horáček. Nonlinear formulation of oscillations of a profile for aero-hydroelastic computations. In I. Dobiáš, editor, *Dynamics of Machines*, pages 51–56. Institute of Thermomechanics AS CR, 2003. 171

[HR00] M. Hubbard and P. Roe. Compact high-resolution algorithms for time-dependent advection on unstructured grids. *International Journal for Numerical Methods in Fluids*, 33(5):711–736, 2000. 15

[HRTV04] V. Hernandez, J. E. Roman, A. Tomas, and V. Vidal. SLEPc home page. URL `http://www.grycap.upv.es/slepc`. 2004. 156

[HRV03] V. Hernandez, J. E. Roman, and V. Vidal. SLEPc: Scalable Library for Eigenvalue Problem Computations. *Lecture Notes in Computer Science*, 2565:377–391, 2003. 156

[HS02] B. Hægland and B. Skaflestad. A survey of some methods for moving grid and grid adaption. Technical Report Preprint Numerics no. 2/2002, Department of Mathematical Sciences, Norwegian University of Science and Technology, N-7491 Trondheim, Norway., 2002. URL `http://www.math.ntnu.no/preprint/numerics/2002/N2-2002.ps`. 19

[Hub06] M. Hubbard. Very high order, non-oscillatory fluctuation disctribution schemes. In H. Deconinck and E. Dick, editors, *4th ICCFD Conference*, Ghent, Belgium, July 2006. 15

[HWS03] W. Haase, B. Winzell, and V. Selmin, editors. *Progress in Computational Flow–Structure Interaction: Results of the Project UNSI supported by European Union*, volume 81 of *Notes on Numerical Fluid Mechanics and Multidisciplinary Design*. Springer–Verlag, 2003. ISBN 3-540-43902-1. 182

[ICE06] ICEM CFD mesh generation software, 2006. URL `http://www-berkeley.ansys.com/products/pre_processing.html`. 95

[Iso79] K. Isogai. On the transonic-dip mechanism of flutter of a sweepback wing. *AIAA J.*, 17(7):793–795, 1979. 171

[Iso80] K. Isogai. Numerical study of transonic flutter of a two-dimensional airfoil. Technical Report NAL TR-617T, National Aerospace Institue, Tokyo, Japan, 1980. 171

[Iso81] K. Isogai. On the transonic-dip mechanism of flutter of a sweepback wing: Part II. *AIAA J.*, 19(9):1240–1242, 1981. 171

[Iss97] E. Issman. *Implicit Solution Strategies for Compressible Flow Equations on Unstructured Meshes*. PhD thesis, Université Libre de Bruxelles, Faculté de Sciences Appliquées and Von Karman Institute for Fluid Dynamics, October 1997. 15, 68

[Jam] A. Jameson. Analysis and design of numerical schemes for gas dynamics 1 artificial diffusion, upwind biasing, limiters and their effect on accuracy and multigrid convergence. 34

[Jam04] A. Jameson. *Encyclopedia of Computational Mechanics*, volume 3, Fluids, chapter Aerodynamics. John Wiley and Sons, Ltd, 2004. ISBN 0-470-84699-2. 14

[JBW86] A. Jameson, T. J. Baker, and N. P. Weatherill. Calculation of inviscid transonic flow over a complete aircraft. AIAA paper 86-0103, AIAA, 1986. Presented at AIAA 24th Aerospace Sciences Meeting, Reno. 14

[JMC03] G. Jothiprasad, D. J. Mavriplis, and D. A. Caughey. Higher-order time integration schemes for the unsteady navier-stokes equations on unstructured meshes. *Journal of Computational Physics*, 191(2):542–566, 2003. URL `http://www.sciencedirect.com/science/article/B6WHY-4967DN4-1/2/01bd07752d35bd56c5121aba997e187e`. 15

[JP77] J. N. Juang and R. S. Pappa. An eigensystem realization algorithm for modal parameter identification and model reduction. *Journal of Guidance, Control and Dynamics*, 8(5):620–627, 1977. 198

[JT94] A. A. Johnson and T. E. Tezduyar. Mesh update strategies in parallel finite element computations of flow problems with moving boundaries and interfaces. *Computer Methods in Applied Mechanics and Engineering*, 119(1-2):73–94, Nov 1994. 165, 167

[JT96] A. A. Johnson and T. E. Tezduyar. Simulation of multiple spheres falling in a liquid-filled tube. *Computer Methods in Applied Mechanics and Engineering*, 134(3-4):351–373, Aug 1996. 165, 167

[JU56] G. W. Jones and J. R. Unangst. Investigation to determine effects of center-of-gravity location of transonic flutter characteristics of a 45° sweptback wing. Technical Report RM L55K30, NACA, 1956. 182, 186

[KF99] B. Koobus and C. Farhat. Second-order time-accurate and geometrically conservative implicit schemes for flow computations on unstructured dynamic meshes. *Comput. Methods Appl. Mech. Engrg.*, 170(1–2):103–129, 1999. 15, 83, 195

[KK99] G. Karypis and V. Kumar. A fast and high quality multilevel scheme for partitioning irregular graphs. *SIAM Journal on Scientific Computing*, 20(1):359–392, 1999. 85, 86

[Krö97] D. Kröner. *Numerical Schemes for Conservatino Laws*. John Wiley & Sons Ltd., 1997. ISBN 0-471-96793-9. xi, xii, 13, 14, 25, 27, 75, 76, 97

[KRW96] D. Kröner, M. Rokyta, and M. Wierse. A Lax-Wendroff type theorem for upwind finite volume schemes in 2-d. *East-West J. Numer. Math.*, 4:279–292, 1996. 97

[KT00] V. Kalro and T. E. Tezduyar. A parallel 3D computational method for fluid-structure interactions in parachute systems. *Computer Methods in Applied Mechanics and Engineering*, 190(3-4):321–332, 2000. 167

[KvdVvdV06] C. Klaij, J. J. W. van der Vegt, and H. van der Ven. Space-time discontinuous galerkin method for the compressible navier-stokes equations. *Journal of Computational Physics*, 217(2):589–611, 2006. URL `http://www.sciencedirect.com/science/article/B6WHY-4JB9W61-1/2/c0414d638fa30f4339726a63073ee93a`. 15

[LC01] A. Lerat and C. Corre. A residual-based compact scheme for the compressible Navier-Stokes equations. *Journal of Computational Physics*, 170(2):642–675, 2001. 15

[LCJS93] M.-S. Liou and J. Christopher J. Steffen. A new flux splitting scheme. *Journal of Computational Physics*, 107(1):23–39, 1993. URL `http://www.sciencedirect.com/science/article/B6WHY-45P124G-36/2/ab7ede9faab8ca6ec7efe6cd4a2f70d5`. 14

[Lep04] I. Lepot. *A parallel high-order implicit finite volume method for three-dimensional inviscid compressible flows on deforming unstructured meshes.* PhD thesis, University of Liege, 2004. 34, 79, 103

[LeV99] R. J. LeVeque. *Numerical Methods for Conservation Laws.* Birkhäuser, 1999. ISBN 3-7643-2723-5. 19, 20, 25, 67, 96

[LeV02] R. J. LeVeque. *Finite Volume Methods for Hyperbolic Problems.* Cambridge University Press, 2002. ISBN 0-521-81987-6. 14, 19, 20, 25, 75, 78, 96, 149

[LF93] M. Lesoinne and C. Farhat. Stability analysis of dynamic meshes for transient aeroelastic computations. AIAA Paper 93-3325, AIAA, 1993. 11th AIAA Computational Fluid Dynamics Conference, July 6–9, Orlando, Florida. 161

[MA02] M. Mezine and R. Abgrall. Upwind multidimensional residual schemes for steady and unsteady flows. In *ICCFD2, International Conference on Computational Fluid Dynamics 2*, pages 165–170, Sydney, Australia, 15-19 July 2002. 31, 53

[Mae96] J. Maerz. Improving time accuracy for residual distribution schemes. Project Report 1996-17, Von Karman Institute for Fluid Dynamics, Belgium, Chausée de Waterloo 72, B-1640 Rhode Saint Genèse, Belgium, June 1996. 31

[Mah06a] Hawaii forestry trees s, 2006. URL `http://www.ctahr.hawaii.edu/forestry/Data/Species_Pages/Page_S.html`. 183

[Mah06b] Honduras mahagony (swietenia macrophylla), 2006. URL `http://www.nparks.gov.sg/nursery/uploadfiles/swieteniamacrophylla01p454.jpg`. 183

[Maj84] A. Majda. *Compressible Fluid Flow and Systems of Conservation Laws in Several Space Variables.* Springer, 1984. ISBN 0387960376. 20

[Mar58] D. J. Martin. Summary of flutter experiences as a guide to the preliminary design of lifting surfaces on missiles. Technical Report TN 4197, NACA, 1958. supersedes NACA RM L51J30. 177

[Mar99] F. Maršík. *Termodynamika kontinua.* Academia, Praha, 1999. ISBN 80-200-0758-X. In Czech. 24, 25

[Mec73] E. A. Mechtly. The international system of units. Physical constants and conversion factors. Second revision. Technical Report NASA SP–7012, NASA, 1973. 182

[Met06] Metis home page, 2006. URL `http://glaros.dtc.umn.edu/gkhome/metis/metis`. 68, 85

[Meu99] G. Meurant. *Computer Solution of Large Linear Systems*, volume 28 of *Studies in Mathematics and Its Applications.* North-Holland, 1999. ISBN 0-444-50169-X. 84

[Mez02] M. Mezine. *Conception de Schémas Distributifs pour l'aérodynamique stationnaire et instationnaire.* PhD thesis, École doctorale de mathmatiques et informatique, Université de Bordeaux I, 2002. in French. 15, 35, 50, 52

[Mic00] C. Michler. Development of an arbitrary Lagrangian Eulerian formulation for unsteady flow computations on moving meshes using residual distribution schemes. Project Report 2000-13, Von Karman Institute for Fluid Dynamics, Belgium, Chausée de Waterloo 72, B-1640 Rhode Saint Genèse, Belgium, June 2000. 59, 66

[MJ87] D. Mavriplis and A. Jameson. Multigrid solution of the euler equations on unstructured and adaptive meshes. Technical Report ICASE-87-53; NAS 1.26178346; NASA-CR-178346, NASA Langley Research Center, 1987. URL `http://ntrs.nasa.gov/archive/nasa/casi.ntrs.nasa.gov/19870017447_1987017447.pdf`. 14

[MPI06] Mpi forum home page, 2006. URL `http://www.mpi-forum.org`. 68

[MRAD03] M. Mezine, M. Ricchiuto, R. Abgrall, and H. Deconinck. Monotone and stable residual distribution schemes on prismatic space-time elements for unsteady conservation laws. *33rd Computational Fluid dynamics Course, Von Karman Institute for Fluid Dynamics*, 2003. 31, 47, 50, 52, 53, 55

[MSD03] C. Michler, H. D. Sterck, and H. Deconinck. An arbitrary Lagrangian Eulerian formulation for residual distribution schemes on moving grids. *Computers and Fluids*, 32(1):59–71, 2003. 13, 59, 66, 194

[MvBdB04] C. Michler, E. H. van Brummelen, and R. de Borst. An interface newton-krylov solver for fluid-structure interaction. *Int. J. Num. Meth. Fluids*, 2004. (To appear). 166

[MW04] J. Majewski and R. Wieteska. Investigation of WENO schemes for 3D unstructured grids. In *XXI ICTAM, 15–21 August*, Warsaw University Of Technology, Institute of Aeronautics and Applied Mechanics, Nowowiejska 24, Warsaw, Poland, 2004. 89

[MY06] D. J. Mavriplis and Z. Yang. Construction of the discrete geometric conservation law for high-order time-accurate simulations on dynamic meshes. *Journal of Computational Physics*, 213(2):557–573, 2006. URL `http://www.sciencedirect.com/science/article/B6WHY-4H80T5R-4/2/1a7fbc45abb181f8e24262ea79834c9d`. 34, 115

[Ni81] R. H. Ni. A multiple grid scheme for solving Euler equations. *AIAA Journal*, 20(1), 1981. 27, 43

[NR04] H. Nishikawa and P. Roe. On high-order fluctuation splitting schemes for Navier-Stokes equations. In *ICCFD 3. 3rd Interational Conference on Computational Fluid Dynamics*. Springer-Verlag, 2004. 15

[Pai95] H. Paillère. *Multidimensional Upwind Residual Distribution Schemes for the Euler and Navier-Stokes Equations on Unstructured Grids*. PhD thesis, Université Libre de Bruxelles, Von Karman Institute for

Fluid Dynamics, June 1995. 15, 25, 27, 34, 40, 45, 68, 69, 71, 73, 89, 179

[PET07] PETSc home page. URL `http://www.mcs.anl.gov/petsc`. 2007. 68, 85

[PF01] S. Piperno and C. Farhat. Partitioned procedures for the transient solution of coupled aeroelastic problems part II: Energy transfer analysis and three-dimensional applications. *Comput. Meths. Appl. Mech. Engrg.*, 190(24):3147–3170, 2001. 177, 192

[PPRN05] P. D. Palma, G. Pascazio, G. Rossiello, and M. Napolitano. A second-order-accurate monotone implicit fluctuation splitting scheme for unsteady problems. *Journal of Computational Physics*, 208(1):1–33, 2005. 15, 31, 89

[RA06] M. Ricchiuto and R. Abgrall. Stable and covergent RD schemes for steady and time dependent conservation laws. In J. Příhoda and K. Kozel, editors, *Proceedings of "Topical Problems of Fluid Mechanics 2006"*, pages 27–30. IT CAS CZ, February 2006. ISBN 80-85918-98-6. 129, 132

[RAD03] M. Ricchiuto, R. Abgrall, and H. Deconinck. Construction of very high order residual distribution schemes for unsteady scalar advection: Preliminary results. *33rd Computational Fluid dynamics Course, Von Karman Institute for Fluid Dynamics*, 2003. 31

[RAD06] M. Ricchiuto, R. Abgrall, and H. Deconinck. Application of conservative residual distribution schemes to the solution of the shallow water equations on unstructured meshes. *Journal of Computational Physics*, 2006. submitted. 33

[RCD04] M. Ricchiuto, Á. Csík, and H. Deconinck. Conservative non-linear residual distribution schemes for the solution of general unsteady systems of conservation laws. 2004. Presented at ICCFD3 Toronto, Canada, July 2004. 31, 40

[RCD05] M. Ricchiuto, A. Csík, and H. Deconinck. Residual distribution for general time-dependent conservation laws. *Journal of Computational Physics*, 209(1):249–289, 2005. 30, 31, 33, 39, 40, 47, 49

[RD99] M. Ricchiuto and H. Deconinck. Time accurate solution of hyperbolic partial differential equations using FCT and residual distribution. Stagiarie Report VKI SR 1999-33, Von Karman Institute for Fluid

Dynamics, Belgium, Chausée de Waterloo 72, B-1640 Rhode Saint Genèse, Belgium, 1999. 31

[Rek95] K. Rektorys. *Přehled užité matematiky (Overview of Applied Mathematics).* Prometheus, Praha, 1995. ISBN 80-85849-72-0. In Czech. 23, 184

[Ric01] M. Ricchiuto. Space-time residual distribution schemes and application to unsteady two-phase flow computations on unstructured meshes. Project Report 2001-23, Von Karman Institute for Fluid Dynamics, Belgium, Chausée de Waterloo 72, B-1640 Rhode Saint Genèse, Belgium, June 2001. 31, 53

[Ric05] M. Ricchiuto. *Construction and Analysis of Compact Residual Discretizations for Conservation Laws on Unstructured Meshes.* PhD thesis, Université Libre de Bruxelles, Von Karman Institute for Fluid Dynamics, 2005. ISBN 2-930389-16-8. 15, 16, 27, 30, 31, 32, 33, 34, 35, 39, 40, 41, 49, 94, 96

[Roe81] P. L. Roe. Approximate Riemann solvers, parameter vectors, and difference schemes. *J. Comput. Phys.*, 43:357–372, 1981. 14, 16, 28, 30, 67, 78, 82, 173

[Roe82] P. L. Roe. Fluctuations and signals – a framework for numerical evolution problems. In K. W. Morton and M. J. Baines, editors, *Numerical Methods for Fluid Dynamics*, pages 219–257. Academic Press, 1982. 13, 27

[Roe90] P. L. Roe. The 'optimum' upwind advection on a triangular mesh. Technical Report NASA-CR-187459, ICASE-90-75, NASA Center for AeroSpace Information (CASI), 1990. URL `http://ntrs.nasa.gov/archive/nasa/casi.ntrs.nasa.gov/19910000937_1991000937.pdf`. 89

[RR92] M. Renardy and R. C. Rogers. *An Introduction to Partial Differential Equations.* Texts in Applied Mathematics. Springer-Verlag, New York Berlin Heidelberg, May 1992. ISBN 0-387-97952-2. 20

[RVAD05] M. Ricchiuto, N. Villedieu, R. Abgrall, and H. Deconinck. High order residual distribution schemes: Discontinuity capturing crosswind dissipation and extension to advection–diffusion. CFD – High Discretization Methods. VKI Lecture Series 2006–01, Von Karman Institute for Fluid Dynamics, Chausée de Waterloo 72, B-1640 Rhode Saint Genèse, Belgium, 2005. 15, 33, 63

[RVAD07] M. Ricchiuto, N. Villedieu, R. Abgrall, and H. Deconinck. On uniformly high-order accurate residual distribution schemes for advection-diffusion. *Journal of Computational and Applied Mathematics*, 2007. URL `http://www.sciencedirect.com/science/article/B6TYH-4MM7T95-3/2/1ce4887906d9be71ec81fd9a5b11ce66`. 15

[SBK+00] K. Stein, R. Benney, V. Kalro, T. E. Tezduyar, J. Leonard, and M. Accorsi. Parachute fluid-structure interactions: 3-d computation. *Computer Methods in Applied Mechanics and Engineering*, 190(3-4):373–386, 2000. 167

[SBTP01] K. Stein, R. Benney, T. Tezduyar, and J. Potvin. Fluid-structure interactions of a cross parachute: numerical simulation. *Computer Methods in Applied Mechanics and Engineering*, 191(6-7):673–687, 2001. 167

[SC79] V. Schmitt and F. Charpin. Pressure distributions on the Onera–M6–wing at transonic Mach numbers. Advisory Report AGARD-AR-138, Advisory Group for Aerospace Research & Development, 1979. 123

[SD03] K. Sermeus and H. Deconinck. Drag prediction validation of a multi-dimensional upwind solver. CFD-based aircraft drag prediction and reduction, VKI Lecture Series 2003–02, Von Karman Institute for Fluid Dynamics, Chausée de Waterloo 72, B-1640 Rhode Saint Genèse, Belgium, 2003. 15

[SdBH04] E. Stein, R. de Borst, and T. J. R. Huges, editors. *Encyclopedia of Computational Mechanics.* John Wiley & Sons, Ltd., 2004. ISBN 978-0-470-84699-5. 16, 75

[SFH05] P. Sváček, M. Feistauer, and J. Horáček. Numerical simulation of flow induced airfoil vibrations with large amplitudes. *Journal of Fluids and Structures*, 2005. URL `http://www.karlin.mff.cuni.cz/ms-preprint`. To appear. Also avalible as Preprint No. MATH-knm-2005/1. 171, 194

[Shu99] C.-W. Shu. *High-Order Methods for Computational Physics*, chapter High Order ENO and WENO Schemes for Computational Fluid Dynamics, pages 439–582. Lecture Notes in Computational Science and Engineering. Springer-Verlag Berlin Heidelberg New York, 1999. ISBN 3-540-65893-9. 80, 81

[Shu03] C. W. Shu. Introduction to essentially non oscillatory, weighted essentially non oscillatory and discontinuous galerkin finite element schemes. 33rd Computational Fluid Dynamics course, VKI Lecture Series 2003–05, Von Karman Institute for Fluid Dynamics, Chausée do Waterloo 72, B-1640 Rhode Saint Genèse, Belgium, 2003. 14

[Ski98] S. S. Skiena. *The Algorithm Design Manual.* Springer-Verlag New York, Inc., 1998. ISBN 0-387-94860-0. 84

[SR95] D. Sidilkover and P. L. Roe. Unification of some advection schemes in two dimensions. Technical Report NASA-CR-195044, ICASE-Report-95-10, NASA, ICASE, 1995. URL `http://hdl.handle.net/2002/14561`. 15, 89

[SWL06] Y. Sun, Z. J. Wang, and Y. Liu. Spectral (finite) volume method for conservation laws on unstructured grids vi: Extension to viscous flow. *Journal of Computational Physics*, 215(1):41–58, 2006. 15

[TA06] C. Tave and R. Abgrall. Construction and stabilization of a third order residual distribution scheme. In H. Deconinck and E. Dick, editors, *4th ICCFD Conference*, Ghent, Belgium, July 2006. 15

[Tad88] E. Tadmor. Convenient total variation diminishing conditions for nonlinear difference schemes. *SIAM J. Num. Anal.*, 25:1002–1014, 1988. 34

[Tec06] Tecplot home page, 2006. URL `http://www.tecplot.com`. 94

[Tez04] T. E. Tezduyar. *Encyclopedia of Computational Mechanics*, volume 3, Fluids, chapter Finite Element Methods for Fluid Dynamics with Moving Boundaries and Interfaces. John Wiley & Sons, Ltd., 2004. ISBN 0-470-84699-2. 14

[TH82] T. Tezduyar and T. Hughes. Development of time-accurate finite element techniques for first-order hyperbolic systems with particular emphasis on the compressible euler equations. Technical Report NASA-CR-204772, NASA Ames Research Center, 1982. URL `http://ntrs.nasa.gov/archive/nasa/casi.ntrs.nasa.gov/19970023187_1997034954.pdf`. 14

[The35] T. Theodorsen. General theory of aerodynamic instability and the mechanism of flutter. Report 496, NACA, 1935. 177

[The40] T. G. Theodorsen. Mechanism of flutter, a theoretical and experimental investigation of the flutter problem. NACA Report 685, NACA, 1940. 177

[TO01a] T. Tezduyar and Y. Osawa. Fluid-structure interactions of a parachute crossing the far wake of an aircraft. *Computer Methods in Applied Mechanics and Engineering*, 191(6-7):717–726, 2001. 167

[TO01b] T. Tezduyar and Y. Osawa. The multi-domain method for computation of the aerodynamics of a parachute crossing the far wake of an aircraft. *Computer Methods in Applied Mechanics and Engineering*, 191(6-7):705–716, 2001. 167

[Tor97] E. F. Toro. *Riemann Solvers and Numerical Methods for Fluid Dynamics*. Springer, 1997. ISBN 3540616764. 78

[TS06] T. E. Tezduyar and M. Senga. Stabilization and shock-capturing parameters in SUPG formulation of compressible flows. *Computer Methods in Applied Mechanics and Engineering*, 195(13-16):1621–1632, 2006. 14

[vdW98] E. T. A. van der Weide. *Compressible Flow Simulation on Unstructured Grids Using Multi-dimensional Upwind Schemes*. PhD thesis, Technische Universiteit Delft, Von Karman Institute for Fluid Dynamics, 1998. 15, 27, 34, 35, 71, 73, 89, 179, 197

[Ven95a] V. Venkatakrishnan. Convergence to steady state solutions on the euler equations on unstructured grids with limiters. *J. Comput. Phys.*, 118:120–130, 1995. 79

[Ven95b] V. Venkatakrishnan. A perspective on unstructured grid flow solvers. Technical Report ICASE-Report-95-3, NASA-CR-195025, NASA LaRC Technical Library Digital Repository, 1995. URL `http://hdl.handle.net/2002/14570`. 78

[VM95] V. Venkatakrishnan and D. J. Mavriplis. Implicit method for the computation of unsteady flows on unstructured grids. Technical Report ICASE-Report-95-60, NASA-CR-198206, NASA LaRC Technical Library Digital Repository, 1995. URL `http://hdl.handle.net/2002/14583`. 78

[VM96] V. Venkatakrishnan and D. J. Mavriplis. Implicit method for the computation of unsteady flows on unstructured grids. *Journal of Computational Physics*, 127(2):380–397, 1996. URL `http://www.sciencedirect.com/science/article/B6WHY-45MGW4X-2Y/2/539074ed2827e91469ec9e631bc68a6c`. doi:10.1006/jcph.1996.0182. 78

[WH74] R. Warming and Hyett. The modified equation approach to the stability and accuracy analysis of finite-difference methods. *Journal of Copmutational Physics*, (14):159–179, 1974. 92

[WH94] N. P. Weatherill and O. Hassan. Efficient three-dimensional Delaunay triangulation with automatic point creation and imposed boundary constraints. *International Journal for Numerical Methods in Engineering*, 37(12):2005–2039, June 1994. 94

[WK98] W. A. Wood and W. L. Kleb. Comments on the diffusive behavior of two upwind schemes. Technical memorandum NASA/TM-1998-208738, NASA, 1998. URL `http://hdl.handle.net/2002/14811`. 89

[Woo01] W. A. Wood. *Multi-dimensional Upwind Fluctuation Splitting Scheme with Mesh Adaption for Hypersonic Viscous Flow.* PhD thesis, Virginia Polytechnic Institute and State University, 2001. URL `http://scholar.lib.vt.edu/theses/available/etd-11292001-094038`. 89

[YKM+03] Z. Yosibash, R. M. Kirby, K. Myers, B. Szabó, and G. Karniadakis. High-order finite elements for fluid-structure interaction problems. In *44th AIAA/ASME/ASCE/AHS Structures, Structural Dynamics, and Materials Conference, 7-10 April, Norfolk, Virginia*, number 2003-1729. AIAA, 2003. URL `http://www.dam.brown.edu/people/yosibash/home_files/2003_1729.pdf`. 182, 183, 185

[YM05] Z. Yang and D. J. Mavriplis. Unstructured dynamic meshes with higher-order time integration schemes for the unsteady navier-stokes equation. AIAA Paper 2005-1222, AIAA, Jan 2005. 43rd AIAA Aerospace Sciences Meeting, Reno NV. 165

[ZH76] M. J. Zucrow and J. D. Hoffman. *Gas Dynamics.* John Wiley and Sons, Inc., 1976. ISBN 0-471-98440-X. 132, 201

[ZT00a] O. C. Zienkiewicz and R. L. Taylor. *Finite Element Method*, volume The Basis. McGraw-Hill, fifth edition, 2000. ISBN ISBN 0-7506-5049-4. 16

[ZT00b] O. C. Zienkiewicz and R. L. Taylor. *Finite Element Method*, volume 1 – The Basis. Butterworth Heinemann, London, 2000. ISBN 0750650494. 152, 153

# Index